

Florian König

Prompt Photon Production Predictions  
at NLO and in POWHEG

2016



Theoretische Physik

Prompt Photon Production Predictions  
at NLO and in POWHEG

Inaugural-Dissertation  
zur Erlangung des Doktorgrades  
der Naturwissenschaften im Fachbereich Physik  
der Mathematisch-Naturwissenschaftlichen Fakultät  
der Westfälischen Wilhelms-Universität Münster

vorgelegt von  
Florian König  
aus Coesfeld  
– 2016 –

Dekan/Dekanin:	Prof. Dr. Christian Weinheimer
Erster Gutachter:	Prof. Dr. Michael Klasen
Zweiter Gutachter:	Prof. Dr. Gernot Münster
Datum der mündlichen Prüfung:	5.12.2016
Tag der Prüfung:	5.12.2016

## **Zusammenfassung**

In Hadronenkollisionen erzeugte harte Photonen gelten seit Langem als eine der wichtigsten Observablen für die Erfassung der dynamischen Eigenschaften der starken Wechselwirkung. Insbesondere in Schwerionenkollisionen, gelten sie, bei kleinen Transversalimpulsen, als ein mögliches Signal des erzeugten, stark wechselwirkenden Mediums. In dieser Arbeit präsentiere ich eine Berechnung des Photonproduktionsprozesses in nächstführender Ordnung der Störungstheorie der Quantenchromodynamik, Vorhersagen bei niedrigen Transversalimpulsen mit Hilfe des Programmes **JETPHOX** und eine Anpassung meiner Rechnung an Partonschauergeneratoren mit Hilfe des **POWHEG BOX** Frameworks. Die Rechnung nächstführender Ordnung wird hinsichtlich ihrer theoretischen Unsicherheiten untersucht. Weiterhin wird geprüft und letztendlich bestätigt, dass Daten des ALICE Experiments zu direkten Photon vereinbar sind mit einem Überschuss an Photonen, welcher als thermisches Photonsignal interpretiert werden kann. Zuletzt wird gezeigt, dass die an Partonschauer angepassten Berechnungen die Beschreibung von PHENIX Daten, im Vergleich zu der Rechnung endlicher Ordnung, qualitativ verbessern.

## **Abstract**

Prompt photons produced in hadron collisions have long been established as one of the primary observables for accessing strong interaction dynamics. In particular, at low transverse momentum they provide a probe of the strongly interacting medium produced in heavy ion collisions. I present a calculation of prompt photon production at next-to-leading order, predictions at low transverse momentum using `JETPHOX` and a matching of my calculation to parton showers using the `POWHEG BOX` framework. The fixed-order results are examined with regard to theoretical uncertainties and the existence of a non-prompt photon signal, compatible with a thermal photon spectrum, is verified for direct photon data from ALICE. The parton shower matched calculation is shown to qualitatively improve the description of data from PHENIX.

# Contents

<b>1</b>	<b>Introduction</b>	<b>10</b>
<b>2</b>	<b>Quantum Chromodynamics</b>	<b>12</b>
2.1	Parton Model . . . . .	12
2.2	QCD Lagrangian . . . . .	13
2.3	Asymptotic Freedom . . . . .	15
2.4	Perturbation Theory . . . . .	19
2.4.1	Infrared safety . . . . .	19
2.4.2	Factorization . . . . .	22
2.5	Subtraction Methods . . . . .	27
2.5.1	CS dipole subtraction . . . . .	30
2.5.2	FKS subtraction . . . . .	37
2.6	QCD Phases . . . . .	41
<b>3</b>	<b>Prompt Photon Production</b>	<b>45</b>
3.1	QED Lagrangian . . . . .	46
3.2	Hadronic Structure of the Photon . . . . .	47
3.3	Calculation . . . . .	51
3.3.1	NLO direct and LO fragmentation . . . . .	51
3.3.2	Consistency checks . . . . .	54
3.4	phoSec . . . . .	59
3.5	JETPHOX . . . . .	73
<b>4</b>	<b>Photon Fragmentation Functions</b>	<b>75</b>
4.1	Determination . . . . .	75
4.2	Comparison at low $p_T$ . . . . .	77
<b>5</b>	<b>Heavy Ion Collisions</b>	<b>83</b>
5.1	Collision Stages . . . . .	83
5.2	Initial State Effects . . . . .	86
5.2.1	Glauber approach . . . . .	87
5.2.2	Nuclear PDFs . . . . .	90
5.3	Direct and Prompt Photon Production . . . . .	95
5.3.1	Slope parameter . . . . .	96
5.3.2	Effect of pQCD uncertainties . . . . .	97

<b>6</b>	<b>Parton Shower Matching</b>	<b>104</b>
6.1	Parton Showers . . . . .	105
6.1.1	Branching probabilities . . . . .	106
6.1.2	Evolution variables . . . . .	109
6.1.3	Large- $N_c$ limit . . . . .	110
6.2	NLO Matching . . . . .	112
6.2.1	MC@NLO . . . . .	112
6.2.2	POWHEG method . . . . .	114
6.2.3	POWHEG BOX . . . . .	115
6.3	Prompt Photon Production . . . . .	118
6.3.1	POWHEG BOX implementation . . . . .	118
6.3.2	Born zero . . . . .	126
6.3.3	Simulation of the fragmentation contribution . . . . .	130
6.3.4	Parton shower with PYTHIA 8 . . . . .	131
6.3.5	Photon rate enhancement . . . . .	137
6.4	Comparison with LO and PHENIX Data . . . . .	143
6.4.1	Prompt photon transverse momentum spectrum . . . . .	144
6.4.2	Isolated photons . . . . .	147
6.4.3	Leading jet and charged hadron . . . . .	149
6.4.4	Transverse momentum of photon-jet and -hadron pairs . . . . .	150
6.4.5	Rapidity correlation of photon-hadron-pairs . . . . .	152
6.4.6	Azimuthal correlation of photon-hadron-pairs . . . . .	153
<b>7</b>	<b>Conclusion and Outlook</b>	<b>156</b>
<b>A</b>	<b>Conventions</b>	<b>158</b>
<b>B</b>	<b>Feynman Rules</b>	<b>160</b>
<b>C</b>	<b>Prompt Photon Production Cross Section</b>	<b>162</b>
C.1	Leading Order Direct . . . . .	162
C.1.1	Matrix elements . . . . .	162
C.1.2	Phase space . . . . .	163
C.1.3	Cross section . . . . .	165
C.2	Next to Leading Order Direct . . . . .	166
C.2.1	Virtual corrections . . . . .	166
C.2.2	Real corrections . . . . .	180
C.2.3	Real phase space . . . . .	183
C.2.4	NLO cross section . . . . .	184
C.2.5	QCD Dipoles . . . . .	185
C.2.6	QED Dipoles . . . . .	196
C.2.7	NLO cross section with CS dipoles . . . . .	206
C.3	Leading Order Fragmentation . . . . .	207



<b>D Splitting functions at LO</b>	<b>208</b>
D.1 Sudakov decomposition . . . . .	208
D.2 Phase space factorization . . . . .	209
D.3 Quark to quark splitting . . . . .	210
D.4 Gluon to quark splitting . . . . .	212
D.5 Gluon to gluon splitting . . . . .	213
D.6 Quark to gluon splitting . . . . .	216
<b>Bibliography</b>	<b>217</b>

# 1 Introduction

For several decades, Quantum Chromodynamics (QCD) has written a history of successes. Even though it is a theory which is, at easily accessible energy scales, non-perturbative, it has been possible to construct a highly precise, perturbative description of high energy particle collisions with the help of factorization theorems, which separate the non-perturbative and perturbative components of an observable. The development of the theoretical tools always went hand in hand with the construction of particle colliders that reached for the boundaries of what has been technologically possible. Nowadays, the techniques for experimental measurements have become so sophisticated and precise that higher order corrections, beyond the leading order (LO) and indeed beyond the next-to-leading order (NLO), to QCD processes can no longer be neglected. In the age of the LHC, the Large Hadron Collider, achieving the highest precision in QCD predictions is of tremendous importance to assess the background to not yet observed hypothetical processes beyond the verified standard model (SM). For instance, it has become possible to finally detect the last missing piece of the SM, the Higgs-boson.

Likewise, through the increasing center of mass (CM) energies available for heavy ion collisions, the creation and indirect detection of a new state of QCD matter, the quark-gluon-plasma (QGP), came into reach. To that end, the production of highly energetic photons in hadron collisions has long been regarded as one of the key processes to access the properties of QCD. For instance, supposed to be a rather clean probe, they allow the assessment of initial state effects, i.e. the parton distribution functions (PDFs), already at LO in hadroproduction. However, often the experimental measurements have been focused on isolated photon production. In its role as an electromagnetic probe created in thermalized QCD matter, with its high multiplicity hadron background, it is though no longer possible to isolate the photon. This, on the other hand, introduces complications due to the existence of effects, which obfuscate the simple LO interpretation of the photon production process, as a process where a photon is created in the medium back to back with other partons and traverses it without interactions: In fact, non-isolated photons can be produced by fragmentation in a jet of particles, which can interact with the medium prior to fragmenting. These contributions are of a non-perturbative nature and not very well constrained, as the latest fits are about two decades old.

Other than by providing new and better fits to the fragmentation contributions and the PDFs, fixed order calculations can be improved upon by resumming certain dominant contributions from higher orders. A variant of such a resummation is provided by parton shower generators, which aim at a simulation of the event and allow for a complete and realistic theoretical analysis of particle collisions. However, since these event generators are normally based on LO results, a logical step forward is the inclusion of

NLO corrections in these programs. But this is not easily done and requires a careful matching of the fixed order and resummed contributions.

Retracing some of the historical beginnings of QCD, I will in Chapter 2 review some of the key properties of strong interactions and the specific techniques used for the perturbative calculations in this thesis. In the following Ch. 3 the production of prompt photons is discussed and implementations of fixed order calculations are presented. Ch. 4 is a study of existing photon fragmentation function parametrizations by means of proton-proton collision data. The role of photons in the measurement of the QGP created in heavy ion collisions is discussed and evaluated in detail in Ch. 5. Afterwards, in Ch. 6, parton showers and NLO matching are discussed and an implementation of prompt photon production in the POWHEG BOX framework is presented and its predictions are compared to experimental measurements.

In the extensive appendix, the concrete calculations for the process are documented in detail.

## 2 Quantum Chromodynamics

The phenomenology of high energy particle colliders hinges on a well-founded understanding of the strong interaction dynamics of hadrons and their constituents. Fortunately, experimental studies of strong interactions have a long, successful history, first and foremost in the collider experiments of the 1960s and 1970s and the verification of Quantum Chromodynamics (QCD). In essence, three types of collision experiments are prevalent, classifiable by where strong interactions come into play. At  $e^+e^-$  colliders such as SPEAR and SLC at SLAC, PETRA at DESY and LEP at CERN the effects of strong interactions on the produced particles have been studied most cleanly, allowing for the first observation of quark-jets [1] and gluon-jets [2]. On the other hand, the exploration of  $eA$  collisions – for example fixed target experiments at SLAC and HERA at DESY – has shed light on the initial state hadron and its constituents, culminating in the validation of Bjorken scaling and the parton model [3]. Furthermore,  $p\bar{p}$  collisions at Tevatron and  $pp$ ,  $pA$  and  $AA$  collisions at RHIC and LHC, with its completely hadronic initial state, allowed and still allow the study of purely strong interactions; with heavy ion collisions even achieving the creation of thermalized matter. In all these cases, depending on the observable, strong interactions make up either the bulk of the background that is to be understood and suppressed or are indeed themselves the object of study. As such, strong interactions and its quantum field theoretic formulation – QCD – lie at the core of collider phenomenology.

The present chapter aims at presenting an overview of the properties of QCD, especially those central to the work presented in this thesis: I will shortly explain the parton model, introduce the mathematical representation of QCD, followed by a look on asymptotic freedom and its implications on QCD's poster child, deep inelastic scattering, and discuss problems of perturbation theory and their solutions. Finally, the phase diagram of QCD is reviewed. Since much of the literature on QCD relies on historically grown concepts predating QCD, some corner stones of the historical development are cited along the presentation in the following sections. General introductions to (perturbative) QCD can be found for example in [4, 5, 6, 7, 8].

### 2.1 Parton Model

A crucial move towards a Quantum Field Theory of strong interactions has been made with the introduction of quarks as elementary constituents of hadrons in 1964 by Gell-Mann [9] and Zweig (as “aces”) [10] to explain the observed abundance and classification of hadrons on grounds of a broken  $SU(3)_F$  flavour symmetry. Later in 1968 Bjorken computed the scaling behaviour of structure functions in deep inelastic scattering (DIS) of leptons on nucleons using current algebra techniques [11], without referring to some

particular constituent model. These findings were then reinterpreted by Feynman [12] and Bjorken and Paschos [13] in terms of a scattering off point-like constituents of the nucleons: the parton model.

With Quantum Electrodynamics having been already a fully developed and verified theory, the leptonic part of the interaction in DIS was known: An electron scatters on the hadronic target by radiating off a virtual photon which then interacts with the hadron's electromagnetic current. Feynman, Bjorken and Paschos then proposed that the interaction with the hadronic current takes place by the photon scattering on quasi-free partons; the underlying assumption being that, due to the high energy involved in the scattering, the time-dilatation and length-contraction resulting from a boost into the center of mass (CM) frame of the electron-proton-system suspends the strong interactions of the partons which bind them in the nucleon. A sketch of this idea is given in Fig. 2.1.

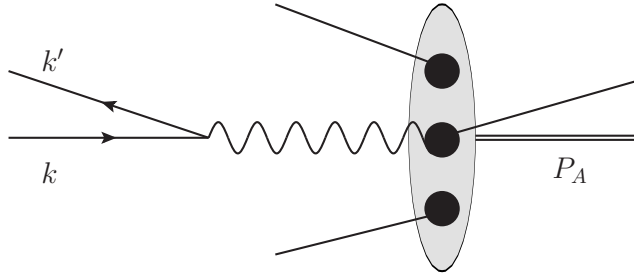


Figure 2.1: Schematic draft of DIS in the parton model. A lepton (left) radiates a virtual photon, which hits and breaks free a constituent of a length-contracted “hadronic pancake” (right).

In computations this idea was formalized by the introduction of parton distribution functions (PDFs)  $f_{a/A}(x)$  that give the probability of finding a parton of type  $a$  in hadron  $A$  with a momentum fraction  $x$ , i.e. the parton's momentum is related via  $p_a = xP_A$  to the hadron's momentum  $P_A$ . With a PDF taken into account, the cross section of an electron of momentum  $k$  scattering on a hadron  $A$  can then be written

$$d\sigma_{eA}(k, P_A) = \sum_a \int_0^1 dx f_{a/A}(x) d\sigma_{ea}(k, xP_A), \quad (2.1)$$

with the sum over  $a$  running over the set of partons and  $\sigma_{ea}$  representing the cross section of the electron parton scattering. This corresponds to an incoherent superposition of electron parton scatterings, neglecting the interference of contributions from the scattering on different partons.

## 2.2 QCD Lagrangian

To reconcile the quark model of hadrons with the Pauli exclusion principle, among other issues, an additional internal degree of freedom for quarks, carrying the fundamental

## 2 Quantum Chromodynamics

representation of  $SU(3)$ , was introduced by Han and Nambu in 1965 [14]. This global symmetry was later elevated to a gauge theory by Fritzsch and Gell-Mann in 1972 [15], building upon the description of non-Abelian gauge theory in 1954 by Yang and Mills [16] – Quantum Chromodynamics was born (with “chromo” referring to the  $SU(3)$  charge being coined “colour” and the gauge group hence often being written as  $SU(3)_c$ ).

The Lagrangian of this theory in a covariant gauge is

$$\mathcal{L}_{\text{QCD}} = -\frac{1}{4}G_0^{a\mu\nu}G_{0\mu\nu}^a + \bar{\Psi}_0^f \left( i\not{D}_0 - m_0^f \right) \Psi_0^f + \partial_\mu \bar{\eta}_0^a D_0^\mu \eta_0^a - \frac{1}{2\xi_0} (\partial_\mu A_0^{a\mu})^2. \quad (2.2)$$

It is well known that quantum field theories are afflicted with divergences when evaluated in perturbation theory. The ultraviolet (UV) divergences can be cured by a well-defined renormalization procedure. To signify the fact that the fields and parameters in the Lagrangian are unrenormalized, bare quantities, they are marked by the subscript 0.

The first term includes the gluon field strength tensor

$$G_0^{a\mu\nu} = \partial^\mu A_0^{a\nu} - \partial^\nu A_0^{a\mu} + g_{s0} f^{abc} A_0^{b\mu} A_0^{c\nu} \quad (2.3)$$

and leads to the gluon kinetic term and, via the last term in (2.3), to its self-interactions.  $g_{s0}$  is the bare strong coupling. In an Abelian gauge theory, in comparison, the structure constants  $f^{abc}$  of the gauge group would vanish due to commuting generators and vector boson self-interaction would be absent.

The second term consists of the quark mass term, which in the Standard Model is generated through Yukawa couplings of the quark fields to the scalar field of the Higgs mechanism. Since this work is not concerned with weak interaction phenomenology, the Higgs mechanism and electroweak symmetry breaking is not elaborated on and (2.2) shows only the resultant Dirac mass term. Besides the mass term, term two includes the kinetic term of the quark fields and its interaction with the gluons through the gauge-covariant derivative

$$D_0^\mu = \partial^\mu - ig_{s0} A_0^{a\mu} T^a. \quad (2.4)$$

Here,  $T^a$  denotes the  $a$ th generator of  $SU(3)_c$ . From the fact that the gluon field  $A_0^a$  carries the index of the generators follows that there are  $N_c^2 - 1$  gluons for  $SU(N_c)$ , i.e. eight gluons in QCD. Furthermore, global  $SU(3)_c$  transformations act in the adjoint representation on the gluon fields.

The last two terms arise through gauge fixing, which is needed to define the gluon propagator, and can be constructed following the Faddeev-Popov method for a covariant gauge or equivalently by requiring the Lagrangian to be BRST invariant (as described in most introductions to gauge theory, e.g. [17, 5]). As usual  $\eta$  and  $\bar{\eta}$  are bosonic Grassmann fields – i.e. they violate the spin-statistics-theorem and are hence unphysical – called “ghosts”. The term proportional to  $\xi_0^{-1}$  constitutes the longitudinal part of the gauge boson propagator.

To absorb the UV divergences arising in perturbation theory beyond the leading order in  $g_{s0}$ , it is customary to introduce renormalization constants which relate bare parameters and fields to their renormalized counterparts:

$$A_0 = \sqrt{Z_A} A, \quad (2.5)$$

$$\Psi_0 = \sqrt{Z_\Psi} \Psi, \quad (2.6)$$

$$\eta_0 = \sqrt{Z_\eta} \eta, \quad (2.7)$$

$$g_{s0} = \tilde{Z}_g g_s = \frac{Z_g}{\sqrt{Z_A} Z_\Psi} g_s, \quad (2.8)$$

$$m_0 = \tilde{Z}_m m = \frac{Z_m}{Z_\Psi} m, \quad (2.9)$$

$$\xi_0^{-1} = \tilde{Z}_\xi \xi^{-1} = \frac{Z_\xi}{Z_A} \xi^{-1}. \quad (2.10)$$

Here, the last three definitions have been chosen such that the number of renormalization constants in each term of the Lagrangian is small. Inserting a zero by adding and subtracting each of the terms in (2.2) with renormalized instead of bare quantities leads to

$$\begin{aligned} \mathcal{L}_{\text{QCD}} = & -\frac{1}{4} G^{a\mu\nu} G_{\mu\nu}^a + \bar{\Psi}^f \left( i \not{D} - m^f \right) \Psi^f + \partial_\mu \bar{\eta}^a D^\mu \eta^a - \frac{1}{2\xi} (\partial_\mu A^{a\mu})^2 \\ & - \delta Z_A \frac{1}{4} (\partial^\mu A^{a\nu} - \partial^\nu A^{a\mu}) (\partial_\mu A_\nu^a - \partial_\nu A_\mu^a) \\ & - \delta Z_{g3} g_s f^{abc} A^{b\mu} A^{c\nu} \partial_\mu A_\nu^a - \delta Z_{g4} \frac{1}{4} g_s^2 f^{abc} f^{ade} A^{b\mu} A^{c\nu} A_\mu^d A_\nu^e \\ & + \delta Z_\Psi i \bar{\Psi}^f \not{D} \Psi^f + \delta Z_{g5} \bar{\Psi}^f A^a T^a \Psi^f - \delta Z_m m^f \bar{\Psi}^f \Psi^f \\ & + \delta Z_\eta \partial^\mu \bar{\eta}^a \partial_\mu \eta^a + \delta Z_{g6} g_s f^{abc} \partial^\mu \bar{\eta}^a A_\mu^b \eta^c \\ & - \delta Z_\xi \frac{1}{2\xi} (\partial_\mu A^{a\mu})^2, \end{aligned} \quad (2.11)$$

where  $\delta Z_{g3} = Z_g Z_A / Z_\Psi - 1$ ,  $\delta Z_{g4} = Z_g^2 Z_A / Z_\Psi^2 - 1$ ,  $\delta Z_{g5} = Z_g Z_\eta / Z_\Psi - 1$  and  $\delta Z_i = Z_i - 1$  in the other cases. Actually,  $\delta Z_\xi$  can be chosen to vanish, since a Slavnov-Taylor identity prohibits corrections to the longitudinal part of the gluon propagator and thus this counterterm is never needed [8].

The Feynman rules generated by this Lagrangian can be found in App. B.

## 2.3 Asymptotic Freedom

As the rationale behind the parton model is the absence of inter-parton interactions in the high-energy limit, a QFT exhibiting such limiting behaviour was needed and indeed found in the form of non-Abelian gauge theory, such as QCD. In 1973 Gross and Wilczek [18, 19, 20] and Politzer [21] were able to show that these theories exhibit the sought-after property of asymptotic freedom: Taking either a pure Yang-Mills theory without

## 2 Quantum Chromodynamics

matter fields or a theory with fermions, where the maximum number of fermions allowed depends on the gauge group, they computed that the coupling vanishes if the momentum scale is taken to infinity.

To retrace this crucial result, one starts with a coupling small enough to justify the use of perturbation theory and computes higher order QCD corrections to some amplitude. Carrying through with the renormalization program of employing a regularization scheme for the UV regions of loop momenta and the absorption of UV divergences in counterterms, the renormalized coupling obtains a scale dependence that is governed by renormalization group equations (RGE). For example, bearing on the calculation presented in App. C.2.1 using the  $\overline{\text{MS}}$  renormalization scheme, the bare coupling  $g_{s0}$  and the renormalized coupling  $g_s$  are related in  $D = 4 - 2\varepsilon$  dimensions via

$$g_{s0}^{(\varepsilon)} = \tilde{Z}_g g_s \mu^\varepsilon. \quad (2.12)$$

Of course, (2.12) is just a version of (2.8) adjusted to keep  $g_s$  dimensionless for  $\varepsilon \neq 0$  by introducing the arbitrary scale  $\mu$ . Since the bare coupling does not depend on any scale, a change of  $\mu$  can have no effect:

$$\mu \frac{\partial}{\partial \mu} g_{s0}^{(\varepsilon)} = 0. \quad (2.13)$$

From this, the  $\beta$ -function of QCD can be derived by using the results (C.33), (C.49), (C.57) to compute  $\tilde{Z}_g$  and carefully taking the limit  $\varepsilon \rightarrow 0$ , yielding at one-loop order

$$\beta(g_s) = \mu \frac{\partial}{\partial \mu} g_s = -g_s \frac{g_s^2}{16\pi} \left[ \frac{11}{3} C_A - \frac{2}{3} N_f \right]. \quad (2.14)$$

Since this is negative as long as the number of quark flavours satisfies

$$N_f < \frac{33}{6} C_A,$$

i.e. as long as there are at most 16 flavours, the strong coupling decreases with an increasing scale and converges to the UV fixed point  $g_s = 0$ . The solution to (2.14) is given for

$$\alpha_s = g_s^2 / (4\pi) \quad (2.15)$$

by

$$\alpha_s(\mu_R^2) = \frac{12\pi}{[11C_A - 2N_f] \ln \left( \frac{\mu_R^2}{\Lambda_{\text{QCD}}^2} \right)}. \quad (2.16)$$

where  $\Lambda_{\text{QCD}}$  is the constant of integration that signifies the divergence of the perturbative coupling. Alternatively, rewriting (2.16) in terms of the coupling at another scale  $\mu'$ , one has

$$\alpha_s(\mu'^2) = \frac{\alpha_s(\mu_R^2)}{1 + \frac{\alpha_s(\mu_R^2)}{4\pi} [11C_A - 2N_f] \ln \left( \frac{\mu'^2}{\mu_R^2} \right)}. \quad (2.17)$$



If the fraction in this expression is expanded in a geometric series and the result plugged into the expression for a Feynman diagram, one can infer that solving the  $\beta$ -function amounts to a resummation of vertex corrections with loop-momenta above the renormalization scale  $\mu_R$  [22].

In general the form of the renormalization group equations, and particularly the  $\beta$ -function, depend on the renormalization scheme. However, it can be shown that the one-loop result (2.14) is scheme-independent [17] and even more, that the full renormalization group equations which govern the energy scaling of amplitudes agree in the high energy limit [5], so that the manifestation of asymptotic freedom hinges not on a specific choice of a renormalization scheme.

Qualitatively, the zero coupling UV fixed point of QCD supports the general idea of the parton model that there are quasi-free partons at high energies. But, moreover, this result leads to a quantitative prediction of Bjorken scaling in DIS and its violation. To see this, a short review of Bjorken scaling is in order.

In DIS, where a lepton scatters on a hadron and only the final state lepton is measured, the amplitude can be written as the contraction of a leptonic and a hadronic tensor. The hadronic part of the amplitude is given by the spin-averaged expectation value of electromagnetic currents between hadron states. Via this matrix element the structure functions  $W_1(\nu, q^2)$ ,  $W_2(\nu, q^2)$  are defined as coefficients of Lorentz structures:

$$\begin{aligned} & \int d^4x e^{-iq \cdot x} \langle H(p) | J^\sigma(x) J^\rho(0) | H(p) \rangle \\ & \propto \left( -g^{\rho\sigma} + \frac{q^\rho q^\sigma}{q^2} \right) W_1(\nu, q^2) \\ & \quad + \frac{1}{m_H^2} \left( p^\rho - \frac{p \cdot q}{q^2} q^\rho \right) \left( p^\sigma - \frac{p \cdot q}{q^2} q^\sigma \right) W_2(\nu, q^2), \end{aligned} \quad (2.18)$$

where  $H$  is a hadron of momentum  $p$  on which the virtual photon of momentum  $q$ , that has been emitted by the lepton, scatters. The variable

$$\nu \equiv \frac{-q \cdot p}{m_H}$$

is the photon energy in the hadron rest frame. Bjorken scaling now refers to the asymptotic behaviour

$$\begin{aligned} W_1(\nu, q^2) & \rightarrow F_1(x), \\ \nu W_2(\nu, q^2) & \rightarrow F_2(x), \end{aligned} \quad (2.19)$$

for  $-q^2 \rightarrow \infty$  with fixed Bjorken- $x$

$$x \equiv -q^2 / (2m_H \nu) \quad (2.20)$$

– i.e. the structure functions are independent of  $q^2$  for a large virtuality  $-q^2$ .

What this has to do with asymptotic freedom can be seen by sketchily following the argument given in [17], making use of dimensional analysis and the operator product expansion (OPE). In an asymptotically free theory the current expectation value in

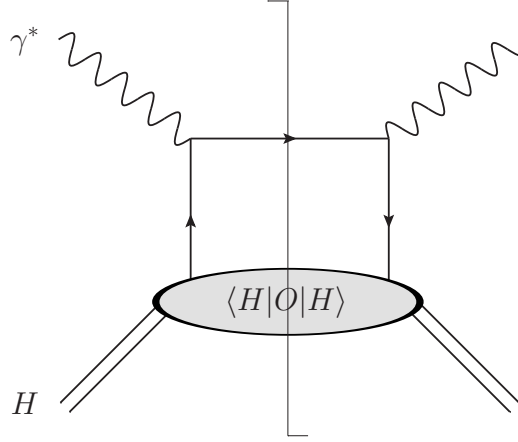


Figure 2.2: Leading diagram for DIS, with the blob representing the long-distance contributions.

(2.18) (and indeed every correlation function) scales in the high-energy limit with its canonical dimension, as it would do in a free theory, up to logarithmic corrections. That means a change of the momenta  $p$  and  $q$  by a factor  $\kappa$  changes (2.18) by a factor  $\kappa^{2d(J)-4}$ , corresponding to the “momentum dimension” of the expression, times some logarithm of  $\kappa$ . Here,  $d(J) = 3$  is the dimension of the current  $J$ . Taking now only  $q$  to infinity and keeping  $p$  fixed, allows the use of the OPE, which relates a product of operators, here  $J(z)J(0)$ , with some of its momenta becoming asymptotically large to a series of operators  $O$ , evaluated at the finite momenta  $p$ , times coefficient functions of the asymptotically large momenta  $q$ :

$$\int d^4x e^{-iq \cdot z} \langle H|J(z)J(0)|H \rangle \rightarrow \sum_O C_O(q) \langle H|O|H \rangle, \quad (2.21)$$

where  $\langle H|O|H \rangle$  depends only on  $p$  and the Lorentz indices have been suppressed. In QCD the operators  $O$  are combinations of quark and gluon field operators and derivatives. To match the dimension of the left hand side, the canonical dimension of the Wilson coefficients  $C_O$  has to be  $2d(J) - 4 - d(O) = 2 - d(O)$ . The expectation values of all possible QCD operators,  $\langle H|O|H \rangle$ , can be classified by irreducible representations of the Lorentz group. These representations can be distinguished by Lorentz structures made up of  $s$  factors of the four-vector  $p^\mu$  [23], such that  $\langle H|O|H \rangle \sim p^{\mu_1} \dots p^{\mu_s}$ . These  $s$  vectors  $p$  have to be contracted with  $s$  of the  $2 - d(O)$  vectors  $q$  from the coefficient function  $C_O$  to form  $s$  variables  $\nu$ , so that the high energy scaling behaviour of the first structure function, corresponding to a term with an operator  $O$  with  $s$  factors  $p^\mu$ , is given by

$$W_1(\nu, q) \sim q^{2-d(O)-s} \nu^s \quad (2.22)$$

or using the definition of Bjorken- $x$

$$W_1(\nu, q) \sim q^{2-d(O)+s} x^{-s}. \quad (2.23)$$

For  $W_2$  one has to take account of the two factors of  $p^\mu$  in the tensor with which it is multiplied in (2.18), giving

$$\nu W_2(\nu, q) \sim q^{4-d(O)-s} \nu^{s-1} \sim q^{2-d(O)+s} x^{-s+1}. \quad (2.24)$$

Constructing operators from quark and gluon fields, leads to the conclusion that operators  $O$  for which  $d(O)-s = 2$  give the leading contribution to (2.21); the quantity  $d(O)-s$  is called “twist”. Then each of the terms with leading twist operators contributes

$$W_1(\nu, q) \sim x^{-s}, \quad (2.25)$$

$$\nu W_2(\nu, q) \sim x^{-s+1}. \quad (2.26)$$

This means that every leading twist term in the operator expansion of the structure functions is independent of powers of  $q$ , in accordance with Bjorken scaling (2.19). A diagrammatic depiction of a leading twist term is given in Fig. 2.2.

It must be stressed again that this analysis relies completely on the fact that the scaling and the canonical dimensions are identical. In a theory without asymptotic freedom, the scaling dimension in the high-energy limit would differ from the canonical dimension by a non-zero anomalous dimension, thus invalidating the counting of factors of momentum in the reasoning above. Furthermore, as mentioned above, this argument holds up to logarithmic dependencies on  $q$ . The fact, that these can actually be computed in QCD and predict scaling violations in agreement with the experiment, further established that QCD is the correct theory of strong interactions.

The methods mentioned above make it possible to construct a perturbation theory for strong interactions. Since the OPE as an operator identity is independent of the process in question, the coefficient functions  $C_O$  can be computed in a small coupling expansion by sandwiching the OPE between quark and gluon states (instead of hadron states). This leads to the possibility of computing processes by means of a perturbation theory of quarks and gluons, assuming one somehow obtains knowledge of the non-perturbative hadronic matrix elements  $\langle H|O|H \rangle$ . This is part of the subject of Sec. 2.4.2.

## 2.4 Perturbation Theory

### 2.4.1 Infrared safety

Due to asymptotic freedom, the interactions of quarks and gluons can be computed in an expansion in the coupling  $\alpha_s$ , using the Feynman rules in App. B, as long as the renormalization scale is chosen to be large enough to have  $\alpha_s(\mu_R) \ll 1$ . However, apart from the obvious problem, that partons are not observable, the vanishing mass of the gauge boson poses a problem in naive perturbation theory in QCD as well as in QED. In general, a total cross section for a theory without massless particles, computed in perturbation theory and renormalized, can be written on dimensional grounds in terms of a dimensionless function of the ratios of all scales involved

$$\sigma(g, \sqrt{s}, m_1, \dots, m_n, \mu_R) = \frac{1}{\mu_R^2} f\left(g, \frac{\sqrt{s}}{\mu_R}, \frac{m_1}{\mu_R}, \dots, \frac{m_n}{\mu_R}, 1\right). \quad (2.27)$$

## 2 Quantum Chromodynamics

Usually, to minimize the impact of large ratios, the arbitrary renormalization scale is chosen to be proportional to one of the other scales, e.g.

$$\mu_R \propto \sqrt{s},$$

and

$$\sigma(g, \sqrt{s}, m_1, \dots, m_n, \sqrt{s}) = \frac{1}{s} f(g, 1, \frac{m_1}{\sqrt{s}}, \dots, \frac{m_n}{\sqrt{s}}, 1).$$

But there are still ratios present which may be large. That this is problematic can be seen in the extreme case where some of the ratios are made to vanish, e.g. by taking  $s$  to infinity or some mass to zero: Then there is the possibility of a divergence in  $f$ , if the ratios in question enter  $f$  logarithmically or as negative powers.

The occurrence of divergences related to zero masses (“mass divergences”) depends on the theory and their analysis is related to the analytic structure of general Feynman amplitudes (extensive reviews how to perform such an analysis can be found for example in [24, 25]). It turns out that the coupling of massless gauge bosons to (massive or massless) fermions can produce singularities in higher order corrections, called infrared (IR) or soft divergences. In the Standard Model, soft divergences are usually produced by connecting external on-shell lines by zero-momentum gauge bosons. Yet another type of singularities is associated with additionally vanishing fermion mass or with the self-interaction of massless gauge bosons: If the massless particles meeting in a vertex have collinear on-shell momenta, collinear divergences arise. However, it is common to use the term “infrared” for both types of singularities. Typically, both types of divergences arise through a logarithmic dependence on the mass parameters [8].

Luckily, there are theorems which prevent the occurrence of these singularities in observables. The Bloch-Nordsieck theorem [26] establishes that, in QED (with massive fermions), rather than diverge, transition probabilities for the production of a fixed number of photons have to vanish. This means that there can be no production of a definite number of massless gauge bosons. Conversely, the inclusion of processes with unmeasured photons – e.g. those with energies below a detector threshold – leads to a cancellation of IR divergences and a finite transition probability. Thus, if one is about to compute a loop correction to a  $n$  photon production process at leading order, real radiation of an additional photon has also to be taken into account. This result is extended to collinear singularities by the Kinoshita-Lee-Nauenberg theorem [27, 28], which states that (apart from pathological renormalization schemes, unlike e.g.  $\overline{\text{MS}}$ ) in a calculation of a total cross section in which all experimentally degenerate, i.e. indistinguishable, states, including collinear states, are summed over in the initial and final state, all mass divergences cancel. As a generalization, those quantities which are defined such, that a cancellation of IR divergences occurs, are called “infrared safe”. In practice, IR safety means that measurable quantities, such as the cross section, have to take into account some finite angular and energy resolution. In investigations on QCD, for example, it is common to compute jet cross sections, where jets are defined as cone-like sprays of partons (corresponding to hadrons deploying the amount of energy associated theoretically with the partons distributed over some measure of angle in the detector).

To formalize IR safety, it is common to introduce a “jet-defining function”  $F_J^{(n)}(\Phi^{(n)})$  [29] of the  $n$  final state momenta, collectively denoted by  $\Phi^{(n)}$ , which defines the observable in question for an arbitrary number of partons. Disregarding hadronic states for the moment, a general IR unsafe cross section for  $n$  final state partons is defined via the flux factor  $F$  (C.12), the squared amplitude  $|\mathcal{M}_n|^2$  to some order, say  $\alpha_s^N$ , and the Lorentz-invariant phase space  $d\Phi^{(n)}$  (C.6) by

$$d\sigma = \frac{1}{4F} |\mathcal{M}_n|^2 d\Phi^{(n)}. \quad (2.28)$$

To make this IR safe, the KLN theorem establishes that one has to sum over all virtual and real corrections to some fixed order for a cancellation of IR divergences to take place. Up to now, (2.28) can include only virtual corrections. A definition of an IR safe counterpart of order  $\alpha_s^N$  can be given using the jet-defining functions  $F_J$  via

$$d\sigma = \frac{1}{4F} \sum_{i=0}^N |\mathcal{M}_{n+i}|^2 F_J^{(n+i)}(\Phi^{(n+i)}) d\Phi^{(n+i)}. \quad (2.29)$$

This allows for a cancellation of divergences between the different terms, if the jet-defining functions  $F_J^{(n)}(\Phi^{(n)})$  have the property that they reduce to their definitions at lower orders for each configuration of the final state momenta that leads to an IR divergence. For example,

$$F_J^{(n+1)}(\Phi^{(n+1)}) \rightarrow F_J^{(n)}(\Phi^{(n)}) \quad (2.30)$$

if one of the  $n+1$  momenta becomes soft or collinear to another momentum. A trivial example would be  $F_J^{(n)}(\Phi^{(n)}) = 1$  for a total cross section, i.e. inclusive process<sup>1</sup>, whereas for a jet cross section  $F_J^{(n)}(\Phi^{(n)})$  would represent some jet-finding algorithm.  $F_J$  may also simply include  $\theta$ -distributions to cut out regions of the phase space.

It is important to note that even if IR singularities are regulated by finite masses or cancel in IR safe observables, the logarithmic nature of the divergence means that higher order corrections introduce logarithms of potentially large ratios. Thus, the perturbative series of a partonic cross section is in fact not an expansion in the coupling  $\alpha_s$  but, for example, in  $\alpha_s \ln(m^2/s)$  or  $\alpha_s \ln(\delta^2/s)$  with  $\delta$  some energy-resolution. This situation may invalidate perturbation theory, as the effective expansion parameter is eventually greater than unity. In that sense, calculations in the massless limit signify the breakdown of perturbation theory, even if physical masses would prevent the divergence itself. This problem can be overcome if it is possible to resum these contributions to all orders in a converging series: Often, the pathological, large ratios of scales are related to certain subdiagrams that enter in every order of perturbation theory. These contributions can then be accounted for without computing the full higher order expressions. In fact, the parton shower generators to be discussed in Sec. 6.1 provide a numerical variant of such a resummation of IR logarithms.

<sup>1</sup>Inclusive means in general, that the final state includes undetermined particles. Fixed order calculations are always to some extent inclusive, especially so for inelastic hadron scattering, where the beam remnants are usually not accounted for. The antonym is exclusive, i.e. the final state is known.

### 2.4.2 Factorization

In DIS, the fact that it is fully inclusive in final state hadrons leads to the formulation of the process' amplitude in terms of an operator expectation value evaluated in the incoming hadron state, which can then be expanded in a series of terms where long- (IR) and short-distance (UV) behaviour are separated, cf. (2.21). The two regimes are said to “factorize” in DIS. Factorization properties like this are central to most calculations in perturbative QCD (pQCD).<sup>2</sup>

Generalizing from the DIS case, factorization theorems state that in the cross section of a high-energy collision involving hadrons the long- and short-distance phenomena are subsumed in two different types of functions, where the UV function, the hard scattering coefficient  $\hat{\sigma}$ , is calculable from the perturbation theory of parton scatterings. The long-distance functions are defined as expectation values of parton number operators in single hadron states [30]: In the initial state these functions are the parton distribution functions (PDFs)  $f_{a/A}$  or, in case of identified hadrons in the final state, the fragmentation functions (FFs)  $D_{C/c}$ . As they embody the low-energy contributions related to the asymptotic states of QCD, they can not be computed in perturbation theory. However, as is shown later on, the evolution of these functions with changing energy scales is determined by perturbation theory.

In general, factorization theorems may be viewed as a well-explored working hypothesis – with rigorous proofs existing for the benign processes DIS and Drell-Yan [30] – facilitating perturbative calculations in QCD. For a process  $AB \rightarrow CX$  with hadrons  $A$ ,  $B$ , and  $C$ , while  $X$  denotes the undetected remains, a factorized cross section is given by

$$\begin{aligned} d\sigma_{AB \rightarrow CX}(p_A, p_B, p_C) &= \sum_{a,b,c,x} \int_0^1 dx_a \int_0^1 dx_b \int_0^1 dz f_{a/A}(x_a, \mu_F) f_{b/B}(x_b, \mu_F) \\ &\quad \cdot d\hat{\sigma}_{ab \rightarrow cx} \left( x_a p_A, x_b p_B, \frac{p_C}{z}, \mu_F \right) D_{C/c}(z, \mu_F), \end{aligned} \quad (2.31)$$

up to terms subleading in the hard scale (e.g. the collision energy). The suppressed subleading terms are, analogously to the OPE, called “higher twist” contributions.

In principle, it would be possible to have a different factorization scale for each long-distance function, but it is common to chose them to be equal as has been done here. A graphic representation of (2.31) is given in Fig. 2.3. The factorization theorem for DIS, on the other hand, has already been given in (2.1) – it is formally equivalent to the parton model ansatz. To that effect, factorization theorems are the realization of the parton model ideas in pQCD.

It is important to realize, that despite the fact that PDFs and FFs can not be computed in perturbation theory, a formula like (2.31) obtains its predictive power from the

---

<sup>2</sup>One of the simplifications in the sketch in Sec. 2.3 is that the OPE is actually applied not to the operator (2.18) but to its time-ordered counterpart. The results of the corresponding OPE can be shown to be related to the structure functions via a Mellin transformation, i.e.  $f(x) \rightarrow \tilde{f}(x) = \int dx x^{n-1} f(x)$ . That means the proper factorization, in the sense of a multiplication of factors, takes place in Mellin space.

universality of the long-distance functions. After all, they depend only on the hadron in question and thus have to be measured only once – e.g. by comparing a calculated DIS cross section with the measured cross section at some center of mass energy – to be afterwards used in conjunction with arbitrary hard scattering coefficients corresponding to any hard process.

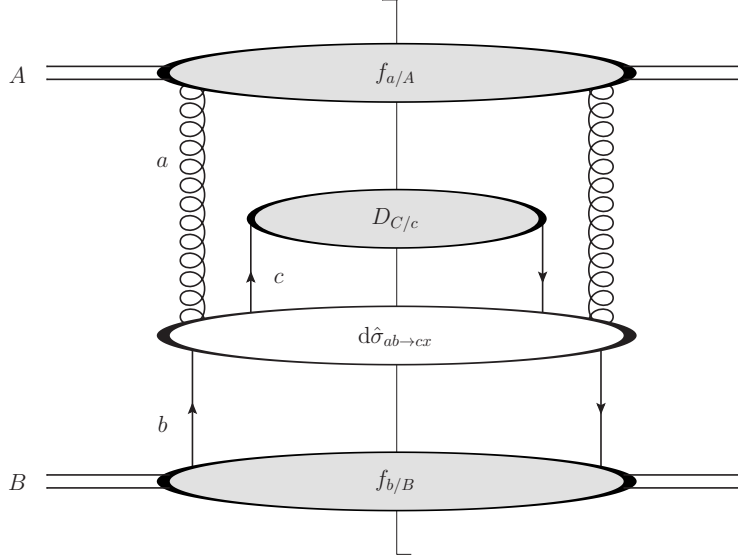


Figure 2.3: A factorized process, where the shaded blobs represent the long-distance functions and the white blob stands for the hard scattering. The cut commemorates the fact that this corresponds to a squared amplitude w.r.t. which these functions are defined.

The hard scattering coefficient  $\hat{\sigma}$  is often said to be a partonic scattering cross section with “identified partons”, i.e. – in case of (2.31) – two incoming partons  $a$ ,  $b$  and a final state parton  $c$  moving in definite directions. In that case,  $\hat{\sigma}$  can not be IR safe (irrespective of the energy and angle resolution in the final state). As a matter of fact, parton scattering cross sections for such identified partons beyond the leading order introduce mass divergences related to collinear emissions from the identified parton which do not cancel between real and virtual corrections. Therefore, to be meaningful, factorization theorems must imply the statement that these collinear divergences are, first of all, universal, i.e. independent of the parton scattering process, and, second, are cancelled by contributions from the likewise universal long-distance functions. The rigorous way to show this – the operator point of view – is to first apply (2.31) to a purely partonic process. In this case, it is possible to compute the parton-in-parton PDF/FF via its operator definition in perturbation theory. After computing the hard parton scattering and renormalizing both the partonic long-distance function and the parton scattering, one can redefine the hard scattering coefficient  $\hat{\sigma}$  by shifting the long-distance contributions (i.e. collinear divergences) into the parton PDF/FF. Indeed, it is shown in

[30] that the partonic long distance functions entail IR divergences that cancel the left-over mass divergences of the parton scattering and thus that the factorized cross section are completely free of IR divergences.<sup>3</sup> Evidently, it is this redefined hard scattering coefficient  $\hat{\sigma}$ , which is a function depending solely on UV phenomena, that is to be used alongside hadronic long-distance functions in realistic calculations.

A less rigorous and more practical take on this – sometimes called the infrared approach [31, 7] – is to just assume that the hadron PDFs cancel the pathological collinear singularities of the partonic scattering cross section order by order. An illustration of the latter approach follows.

If a cross section for a process with (for simplicity) one initial hadron  $A$  and  $n$  well-separated final state jets is computed up to the next-to-leading order in  $\alpha_s$ , it can be written (suppressing all unrelated dependencies, like on  $\mu_R$ )

$$d\sigma_A(p_A) = \sum_a \int_0^1 dx_a f_{a/A}^{(0)}(x_a) \left( d\hat{\sigma}_a^{(n)}(x_a p_A) F_J^{(n)} + d\hat{\sigma}_a^{(n+1)}(x_a p_A) F_J^{(n+1)} \right), \quad (2.32)$$

with  $d\hat{\sigma}^{(n)}$  including the Born and renormalized one-loop results for parton scattering and a real radiation correction  $d\hat{\sigma}^{(n+1)}$ . For the latter, an integration over the momentum of the extra particle is implied.  $f_{a/A}^{(0)}$  is an “IR bare” PDF that is assumed to include collinear divergences that exactly match the uncanceled divergences of the partonic scattering, which are conventionally called collinear counterterms.

The initial state collinear divergences in  $d\hat{\sigma}^{(n+1)}$  at this order are universally of the form (see App. D)

$$d\hat{\sigma}_a^{(n+1)}(p_a, \dots, k, \dots) \rightarrow \int_0^1 dz \int \frac{d|\vec{k}_T|^2}{|\vec{k}_T|^2} \sum_j d\hat{\sigma}_j^{(n)}(z p_a, \dots) \frac{\alpha_s}{2\pi} \hat{P}_{ja}(z), \quad (2.33)$$

where  $k_T$  is the transverse momentum of  $k$  w.r.t.  $p_a$ ,  $z$  is the momentum fraction entering the hard scattering after the radiation of the collinear particle and  $\hat{P}_{ja}$  are the splitting functions (D.16), (D.21), (D.32) or (D.34). That is to say, the real radiation correction, can, in its collinear limit, be written as the underlying process (without radiation) times a splitting.

The splitting functions in (2.33) might in general contain divergences for  $z \rightarrow 1$ . These correspond to soft-collinear divergences, as the momentum of the radiated parton vanishes, and are cancelled by collinear divergences in the virtual corrections in  $d\sigma^{(n)}$  in (2.32). To formally account for this cancellation, the divergent terms in the splitting functions are rewritten in terms of the plus-distribution, which for a function  $f$  with a simple pole at  $z = 1$  is defined by

$$\int_0^1 dz f_+(z) g(z) = \int_0^1 dz f(z) (g(z) - g(1)). \quad (2.34)$$

---

<sup>3</sup>Personally, I was often confused by statements, that the IR divergences are cancelled by a renormalization of the PDFs. This is due to the fact that in dimensional regularization UV and IR poles in the unrenormalized PDFs cancel and then the renormalization counterterm is used to subtract the IR divergence in the hard scattering coefficient [7]. Conceptually, renormalization is still strictly related to UV phenomena.



Then one has

$$P_{qq}(z) \equiv \left( \hat{P}_{qq}(z) \right)_+ = C_F \left[ \left( \frac{1}{1-z} \right)_+ (1+z^2) + \frac{3}{2} \delta(1-z) \right], \quad (2.35)$$

$$P_{qg}(z) \equiv \hat{P}_{qg}(z) = \frac{1}{2} (z^2 + (1-z)^2), \quad (2.36)$$

$$P_{gg}(z) \equiv \hat{P}_{gg}(z) = C_F \frac{1 + (1-z)^2}{z}. \quad (2.37)$$

The regularization of  $\hat{P}_{gg}$  is more complicated, since it is matched against collinear divergences from gluon and quark loops giving

$$P_{gg}(z) \equiv 2C_A \left[ \left( \frac{1}{1-z} \right)_+ z + z(1-z) + \frac{1-z}{z} \right] + \left( \frac{11}{6} C_A - \frac{1}{3} N_f \right) \delta(1-z). \quad (2.38)$$

These regularized splitting functions  $P_{ja}(z)$  are called Altarelli-Parisi splitting kernels [32] and can, at this order, be interpreted as probabilities for the parton  $j$  to split off parton  $a$ . Using from now on these kernels in (2.33), it has to be understood that  $d\hat{\sigma}^{(n)}$  in (2.32) does no longer include those collinear divergences that have been used for the regularization of the splitting functions.

After regularizing the logarithmic divergence in  $k_T$  in (2.33), it can be absorbed into the PDF and one has the freedom to absorb arbitrary finite contributions along with it. The prescription specifying this is called a factorization scheme. IR divergences are, like UV divergences, often regulated by continuing the theory in  $D = 4 - 2\varepsilon$  dimensions, but now with  $\varepsilon < 0$ , whereby (2.33) translates to

$$\begin{aligned} & d\hat{\sigma}_a^{(n+1)}(p_a, \dots, k, \dots) \\ & \rightarrow \int_0^1 dz \int \frac{d|\vec{k}_T|^2}{|\vec{k}_T|^{2+2\varepsilon}} \sum_j d\hat{\sigma}_j^{(n)}(zp_a, \dots) \frac{\alpha_s}{2\pi} P_{ja}^{(\varepsilon)}(z) \frac{(4\pi\mu^2)^\varepsilon}{\Gamma(1-\varepsilon)}. \end{aligned} \quad (2.39)$$

The arbitrary scale  $\mu$ , which has been introduced to keep the dimension of integral fixed, can be identified with the renormalization scale  $\mu_R$ . Integrating  $k_T$  from zero up to a scale  $\mu_F$ , below which the collinear approximation (2.39) is deemed viable, gives

$$\int_0^1 dz \sum_j d\hat{\sigma}_j^{(n)}(zp_a, \dots) \frac{\alpha_s}{2\pi} P_{ja}(z) \left( \frac{4\pi\mu_R^2}{\mu_F^2} \right)^\varepsilon \frac{1}{\Gamma(1-\varepsilon)} \frac{1}{-\varepsilon}.$$

Plugging this into (2.32), one sees that the singular contribution from the initial state collinear region to  $d\sigma_A$  is

$$- \sum_a \int_0^1 dx_a f_{a/A}^{(0)}(x_a) \sum_j \frac{\alpha_s}{2\pi} \frac{1}{\varepsilon} \left( \frac{4\pi\mu_R^2}{\mu_F^2} \right)^\varepsilon \frac{1}{\Gamma(1-\varepsilon)} \int_0^1 dz P_{ja}(z) d\hat{\sigma}_j^{(n)}(zx_a p_A, \dots).$$

In the  $\overline{\text{MS}}$  factorization scheme, this pole along with the  $\varepsilon$ -dependent prefactors is to be absorbed into the PDF, amounting to a redefinition

$$f_{j/A}^{\overline{\text{MS}}}(x, \mu_F) = f_{j/A}^{(0)}(x) - \sum_a \int_x^1 \frac{dz}{z} \frac{\alpha_s}{2\pi} P_{ja}(z) \left( \frac{4\pi\mu_R^2}{\mu_F^2} \right)^\varepsilon \frac{1}{\Gamma(1-\varepsilon)} \frac{1}{\varepsilon} f_{a/A}^{(0)}\left(\frac{x}{z}\right), \quad (2.40)$$

## 2 Quantum Chromodynamics

whereby the integrand in (2.32) can be rewritten (up to terms beyond NLO) as a product of finite functions,

$$\begin{aligned} d\sigma_A(p_A) = \sum_a \int dx_a f_{a/A}^{\overline{\text{MS}}}(x_a, \mu_F) \\ \cdot \left( d\hat{\sigma}_a^{(n)}(x_a p_A) F_J^{(n)} + d\hat{\sigma}_a^{\overline{\text{MS}}(n+1)}(x_a p_A, \mu_F) F_J^{(n+1)} \right). \end{aligned} \quad (2.41)$$

The  $(n+1)$ -contribution is now understood to be subtracted by the term absorbed into the PDFs and the implicit integration over the additional particle no longer contains initial state collinear divergences.<sup>4</sup> In this sense the hard scattering coefficient is no longer identical to a partonic cross section and the PDF can no longer be interpreted unconditionally as a probability – a breakdown of the naive parton model ideas.

Eq. (2.41) shows that, in analogy to the renormalization program to eliminate UV divergences, the absorption of IR divergences introduces a new scale, the factorization scale  $\mu_F$ . It is best thought of as a transverse momentum scale which marks the transition from the UV to the IR region, i.e. a lower bound on transverse momenta,  $k_T^2 \geq \mu_F^2$ , for which two particles with relative  $k_T$  are resolved as different particles in the hard process, and conversely an upper bound on the effects included in PDFs and FFs. But in the end it is an arbitrary scale and the full theory should not depend on it. However in practice, as for  $\mu_R$ , a residual  $\mu_F$ -dependence usually remains in perturbation theory, albeit governed by evolution equations similar to RGEs. These equations are called Dokshitzer-Gribov-Lipatov-Altarelli-Parisi (DGLAP) equations [33, 34, 32]. The DGLAP equations in leading order<sup>5</sup> of  $\alpha_s$  can be derived from (2.40) by differentiating w.r.t.  $\mu_F$ ,

$$\mu_F^2 \frac{d}{d\mu_F^2} f_{j/A}^{\overline{\text{MS}}}(x, \mu_F) = \sum_a \int_x^1 \frac{dz}{z} \frac{\alpha_s}{2\pi} P_{ja}(z) f_{a/A}^{\overline{\text{MS}}}\left(\frac{x}{z}, \mu_F\right). \quad (2.42)$$

In the rigorous operator approach these equations are equivalent to the RGE for the PDF [30]. Thanks to these equations, the scale-dependence of the long-distance functions does not restrict the predictive power of pQCD, since the functions have to be measured only once at some fixed scale  $Q$  and the continuation to other scales is dictated by perturbation theory through (2.42).

This program of computing partonic cross sections and the absorption of collinear divergences into long-distance functions works the same for all identified particles, e.g.

<sup>4</sup>It will, however, contain terms, corresponding to the formerly divergent diagrams, with logarithms of a ratio of  $\mu_F$  and another scale, e.g. the CM energy, multiplying the coupling,  $\alpha_s \log(\mu_F)$ . At the next order, the divergence absorption procedure will generate the same logarithm again, so one has terms with  $\alpha_s^2 \log(\mu_F)^2$  for doubly divergent diagram topologies, but also terms with  $\alpha_s^2 \log(\mu_F)$  corresponding to diagrams which only became divergent through the additional radiation. Resumming the former terms is called leading log (LL) approximation, the latter next-to-leading log (NLL), and so on.

<sup>5</sup>The solutions are commonly called leading order PDFs and are, like the running coupling, used in LO calculations, even though the evolution results from a NLO or LL calculation.

in the final state by absorption into FFs. The final state analog to (2.33) for two particles  $i, j$  becoming collinear is

$$\begin{aligned} & d\hat{\sigma}_{ij}^{(n+1)}(\dots, k_i, \dots, k_j, \dots) \\ & \rightarrow \int_0^1 dz \int \frac{d|\vec{k}_T|^2}{|\vec{k}_T|^2} \sum_{[ij]} d\hat{\sigma}_{[ij]}^{(n)}(\dots, k_{[ij]} = k_i + k_j, \dots) \frac{\alpha_s}{2\pi} \hat{P}_{j[ij]}^{(T)}(z), \end{aligned} \quad (2.43)$$

where the particles  $i$  and  $j$  have been replaced by the particle  $[ij]$  from which they originate<sup>6</sup> in  $d\hat{\sigma}^{(n)}$  and  $\hat{P}_{j[ij]}^{(T)}(z)$  is the time-like splitting function for  $j$  to split from  $[ij]$ .<sup>7</sup> The DGLAP equations for final state evolution are accordingly

$$\mu_F^2 \frac{d}{d\mu_F^2} D_{C/c}(x, \mu_F) = \sum_i \int_x^1 \frac{dz}{z} \frac{\alpha_s}{2\pi} P_{ic}^{(T)}\left(\frac{x}{z}\right) D_{C/i}(z, \mu_F). \quad (2.44)$$

It turns out that the LO splitting kernels for space-like and time-like splitting are identical

$$P_{ab}^{(T)}(z) = P_{ab}(z).$$

This relation is called Gribov-Lipatov reciprocity; it is broken in higher orders [35].

Solutions to the integro-differential equations (2.42) and (2.44) are found by going to Mellin-space, where the integral over  $z$  becomes a multiplication of the integrands. These solutions can, similar to the solutions of the  $\beta$  function, be interpreted in terms of a summation of subdiagrams to all orders; namely ladder diagrams, where collinear splittings of a parton leaving the long-distance function are stacked above each other with increasing  $k_T$ -scale (called  $k_T$ -ordering) [8]. As such, the use of the DGLAP equations is another example of the resummation of problematic subdiagrams shortly mentioned at the end of the last section.

## 2.5 Subtraction Methods

In the course of the last sections the occurrence of IR divergences in perturbation theory and the way to get rid of them – by means of defining IR safe observables, the KLN theorem and factorization – have been discussed. Now I want to discuss how these cancellations are put into practice.

In a NLO calculation with  $n$ -final state particles, one has to compute the squared amplitudes of the LO process without loops,

$$|\mathcal{M}_n^{(0)}|^2,$$

---

<sup>6</sup>If  $i, j$  are quark and antiquark, then  $[ij]$  is a gluon; if  $i, j$  are (anti)quark and gluon,  $[ij]$  is a (anti)quark; if  $i, j$  are gluons,  $[ij]$  is a gluon.

<sup>7</sup>“Time-like” refers to the fact that the momentum of  $[ij]$  has to be time-like to allow a splitting into two on-shell particles, where as in the initial state the initial on-shell particle splits into an on-shell particle and a particle with space-like momentum.

## 2 Quantum Chromodynamics

the interference diagrams of the first loop correction

$$\mathcal{M}_n^{(0)} \mathcal{M}_n^{(1)\dagger} + \mathcal{M}_n^{(1)} \mathcal{M}_n^{(0)\dagger} = 2 \operatorname{Re} \left( \mathcal{M}_n^{(1)} \mathcal{M}_n^{(0)\dagger} \right),$$

and the real radiation correction with an additional parton in the final state (without loops)

$$|\mathcal{M}_{n+1}^{(0)}|^2,$$

where each  $\mathcal{M}$  is, of course, a sum of Feynman diagrams of the respective order. UV-divergences arise only in  $\mathcal{M}_n^{(1)}$  and are handled by renormalization. IR divergences arise both in  $\mathcal{M}_n^{(1)}$  and when integrating  $|\mathcal{M}_{n+1}^{(0)}|^2$  over the  $n+1$ -particle phase space. As noted before, one can formally define an IR safe cross section by introducing a jet-defining function  $F_J$ , cf. (2.29). Assuming two identified initial state partons, one can write the fully differential cross sections for the  $n$ - and  $n+1$ -particle contributions as

$$\begin{aligned} d\sigma^{(n)}(p_A, p_B, p_1, \dots, p_n) &= \int_0^1 dx_a \int_0^1 dx_b f_{a/A}^{(0)}(x_a, \mu_F) f_{b/B}^{(0)}(x_b, \mu_F) \frac{1}{4F(x_a p_A, x_b p_B)} \\ &\quad \cdot \left( |\mathcal{M}_n^{(0)}|^2 + 2 \operatorname{Re} \left( \mathcal{M}_n^{(1)} \mathcal{M}_n^{(0)\dagger} \right) \right) (x_a p_A, x_b p_B, p_1, \dots, p_n) \\ &\quad \cdot F_J^{(n)}(\Phi^{(n)}) d\Phi^{(n)}(x_a p_A, x_b p_B) \\ &\equiv \int_0^1 dx_a \int_0^1 dx_b f_{a/A}^{(0)}(x_a, \mu_F) f_{b/B}^{(0)}(x_b, \mu_F) \\ &\quad \cdot \left( \mathcal{B}(\Phi^{(n)}) + \mathcal{V}(\Phi^{(n)}) \right) d\Phi^{(n)}(x_a p_A, x_b p_B), \end{aligned} \tag{2.45}$$

and

$$\begin{aligned} d\sigma^{(n+1)}(p_A, p_B, p_1, \dots, p_{n+1}) &= \int_0^1 dx_a \int_0^1 dx_b f_{a/A}(x_a) f_{b/B}(x_b) \frac{1}{4F(x_a p_A, x_b p_B)} \\ &\quad \cdot |\mathcal{M}_{n+1}^{(0)}|^2(x_a p_A, x_b p_B, p_1, \dots, p_{n+1}) \\ &\quad \cdot F_J^{(n+1)}(\Phi^{(n+1)}) d\Phi^{(n+1)}(x_a p_A, x_b p_B) \\ &\equiv \int_0^1 dx_a \int_0^1 dx_b f_{a/A}(x_a) f_{b/B}(x_b) \\ &\quad \cdot \mathcal{R}(\Phi^{(n+1)}) d\Phi^{(n+1)}(x_a p_A, x_b p_B). \end{aligned} \tag{2.46}$$

For brevity the sum over and dependence on initial state parton type is not made explicit. Furthermore, I have defined the shortcuts  $\mathcal{B}$ ,  $\mathcal{V}$  and  $\mathcal{R}$  as shortcuts for the Born, virtual and real matrix elements including the flux factor, for later reference. In principle, any type of cross section, such as a differential or a totally inclusive cross section, can be defined by a suitable choice of  $F_J$  and then any cross section can be written as a sum of cross sections with different final state multiplicities integrated over their respective phase space, i.e. at NLO

$$\sigma = \int_n d\sigma^{(n)} + \int_{n+1} d\sigma^{(n+1)}. \tag{2.47}$$

The left hand side is known to be finite, the right hand side is a sum of separately divergent terms.

The IR divergences in  $d\sigma^{(n)}$  can usually be obtained analytically, as the master integrals for one-loop-corrections are well-known [36], and appear as  $1/\varepsilon$  and  $1/\varepsilon^2$  poles in dimensional regularization. On the other hand, usually, an analytic integration over the phase space is not feasible, so that in practice numerical integration methods, e.g. Monte Carlo methods, are used. Then the integration over the  $n+1$  particle phase space is numerical infinity, which is impossible to correctly cancel against the  $\varepsilon$ -poles. With other words, one has to find a way to extract the divergences in the second term of the right hand side of (2.47) as an analytic expression. One rather obvious possibility is phase space slicing, whereby the regions of the  $n+1$ -phase space with collinear or soft configuration are treated analytically, and the rest is integrated numerically. The slices are chosen such, that the soft and collinear approximations for the cross sections can be used instead of the complete expressions for  $d\sigma^{(n)}$ ; these can then be continued to  $D$  dimensions and integrated analytically, resulting in poles in  $\varepsilon$  (like in (2.39)), which are cancelled against the divergences in the virtual contributions and the long-distance functions, and finite terms which are added back to the non-singular integrals. Afterwards the sum of the finite results should be independent of the cutoff parameters that defined the slices.

Somewhat more practical and systematic approaches are subtraction methods, whereby one has some known, readily integrable functions  $\mathcal{D}(\Phi^{(n+1)})$  which depend on the process and mimic the divergence structure of the real amplitude, such that

$$\int_{n+1} \left[ d\sigma^{(n+1)} - d\Phi^{(n+1)} \mathcal{D} \right]$$

is finite. The functions  $\mathcal{D}$  are chosen in such a way that they have only one singular region, i.e. only one of the momentum configurations corresponding to a soft or collinear divergence in  $d\sigma^{(n+1)}$  leads to a singularity for each  $\mathcal{D}$  (for brevity I write only one  $\mathcal{D}$  explicitly). Furthermore, the  $D$ -dimensional integration over the momentum leading to this singularity is known. It is clear, that in the singular limits the  $n+1$ -particle phase space can be written as an underlying  $n$ -particle phase space times the phase space of one radiated particle, e.g. App. D.2. The functions  $\mathcal{D}$  are however supposed to be defined at least in a finite region around the singular regions of phase space, so that they are numerically integrable. Thus, the definition of a subtraction term  $\mathcal{D}$  always includes the definition of a map  $\Phi^{(n+1)} \leftrightarrow \{\bar{\Phi}^{(n)}, \Phi_{\text{rad}}\}$  from the  $n+1$ -particle phase space to the underlying  $n$ -particle phase space and a set of variables describing the radiation or splitting process. Then one can use  $\mathcal{I}(\Phi^{(n)})$  defined by

$$d\bar{\Phi}^{(n)} \mathcal{I}(\bar{\Phi}^{(n)}) \equiv d\bar{\Phi}^{(n)} \int d\Phi_{\text{rad}} \mathcal{D}(\{\bar{\Phi}^{(n)}, \Phi_{\text{rad}}\}),$$

## 2 Quantum Chromodynamics

where the integral over  $\Phi_{\text{rad}}$  is performed in  $D$  dimensions, to cancel the poles of the  $n$ -particle contributions analytically. Accordingly, the integrands for the  $n$ -particle and  $n + 1$ -particle phase space can be made finite separately by using

$$\sigma = \int_n \left( d\sigma^{(n)} + d\Phi^{(n)} \mathcal{I} \right) + \int_{n+1} \left( d\sigma^{(n+1)} - d\Phi^{(n+1)} \mathcal{D} \right). \quad (2.48)$$

The two contributions of different multiplicity can now be integrated numerically.

In anticipation of the absorption of initial state collinear divergences into the PDFs, (2.45) has been written in terms of IR-bare PDFs. Since, by solving (2.40) for  $f^{(0)}$  (when using the  $\overline{\text{MS}}$ -factorization scheme), the bare PDF can be rewritten as the IR finite PDF  $f$  plus an IR counterterm, (2.45) can also be understood as a sum of a differential cross section free of initial state collinear singularities (redefining  $d\sigma^{(n)}$  in terms of the finite PDFs) and a counterterm for each identified initial state parton

$$d\sigma^{(n)} + d\sigma_{Ca}^{(n)} + d\sigma_{Cb}^{(n)}.$$

Doing this just makes explicit the initial state collinear divergences. In that case (2.48) becomes

$$\begin{aligned} \sigma = & \int_n \left( d\sigma^{(n)} + d\sigma_{Ca}^{(n)} + d\sigma_{Cb}^{(n)} + d\Phi^{(n)} \mathcal{I} \right) \\ & + \int_{n+1} \left( d\sigma^{(n+1)} - d\Phi^{(n+1)} \mathcal{D} \right), \end{aligned} \quad (2.49)$$

where the sum

$$d\sigma_{Ca}^{(n)} + d\sigma_{Cb}^{(n)} + d\Phi^{(n)} \mathcal{I}$$

now includes only divergences that are cancelled against virtual corrections.

There are different systematic choices for the functions  $\mathcal{D}$ . The two most prominent – and most relevant for this work – are the Catani-Seymour (CS) Dipole Subtraction method [29, 37] and the Frixione-Kunszt-Signer (FKS) method [38, 39, 40], which are reviewed in the next two sections.

### 2.5.1 CS dipole subtraction

The dipole subtraction method is based on a generalization of the soft and collinear limits of a cross section. First, I want to explore the rationale behind the dipole idea for amplitudes with QCD partons only in the final state, then generalize to amplitudes with arbitrary partons, and finally explicitly note the steps that have to be taken to compute the dipoles.

In the limit where a gluon becomes soft, a matrix element is dominated by those diagrams where the soft gluon couples to an external particle, which in turn can be written as a diagram without the soft gluon times a so-called eikonal current, see Fig. 2.4. For example, a  $n + 1$ -particle matrix element

$$\mathcal{M}_{c_1 \dots c_n}^{(n+1)a}(p_1, \dots, p_n, k),$$

with an external final state gluon  $a$  of momentum  $k$  and polarization  $\varepsilon_\lambda$ , and quarks with colours  $c_1, \dots, c_n$  and momenta  $p_1, \dots, p_n$ , can be written in the soft gluon limit as

$$\mathcal{M}_{c'_1 \dots c'_n}^{(n)}(p_1, \dots, p_n) \sum_{i=1}^n \delta_{c'_1 c_1} \dots (-g_s) T_{c_i c'_i}^a \frac{p_i \cdot \varepsilon_\lambda}{p_i \cdot k} \dots \delta_{c'_n c_n},$$

where  $T^a$  is in the fundamental representation of the Lie-algebra of  $SU(N_c)$  and the sum of terms is the eikonal current.

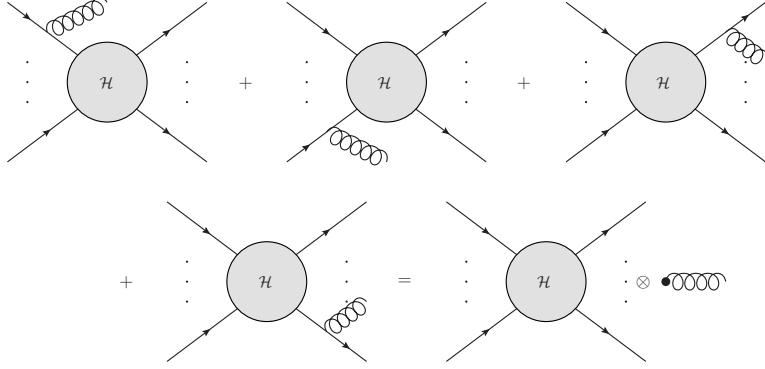


Figure 2.4: The dominant diagrams in the soft limit can be decomposed into a diagram without the soft gluon and an eikonal current that basically attaches a soft gluon to each external line.

Hence, the averaged and squared amplitude in the soft limit reduces as

$$\begin{aligned} & \overline{|\mathcal{M}^{(n+1)}(p_1, \dots, p_n, k)|^2} \\ & \rightarrow -\mathcal{N} 4\pi\alpha_s \sum_{\substack{\text{spins} \\ \text{colours}}} \mathcal{M}_{c'_1 \dots c'_n}^{(n)}(p_1, \dots, p_n) \mathcal{M}_{c''_1 \dots c''_n}^{(n)\dagger}(p_1, \dots, p_n) \\ & \quad \cdot \sum_{i,j=1}^n \delta_{c'_1 c_1} \delta_{c''_1 c_1} \dots T_{c_i c'_i}^a T_{c'_j c_j}^a \frac{p_i \cdot p_j}{(p_i \cdot k)(p_j \cdot k)} \dots \delta_{c'_n c_n} \delta_{c''_n c_n}, \end{aligned}$$

where  $\mathcal{N}$  includes all averaging factors, the negative sign stems from the gluon polarization sum and all terms with lower degree of divergence have been neglected.<sup>8</sup>

By introducing a general colour charge operator  $\mathcal{T}^a$ , which can be in the fundamental, the dual fundamental or the adjoint representation, the soft limit can be given for soft gluon radiation from all possible external particles: In general, with a slight change of notation,

$$\overline{|\mathcal{M}^{(n+1)}|^2} \rightarrow -\mathcal{N} 4\pi\alpha_s \sum_{\substack{\text{spins} \\ \text{colours}}} \sum_{i,j} \mathcal{M}_{\{c_k\}}^{(n)} \left( \mathcal{M}_{\{c_k\}}^{(n)\dagger} \right)_{\substack{c_i \rightarrow c'_i \\ c_j \rightarrow c'_j}} \mathcal{T}_{c'_i c_i}^a \mathcal{T}_{c'_j c_j}^a \frac{p_i \cdot p_j}{(p_i \cdot k)(p_j \cdot k)}. \quad (2.50)$$

<sup>8</sup>The reason that soft quarks do not lead to divergences, is that the fermion trace would introduce another factor  $k$  in the nominator. The divergence of the amplitude is then integrable over the phase space.

## 2 Quantum Chromodynamics

Here, all fundamental and adjoint colour indices of the matrix elements are subsumed in the set  $\{c_k\}$ . The colour charge operator  $\mathcal{T}^a$  is then

$$\mathcal{T}_{c'_i c_i}^a = \begin{cases} T_{c'_i c_i}^a, & \text{if particle } i \text{ is a FS quark or IS antiquark,} \\ -T_{c_i c'_i}^a, & \text{if particle } i \text{ is a FS antiquark or IS quark,} \\ -if^{ac'_i c_i}, & \text{if particle } i \text{ is a gluon.} \end{cases} \quad (2.51)$$

Since these operators are the generators of colour transformations of the external states of a process, and a global change of the colours of all external particles can not change the amplitude, it follows that colour conservation is given by the relation

$$\sum_i \mathcal{T}_{bc_i}^a \mathcal{M}_{\{c_k\}} = 0, \quad (2.52)$$

with the sum running over all coloured legs  $i$  and an implicit contraction of the colour index  $c_i$ .

From (2.50) it is obvious, that the soft limit does not factorize into the exact  $n$ -particle amplitude times some divergent factor. Rather there is a sum of factorized terms, the factors being a so-called colour-correlated or colour-linked amplitude

$$\propto \sum_{\substack{\text{spins} \\ \text{colours}}} \mathcal{M}_{\{c_k\}}^{(n)} \left( \mathcal{M}_{\{c_k\}}^{(n)\dagger} \right)_{\substack{c_i \rightarrow c'_i \\ c_j \rightarrow c'_j}} \mathcal{T}_{c'_i c_i}^a \mathcal{T}_{c'_j c_j}^a,$$

and a divergent kinematic factor

$$\propto \frac{p_i \cdot p_j}{(p_i \cdot k)(p_j \cdot k)}.$$

The latter includes soft divergences and, in case of  $\vec{p}_i \parallel \vec{k}$  or  $\vec{p}_j \parallel \vec{k}$ , collinear divergences. The collinear divergences can be disentangled, such that the sum over  $i, j$  in (2.50) is rewritten as a sum of terms which include only one collinear divergence:

$$\begin{aligned} & \overline{|\mathcal{M}^{(n+1)}|^2} \rightarrow \\ & -\mathcal{N}8\pi\alpha_s \sum_{\substack{\text{spins} \\ \text{colours}}} \sum_i \sum_{j \neq i} \mathcal{M}_{\{c_k\}}^{(n)} \left( \mathcal{M}_{\{c_k\}}^{(n)\dagger} \right)_{\substack{c_i \rightarrow c'_i \\ c_j \rightarrow c'_j}} \mathcal{T}_{c'_i c_i}^a \mathcal{T}_{c'_j c_j}^a \frac{p_i \cdot p_j}{(p_i \cdot k)((p_i + p_j) \cdot k)}. \end{aligned} \quad (2.53)$$

In this equation the terms now have for each combination of  $i, j$  a dipole structure, i.e. each term depends only on the colours and momenta of two partons of the  $n$ -particle process plus the momentum of the soft particle. Particle  $i$  is called the emitter,  $j$  the spectator and the particle with momentum  $k$  is the emitted parton.

In the collinear limit on the other hand, the amplitude does not factorize either, if the emitter particle is a gluon and the azimuthal angle around the gluon direction is not integrated out (e.g. (D.27)); instead it can be written as a contraction of a so-called spin-correlated amplitude ( $\sim \mathcal{H}_{\mu\nu}$  in (D.27)) and a type of splitting function that depends on the azimuthal direction of the emitted particle. Still, the collinear limit of a



particle  $i$  splitting into a particle with momentum  $k$  is proportional to  $1/(p_i \cdot k)$ , just like (2.53). This can be used to combine the expressions for the soft and collinear limits in a function that reproduces both limits correctly and depends only on the emitter, emitted and spectator particle and thus has a dipole structure.

In the notation of [29], a matrix element for  $n$  final state partons is written as a tensor in the product-space of spin and colour

$$|1, \dots, n\rangle_n = \sum_{\{c_k\}, \{s_k\}, \{\lambda_k\}} \mathcal{M}_{\{c_k\}, \{s_k\}, \{\lambda_k\}}^{(n)} |\{c_k\}\rangle \otimes |\{s_k\}\rangle \otimes |\{\lambda_k\}\rangle, \quad (2.54)$$

where the sets of indices denote the colour  $c_k$ , the spin  $s_k$  or instead for vector bosons the helicity  $\lambda_k$  of the external particles.  $\mathcal{M}_{\{c_k\}, \{s_k\}, \{\lambda_k\}}^{(n)}$  is just the usual matrix element for the scattering of particles with colours  $\{c_k\}$ , spins  $\{s_k\}$  and gluon-helicities  $\{\lambda_k\}$ . Then an  $n$  particle squared amplitude summed over the colours and spins is given by

$$\sum_{\substack{\text{spins} \\ \text{colours}}} |\mathcal{M}^{(n)}|^2 = {}_n\langle 1, \dots, n | 1, \dots, n \rangle_n$$

and, for example, (2.53) becomes

$$\begin{aligned} & {}_{n+1}\langle 1, \dots, i, \dots, j, \dots, n+1 | 1, \dots, i, \dots, j, \dots, n+1 \rangle_{n+1} \rightarrow \\ & -8\pi\alpha_s \sum_i \sum_{j \neq i} \frac{p_i \cdot p_j}{(p_i \cdot k)((p_i + p_j) \cdot k)} \\ & \cdot {}_n\langle 1, \dots, [ij], \dots, n | \mathbf{T}_i \cdot \mathbf{T}_j | 1, \dots, [ij], \dots, n \rangle_n. \end{aligned} \quad (2.55)$$

Here, the index  $[ij]$  again signifies the replacement of the particles  $i$  and  $j$  by its predecessor and the operators  $\mathbf{T}_i$  are defined through

$$\mathbf{T}_i = \mathcal{T}_{c'_i c_i}^a |a\rangle \otimes |c'_i\rangle \langle c_i|, \quad (2.56)$$

where all indices are summed over. Then, colour-conservation is given by

$$\sum_i \mathbf{T}_i |1, \dots, n\rangle = 0. \quad (2.57)$$

Accordingly, the dipoles to counter final state singularities originating from  $p_i \cdot p_j \rightarrow 0$  are defined by

$$\mathcal{D}_{ij,k} = -\frac{1}{2p_i \cdot p_j} {}_n\langle 1, \dots, \tilde{i}j, \dots, \tilde{k}, \dots, n | \frac{\mathbf{T}_k \cdot \mathbf{T}_{ij}}{\mathbf{T}_{ij}^2} \mathbf{V}_{ij,k} | 1, \dots, \tilde{i}j, \dots, \tilde{k}, \dots, n \rangle_n, \quad (2.58)$$

where  $k$  runs over all spectator partons, i.e. for  $p_i \cdot p_j \rightarrow 0$

$$\begin{aligned} & {}_{n+1}\langle 1, \dots, i, \dots, j, \dots, n+1 | 1, \dots, i, \dots, j, \dots, n+1 \rangle_{n+1} \\ & \rightarrow \sum_{k \neq i, j} \mathcal{D}_{ij,k} + \text{finite}. \end{aligned} \quad (2.59)$$

## 2 Quantum Chromodynamics

The operators  $\mathbf{V}$  are matrices in spin- and Minkowski space and, as noted above, generalizations of spin-dependent splitting functions, to which they reduce in the collinear limit. Their explicit expression can be found in [29] in form of their components  $\langle s|\mathbf{V}|s'\rangle$  or  $\langle \mu|\mathbf{V}|\nu\rangle$ . The latter is to be interpreted via

$$|\mu\rangle = \sum_{\lambda} \varepsilon_{\lambda}^{\mu} |\lambda\rangle,$$

where  $\varepsilon_{\lambda}^{\mu}$  is the polarization tensor of the gluon with helicity  $\lambda$ . As usual, the sum over all physical helicity states of a gluon can be written as a kind of projection operator

$$\sum_{\lambda} \varepsilon_{\lambda}^{*\mu} \varepsilon_{\lambda}^{\nu} = -g^{\mu\nu} + \frac{p^{\mu}\eta^{\nu} + p^{\nu}\eta^{\mu}}{p \cdot \eta}, \quad (2.60)$$

with a time-like auxiliary vector  $\eta$ , that, together with the polarizations  $\varepsilon_{\lambda}$  and the momentum  $p$  of the gluon, spans the Minkowski space. Hence,  $\langle \mu|\mathbf{V}|\nu\rangle$  can be used in

$$\langle \dots |\mathbf{V}| \dots \rangle = \langle \dots |\mu\rangle \langle \mu|\mathbf{V}|\nu\rangle \langle \nu| \dots \rangle,$$

where  $\langle \dots |\mu\rangle \langle \nu| \dots \rangle$  is the spin-correlated amplitude, that is obtained by replacing the polarization tensors  $\varepsilon_{\lambda_j}^{\mu}$  and  $\varepsilon_{\lambda_j}^{*\mu'}$  for gluon  $j$  in the amplitude by its physical polarization sums  $(-g^{\mu\nu} + \dots)$ ,  $(-g^{\mu'\nu'} + \dots)$  and leaving the Lorentz indices  $\nu, \nu'$  uncontracted.<sup>9</sup> The unphysical vector  $\eta$  in the end generally drops out of the dipole formulas, as they represent kinematical limits of physical amplitudes.

Since the dipole (2.58) is defined using an underlying Born amplitude  $\langle \dots | \dots \rangle$ , a map from  $\Phi^{(n+1)}$  to  $\Phi^{(n)}$  has to be specified and is indicated by the tildes. Care has to be taken that momentum conservation holds for the momenta of the  $n$ -particle amplitude including the momentum of the particle  $[ij]$  before splitting,  $p_{[ij]}$ . This is non-trivial, because the emitter particle  $[ij]$  in the  $n$ -particle amplitude would have to be off-shell to split into two on-shell particles away from the collinear and soft limits. Here, another feature of the dipole formalism becomes apparent, namely, that the sum of  $n+1$  final state on-shell momenta can be rewritten in terms of  $n$  on-shell momenta by modifying only the momenta of the emitter and spectator, effectively, defining a mapping  $\Phi^{(n+1)} \rightarrow \tilde{\Phi}^{(n)}$ .<sup>10</sup> Particularly, the tilde in (2.58) specifies that the momenta of the emitter and spectator are replaced by

$$\begin{aligned} \tilde{p}_k^{\mu} &= \frac{1}{1 - y_{ij,k}} p_k^{\mu}, \\ \tilde{p}_{ij}^{\mu} &= p_i^{\mu} + p_j^{\mu} - \frac{y_{ij,k}}{1 - y_{ij,k}} p_k^{\mu}, \\ y_{ij,k} &= \frac{p_i \cdot p_j}{p_i \cdot p_j + p_j \cdot p_k + p_k \cdot p_i}, \end{aligned}$$

<sup>9</sup>Unfortunately, Ref. [29] is not very clear when it comes to spin-correlations. They are sometimes interpreted simply as amplitudes where the polarization vectors for a gluon have been left out, which has in most cases the same effect as the described prescription, but not in general.

<sup>10</sup>This is a feature of kinematics that is well-used also in dipole-based parton showers, where only the momenta of the emitter and the recoiler (i.e. spectator) are changed after the generation of a radiation, cf. Sec. 6.1.

such that  $[ij]$  and  $k$  are on-shell and

$$p_i + p_j + p_k = \tilde{p}_{ij} + \tilde{p}_k.$$

Now, the  $n + 1$ -particle contribution in (2.49) can be written in terms of dipoles as

$$\begin{aligned} \frac{1}{4F} \int d\Phi^{(n+1)} \left\{ \overline{|\mathcal{M}_{n+1}^{(0)}|^2} F_J^{(n+1)}(p_1, \dots, p_i, \dots, p_j, \dots, p_k, \dots, p_{n+1}) \right. \\ \left. - \mathcal{N} \sum_{i,j} \sum_{k \neq i,j} \mathcal{D}_{ij,k} F_J^{(n)}(p_1, \dots, \tilde{p}_{ij}, \dots, \tilde{p}_k, \dots, p_{n+1}) \right\}. \end{aligned} \quad (2.61)$$

The  $\mathcal{I}$ -contribution to the  $n$ -particle phase space in (2.49) is obtained by performing the  $D$ -dimensional integration over the momentum  $p_i$  of the emitted parton in the second line above; the result, which is to be added to the one-loop corrections, can be written in terms of an operator  $\mathbf{I}(\varepsilon)$  inserted in the amplitude of the underlying process in  $D$  dimensions

$$\begin{aligned} \frac{\mathcal{N}}{4F} \int d\Phi^{(n+1)} \sum_{i,j} \sum_{k \neq i,j} \mathcal{D}_{ij,k} F_J^{(n)}(p_1, \dots, \tilde{p}_{ij}, \dots, \tilde{p}_k, \dots, p_{n+1}) \\ = \frac{\mathcal{N}}{4F} \int d\Phi^{(n)} \langle 1, \dots, n | \mathbf{I}(\varepsilon) | 1, \dots, n \rangle F_J^{(n)}(p_1, \dots, p_n), \end{aligned} \quad (2.62)$$

with

$$\mathbf{I}(\varepsilon) = -\frac{\alpha_s}{2\pi} \frac{1}{\Gamma(1-\varepsilon)} \sum_i \frac{1}{\mathbf{T}_i^2} \mathcal{V}_i(\varepsilon) \sum_{k \neq i} \mathbf{T}_i \cdot \mathbf{T}_k \left( \frac{4\pi\mu^2}{2p_i \cdot p_k} \right)^\varepsilon \quad (2.63)$$

and some functions  $\mathcal{V}_i(\varepsilon)$  tabulated in [29]. Thus, by computing  $\mathcal{D}_{ij,k}$  in  $D = 4$  and

$$\langle 1, \dots, n | \mathbf{I}(\varepsilon) | 1, \dots, n \rangle,$$

in  $D = 4 - 2\varepsilon$ , the singularities in the  $n$ - and  $n + 1$ -particle contributions can be cancelled separately.

Up to this point, the emitter and spectator were only allowed to be in the final state. Ref. [29] provides dipoles for more general situations, where the above prescriptions have been supplemented to accommodate initial state partons from PDFs and related singularities, as well as identified final state partons coupled to fragmentation functions. Initial state partons are specified in the ket-notation as indices  $a, b$

$$|1, \dots, n; a, b\rangle,$$

and can act as spectator or emitter. A final state singularity with initial state spectator is cancelled by

$$\begin{aligned} \mathcal{D}_{ij}^a = -\frac{1}{2p_i \cdot p_j} \frac{1}{x_{ij,a}} \\ \cdot {}_{n,a} \langle 1, \dots, \tilde{ij}, \dots, n+1; \tilde{a}, \dots | \frac{\mathbf{T}_a \cdot \mathbf{T}_{ij}}{\mathbf{T}_{ij}} \mathbf{V}_{ij}^a | 1, \dots, \tilde{ij}, \dots, n+1; \tilde{a}, \dots \rangle_{n,a}, \end{aligned} \quad (2.64)$$

an initial state singularity with a final state spectator is cancelled by

$$\mathcal{D}_k^{ai} = -\frac{1}{2p_a \cdot p_i} \frac{1}{x_{ik,a}} \cdot_{n,a} \langle 1, \dots, \tilde{k}, \dots, n+1; \tilde{ai}, \dots | \frac{\mathbf{T}_k \cdot \mathbf{T}_{ai}}{\mathbf{T}_{ai}} \mathbf{V}_k^{ai} | 1, \dots, \tilde{k}, \dots, n+1; \tilde{ai}, \dots \rangle_{n,a}, \quad (2.65)$$

and an initial state singularity with an initial state spectator is cancelled by

$$\mathcal{D}^{ai,b} = -\frac{1}{2p_a \cdot p_i} \frac{1}{x_{i,ab}} \cdot_{n,ab} \langle \widetilde{1}, \dots, \widetilde{n+1}; \tilde{ai}, b | \frac{\mathbf{T}_b \cdot \mathbf{T}_{ai}}{\mathbf{T}_{ai}} \mathbf{V}^{ai,b} | \widetilde{1}, \dots, \widetilde{n+1}; \tilde{ai}, b \rangle_{n,ab}, \quad (2.66)$$

where in all cases different definitions for the variable  $x$  and the operator  $\mathbf{V}$  apply. Eq. (2.66) shows that in case of an initial state singularity with initial state spectator, all final state momenta (including those of non-QCD particles) have to be reshuffled to leave the spectator momentum  $p_b$  unchanged.<sup>11</sup>

IR divergences of a process with initial and final state partons are cancelled by a sum of dipoles of the types  $\mathcal{D}^{ai,b}$ ,  $\mathcal{D}_k^{ai}$ ,  $\mathcal{D}_{ij}^a$  and  $\mathcal{D}_{ij,k}$ . Integrating this sum is rather complex, but can be subsumed in three operators  $\mathbf{I}$ ,  $\mathbf{K}$  and  $\mathbf{P}$ , where the  $\mathbf{I}$ -operator, much like (2.63), includes all the divergences that are cancelled by the virtual contribution as poles in  $\varepsilon$ .  $\mathbf{K}$  and  $\mathbf{P}$  are finite and have to be integrated over the  $n$ -particle phase space and additionally over the momentum fraction of the collinear initial state splitting. The terms with the  $\mathbf{K}$ - and  $\mathbf{P}$ -operators may collectively be called collinear remnants, as they are the leftovers from a cancellations of divergences and IR counterterms.

The steps to follow to correctly use the dipole subtraction formalism are as follows:

1. See if the process has identified partons, i.e. are there any partons coming from hadrons/PDFs or fragmenting into hadrons via FFs. There are dipole formulae for all possible situations, namely, no identified partons, one or two initial state identified parton, one final state identified parton and so-called multi-particle correlations, which allow an arbitrary number of identified partons. The relevant formulae for all these cases are summarized or referenced in Chapters. 7 to 11 in Ref. [29].
2. Identify all partonic  $n$ - and  $n+1$ -particle subprocesses.
3. For all  $n$ -particle subprocesses compute the colour- and spin-correlated amplitudes, i.e.

$$_n \langle \dots ; \dots | \mathbf{T}_i \cdot \mathbf{T}_j | \dots ; \dots \rangle_n$$

<sup>11</sup>A point which is not entirely obvious from [29]: As the matrix elements  $|\dots\rangle$  also depend on the scale  $\mu_R$ , the scale has to be reshuffled, too, if it is related to one of the final state momenta. E.g. if  $\mu_R = p_T$  in the real correction, it becomes  $\mu_R = \widetilde{p}_T$  in the dipole! In App. C.2.5 I show that the same must hold for  $\mu_F$ .

with  $i, j$  running over all unordered selections of coloured particles in the initial and final state and

$$\sum_{\lambda'_j, \lambda_j} n \langle \dots ; \dots | \lambda'_j \rangle \varepsilon_{\lambda'_j}^{*\mu} \varepsilon_{\lambda_j}^\nu \langle \lambda_j | \dots ; \dots \rangle_n$$

with  $j$  running over all gluons.

4. For all combinations of emitter, emitted and spectator, compute  $\mathcal{D}_{ij,k}$  or the relevant equivalent. To that end, use the formulae for  $\mathcal{D}_{ij}$  in [29] which specify the operators  $\mathbf{V}$  and variables  $x_{\dots}$  and the replacement of momenta  $p \rightarrow \tilde{p}$  in the colour- and spin-correlated amplitudes. The result times the jet-defining function for  $n$  partons is to be subtracted from the  $n + 1$ -parton amplitude times the corresponding jet-defining function to cancel its divergences.
5. Likewise, use the colour-correlated amplitudes to compute the insertion of the operator  $\mathbf{I}(\varepsilon)$  in all LO  $n$ -parton amplitudes

$$n \langle \dots ; \dots | \mathbf{I}(\varepsilon) | \dots ; \dots \rangle_n,$$

where the definition of  $\mathbf{I}$  depends on the type of process identified in Step 1. These are added to the virtual corrections to cancel their divergences. Furthermore, for identified particles there are additional operators  $\mathbf{P}$  and  $\mathbf{K}$  (and additionally, for final state identified partons,  $\mathbf{H}$ ), which are finite remnants and have to be integrated over an additional momentum fraction.

It is obvious, that these prescriptions are universal in that they only depend on the types of emitter, emitted and spectator, not on the complete process in question. However, the calculation is quite tedious for a process with a large number of partonic subprocesses, since no use of crossing symmetry between initial and final state can be made, due to the different treatment of initial state (i.e. identified) and final state partons. To simplify the bookkeeping, some programs are available which automate the generation of dipoles, like `AutoDipole` [41] or `MadDipole` [42]. Furthermore, there exist generalizations of the CS dipole method to the case of massive partons [43] and to QED [44]. An explicit application of the dipole method to prompt photon production and its peculiarities is presented in App. C.2.5.

### 2.5.2 FKS subtraction

The subtraction scheme introduced in [38] (and generalized in [40]; though, I follow the description and notation of [45]) is somewhat related to the idea of phase space slicing in that it, too, is based on a partition of the  $n + 1$ -particle phase space. This partition takes place by introducing a “partition of unity”, i.e. set of functions  $\mathcal{S}(\Phi^{n+1})$  such that

$$\sum_{i,j} \mathcal{S}_{ij} = 1 \tag{2.67}$$

## 2 Quantum Chromodynamics

for all phase space points. The sum over  $i, j$  in (2.67) runs over all partons of a given real correction process and the functions  $\mathcal{S}$  have to be chosen such that  $\mathcal{S}_{ij}$  vanishes in all regions of the phase space where the real correction matrix elements diverges, apart from the regions where either  $i$  and  $j$  become collinear or  $i$  is soft. A  $n + 1$ -parton process  $\mathcal{R}$  (as defined in (2.46)) can then be decomposed into parts  $\mathcal{R}_{ij}$ , which include only the soft and collinear divergences related to parton  $i$ , by simply multiplying with the partition of unity

$$\mathcal{R} = \sum_{i,j} \mathcal{S}_{ij} \mathcal{R} \equiv \sum_{i,j} \mathcal{R}_{ij}. \quad (2.68)$$

Now, the phase space integral for each of the  $\mathcal{R}_{ij}$  can be rewritten such that the singularities related to the radiated parton  $i$  lie on the end points of the integral over  $p_i$  in terms of spherical coordinates in  $D$  dimensions:

$$\frac{d^{D-1}p_i}{(2\pi)^{D-1}2p_i^0} = d\xi_i dy d\Omega_{D-2} \frac{s^{1-\varepsilon}}{(4\pi)^{3-2\varepsilon}} \xi_i^{1-2\varepsilon} (1 - y_{ij}^2)^{-\varepsilon} \quad (2.69)$$

where

$$\xi_i \equiv \frac{2p_i^0}{\sqrt{s}} \in [0, 1], \quad (2.70)$$

$$y_{ij} \equiv \cos(\theta_{ij}) \in [-1, 1], \quad (2.71)$$

$\theta_{ij}$  is the angle between  $i$  and  $j$  and  $d\Omega_{D-2}$  is the  $D - 2$ -dimensional solid-angle relative to the momentum of parton  $j$ . The soft singularity of  $\mathcal{R}_{ij}$  is then encountered for  $\xi_i \rightarrow 0$  and the collinear singularity for  $y_{ij} \rightarrow 1$ . Since the soft divergence in  $\mathcal{R}_{ij}$  is of the form  $(p_i \cdot p_j p_i \cdot p_k)^{-1} \propto \xi_i^{-2}$  (cf. (2.50)) and the collinear divergence is  $(p_i \cdot p_j)^{-1} \propto (1 - y)^{-1}$  (cf. App. D), it follows that  $\xi_i^2(1 - y)\mathcal{R}_{ij}$  is finite. Thus, by writing

$$\begin{aligned} & \int \frac{d^{D-1}p_i}{(2\pi)^{D-1}2p_i^0} \mathcal{R}_{ij} \\ &= \int_0^1 d\xi_i \int_{-1}^1 dy \int d\Omega_{D-2} \frac{s^{1-\varepsilon}}{(4\pi)^{3-2\varepsilon}} \xi_i^{-1-2\varepsilon} (1 + y_{ij})^{-\varepsilon} (1 - y_{ij})^{-1-\varepsilon} \\ & \quad \cdot [\xi_i^2(1 - y)\mathcal{R}_{ij}] \end{aligned} \quad (2.72)$$

all divergences are extracted to the factors outside the square brackets and can be made explicit by an expansion in terms of  $\delta$ - and plus-distributions. The expansions are given by the following equality, which is understood to be true when integrated along with a test-function, while approaching the limit  $\varepsilon = 0$  from  $\varepsilon < 0$ :

$$\xi_i^{1-2\varepsilon} = -\frac{1}{2\varepsilon} \delta(\xi_i) + \left(\frac{1}{\xi_i}\right)_+ - 2\varepsilon \left(\frac{\ln(\xi_i)}{\xi_i}\right)_+ + \mathcal{O}(\varepsilon^2), \quad (2.73)$$

$$(1 - y_{ij})^{-1-\varepsilon} = -\frac{2^{-\varepsilon}}{\varepsilon} \delta(1 - y_{ij}) + \left(\frac{1}{1 - y_{ij}}\right)_+ - \varepsilon \left(\frac{\ln(1 - y_{ij})}{1 - y_{ij}}\right)_+ + \mathcal{O}(\varepsilon^2). \quad (2.74)$$

Here, the plus-distributions are defined to induce subtractions at  $\xi_i = 0$  and  $y_{ij} = 1$ , e.g.

$$\int_0^1 d\xi_i \left( \frac{1}{\xi_i} \right)_+ g(\xi_i) = \int_0^1 d\xi_i \left( \frac{1}{\xi_i} \right) (g(\xi_i) - g(0)) , \quad (2.75)$$

$$\int_{-1}^1 dy \left( \frac{1}{1 - y_{ij}} \right)_+ g(y_{ij}) = \int_{-1}^1 dy \left( \frac{1}{1 - y_{ij}} \right) (g(y_{ij}) - g(1)) . \quad (2.76)$$

By inserting (2.73) and (2.74) in (2.72) one has explicitly extracted all divergences of the real correction as poles  $\varepsilon^{-1}$  and  $\varepsilon^{-2}$ ; these can again be cancelled against the poles of the virtual corrections and the IR-bare long-distance functions. The subtraction terms induced by the plus-distributions correspond to the functions  $\mathcal{D}$  of Eq. (2.49). However, since the  $\mathcal{R}_{ij}$  taken at the subtraction points  $\xi_i = 0$  and  $y_{ij} = 1$  decompose into matrix-elements of the underlying  $n$ -particle process times a universal divergence, the result of (2.72) also has a universal structure, i.e. it depends only on the process through  $\mathcal{R}_{ij}$  and its underlying process where  $i$  and  $j$  are replaced by their mother parton  $[ij]$ .

In the FKS subtraction scheme the virtual contributions have to be given in the conventional dimensional regularization (CDR) scheme. In the CDR-scheme the (renormalized) virtual contributions  $\mathcal{V}$  can be written with the IR poles made explicit:

$$\mathcal{V} = \frac{(4\pi)^\varepsilon}{\Gamma(1 - \varepsilon)} \frac{\alpha_s}{2\pi} \left[ \frac{1}{\varepsilon^2} a\mathcal{B} + \frac{1}{\varepsilon} \sum_{i,j} c_{ij} \mathcal{B}_{ij} + \mathcal{V}_{\text{fin}} \right] , \quad (2.77)$$

where the coefficients  $a$  and  $c_{ij}$  are independent of  $\varepsilon$ , while the Born amplitude  $\mathcal{B}$ , and the colour-correlated Born amplitude  $\mathcal{B}_{ij}$  are given in  $D$  dimensions and thus depend on  $\varepsilon$ . The values for the coefficients can be extracted from [38]<sup>12</sup>

$$a = - \sum_i C_i , \quad (2.78)$$

$$c_{ij} = (1 - \delta_{ij}) \left[ -\frac{\gamma_i}{C_i} + \ln \left( \frac{2p_i \cdot p_j}{\mu_R^2} \right) \right] , \quad (2.79)$$

where  $i, j$  run over all coloured legs and  $C_i$  is just the Casimir constant for the representation to which parton  $i$  belongs. The constants  $\gamma_i$  are given by

$$\gamma_{q,\bar{q}} = \frac{3}{2} C_F , \quad (2.80)$$

$$\gamma_g = \frac{11}{6} C_A - \frac{2}{3} T_F N_f , \quad (2.81)$$

<sup>12</sup>Alternatively, they can be won by comparing the singular terms of the CS dipoles and (2.77). I have checked the equality of those terms.

## 2 Quantum Chromodynamics

where usually  $T_F = 1/2$ . The colour-correlated amplitudes  $\mathcal{B}_{ij}$  are defined in terms of the colour-charge operators (2.51) by<sup>13</sup>

$$\mathcal{B}_{ij} = -\frac{\mathcal{N}}{4F} \sum_{\substack{\text{spins} \\ \text{colours}}} \mathcal{M}_{\{c_k\}} \left( \mathcal{M}_{\{c_k\}}^\dagger \right)_{c_i \rightarrow c'_i, c_j \rightarrow c'_j} \mathcal{T}_{c'_i, c_i}^a \mathcal{T}_{c'_j, c_j}^a. \quad (2.82)$$

By combining (2.77), the IR-counterterms from the PDFs and the real corrections in the form (2.72) all divergences drop out and one ends up with the following finite contributions to the cross section additional to  $\mathcal{B}$ :

- A “soft-virtual” term (Eq. (2.99) in [45])

$$\mathcal{V}_{\text{sv}} = \frac{\alpha_s}{2\pi} \left( \mathcal{Q}\mathcal{B} + \sum_{ij} \mathcal{I}_{ij} \mathcal{B}_{ij} + \mathcal{V}_{\text{fin}} \right), \quad (2.83)$$

replaces the virtual contribution  $\mathcal{V}$ .  $\mathcal{Q}$  and  $\mathcal{I}$  are given in Eqs. (2.100) and (2.101) of [45]<sup>14</sup>:

$$\begin{aligned} \mathcal{Q} = \sum_i & \left[ \gamma'_i - \ln \left( \frac{s}{\mu_R^2} \right) \left( \gamma_i - 2C_i \ln \left( \frac{2E_i}{\xi_c \sqrt{s}} \right) \right) \right. \\ & \left. + 2C_i \left( \ln^2 \left( \frac{2E_i}{\sqrt{s}} \right) - \ln^2(\xi_c) \right) - 2\gamma_i \ln \left( \frac{2E_i}{\sqrt{s}} \right) \right], \end{aligned} \quad (2.84)$$

$$\begin{aligned} \mathcal{I}_{ij} = & \frac{1}{2} \ln^2 \left( \frac{\xi_c^2 s}{\mu_R^2} \right) + \ln \left( \frac{\xi_c^2 s}{\mu_R^2} \right) \ln \left( \frac{p_j \cdot p_i}{2E_j E_i} \right) - \text{Li}_2 \left( \frac{p_j \cdot p_i}{2E_j E_i} \right) \\ & + \frac{1}{2} \ln^2 \left( \frac{p_j \cdot p_i}{2E_j E_i} \right) - \ln \left( 1 - \frac{p_j \cdot p_i}{2E_j E_i} \right) \ln \left( \frac{p_j \cdot p_i}{2E_j E_i} \right). \end{aligned} \quad (2.85)$$

- A collinear remnant<sup>15</sup>

$$\begin{aligned} \mathcal{G}^{ab} = \frac{\alpha_s}{2\pi} \sum_{a'} & \left\{ (1-z) \hat{P}_{a'a}(z) \left[ \left( \frac{1}{1-z} \right)_+ \log \frac{s}{\mu_F^2} + 2 \left( \frac{\ln(1-z)}{1-z} \right)_+ \right] \right. \\ & \left. - \left[ \frac{\partial \hat{P}_{a'a}^{(\varepsilon)}(z)}{\partial \varepsilon} \right]_{\varepsilon=0} \right\} \mathcal{B}^{a'b}, \end{aligned} \quad (2.86)$$

<sup>13</sup>Note that the colour-charge operators in [45] are defined to act in the fundamental representation on initial state quarks, whereas I defined (2.51) to act in the dual fundamental on initial state quarks, i.e. the colour-charge operator of [45] is  $-(\mathcal{T}^a)^T$ . For that reason the primes in the definition (2.82) are exchanged w.r.t. the definition in [45].

<sup>14</sup>The parameter  $\xi_c$  stems from a more general definition of the plus-distributions than presented here in order not to divert from the general idea of the method. I give the versions of (2.100) and (2.101) of [45] which I found to be implement in the code of the `POWHEG BOX`. There,  $\xi_c$  is present but set to 1.

<sup>15</sup>Here, I set  $\xi_c = 1$  for brevity.



given in Eq. (2.102) of [45], for each initial state parton  $a$ ,  $b$  has to be integrated over the  $n$ -particle phase space  $\Phi^{(n)}$  and an additional longitudinal momentum fraction  $z$ . The superscripts on  $\mathcal{B}$  indicate that the partons  $a'$  and  $b$  with momenta  $zp_a$  and  $p_b$  enter the Born subprocess.

- And the left-over from (2.72) in  $D = 4$  dimensions,

$$\int_0^1 d\xi_i \int_{-1}^1 dy \int d\varphi \frac{s}{(4\pi)^3} \left( \frac{1}{\xi_i} \right)_+ \left( \frac{1}{1-y_{ij}} \right)_+ [\xi_i^2 (1-y) \mathcal{R}_{ij}] ,$$

gives, when combined with the rest of the measure  $d\Phi^{(n+1)}$  that has been disregarded in (2.72), the subtracted real contribution.

The FKS subtraction is implemented in the POWHEG BOX [46] which will be discussed in Sec. 6.2.

## 2.6 QCD Phases

Up to this point, the preceding sections were concerned only with localized, high-energy scattering events, that, thanks to factorization theorems, could be interpreted as QCD parton scatterings. A tacit assumption – which is indeed an experimental fact – was that only colour-neutral objects, hadrons, are found at low energies. This fact is formalized by the confinement hypothesis, which states that some non-perturbative mechanism in QCD forces quarks and gluons to be bound in hadrons at low energies. Here, “low energy” refers to an energy below the scale parameter of QCD,  $\Lambda_{\text{QCD}} \sim 200 \text{ MeV}$ .

Of course, the growth of the coupling (2.16) with decreasing scale, as the flip side of asymptotic freedom, called infrared slavery, is consistent with confinement. But after all, the  $\beta$ -function (2.14) is the result of a small coupling expansion, which loses its validity as the scale decreases and the coupling grows accordingly. As such, the phenomenon of confinement is not accessible through perturbation theory. Instead it is approached through the use of lattice QCD [47], i.e. simulations of QCD on a lattice of discrete space-time points, such that it is possible to simulate, for example, the quark-antiquark potential, with the result that it rises linearly as quarks get pulled apart [6] as an indication of confinement.

Confinement can also be studied as a property of extended QCD matter in a low temperature and low density phase. It is then natural to assume that the asymptotic freedom property corresponds to a deconfined phase at high temperatures above  $\Lambda_{\text{QCD}}$  or high density, where quarks and gluons cease to be bound in hadrons – the quark-gluon plasma (QGP). The study of QCD phases requires a formulation of QCD in statistical terms, which allows a description of thermodynamic bulk observables such as the temperature and density. A Statistical Field Theory based on the QCD-Hamiltonian leads to a formulation that is called Thermal Field Theory (TFT) [48, 49], as opposed to the “zero-temperature” QFT used to describe high-energy scatterings of partons. Studies of TFT, by perturbation theory and lattice methods, provide most of what is

theoretically accessible about QCD's equilibrium bulk phenomena and, combined with related effective theories [50], point to a rich phase structure of QCD as sketched in Fig. 2.5.

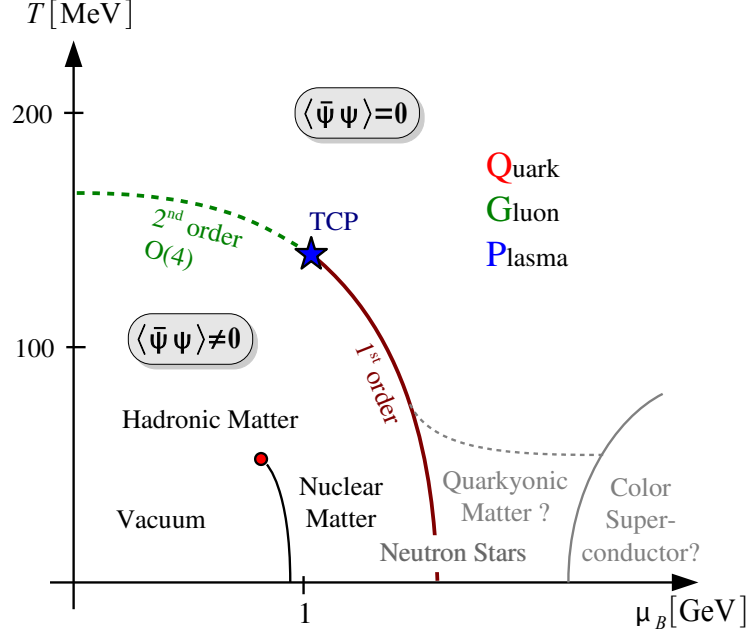


Figure 2.5: Sketch of the QCD phase diagram w.r.t. temperature and baryochemical potential from [51].

The reason that Fig. 2.5 represents just a sketch is that the theoretical tools developed so far are each merely accessing certain areas and features of the phase diagram [50]. As depicted, the state variables are the temperature of the system and its baryochemical potential.<sup>16</sup> At zero baryochemical potential the location of the deconfinement transition is accessible by lattice QCD simulations, where in a recent result a confinement-deconfinement transition was found in the region of [52]

$$T_c = (154.0 \pm 0.9) \text{ MeV} . \quad (2.87)$$

As depicted in the phase diagram, the transition at zero baryochemical potential is not a first order phase transition. Thus, an exact value for the temperature depends on the order parameter used to define the transition. The quoted value is related to the chiral symmetry breaking phase transition extrapolated to QCD with three massive quarks (the heavier quarks play no role as their masses lie well-above the transition temperature). Other measures of the transition temperature discussed in the literature

<sup>16</sup>The baryochemical potential can be understood as being correlated to the net baryon density, i.e. it is a measure of the baryon-antibaryon asymmetry. For that reason the same phase diagram is often depicted with the density on the abscissa.

are for example related to the free energy between infinitely massive (static) quarks or the change of the energy density of a thermalized QCD system [53]. An example of the latter is depicted in Fig. 2.6 which illustrates a transition region signified by a rapid change of the energy density and pressure, which is interpreted as the rise in the number of degrees of freedom, corresponding to the liberation of quarks and gluons (as described by a simple free quark gluon gas) from hadrons (as described, for example, in a simple free pion gas). This figure furthermore shows a remarkable departure from the ideal gas law for massless particles

$$\varepsilon = 3p,$$

indicating that in a region up to  $\sim 2T_c$  the constituents of the gas are still rather strongly coupled. On the confinement side of the transition region,  $T < T_c$ , the bulk behaviour is well-described by an ideal gas of hadrons with masses below the transition temperature, the hadron resonance gas (HRG) [54].

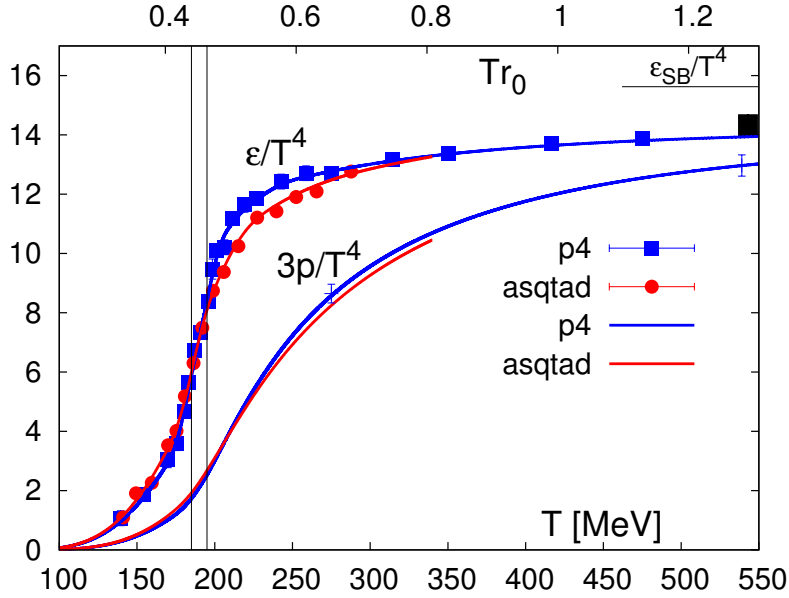


Figure 2.6: Energy density and pressure (for different discretization schemes) rapidly increasing and approaching the free parton Stefan-Boltzmann limit for increasing temperature. The results depicted have not been extrapolated to physical values. From [55].

Research on the phase structure of QCD is not only of interest in itself, but has implications on several regimes of nature where extreme conditions are manifest. An example is cosmology: Since the establishment of General Relativity as the theory of gravitation and the description of the evolution of the universe in the Standard Model of Cosmology [56], it is known that the universe expands and, looking back in time, should up to some point in time after the initial singularity – the big bang – have

## 2 Quantum Chromodynamics

had a temperature greater than  $\Lambda_{\text{QCD}} \sim 10^{12}$  K, i.e. high enough for the formation of a QGP. The confinement phase transition can be extrapolated from the cosmological expansion to have taken place at  $t \approx 10^{-5}$  s after the big bang [57]. In the phase diagram this transition is to be traced near the ordinate at low-baryon density, as the quark-antiquark ratio at the point of the transition is negligible [50]. An example from astronomy is given by the core of a neutron star – the final stadium of a star with a mass between the Chandrasekhar and Oppenheimer-Volkoff limits whose collapse is prevented by its neutron degeneracy pressure – where the density possibly exceeds that of nuclear matter at negligible temperature [58, 59] and some form of deconfinement might occur, as indicated in Fig. 2.5. Of course, in both cases, these examples are not experimentally accessible; the only route to go for an experimental exploration of QCD thermodynamics is through heavy ion collisions (HIC), which probe the low  $\mu_B$ -region in the phase diagram and are discussed in Ch. 5.

### 3 Prompt Photon Production

This chapter aims to present the peculiarities of photon phenomenology in the presence of strong interactions. In interactions of photons with hadrons the photon interacts at low energies with the hadron charge, as expected by QED. However, at higher energies it has been found that the photon exhibits a hadronic structure, in the sense that its interactions with hadrons are observed to be similar to interactions of hadrons with hadrons (at that time a puzzling discovery that has even been discussed in popular science [60]). This has led to the formulation of the vector-meson dominance model (VMD) [61], in which the photon is assumed to fluctuate mainly into  $\rho$ -,  $\omega$ - and  $\phi$ -mesons, which then interact strongly with the target hadron. Finally, in the light of the parton model it has been found that even this picture was lacking, since a high-energy photon can also couple directly to charged partons.

With QCD as the established theory of strong interactions, photons are understood to couple to quarks and the hadronic structure of the photon enters through the non-perturbative nature of the interplay of QED and QCD at low energies. Since the photon is massless, it can fluctuate into QCD particles at a hadronic energy  $\mathcal{O}(\Lambda_{\text{QCD}})$ , i.e. at scales at which free partons cease to exist and are supposed to form bound states.<sup>1</sup> This situation is reflected by the breakdown of perturbation theory through the collinear singularity in the photon-to-quark splitting and the necessity of considering a photon parton distribution or fragmentation function as a means to absorb the singularity.

Reviews of the role of the photon as an initial state particle and its structure can be found for example in [62, 63, 64, 65]. In the final state, prompt photons, i.e. photons generated in a hard scattering process as opposed to photons from hadron decays, promised to be a clean test of QCD in hadron collisions; photons are supposed to be experimentally easier to measure than jets and hadrons [6] and considerably reduce the number of matrix elements that have to be computed, compared to pure QCD processes. Furthermore, compared to other electromagnetic probes, the photon can already at leading order test the gluon distribution of the initial state hadron through the QCD Compton process  $qg \rightarrow \gamma q$ . However, both of these assumptions are valid only approximately as long as the photon is measured in isolation, such that the non-perturbative contributions are suppressed.

At the LHC, the detection of photons has played a huge role in its largest success: The detection of the Higgs boson, partially through its double-photon decay channel [66, 67].<sup>2</sup> Additionally, photons are one of the probes used to detect the creation of a

---

<sup>1</sup>In contrast, the weak bosons for example have masses that provide a scale at which those fluctuations can be treated perturbatively.

<sup>2</sup>Additionally, at the time of writing, there has been quite some excitement about a (in the latest measurements statistically insignificant) double-photon resonance signal at 750 GeV [68, 69].

### 3 Prompt Photon Production

QGP in heavy ion collisions, as will be discussed in Ch. 5. Thus, it is crucial to further minimize the theoretical uncertainties in the predictions for prompt photon production to correctly estimate the background to those signal events. To that end, calculations of prompt photon production beyond LO have already been carried out in the 1980s [70, 71, 72, 73] and full NLO results can be found in [74] and the references therein. Full NNLO results are not available yet, but several resummed results beyond the leading logarithm have been published, e.g. [75, 76, 77, 78, 79, 80].

In the next sections, after introducing the QED Lagrangian, a short review of the hadronic structure of the photon is given, before going into some detail on the NLO calculation of single prompt photon production. A code for the inclusive single photon production cross section, written to test the results of my calculation, Sec. 3.3, is presented and compared to the de facto standard code `JETPHOX` in Sec. 3.4, which itself is described shortly in Sec. 3.5.

## 3.1 QED Lagrangian

Quantum Electrodynamics (QED), as the first QFT, with its long history intertwined with the early developments of Quantum Mechanics, is described basically in every introductory textbook on QFT such as [81, 82, 83], so I will just introduce the Lagrangian here.

The QED interactions are described by

$$\mathcal{L}_{\text{QED}} = Q_f e_0 \bar{\Psi}_0^f \gamma_\mu \Psi_0^f A_0^{(\gamma)\mu} - \frac{1}{4} F_{0\mu\nu} F_0^{\mu\nu} - \frac{1}{2\xi_0} \left( \partial_\mu A_0^{(\gamma)\mu} \right)^2, \quad (3.1)$$

with the Abelian field-strength tensor

$$F_0^{\mu\nu} = \partial^\mu A_0^{(\gamma)\nu} - \partial^\nu A_0^{(\gamma)\mu}. \quad (3.2)$$

Analogously to Sec. 2.2 the counterterms are constructed by redefining the parameters and fields

$$A_0^{(\gamma)} = \sqrt{Z_A^{\text{QED}}} A^{(\gamma)}, \quad (3.3)$$

$$e_0 = \tilde{Z}_e e = \frac{Z_e}{Z_\Psi \sqrt{Z_A^{\text{QED}}}} e \quad (3.4)$$

$$\xi_0 = Z_A^{\text{QED}} \xi, \quad (3.5)$$

with the definition of  $\tilde{Z}_e$  chosen such that the counterterm is proportional to  $Z_e$ , and the redefinition of  $\xi$  chosen such that the corresponding counterterm vanishes similarly to the QCD case. Rewriting Eq. (3.1) gives then

$$\begin{aligned} \mathcal{L}_{\text{QED}} = & Q_f e \bar{\Psi}^f \gamma_\mu \Psi^f A^{(\gamma)\mu} - \frac{1}{4} F_{\mu\nu} F^{\mu\nu} - \frac{1}{2\xi} \left( \partial_\mu A^{(\gamma)\mu} \right)^2 \\ & + \delta Z_e Q_f e \bar{\Psi}^f \gamma_\mu \Psi^f A^{(\gamma)\mu} - \delta Z_A^{\text{QED}} \frac{1}{4} F_{\mu\nu} F^{\mu\nu}. \end{aligned} \quad (3.6)$$

The full Lagrangian of the QED+QCD theory is then given by the sum  $\mathcal{L}_{\text{QCD}} + \mathcal{L}_{\text{QED}}$  of (2.2) and (3.6) and the corresponding Feynman rules are given in App. B. As can be seen the Feynman rules are independent of  $\xi$ . The reason is the original Ward-Takahashi identity which can be derived as a consequence of the conservation of the electric current; it has two prominent implications [82]: First, the contraction of a photon's momentum with the current (fermion line in the diagram) it is attached to always vanishes in the calculation of S-matrix elements. Accordingly, the  $\xi$  dependence of the photon propagator can be ignored. Second, the renormalization constants for the fermion-photon-vertex and for the fermion field are equal

$$\delta Z_e = \delta Z_\Psi. \quad (3.7)$$

As a consequence, the charge renormalization  $\tilde{Z}_e$  is completely determined by corrections to the photon propagator and there is no running charge if no higher order corrections in the electromagnetic coupling  $\alpha$  are computed.

## 3.2 Hadronic Structure of the Photon

In the early days of QCD, it has been suggested to measure the photon structure functions in a manner similar to the nucleon structure functions, by DIS [84], i.e. effectively scatterings of virtual photons  $\gamma^*$  on real photons  $\gamma$  (produced for example as bremsstrahlung of an electron beam). The theoretical analysis of the process is then akin to the analysis of DIS, starting with an ansatz like (2.18), but with charged currents evaluated in a photon state  $|\gamma\rangle$  instead of the hadron state  $|H\rangle$ . In the treatment of the current expectation value, an OPE is used to separate short- and long-distance contributions, enabling a prediction of the scaling behaviour of the photon structure functions. It has been found that the inclusion of QED operators, representing the interaction of the photon with charged partons, introduces a so-called point-like or anomalous component [85] to the scaling behaviour – “anomalous” in the sense that this term represents a deviation from the expected DIS scaling of hadrons. The (expected) hadron- or DIS-like scaling of the photon, on the other hand, could be described by taking the photon to be a superposition of mesons – the VMD – which explicitly states [61, 64]

$$|\gamma\rangle^{\text{hadronic}} = \sum_{V=\rho,\omega,\phi} \frac{e}{f_V} |V\rangle. \quad (3.8)$$

Hence a picture like Fig. 3.1 emerges for the leading diagrams in  $\gamma^*\gamma$  scattering: A contribution due to strong interactions and a contribution due to photon-parton-scattering. It has been shown, that the anomalous term is dominant for asymptotically large energies [86]; as this contribution is completely calculable in perturbation theory, the leading behaviour of the photon structure functions at asymptotic energies is completely determined. Since these early considerations, the photon structure has been tested extensively, experimentally as well as theoretically (reviews are given for example in [63, 64]), and the general picture of photon interactions as developed in the early 1970s still holds. Even

### 3 Prompt Photon Production

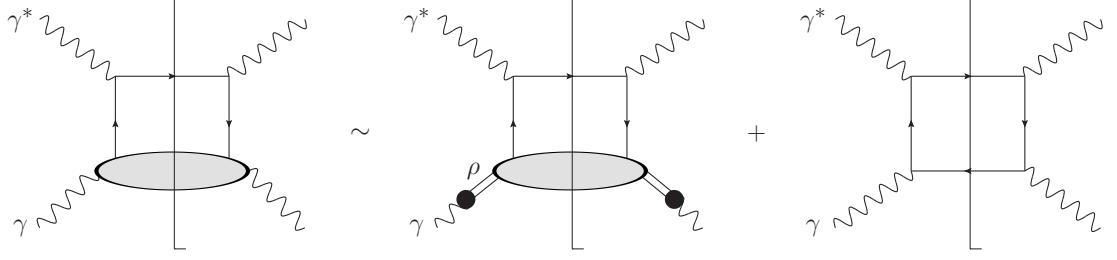


Figure 3.1: The leading contributions in  $\gamma^*\gamma$  scattering. The long-distance contributions, represented by the blob, decompose into the hadronic contribution, described by the VMD which is dominated by the  $\rho$  contribution, and photon-parton coupling.

though, originally discussed in terms of initial state photons, the same considerations can at least qualitatively be applied to final state photons by crossing the processes.

In the language of factorized processes the hadronic content of the photon is embodied in a non-perturbative photon PDF or FF. For example, the process central to this work, the factorized photon-hadroproduction cross section, can be written as (cf. (2.31))

$$\begin{aligned} d\sigma_{AB \rightarrow \gamma X}(p_A, p_B, p_\gamma) = & \sum_{a,b,c} \int_0^1 dx_a \int_0^1 dx_b \int_0^1 dz f_{a/A}(x_A, \mu_F) f_{a/B}(x_B, \mu_F) \\ & \cdot d\hat{\sigma}_{ab \rightarrow cX} \left( x_a p_A, x_b p_B, \frac{p_\gamma}{z}, \mu_F \right) D_{\gamma/c}(z, \mu_F), \end{aligned} \quad (3.9)$$

where the sums over  $a$  and  $b$  include all QCD partons and the sum over  $c$  additionally includes the photon, making use of

$$D_{\gamma/\gamma}(z, \mu_F) \equiv \delta(1 - z). \quad (3.10)$$

The existence of a non-zero photon-in-photon FF causes the point-like/anomalous contribution to the cross section that has been mentioned above. As described in Sec. 2.4, this factorization formula is a result of a theorem, where the PDFs and FF are defined as some operator expectation value that, usually, can not be computed in perturbation theory. On the other hand, as was done in that section, I want to switch to the heuristic IR point-of-view again, to illustrate the practical need for a photon fragmentation function.

Taking the photon as an elementary particle, without considering any hadronic nature of the photon, one might begin a calculation of single photon production by including only hard scattering processes  $d\hat{\sigma}_{ab \rightarrow \gamma X}$  producing photons directly. Up to NLO, i.e.  $\mathcal{O}(\alpha\alpha_s^2)$ , the final state of the contributions is composed either of a photon and one parton in the Born terms and the virtual corrections or a photon and two partons in the real radiation corrections. Consequentially, in the real radiation corrections, configurations where the two partons are collinear or a gluon is soft can occur; these are not problematic if the observable is IR safe with respect to QCD, e.g. no parton is observed. Still, one



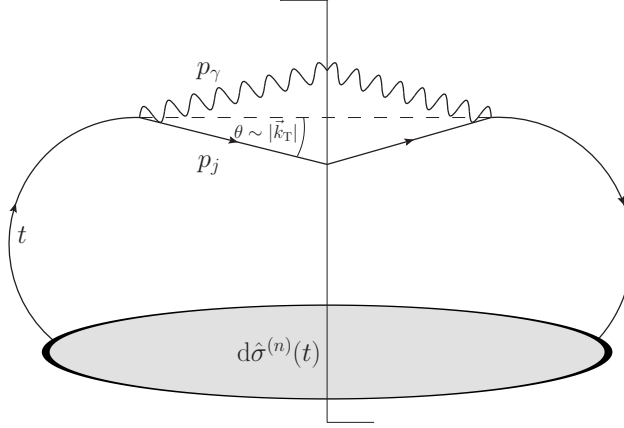


Figure 3.2: Quark line with virtuality  $t^2 \sim k_T^2$  leaving some hard  $n$ -particle process  $d\hat{\sigma}^{(n)}$  and radiating off a photon with transverse momentum  $k_T$  relative to  $t$ .

of the quarks can be collinear w.r.t. the photon, leading to a collinear singularity in diagrams of the type displayed in Fig. 3.2 for  $k_T^2 \rightarrow 0$ .

This type of divergence, as an effect related to the masslessness of the fermion, can also be observed in massless QED, where the factorization of these divergences has been examined in the 1930s for bremsstrahlung photons radiating off electrons – called the Weizsäcker-Williams equivalent photon approximation [87], [88]. The universal singularities related to final state photon splittings are completely analogous to (2.43), one just has to replace the QCD coupling  $\alpha_s$  with the QED coupling  $\alpha$  and the QCD splitting functions by QED splitting functions:

$$\begin{aligned} d\hat{\sigma}_{\gamma c}^{(n+1)}(\dots, p_\gamma, \dots, p_j, \dots) \\ \rightarrow \int_0^1 dz \int \frac{d|\vec{k}_T|^2}{|\vec{k}_T|^2} d\hat{\sigma}_c^{(n)}(\dots, t = p_\gamma + p_c = \frac{p_\gamma}{z}, \dots) \frac{\alpha}{2\pi} P_{\gamma c}(z), \end{aligned} \quad (3.11)$$

or in  $D$  dimensions with  $k_T$  integrated up to  $\mu_F$

$$\begin{aligned} d\hat{\sigma}_{\gamma c}^{(n+1)}(\dots, p_\gamma, \dots, p_c, \dots) \\ \rightarrow \int_0^1 dz d\hat{\sigma}_c^{(n)}(\dots, \frac{p_\gamma}{z}, \dots) \frac{\alpha}{2\pi} P_{\gamma c}^{(\varepsilon)}(z) \left( \frac{4\pi\mu_R^2}{\mu_F^2} \right)^\varepsilon \frac{1}{\Gamma(1-\varepsilon)} \frac{1}{-\varepsilon}. \end{aligned} \quad (3.12)$$

In general, the LO QED splitting functions can be obtained from the QCD splitting functions by simply replacing the Casimir factor for the fundamental  $SU(N_c)$ -representation  $C_F$  by its QED counterpart  $Q_i^2$  (the quark charge in units of  $e$  squared) and the Casimir factor  $C_A$  for the adjoint representation by zero (since the photon is not charged and

### 3 Prompt Photon Production

thus is in the trivial representation of the gauge group). Hence, the quark-to-photon splitting function can be deduced from (2.37), giving<sup>3</sup>

$$P_{\gamma c} = Q_c^2 \frac{1 + (1 - z)^2}{z}. \quad (3.13)$$

Of course, the collinear singularity (3.11) would not arise if the observable were defined such that no partonic energy would be allowed in the direction of the photon, since then  $k_T$  could not vanish. Indeed, photons are often measured in isolation to suppress the background of photons from decaying hadrons (mainly  $\pi^0$ - and  $\eta$ -mesons), but the, in principle, finite energy resolution does not allow for a total isolation of the photon – it may always be accompanied by some undetected hadronic energy, which in the theoretical calculation still gives rise to a collinear singularity. On the other hand, if one were to argue, that a photon were indistinguishable from a jet, this singularity could be cancelled by virtual electromagnetic corrections. However, usually photons can be distinguished from hadron jets. Thus, the only viable way to get rid of the collinear singularity is to introduce a non-perturbative function  $D_{\gamma/c}^{(0)}$ , convoluted with  $\mathcal{O}(\alpha_s^2)$  parton scattering functions  $d\hat{\sigma}_{ab \rightarrow cd}$ , which is able to absorb the singularity (3.11). The complete cross section is then just (3.9) with (3.10) again and the absorption of the photon singularity amounts to a redefinition of this  $D_{\gamma/c}$ , which in the  $\overline{\text{MS}}$ -scheme is similar to (2.40),

$$D_{\gamma/c}^{\overline{\text{MS}}}(x, \mu_F) = D_{\gamma/c}^{(0)}(x) - \int_x^1 \frac{dz}{z} \frac{\alpha}{2\pi} P_{\gamma c}(z) \left( \frac{4\pi\mu_R^2}{\mu_F^2} \right)^\varepsilon \frac{1}{\Gamma(1-\varepsilon)} \frac{1}{\varepsilon} D_{\gamma/\gamma}^{(0)}\left(\frac{x}{z}\right), \quad (3.14)$$

leading to the photon version of the evolution equation (2.44),

$$\begin{aligned} \mu_F^2 \frac{d}{d\mu_F^2} D_{\gamma/c}(x, \mu_F) &= \int_x^1 \frac{dz}{z} \frac{\alpha}{2\pi} P_{\gamma c}\left(\frac{x}{z}\right) D_{\gamma/\gamma}(z, \mu_F) \\ &= \frac{\alpha}{2\pi} P_{\gamma c}(x). \end{aligned} \quad (3.15)$$

This is readily solved by integration, giving

$$D_{\gamma/c}(z, \mu_F) = \frac{\alpha}{2\pi} P_{\gamma c}(x) \ln \left( \frac{\mu_F^2}{\mu_s^2} \right) + D_{\gamma/c}(z, \mu_s), \quad (3.16)$$

with a boundary condition  $D_{\gamma/c}(z, \mu_s)$ , defined at some starting scale  $\mu_s$ , e.g.  $\mu_s = \Lambda_{\text{QCD}}$ , which has to be measured by matching the computed cross section to experimental results.

From the IR point of view, it seems as if the photon-FF has to be introduced only if one goes beyond leading order, i.e. beyond  $\mathcal{O}(\alpha\alpha_s)$ . Yet, if the solution (3.16) with  $\mu_s = \Lambda_{\text{QCD}}$  is compared to the running coupling (2.16), the behaviour of the FF is found to be

$$D_{\gamma/c}(z, \mu_F) \sim \frac{\alpha}{\alpha_s(\mu_F)} \quad (3.17)$$

---

<sup>3</sup>Sometimes the photon splitting function is defined without the charge squared  $Q_i^2$ , which is then combined with the coupling  $\alpha \rightarrow \alpha Q_i^2$ .

– an indication of the importance of the fragmentation contribution as it is now effectively of  $\mathcal{O}(\alpha\alpha_s)$ , instead of  $\mathcal{O}(\alpha\alpha_s^2)$  at which it was introduced. Indeed, the results in the next section show that the naive LO including only direct photons is clearly not sufficient to describe data when going to low  $p_T^\gamma$ .

Additionally, up to this point the gluon-to-photon-FF  $D_{\gamma/g}$  would be scale-independent, since in this case the right hand side of (3.15) vanishes. But NLO corrections to the fragmentation contribution, i.e. the hard processes  $d\hat{\sigma}$  of  $\mathcal{O}(\alpha_s^3)$  convoluted with the photon FF, introduce, additionally to the evolution described by (3.15), the QCD scaling related to parton-to-parton splittings as described by (2.44). Thus, the complete DGLAP for the photon fragmentation functions can be written

$$\begin{aligned} \mu_F^2 \frac{d}{d\mu_F^2} D_{\gamma/c}(x, \mu_F) &= \frac{\alpha}{2\pi} P_{\gamma c}^{(T)}(x) \\ &+ \sum_i \int_x^1 \frac{dz}{z} \frac{\alpha_s}{2\pi} P_{ic}^{(T)}\left(\frac{x}{z}\right) D_{\gamma/i}(z, \mu_F) . \end{aligned} \quad (3.18)$$

In comparison to the pure QCD evolution (2.44), the anomalous contribution to the photon-FF enters through the inhomogeneity in (3.18). Since the solutions to these equations with LO QED and QCD splitting kernels are commonly used in conjunction with hard-scattering coefficients computed at LO, one has an evolution in  $\mu_F$  due to the parton-to-parton splittings even at LO.

At the beginning of this section it has been stated that the anomalous contribution dominates the scaling behaviour of observables at high energies. An indication of this is that the non-anomalous terms in (3.18) are proportional to  $\alpha_s$ , which vanishes at high energies, while the inhomogeneity is constant.

### 3.3 Calculation

Due to the ratio of the QED to the QCD coupling being of order  $10^{-1}$  at energies above roughly 1 GeV (and quickly falling below), the most important corrections to the leading order prompt photon production cross section will come from a higher order in  $\alpha_s$ . Consequently, “next-to-leading” order in this context refers to amplitudes of order  $\mathcal{O}(\alpha\alpha_s^2)$ , instead of  $\mathcal{O}(\alpha^2\alpha_s)$ , which will not be considered here.

#### 3.3.1 NLO direct and LO fragmentation

From the preceding section it is apparent, that the category “prompt photons” can be subdivided into direct and fragmentation photons. At LO, direct photons are produced through the  $\mathcal{O}(\alpha_s\alpha)$  processes quark annihilation  $q\bar{q} \rightarrow \gamma g$  and QCD Compton  $qg \rightarrow \gamma q$ . The fragmentation processes, on the other hand, are induced by  $\mathcal{O}(\alpha_s^2)$  parton scatterings convoluted with a photon fragmentation function. Since these processes diverge if the final state momentum is along the beam-direction or vanishes, a minimum  $p_T$ -cut has to be applied to the photon. Convoluting these hard scattering cross sections with the PDFs for hadrons  $A$  and  $B$ , one has the full LO contribution. At NLO in  $\alpha_s$  the hard

### 3 Prompt Photon Production

process includes all processes with an additional virtual or real parton. Thus one has the following contributions for a NLO prompt photon production cross section:

	Direct	Fragmentation
<b>LO</b>	$\mathcal{O}(\alpha\alpha_s)$	$\mathcal{O}(\alpha_s^2) \cdot D_{\gamma/i}(z)$
<b>NLO</b>	$\mathcal{O}(\alpha\alpha_s^2)$	$\mathcal{O}(\alpha_s^3) \cdot D_{\gamma/i}(z)$

The phenomenology of these contributions is the following: The LO contribution results in a photon back-to-back with a jet, since the momentum of the final state parton is fixed to balance the photon. In the direct contribution the photon carries half of the partonic energy  $\sqrt{\hat{s}}/2$  and exactly balances the jet, whereas in the fragmentation contribution the photon carries only  $z\sqrt{\hat{s}}/2$ . Of course, in the latter case, to balance the away-side jet, the photon has to be accompanied by some hadrons carrying an energy  $(1 - z)\sqrt{\hat{s}}/2$ . That means that the direct contribution corresponds to an essentially isolated photon and the fragmentation contribution to a photon in a jet. At NLO the virtual corrections produce the same signature as the LO contribution. In the real radiation processes the photon is in opposition to one or two jets, depending on the parton direction and the jet-definition. However, here even in the direct contribution one of the jets can enclose a small angle with the photon direction. Hence, at NLO the distinction between direct and fragmentation photons becomes problematic. Following the discussion of the last section it should be clear that this arbitrariness is reflected in the freedom to chose a factorization scheme and scale, as – instead of defining the absorption of divergences via (3.14) in the  $\overline{\text{MS}}$  scheme – one could have chosen to include completely arbitrary finite terms from the real radiation (i.e. direct) contribution in the FF. In fact, these choices of the factorization scheme and scale are a definition of what “direct” and “fragmentation” technically mean beyond the leading order.

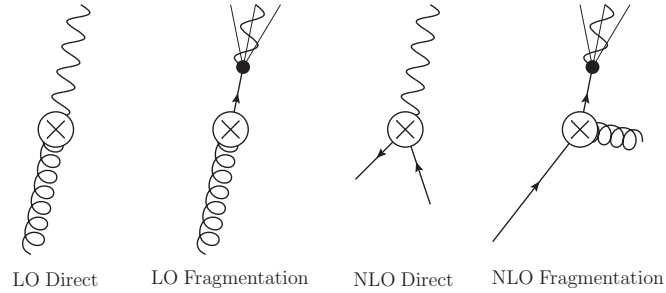


Figure 3.3: Possible final state configurations in the  $p_T$ -plane perpendicular to the beam-direction.

Instead of performing the full NLO calculation, my calculation of the prompt photon cross section includes only the NLO direct and LO fragmentation contributions, as these

are the contributions needed for the POWHEG-implementation described in Sec. 6.2. The explicit expression for (3.9) at this level is

$$\begin{aligned}
& \sigma_{AB \rightarrow \gamma X}(p_A, p_B) \\
&= \sum_{a,b} \int_0^1 dx_a \int_0^1 dx_b f_{a/A}^{(0)}(x_a, \mu_F) f_{b/B}^{(0)}(x_b, \mu_F) \frac{1}{4F(x_a p_A, x_b p_B)} \\
& \cdot \left\{ \sum_c \int d\Phi^{(2)}(x_a p_A, x_b p_B) \left( \overline{|\mathcal{M}_{ab \rightarrow \gamma c}^{(0)}|^2} + 2\text{Re} \left( \overline{\mathcal{M}_{ab \rightarrow \gamma c}^{(1)}} \mathcal{M}_{ab \rightarrow \gamma c}^{(0)\dagger} \right) \right) F_J^{(2)}(p_1) \right. \\
& + \sum_{c,d} \int d\Phi^{(3)}(x_a p_A, x_b p_B) \overline{|\mathcal{M}_{ab \rightarrow \gamma cd}^{(0)}|^2} F_J^{(3)}(p_1) \\
& \left. + \sum_{c,d} \int d\Phi^{(2)}(x_a p_A, x_b p_B) \overline{|\mathcal{M}_{ab \rightarrow cd}^{(0)}|^2} \int_0^1 dz D_{\gamma/c}(z, \mu_F) F_J^{(2)}(z p_1) \right\}, \tag{3.19}
\end{aligned}$$

where the  $2 \rightarrow 2$  amplitudes are functions of  $x_a p_A$ ,  $x_b p_B$ ,  $p_1$ ,  $p_2$  and the  $2 \rightarrow 3$  amplitude is a function of  $x_a p_A$ ,  $x_b p_B$ ,  $p_1$ ,  $p_2$ ,  $p_3$ . The details of the calculation are documented in App. C. By a suitable choice of  $F_J$  the results can be used to generate  $\gamma$ -inclusive and  $\gamma$ +jet-inclusive cross sections. However, in the next section a code is described which numerically integrates this cross section for

$$F_J(p) = \theta(\eta^{\max} - \eta) \cdot \theta(\eta - \eta^{\min}) \cdot \theta(p_T^{\max} - p_T) \cdot \theta(p_T - p_T^{\min}), \tag{3.20}$$

i.e. the photon is integrated over a specified range of transverse momentum  $p_T$  and rapidity  $\eta$ . As mentioned before,  $F_J$  has to implement a  $p_T$ -cut in any case, since otherwise the LO contributions already diverge. Hence, I generally have this choice of the jet-defining function in mind, which is completely inclusive w.r.t. to jets, when writing that  $F_J$  depends only on the photon momentum (equal to  $p_1$  in the direct or  $z p_1$  in the fragmentation contribution).

The results for the LO direct contribution are described in App. C.1 and the NLO direct contribution in App. C.2. At times, I only give partial results for reproducibility as the full results are too long to include in print: The virtual corrections in App. C.2.1 are mainly given as renormalized one-particle irreducible loop diagrams, except for the self-energy corrections which can readily be given as simple multiplicative corrections to the LO diagrams, cf. (C.63), (C.66). On the other hand, the real corrections are completely given in App. C.2.2.

To make these results ready for a numerical integration, one has to implement some kind of subtraction method, as has been described in Sec. 2.5; I have chosen the CS dipole method. It is straightforward to apply this method to the subtraction of QCD divergences, i.e. soft divergences related to QCD partons, as is shown in App. C.2.5 exemplary for one subprocess; but it has to be adapted to the subtraction of the QED singularities related to the photon as well. Concerning the latter, one can simply take the prescriptions for the QCD dipoles and change the QCD specifics, i.e. the non-Abelian colour-

### 3 Prompt Photon Production

generators, to its QED equivalents, i.e. Abelian charge-generators. This is achieved by changing the definitions (2.51) or rather (2.56) to

$$\mathbf{T}_i = \begin{cases} Q_{f_i}, & \text{if particle } i \text{ is a FS particle or IS antiparticle of flavour } f, \\ -Q_{f_i}, & \text{if particle } i \text{ is a FS antiparticle or IS particle of flavour } f, \end{cases} \quad (3.21)$$

such that charge-conservation is encoded in

$$\sum_{i=0}^n \mathbf{T}_i |3, \dots, n; 1, 2\rangle = 0, \quad (3.22)$$

and additionally changing

$$C_F \rightarrow Q_{f_i}^2 \quad (3.23)$$

$$C_A \rightarrow 0 \quad (3.24)$$

$$\alpha_s \rightarrow \alpha \quad (3.25)$$

in the formulae of Ref. [29]. Though, instead of using the complete formulae of [29] (or [44] for that matter), I only use the dipoles for final state collinear singularities related to the photon being collinear to a final state quark. This is guaranteed to cancel all photon singularities as the mandatory low- $p_T$ -cut forbids soft and initial state collinear divergences related to the photon. The integrated counterpart to these dipoles is not one of the insertion operators described in [29], but can be readily derived using the information therein, as is described in App. C.2.6. This integrated dipole then includes exactly that pole which is absorbed into the photon FF via (3.14) and a finite collinear remnant that is to be added to the direct  $2 \rightarrow 2$  contribution.

The complete dipole subtracted direct component of the prompt photon cross section is given in (C.159). And the details of the LO fragmentation contribution are discussed in App. C.3.

#### 3.3.2 Consistency checks

At the level of the analytical expressions, the tree-level amplitudes have been generated by `FormCalc` [89] and the LO amplitudes have been successfully crosschecked against the literature, e.g. [70, 6]. For the virtual contributions, the  $\overline{\text{MS}}$  renormalization constants obtained in the calculation, i.e. the UV divergences, have been found to be identical to those quoted in the literature [8]. Expressions for the dipoles and insertion operators in terms of invariants have been obtained by implementing the formulae of [29] in `FORM` and simplifying the resulting expressions in `Mathematica`. Some of the results related to QCD dipoles, though due to the sheer amount not all, have been compared to the analytical expressions computed by `AutoDipole` and found to be identical.

Consistency checks on the numerical level have been performed mainly with the code described in the next section: For instance, numerical results of QCD dipoles at selected phase space points have been successfully compared to the results generated by

**AutoDipole**, which automatically generates **FORTRAN** codes to evaluate the dipoles generated for a certain process. Besides that, I have used **Mathematica** [90] in an attempt to verify the successful cancellation of divergences in the collinear and soft limits of the dipole-subtracted real amplitudes. This is somewhat problematic though, since both the amplitudes  $|\overline{\mathcal{M}}_{ab \rightarrow \gamma cd}^{(0)}|^2$  and the dipoles  $\mathcal{D}_{ij}$  depend on five invariants, e.g. (C.67)-(C.71), and the collinear or soft limit eliminates only two or three of those, respectively. Thus, numerically the cancellation can only be checked for some phase space points equivalent to a choice of numerical values of the respective three (independent Born variables plus longitudinal momentum fraction) or two (independent Born variables) remaining invariants. Additionally, for divergences related to the initial state, the jet-defining function has to be taken into account for a correct subtraction, which made a check of the soft limits in **Mathematica** unhandy (see App. C.2.5 for details on how the dipoles introduce new soft divergences if not regulated by the jet-defining function).

A way to approach the collinear limit is to choose explicit values for the four-vectors for every particle, except for one particle which is described in terms of another particle's momentum via the Sudakov decomposition (D.1),(D.2). The  $k_T$  component can then be scaled by a parameter  $\lambda \rightarrow 0$  to approach the collinear limit while obeying momentum conservation for every value of  $\lambda$ . Instead of taking this route, for a quick test I simply constructed the collinear limits  $p_i = xp_j$  for the set of Mandelstam variables (C.67)-(C.71) and added a parameter  $\lambda$  to the resulting relations, such that  $\lambda \rightarrow 0$  approaches the collinear limit. The difference to the consistent four-vector approach is that momentum conservation is not obeyed for all finite choices of  $\lambda$ , i.e. I approach the collinear limit from unphysical momentum configurations.

With that said, this are the relevant limiting formulae for the Mandelstam variables (C.67)-(C.71):

$$\begin{aligned}
p_a \parallel p_2 : \quad & t_{a2} = 0 \\
& t_{b1} = \left(1 + \frac{s_{12}}{t_{a1}}\right) (-s_{ab} - t_{a1}) \\
p_a \parallel p_3 : \quad & t_{a2} = -s_{ab} - t_{a1} \\
& t_{b1} = -s_{12} - \frac{s_{12}}{s_{ab}} t_{a1} \\
p_b \parallel p_2 : \quad & t_{a1} = \left(1 + \frac{s_{12}}{t_{b1}}\right) (-t_{b1} - s_{ab}) \\
& t_{a2} = \frac{s_{12}}{t_{b1}} s_{ab} \\
p_b \parallel p_3 : \quad & t_{b1} = -s_{ab} - \frac{s_{ab}}{s_{12}} t_{a1} \\
& t_{a2} = -s_{12} - t_{a1} \\
p_2 \parallel p_3 : \quad & t_{b1} = -t_{a1} - s_{ab} \\
& t_{a2} = -s_{12} - \frac{s_{12}}{s_{ab}} t_{a1}
\end{aligned}$$

### 3 Prompt Photon Production

$$\begin{aligned}
p_1 \parallel p_2 : \quad & s_{12} = 0 \\
& t_{b1} = -\frac{s_{ab} + t_{a1} + t_{a2}}{1 + \frac{t_{a2}}{t_{a1}}} \\
p_1 \parallel p_3 : \quad & t_{a1} = -s_{12} - \frac{s_{12}}{s_{ab}} t_{a2} \\
& t_{b1} = \frac{s_{12}}{s_{ab}} t_{a2} .
\end{aligned}$$

For these limits I have rewritten the amplitudes  $\overline{|\mathcal{M}|^2}$  and dipoles  $\mathcal{D}_{\dots}$  (both functions of  $s_{ab}$ ,  $s_{12}$ ,  $t_{a1}$ ,  $t_{a2}$  and  $t_{b1}$ ), e.g. for  $p_2 \parallel p_3$

$$\overline{|\mathcal{M}|^2}(s_{ab}, s_{12}, t_{a1}, t_{a2}, t_{b1}) \rightarrow \overline{|\mathcal{M}|^2}(s_{ab}, s_{12}, t_{a1}, -s_{12} - \frac{s_{12}}{s_{ab}} t_{a1} + \lambda, -t_{a1} - s_{ab} + \lambda),$$

taking  $\lambda \rightarrow 0$ .

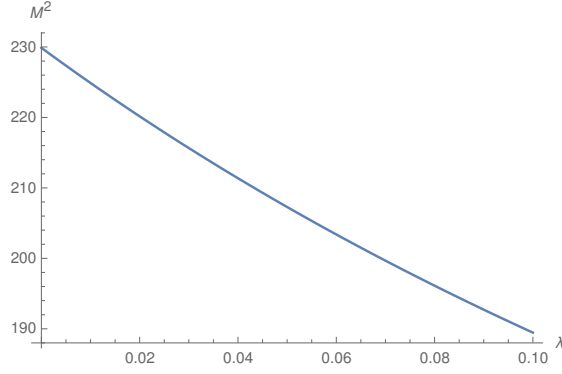


Figure 3.4: Limit  $p_2 \parallel p_3$  of  $gg \rightarrow \gamma q \bar{q}$  in arbitrary units.

In the following, I show the limits for the process  $g(p_a)g(p_b) \rightarrow \gamma(p_1)q(p_2)\bar{q}(p_3)$ . The limit  $p_2 \parallel p_3$  is shown in Fig. 3.4. Obviously, this is not divergent. Correspondingly, there are no dipoles for this limit as the underlying process  $gg \rightarrow \gamma g$  does not exist at  $\mathcal{O}(\alpha\alpha_s)$ .

Fig. 3.5 shows the divergence of the  $p_a \parallel p_2$  limit for some arbitrary phase space point in the unsubtracted amplitude and that it is regularized by the subtraction of the dipoles  $\mathcal{D}^{gq,g}$  and  $\mathcal{D}_{\bar{q}}^{gq}$ . The same is depicted for the remaining limits and the corresponding dipoles in Figs. 3.6-3.9. The last two figures bear witness to the successful subtraction of the divergences related to the photon.

The same test of finiteness of the dipole subtracted real radiation amplitudes has been conducted for other subprocesses and dipoles with the same positive results.



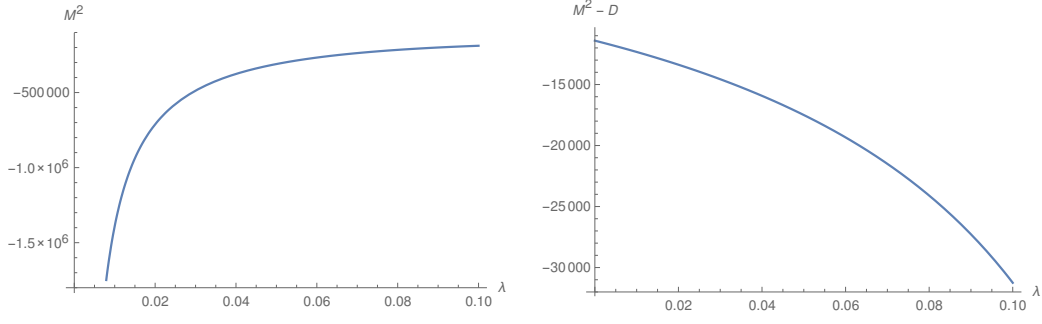


Figure 3.5: Limit  $p_a \parallel p_2$  of  $gg \rightarrow \gamma q \bar{q}$  without and with dipole subtraction in arbitrary units.

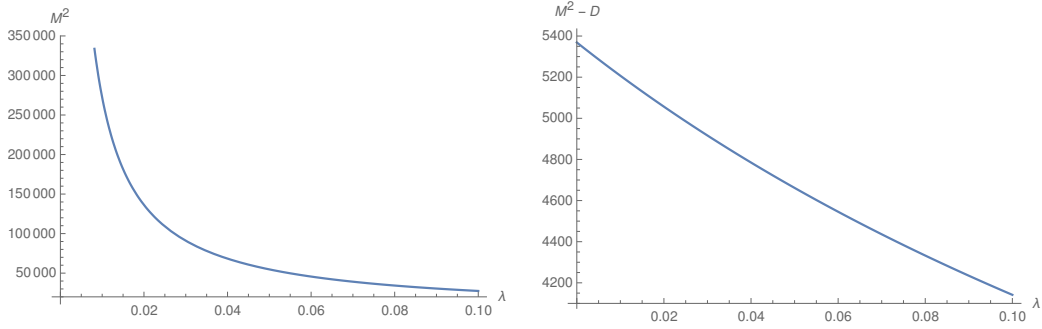


Figure 3.6: Limit  $p_b \parallel p_2$  of  $gg \rightarrow \gamma q \bar{q}$  without and with dipole subtraction in arbitrary units.

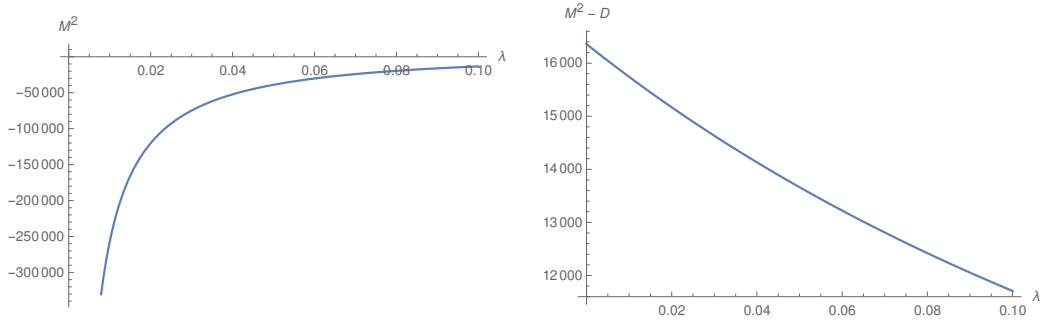


Figure 3.7: Limit  $p_b \parallel p_3$  of  $gg \rightarrow \gamma q \bar{q}$  without and with dipole subtraction in arbitrary units.

### 3 Prompt Photon Production

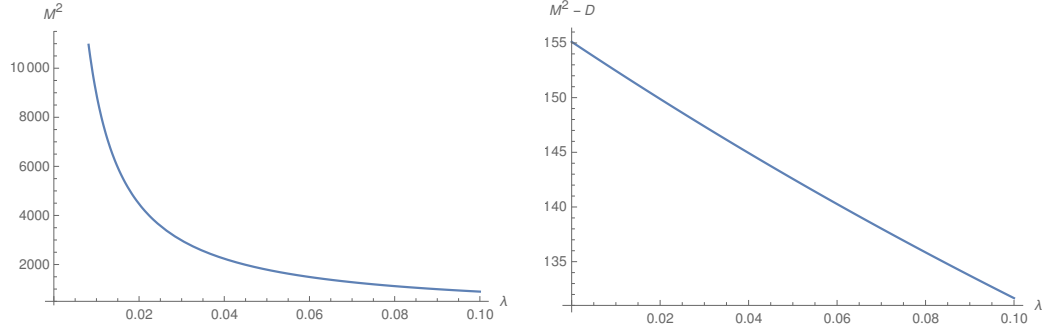


Figure 3.8: Limit  $p_1 \parallel p_2$  of  $gg \rightarrow \gamma q \bar{q}$  without and with dipole subtraction in arbitrary units.

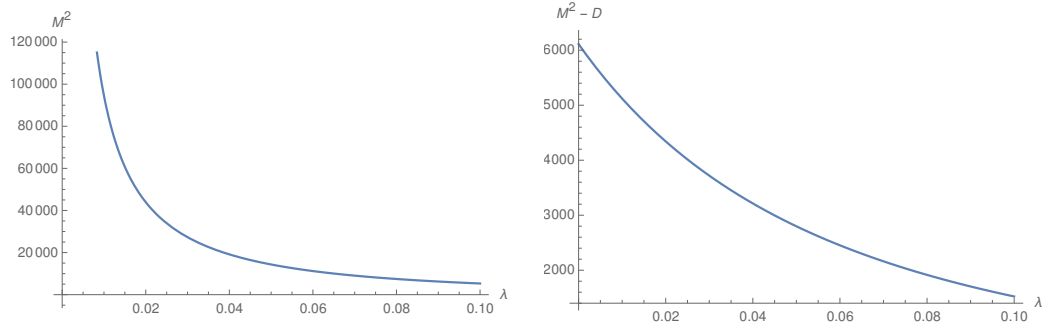


Figure 3.9: Limit  $p_1 \parallel p_3$  of  $gg \rightarrow \gamma q \bar{q}$  without and with dipole subtraction in arbitrary units.

### 3.4 phoSec

For the purpose of testing my calculations, I have written a **FORTRAN** code that simply integrates the partial NLO prompt photon production cross section described in the last section for some  $p_T$ - and  $\eta$ -range of the photon, using the CS dipole method; henceforth this program is called **phoSec**. The code can be subdivided into five parts corresponding to the different integral measures used in the calculation of the cross section (e.g. as displayed in (C.159)): the simple 2-particle phase space integration, the 3-particle phase space integration and the 2-particle phase space plus a momentum fraction integration over the two collinear remnants associated with the QCD dipoles, the QED collinear remnant and the fragmentation contribution.

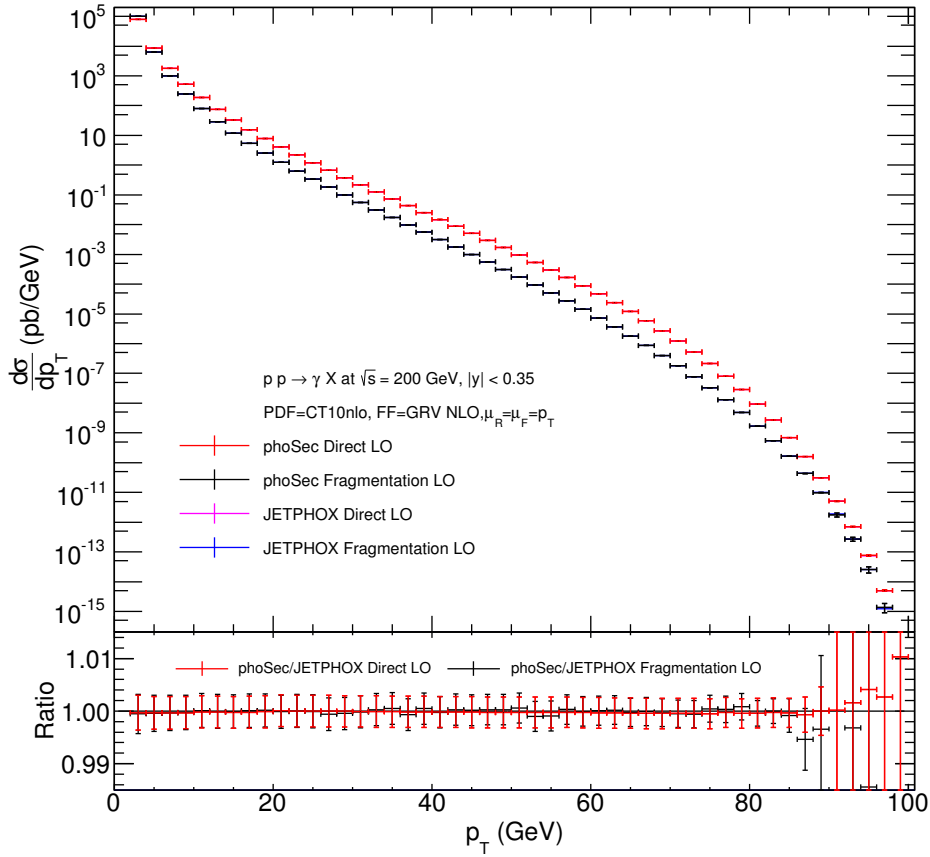


Figure 3.10: Comparison of LO contributions in JETPHOX and phoSec at  $\sqrt{s} = 200$  GeV. JETPHOX results are mostly hidden by phoSec.

### 3 Prompt Photon Production

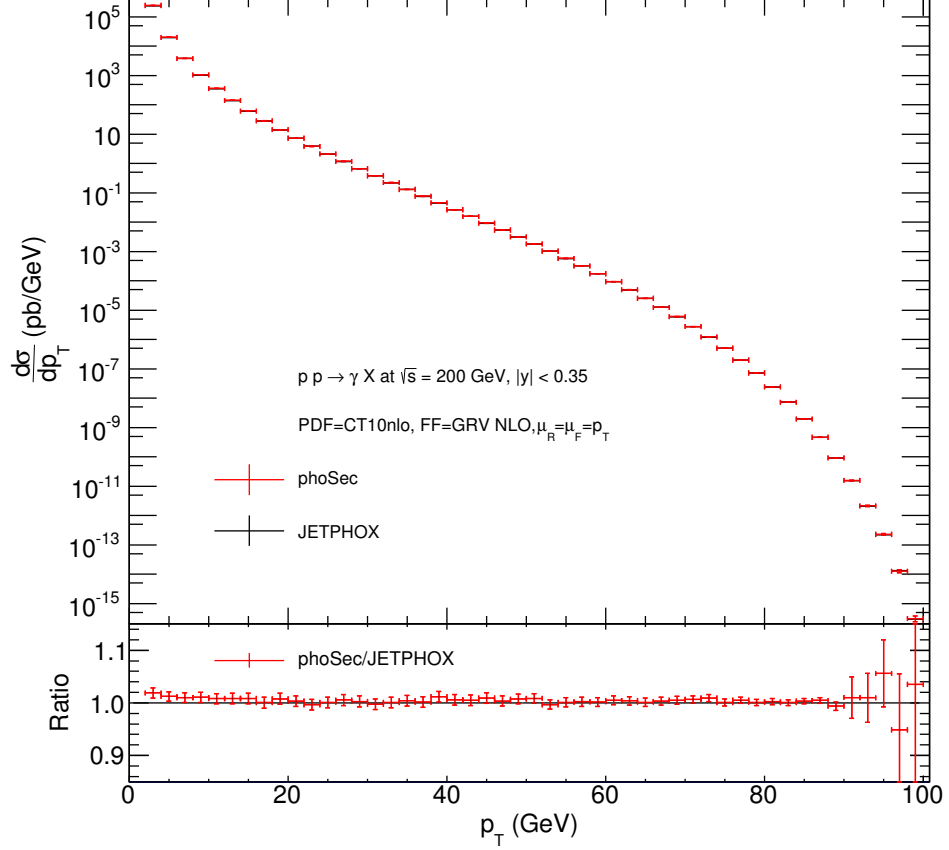


Figure 3.11: Comparison of JETPHOX and phoSec at  $\sqrt{s} = 200$  GeV. JETPHOX results are mostly hidden by phoSec.

As an integration library **Cuba** [91] is employed. **Cuba** provides the user with a variety of integration routines for multiple variables, namely Quadrature and Monte Carlo techniques, where only the latter proved able to integrate the cross section. I found the **Vegas**-routine to be the most reliable and practical, though, with a very large number of integrand evaluations it has also been possible to use the **Suave**-method. Cross checking the convergence and results of the integrals between these two methods constitutes a check of finiteness of the results: When the two methods return grossly different results, i.e. differing by orders of magnitude, it is an indication that some contribution leads to divergences.

The correctness of the phase space measures of each part of the program has been checked by simply integrating over a unit integrand, whereby full agreement (up to

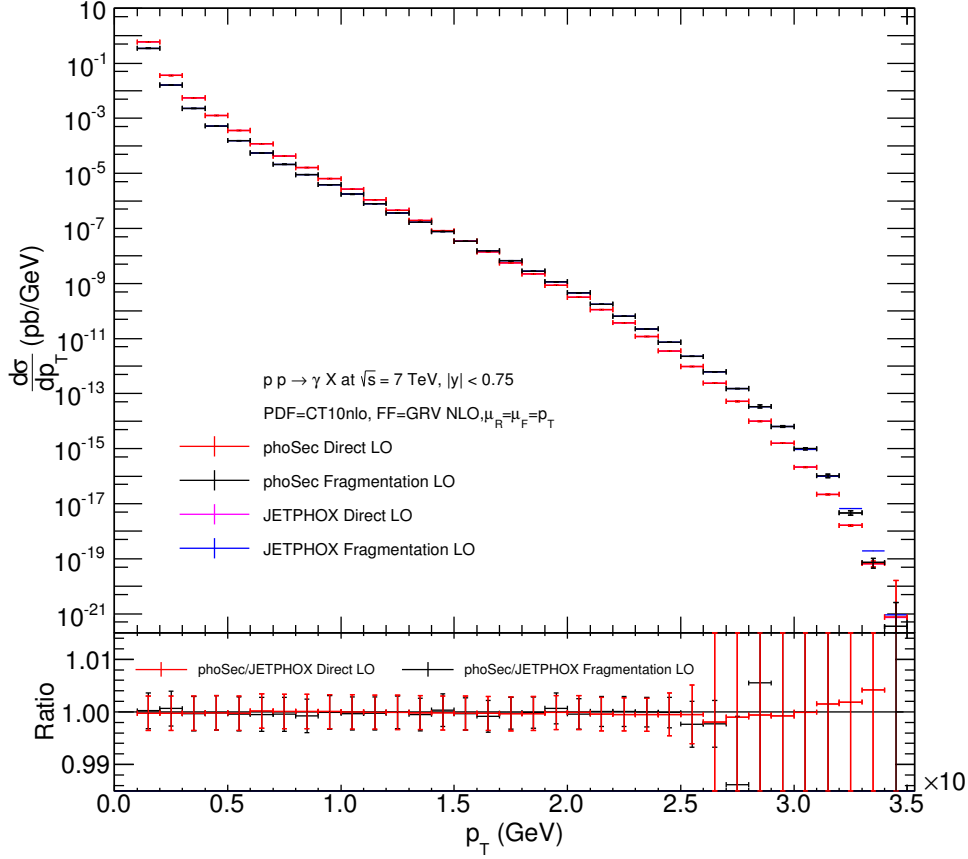


Figure 3.12: Comparison of LO contributions in JETPHOX and *phoSec* at  $\sqrt{s} = 7$  TeV. JETPHOX results are mostly hidden by *phoSec*.

numerical precision of 15 significant figures for double precision floating point values) with the results

$$\int d\Phi^{(2)} = \frac{1}{8\pi} \quad (3.26)$$

$$\int d\Phi^{(3)} = \frac{s_{ab}}{256\pi} \quad (3.27)$$

for massless particles [92] has been found.

Access to PDFs in the code is handled by *LHAPDF* [93] which allows easy access to most commonly used PDFs. As a photon fragmentation function the GRV parametrization [94] is used.<sup>4</sup>

<sup>4</sup>However, a change of these choices requires only minor changes in the code.

### 3 Prompt Photon Production

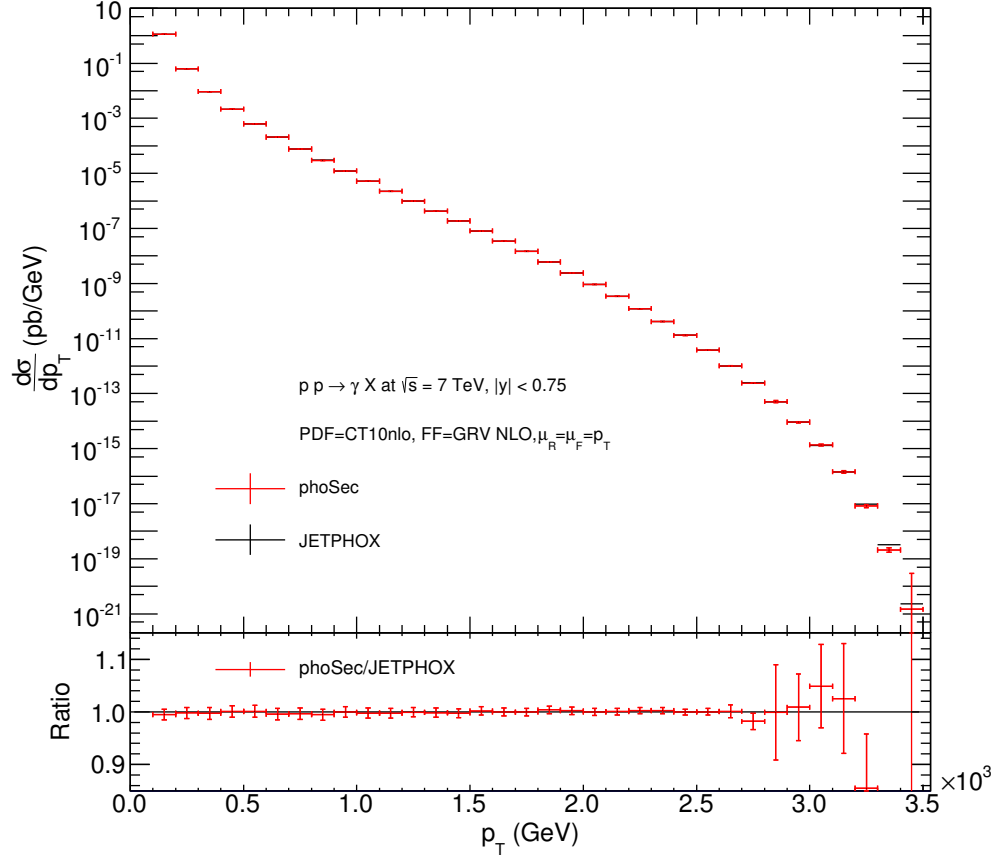


Figure 3.13: Comparison of JETPHOX and phoSec at  $\sqrt{s} = 7$  TeV. JETPHOX results are mostly hidden by phoSec.

The virtual corrections to the  $2 \rightarrow 2$ -contribution include integrals over the virtual loop-momenta, which have to be evaluated separately from the phase space integrals. These integrals are handled by the `LoopTools` [89] library, which implements the standard scalar functions used in the Passarino-Veltman tensor reduction method [36]. Accordingly, the results in App. C.2.1 make use of the conventions of `LoopTools`. The finite part of my results for the virtual corrections has been compared to automatically generated results from `MadLoop` [95] for 100 random phase space points with the greatest relative deviation  $(V_{\text{phoSec}} - V_{\text{MadLoop}})/V_{\text{phoSec}}$  being of  $2 \times 10^{-4} \%$ .<sup>5</sup> Seeing that with `LoopTools` it is possible to return the results of the scalar-integrals as the coefficients of an expansion in  $\varepsilon$ , allows for a direct check of the cancellation of the poles of the vir-

<sup>5</sup>To be precise, the virtual contributions in the form used by `phoSec` had to be transformed to the CDR form (2.77), as described in Sec. 6.2, to be comparable to the `MadLoop` results.

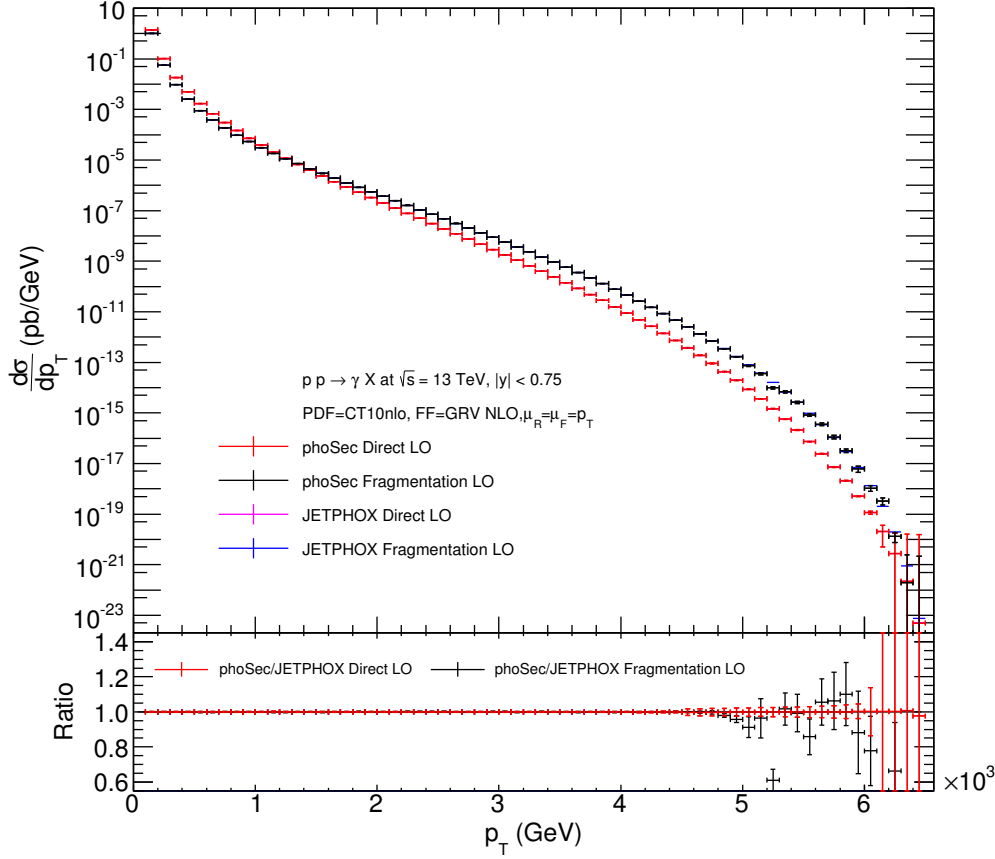


Figure 3.14: Comparison of LO contributions in JETPHOX and *phoSec* at  $\sqrt{s} = 13$  TeV. JETPHOX results are mostly hidden by *phoSec*.

tual contributions, if the coefficients of the UV counterterms and the integrated dipoles are implemented, too. To that end, using the C-precompiler functionality of **gfortran** (thereby not adhering to one of the **FORTTRAN**-standards), I have implemented a functionality that the code can be compiled in several versions: The standard version which computes the cross section, a version where the coefficients of the  $\varepsilon^{-1}$ -poles of the virtual, integrated dipole and UV counterterm contributions are compared and another version where the same is done for the  $\varepsilon^{-2}$ -poles. With the latter two versions of the code I have, in several runs with different setups (specified below), found that the coefficients of the divergences of the dipoles and UV counterterms and the coefficients of the divergences of the virtual corrections are numerically identical (i.e. the relative difference is below  $10^{-14}$ ).

### 3 Prompt Photon Production

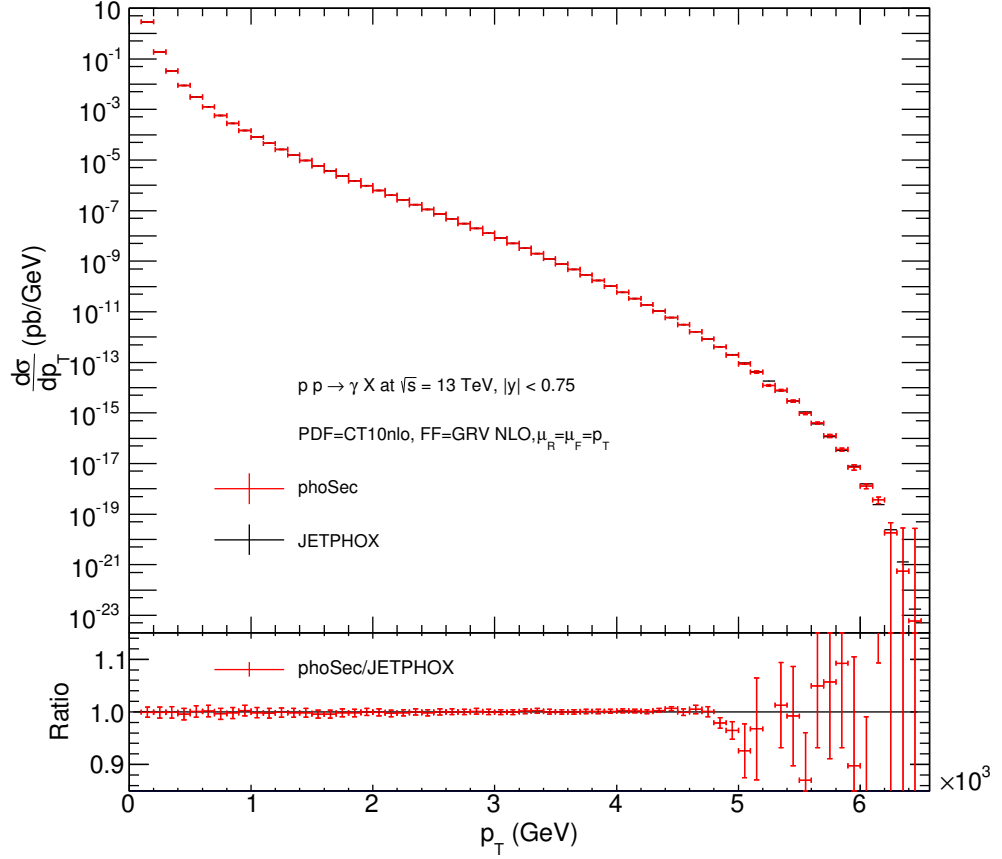


Figure 3.15: Comparison of JETPHOX and phoSec at  $\sqrt{s} = 13$  TeV. JETPHOX results are mostly hidden by phoSec.

This concludes my tests of individual contributions to the cross section with no implication that either the matrix elements, the phase space or the QCD dipoles (more precisely, the real subtraction terms or the divergences of the integrated dipoles) are false. However, the collinear remnants, the convolution with the PDFs and  $\gamma$ -FF and the correct treatment of cuts and the renormalization- and fragmentation-scale can only be tested in a comparison of full results for the cross section against correct results. To generate the results that are assumed to be correct, I use JETPHOX [96] (to be shortly described in the next section). For the runs comparing the results of the two programs I use proton-proton-collisions at

$$\sqrt{s} = 200 \text{ GeV with } |\eta^\gamma| < 0.35,$$



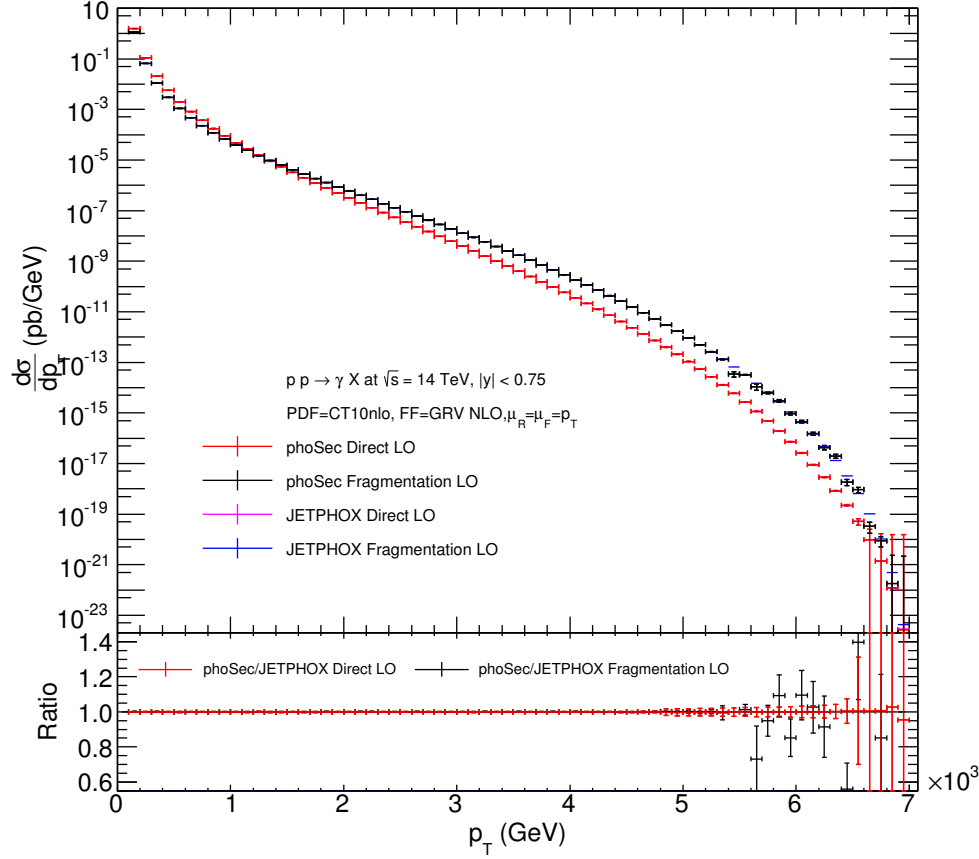


Figure 3.16: Comparison of LO contributions in JETPHOX and *phoSec* at  $\sqrt{s} = 14$  TeV. JETPHOX results are mostly hidden by *phoSec*.

and at

$$\sqrt{s} = 7 \text{ TeV}, \sqrt{s} = 13 \text{ TeV}, \text{ and } \sqrt{s} = 14 \text{ TeV} \text{ with } |\eta^\gamma| < 0.75;$$

in all cases with the CT10nlo central PDF-set [97] and the GRV photon-FF. The number of flavours is set to  $N_f = 5$ , the scales are set to the photon- $p_T$

$$\mu_R = \mu_F = p_T^\gamma$$

and the  $\alpha_s$ -evolution is computed by LHAPDF according to the parametrization used in the PDFs, whereas the electromagnetic coupling is kept fixed at  $\alpha = 1/137$ .

Figs. 3.10-3.17 show the results of the two programs for the LO contributions and the NLO direct plus LO fragmentation contributions in comparison. In all the *phoSec* to JETPHOX ratios the deviation from JETPHOX can be seen to be at maximum about 1 %, except for the high- $p_T$  region. The comparison for the LO direct and LO fragmentation

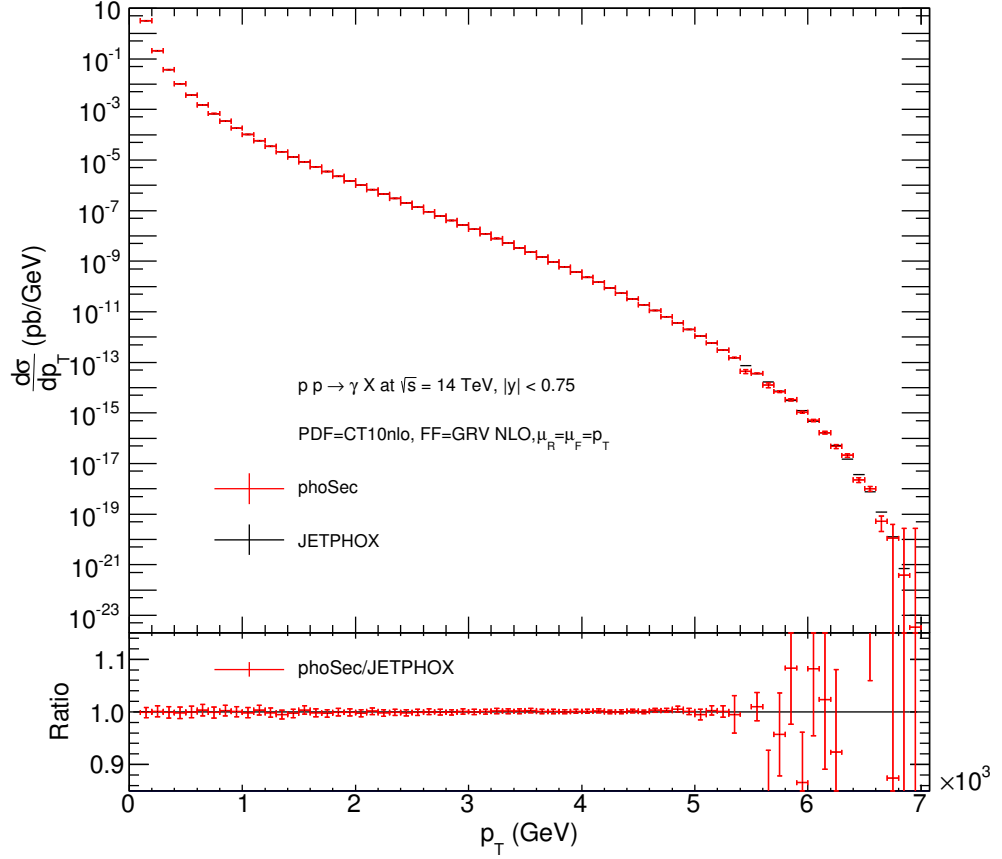


Figure 3.17: Comparison of JETPHOX and phoSec at  $\sqrt{s} = 14$  TeV. JETPHOX results are mostly hidden by phoSec.

contributions shows an even better agreement between the two programs. At the high- $p_T$ -tails the errors become large since the integration in **phoSec** converges very slowly. In this region the momentum fractions  $x_a$ ,  $x_b$  and  $z$  (corresponding to the partons  $a$ ,  $b$  from the PDFs and the photon in the FF, respectively) attain their maximum values near unity where the long-distance functions are very steep. If the PDFs and the FF are not taken into account the integration in that region converges as well as for lower  $p_T$ . All in all these comparisons give no cause for doubting the correctness of my calculations.

Figs. 3.18-3.21 break down the different contributions to the **phoSec**-cross section, where the different contributions refer to the different integrals that contribute to the cross section. It is interesting to note that for all CM energies, apart from the tails of the  $p_T$ -range, the dipoles approximate the  $2 \rightarrow 3$  contributions to the cross section so well that the dipole subtracted real contributions (denoted “Real-Dip”) have only

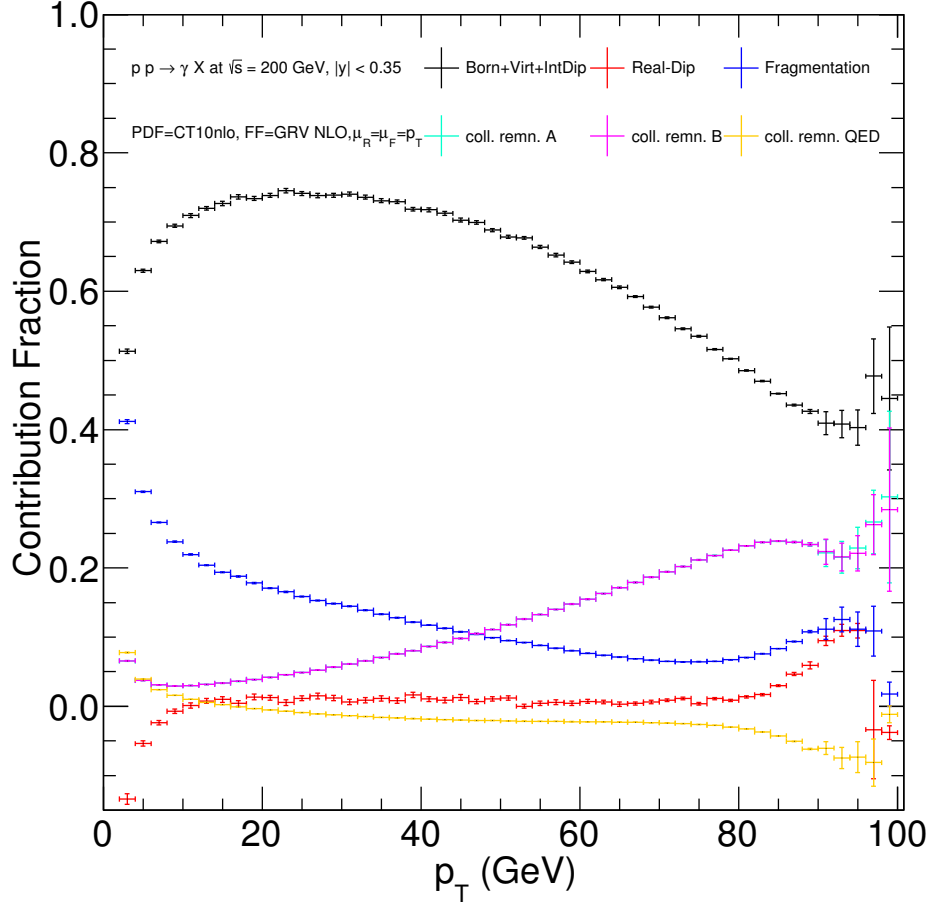


Figure 3.18: Contributions from the different integrals to the full *phoSec*-cross section at  $\sqrt{s} = 200$  GeV.

negligible effects on the complete result. In turn the cross section is, at high CM energies, well-described by the fragmentation contribution and the combination of LO direct, virtual corrections and integrated dipoles (denoted “Born+Virt+IntDip”). The collinear remnants of the QCD dipoles (denoted “coll. remn. A” and “B”) are sizable at  $\sqrt{s} = 200$  GeV, making up up to  $\approx 50\%$  but falling to  $\approx 10\%$  and less at the higher CM energies displayed. As can be seen they are completely symmetric in  $A$  and  $B$ , as they should be when choosing symmetric cuts on the rapidity  $\eta$ . The relative contribution of the collinear remnants increases in the tails of the  $p_T$ -distributions; this is due to their dependence on logarithms of the longitudinal momentum fractions of the collinear

### 3 Prompt Photon Production

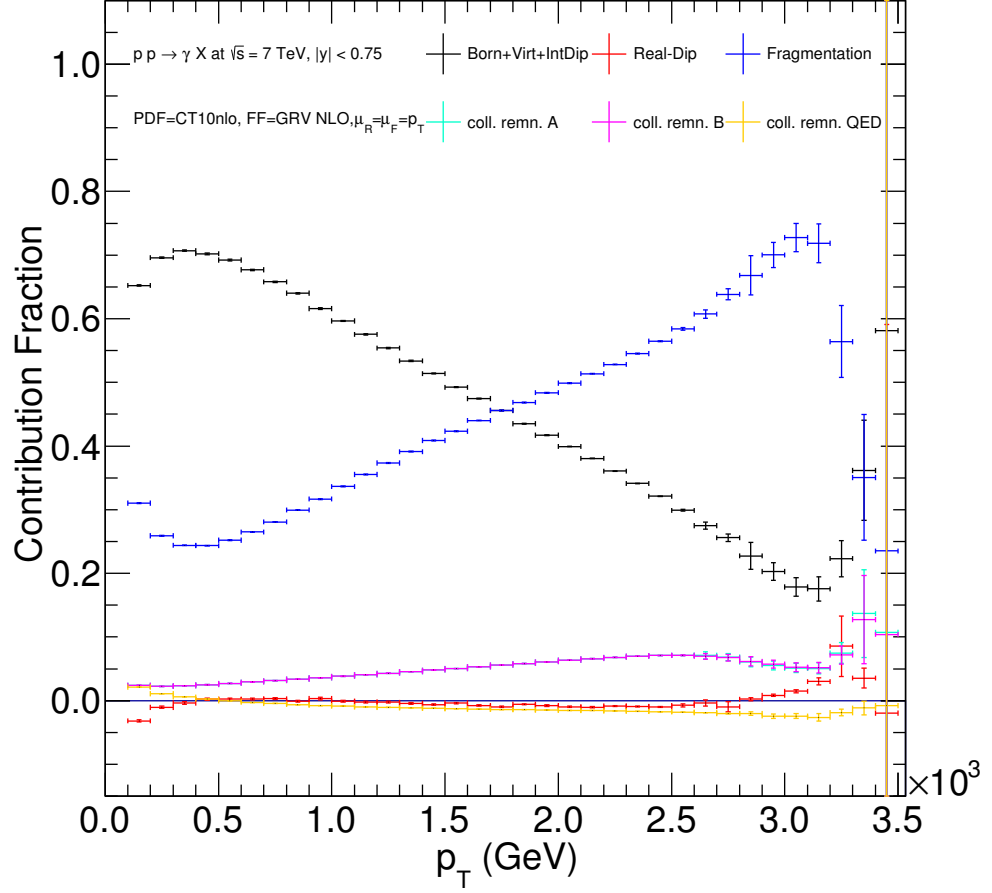


Figure 3.19: Contributions from the different integrals to the full phoSec-cross section at  $\sqrt{s} = 7$  TeV.

splitting processes in the initial or final state (e.g. for the collinear remnant of the QED dipoles (C.157)) which in these tails tend to either 0 or 1, resulting in large logarithms.<sup>6</sup>

In the preceding sections it has already been mentioned that the fragmentation contribution can not be neglected. For the TeV-range CM energies on display it even becomes the dominant contribution over an increasing range of the  $p_T$ -distribution (roughly above  $\approx 1.5$  TeV). Additionally, it becomes comparable to the direct contribution also at very low  $p_T$  values. This is reflected already at LO in Figs. 3.10, 3.12, 3.14 and 3.16.

<sup>6</sup>In App. C.2.5 and C.2.6 I describe how fragmentation and renormalization scales depending on the photon momentum have to be transformed to match the CS dipole prescription. If one were not to follow these rules and instead simply sets  $\mu_R = \mu_F = p_T^\gamma$  in all terms, the dipole subtracted real contribution and the collinear remnants would diverge.

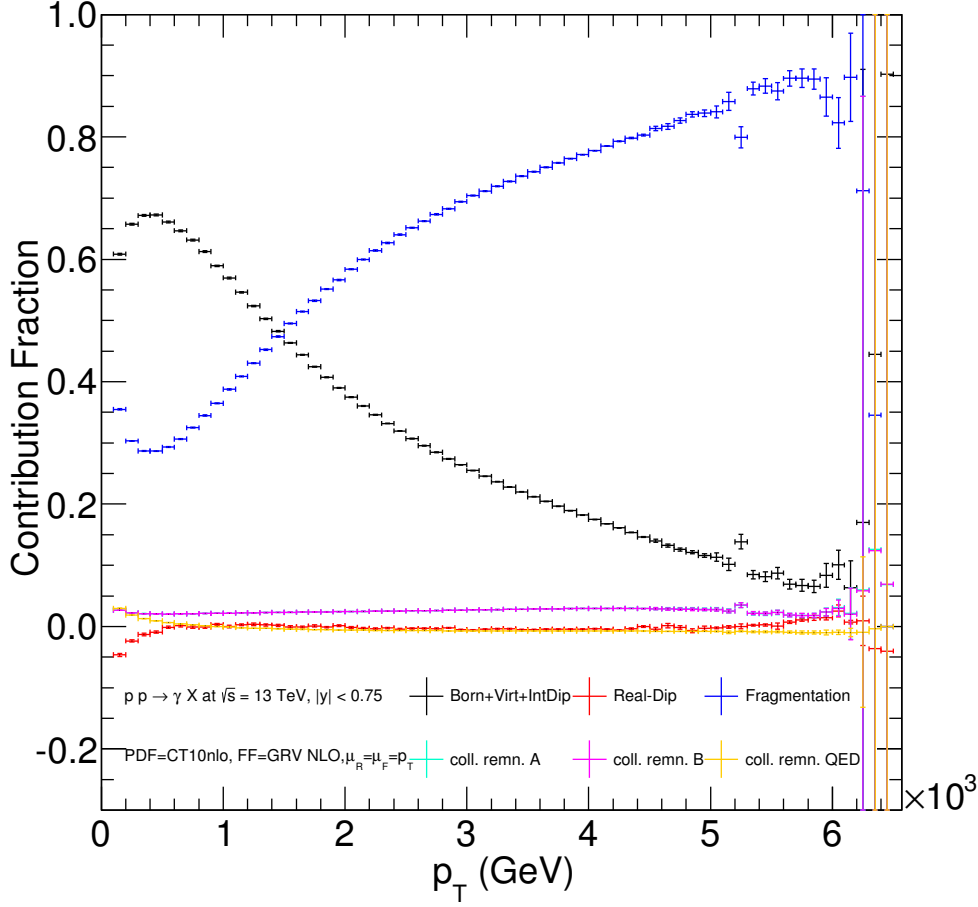


Figure 3.20: Contributions from the different integrals to the full **phoSec**-cross section at  $\sqrt{s} = 13$  TeV.

The factorization (initial state and fragmentation) scale dependencies of the different contributions and the full **phoSec** NLO and Born results are compared in Fig. 3.22. By using a logarithmic scale on the abscissa, simple logarithmic scale dependencies of the QED collinear remnant and the fragmentation contribution (corresponding to the anomalous contribution in  $D_{\gamma/i}$ ) are readily identified. In the range usually used for scale variations, i.e. multiplication and division of  $\mu_F$  by a factor 2, the full **phoSec**-result can be seen to be more stable than the Born (LO direct) result. This shows that the inclusion of higher orders stabilizes the scale dependence.

In general it can be said that for non-isolated prompt photon production the simple LO direct contribution receives large corrections from NLO direct and FF contributions at all displayed CM energies. This is reinforced by Fig. 3.23, which shows the relative fraction of the direct LO result to the full **phoSec**-result (inverse “ $K$ -factor”) and its

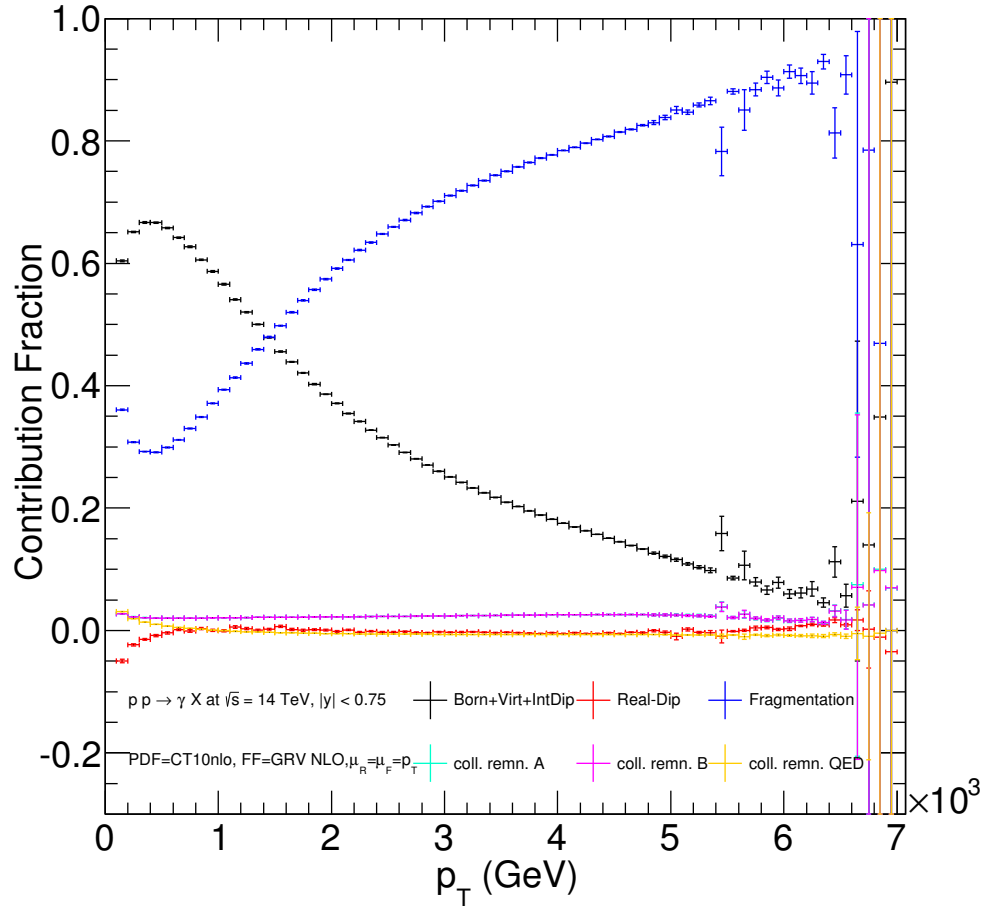


Figure 3.21: Contributions from the different integrals to the full phoSec-cross section at  $\sqrt{s} = 14$  TeV.

decrease with increasing CM energy: The corrections coming from the NLO direct and the LO fragmentation contributions together are at least  $\approx 70\%$  and go up to  $\approx 1900\%$ .

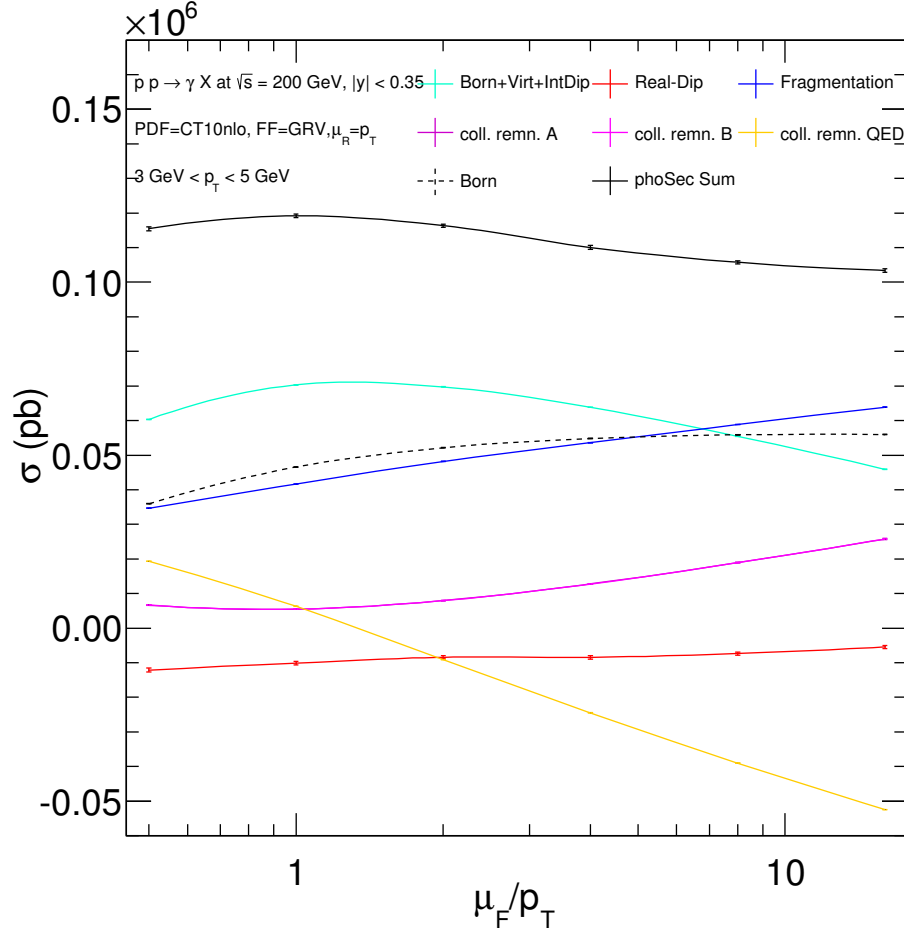


Figure 3.22: The factorization scale dependence of the cross section contributions for a  $3 \text{ GeV} < p_T < 5 \text{ GeV}$  bin at  $\sqrt{s} = 200 \text{ GeV}$ . Splines connect the data points, the errors of which are barely visible.

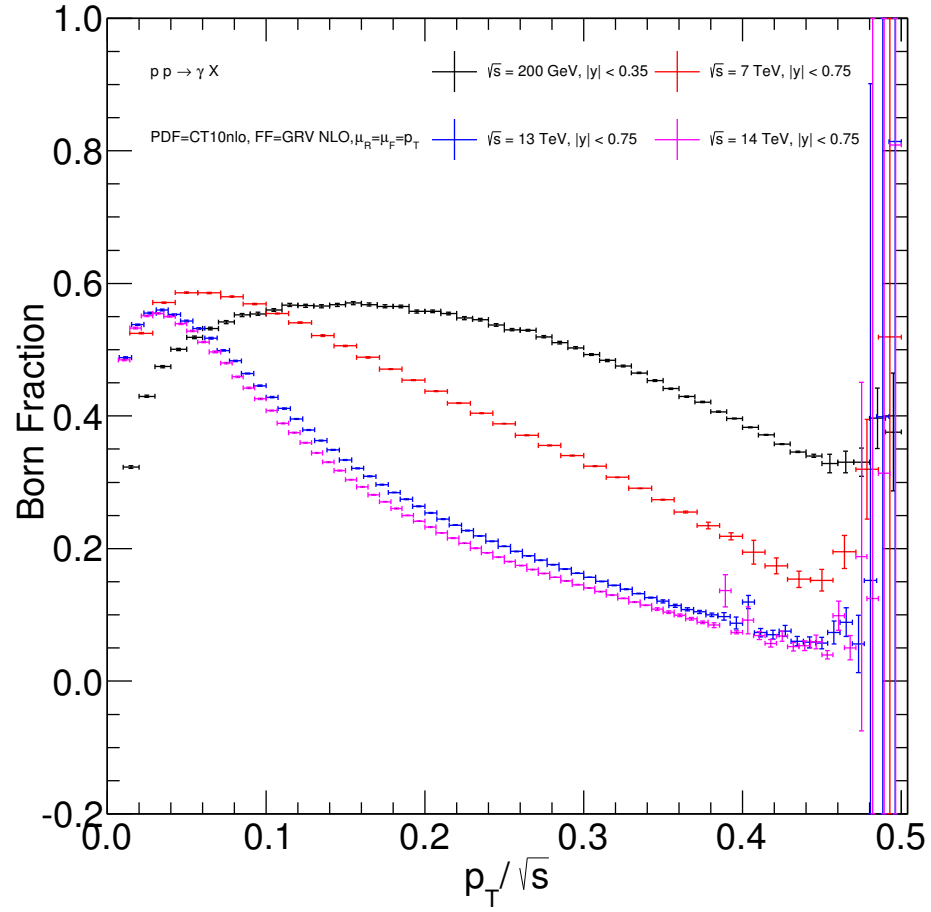


Figure 3.23: Ratio of direct LO to direct NLO plus fragmentation LO for different setups.



### 3.5 JETPHOX

The code described in the preceding section integrates the cross section in a certain  $p_T$ - and  $\eta$ -range which is rather ineffective when the goal is the generation of a differential distribution. JETPHOX [96] on the other hand is internally a parton-level event generator, i.e. it generates events (using the BASES/SPRING-library [98]) with a probability proportional to the completely differential prompt photon cross section. This has the advantage that one can access the momentum four-vectors for all particles involved in an event and create arbitrary differential distributions by adding up the events in bins corresponding to some arbitrary variable derived from the four-momenta. Contrary to general purpose event generators (to be discussed in more detail in Sec. 6.1), however, JETPHOX does not provide the user with events that can be used for a fully exclusive analysis employing parton showering and hadronization. For instance, it is possible that events are generated with a negative weight – a problem that is generally encountered, when trying to construct NLO event generators, as will be discussed in Ch. 6.

The program implements a full NLO prompt-photon production cross section, i.e. it incorporates the NLO direct as well as the NLO fragmentation contributions (though, it has been used in the last section to compare only the NLO direct and LO fragmentation contributions), along with the possibility to apply different jet-finding algorithms on the partons and isolation cuts on the photon – the simplest possibility being a cut on the partonic energy

$$E_{\text{part}} \leq E_{\text{max}} \quad (3.28)$$

that is allowed to be deposited in a cone described in the rapidity  $\eta$ -azimuthal angle  $\phi$ -plane by

$$\sqrt{(\eta - \eta^\gamma)^2 + (\phi - \phi^\gamma)^2} \leq R_{\text{isol}}. \quad (3.29)$$

Instead of using the CS dipole method, as has been done for **phoSec**, JETPHOX relies on a combination of phase space slicing (for soft and initial-state collinear divergences) and subtraction method (for final state collinear divergences). Because of this, the results produced by JETPHOX may exhibit a residual dependence on the phase space slicing parameters (called  $R_{th}$  and  $p_{Tm}$  in Ref. [96]); though, this poses no problem practically, as long as the values of the parameters are chosen reasonably. Since JETPHOX employs the  $\overline{\text{MS}}$ -factorization scheme and allows for the choice  $\mu_R = \mu_F = p_T^\gamma$ , the definitions of “direct” and “fragmentation” in JETPHOX and **phoSec** are equivalent and can be compared directly, as has been done in the last section.

To gauge the importance of the higher order contributions to the fragmentation component, Fig. 3.24 shows the ratio of the NLO fragmentation to the LO fragmentation contribution for the setups established in the last section; but using the same fragmentation function, instead of switching between the LO and NLO parametrizations. The higher order corrections add at least 50 % to the LO fragmentation, rising with the transverse momentum. Thus it is obvious, that at CM energies and for  $p_T$ -regions where the fragmentation contribution is sizable, LO fragmentation is insufficient, even if the importance of the higher orders decreases with  $\sqrt{s}$ .

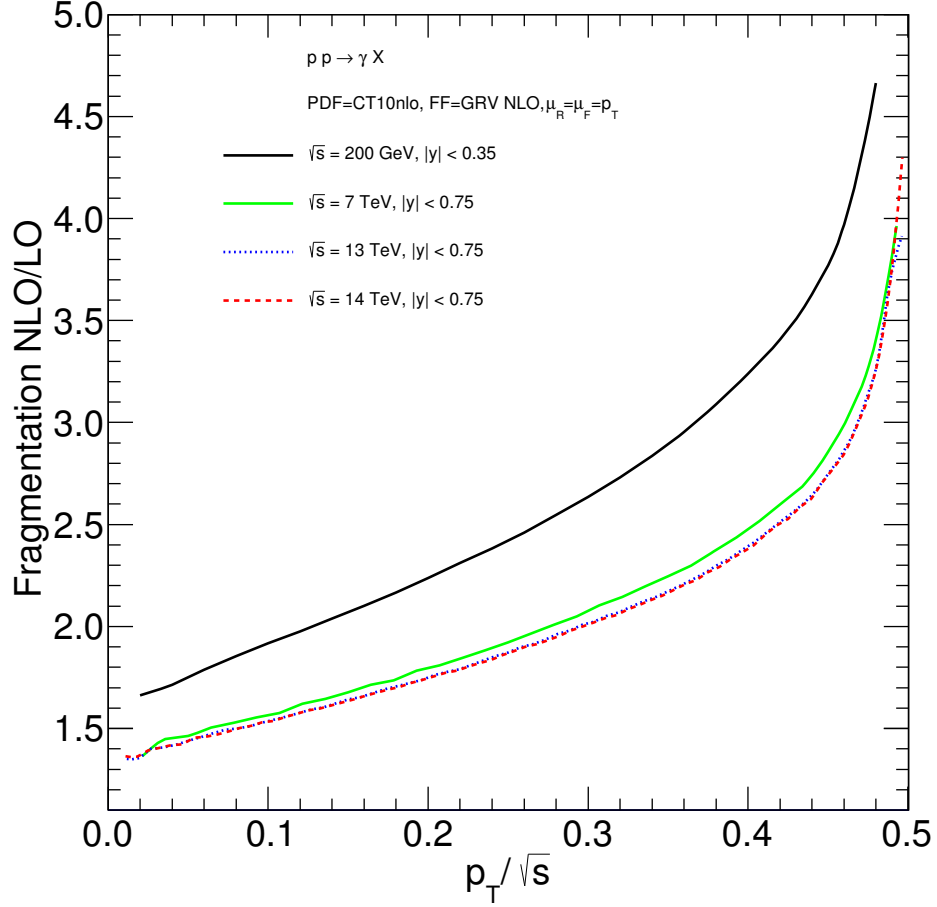


Figure 3.24: Ratio of the NLO and LO fragmentation contributions for different setups, computed with JETPHOX.

The published version of JETPHOX comes with the two BFG sets of photon FFs [99], an interface to LHAPDF to access PDFs plus some nuclear PDFs (nPDFs) to incorporate nuclear effects for heavy ion collisions. For the studies documented in the next sections, I modified the code to include the GRV photon fragmentation functions [94] as well as recent nPDF sets DSSZ [100] and nCTEQ [101]. Furthermore, to enable studies at very low  $p_T$ , the possibility to keep the renormalization and fragmentation scales fixed at  $\mu_R = \mu_F = 1.5 \text{ GeV}$  if the photon- $p_T$  drops below this value, while otherwise having  $\mu_R = \mu_F = p_T$ , was introduced. This is necessary since it is common that PDF-parametrizations require  $\mu_F \geq \sqrt{2} \text{ GeV}$ .

## 4 Photon Fragmentation Functions

For non-isolated prompt-photon production the fragmentation contribution proved to be a crucial component of the full cross section. Even if isolation criteria are implemented, the fragmentation contributions can be sizable: Just as an example, at large  $p_T$  the fragmentation contribution dominates in Fig. 3.21 and, additionally, the photon has to carry most of the energy in the fragmentation process and is then essentially isolated – an isolation cut can not eliminate this dominance of the fragmentation component in the high- $p_T$  tail. Hence a good determination of the fragmentation functions is mandatory not only for precise predictions of the prompt photon cross section at very low  $p_T$ .

In the next section the determination of photon fragmentation functions is discussed. Afterwards prominent FF parametrizations are compared with each other and with low- $p_T$  data from PHENIX.

### 4.1 Determination

In Sec. 3.2 I have discussed the introduction of the photon fragmentation function from an infrared point of view, i.e. as a consequence of the breakdown of perturbation theory caused by collinear divergences related to the photon. In that case it is possible to solve the point-like evolution of the fragmentation function, with the result given in Eq. (3.16). However, even this solution depends on the knowledge of the FF  $D_{\gamma/i}$  at some starting scale  $\mu_s$  from which one starts the evolution. Taking, for instance, the identification of the fragmentation scale  $\mu_F$  with the relative  $p_T$  of mother and daughter partons in a parton splitting literally, one might chose  $\mu_s = p_T^{\min}$  and

$$D_{\gamma/i}(z, \mu_s = p_T^{\min}) = 0,$$

where  $p_T^{\min}$  is the minimal transverse momentum allowed between two partons. This choice effectively constitutes an isolation of the photon, excluding situations where the photon and another parton have a relative  $p_T \leq p_T^{\min}$  [94]. But apart from this very special situation, where the  $\gamma$ -FF is completely determined by the point-like coupling of the photon,  $D_{\gamma/i}(z, \mu_s)$  has to be determined by fitting the calculation to data, i.e. by finding a parametrization of  $D_{\gamma/i}(z, \mu_s)$  as a function of  $z$  such that the data are reproduced in the theoretical prediction. Of course the IR point of view is only a heuristic approach to the introduction of long-distance functions, and in case of the  $\gamma$ -FF at hand one must really consider the full evolution equations (3.18) (which arise naturally in the operator point of view, while in the IR view they are introduced rather ad hoc). This complicates the solution of the evolution equations, but it is clear, that this, too, is an initial value problem, and one still has to find some boundary condition  $D_{\gamma/i}(z, \mu_s)$  such that the theory matches the experimental data.

#### 4 Photon Fragmentation Functions

Since (3.18) is an inhomogeneous ODE, the general solution can be written as a sum of a special solution of the inhomogeneous ODE and the general solution of the homogenized counterpart; i.e. one has

$$D_{\gamma/i}(z, \mu_F) = D_{\gamma/i}^{\text{anom}}(z, \mu_F) + D_{\gamma/i}^{\text{had}}(z, \mu_F). \quad (4.1)$$

Here,  $D_{\gamma/i}^{\text{anom}}$  – the “anomalous” or “point-like” solution – is the special solution to (3.18) with  $D_{\gamma/i}(z, \mu_s) = 0$  and the hadronic component  $D_{\gamma/i}^{\text{had}}$  is the solution to the homogenized DGLAP equation with some non-zero boundary condition, that is to be determined by comparison to experimental data. As the splitting kernels in the DGLAP-equation are scheme dependent beyond LO, and it is especially possible to shift contributions between the homogeneous and inhomogeneous terms, this decomposition is scheme-dependent beyond LO.

Historically, the determination of the non-zero boundary condition has been attempted mainly by using data from  $e^+e^-$  colliders, where no additional uncertainties concerning hadronic initial state effects enter the calculation [64]. Yet, the available data on prompt photons have not been precise enough to sufficiently constrain the hadronic boundary condition, so that additional input was needed. At this point the VMD, Eq. (3.8), is used as a means of acquiring information on the hadronic input by relating the photon-FF to the well-known fragmentation functions for vector-mesons  $\rho$ ,  $\omega$  and  $\phi$

$$D_{\gamma/i}^{\text{had}}(z, \mu_s) = \sum_{V=\rho,\omega,\phi} \frac{4\pi\alpha}{f_V^2} D_{V/i}(z, \mu_s). \quad (4.2)$$

Since  $D_{V/i}(z, \mu_F)$  are solutions to the pure QCD DGLAP equations (2.44), Eq. (4.2) is naturally the solution of (3.18) with vanishing inhomogeneity.

The two most prominent parametrization of the photon fragmentation function, the GRV [94] and BFG [99] sets (available as NLO sets, i.e. following an evolution with NLO splitting kernels), are both based on the decomposition (4.1) and the VMD (4.2). Furthermore, both GRV and BFG follow evolution equations with massless kernels and take the masses of the heavy quarks  $c$  and  $b$  ( $t$  decouples, i.e.  $N_f = 5$ ) into account by using thresholds

$$\begin{aligned} D_{\gamma/c}(z, \mu_F < m_c) &= 0, \\ D_{\gamma/b}(z, \mu_F < m_b) &= 0. \end{aligned}$$

However, the GRV set is defined in the so-called  $\text{DIS}_\gamma$ -scheme and translated into the  $\overline{\text{MS}}$ -scheme only afterwards to be used in calculations. By defining the boundary conditions in the  $\text{DIS}_\gamma$ -scheme – for the hadronic input a parametrization of  $D_{\rho/i}$  is used

$$D_{\gamma/i}^{\text{had}, \text{DIS}_\gamma}(z, \mu_F) = \frac{4\pi\alpha}{f_\rho^2} D_{\rho/i}(z, \mu_F)$$

– the  $\mu_F$  evolution is stabilized compared to the naive  $\overline{\text{MS}}$  definition, which leads to a negative gluon-FF [94]. In the GRV FORTRAN-library it is possible to choose between the

anomalous component alone and the sum of anomalous and hadronic components for both the LO and the NLO parametrization.

The BFG sets on the other hand are defined in the  $\overline{\text{MS}}$ -scheme and use newer, more constrained VMD inputs. To circumvent the problematic instability of the naive  $\overline{\text{MS}}$ -scheme,  $D_{\gamma/i}^{\text{had}}$ , as defined in the  $\overline{\text{MS}}$ -version of (4.1), is analyzed and found to decompose into a scheme-dependent component  $D_{\gamma/i}^{\text{had,dep}}$  and a scheme-independent part  $D_{\gamma/i}^{\text{had,indep}}$  when going beyond LO,

$$D_{\gamma/i}^{\text{had},\overline{\text{MS}}}(z, \mu_F) = D_{\gamma/i}^{\text{had,dep}}(z, \mu_F) + D_{\gamma/i}^{\text{had,indep}}(z, \mu_F).$$

The VMD input is then not directly applied to  $D_{\gamma/i}^{\text{had},\overline{\text{MS}}}$ , as (4.2) suggests, but only to the scheme-independent component,

$$D_{\gamma/i}^{\text{had,indep}}(z, \mu_F) = \sum_{V=\rho,\omega,\phi} \frac{4\pi\alpha}{f_V^2} D_{V/i}(z, \mu_F).$$

As a consequence of not well constrained data on gluon fragmentation, the BFG FORTRAN-library provides two NLO sets differing in the normalization of the gluon fragmentation function [99].

## 4.2 Comparison at low $p_T$

In Sec. 3.4 it has been found that the fragmentation contribution becomes comparable to the direct photon contribution at very low and very large  $p_T$ . In Ref. [102] we have analyzed the possibility to exclude some of the parametrizations by comparison to existing data on non-isolated prompt photons from hadron collisions at low  $p_T$ .<sup>1</sup> As mentioned before, the measurement of non-isolated photons is problematic due to the large background of decay photons mainly from  $\pi^0$ -decays, such that, for example, the ATLAS and CMS experiments at the LHC measure photons in isolation to suppress these backgrounds (e.g. [104, 105]). However, in heavy ion collision, as discussed in more detail in the next chapter, it is important to extract the yield of non-isolated photons in proton-proton (as a baseline) as well as heavy ion collisions. Therefore STAR and PHENIX at RHIC and ALICE at LHC measure non-isolated photons at rather low  $p_T$  (e.g. [106, 107, 108, 109]).

For the analysis in Ref. [102] we have used PHENIX data [110, 107, 111] for inclusive prompt photons produced in  $pp$ -collisions at  $\sqrt{s} = 200 \text{ GeV}$  with  $|\eta| < 0.35$  (as anticipated in the setups used in Sec. 3.4). They cover a range

$$1 \text{ GeV} \leq p_T \leq 25 \text{ GeV}$$

of the photon transverse momentum. To be precise, the data for  $p_T \leq 5 \text{ GeV}$  originate from measurements of the low-mass  $e^+e^-$ -pair (i.e. low-virtuality, quasi-real photon)

---

<sup>1</sup>Recently it has been suggested that it is now feasible to go one step beyond the measurement of non-isolated photons and improve the knowledge on FFs by explicitly measuring and analyzing photons contained in jets [103].

yield at low  $p_T$ , extrapolated to the real photon yield to circumvent difficulties in the distinction of real low- $p_T$  prompt and decay photons [110]. Overlapping with those data, for  $p_T \geq 4$  GeV data have been obtained for real photons [107].<sup>2</sup> The idea of the analysis is that using these fairly recent data, first, the scale uncertainty introduced through the freedom of choice for the renormalization and fragmentation scales – in this section the fragmentation scale for the PDFs, denoted  $\mu_F$ , and for the FF, denoted  $\mu_D$ , are allowed to differ – can be reduced by finding the best combination of choices for  $\mu_R$ ,  $\mu_F$  and  $\mu_D$  reproducing the given data for high  $p_T$ . Second, we can perform a  $\chi^2$ -test in the low- $p_T$  region, where the fragmentation contribution dominates, to establish which FF is favored by the data.

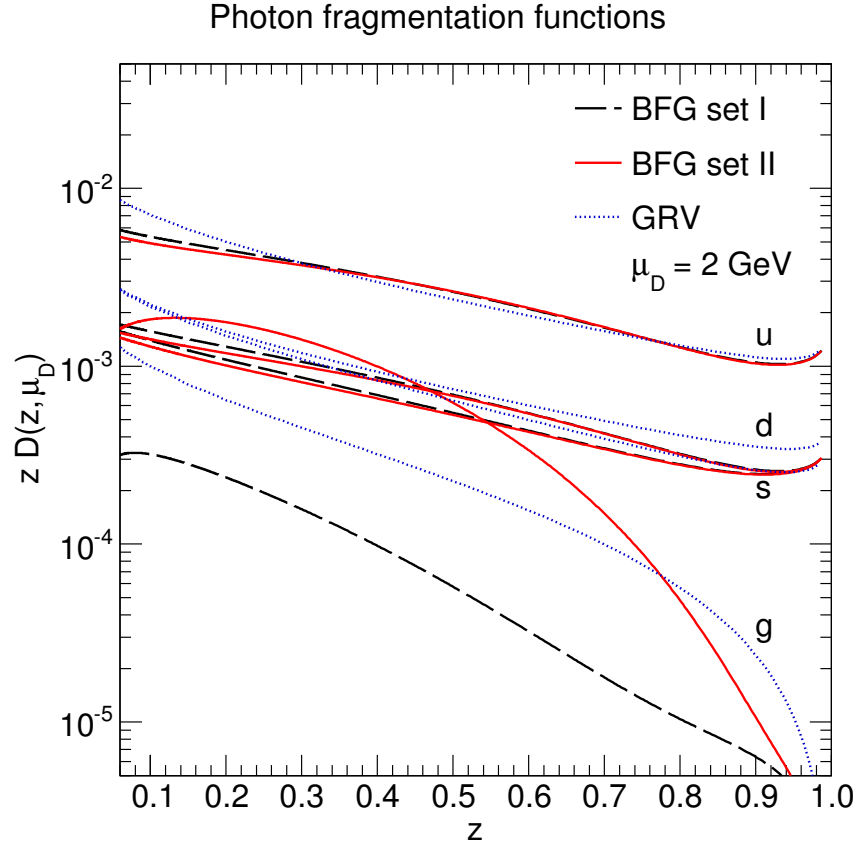


Figure 4.1: The photon FFs BFG I, II and GRV NLO for fragmentation from  $u$ -,  $d$ -,  $s$ -quarks and gluon  $g$  at the fragmentation scale  $\mu_D = 2$  GeV, as shown in [102].

Focusing on three main sets, the BFG I and II sets and the full GRV NLO set, Fig. 4.1 shows the FFs at a scale characteristic for the  $p_T$ -region of the PHENIX data,

<sup>2</sup>The data points displayed in the references are actually shifted towards the center of mass of the respective  $p_T$ -bin. Y. Yamaguchi provided us with the bin-centered data.

$\mu_D = 2 \text{ GeV}$ . Up- and down-type distributions reflect the difference in their charges, which, as indicated by the charge dependence of the splitting function (3.13), enter the fragmentation functions squared. Differences between the BFG and GRV parametrizations are most significant for the gluon fragmentation function which varies over an order of magnitude.

Of course, it is mandatory for our analysis to ensure that the other uncertainties entering the cross section, namely the PDF errors, are not invalidating the result. To that end, an estimate of the momentum fractions  $x_a$  and  $x_b$  can be given through<sup>3</sup>

$$x_T = \frac{2p_T}{\sqrt{s}} \sim 0.01 - 0.1.$$

In this intermediate range of the longitudinal momentum fraction, our PDF choice for this analysis, CT10, is well-constrained [97].

To establish the  $p_T$ -range in which the fragmentation function is most significant we have used JETPHOX to compute the direct and fragmentation contributions (in the  $\overline{\text{MS}}$  factorization scheme) to the full NLO cross section. Using the BFG II set and estimating the uncertainty of the fragmentation contribution by varying only the FF scale  $\mu_D$  about a factor of 2, while setting all scales to the photon- $p_T$  in the central result, we have found that the fragmentation processes become dominant for

$$p_T \leq 5 \text{ GeV},$$

as shown in Fig. 4.2. For  $p_T > 10 \text{ GeV}$  the direct contribution clearly dominates, contributing 65 % – 75 % of the full cross section for the central choice of  $\mu_D = p_T$ . Decreasing  $\mu_D$  about a factor 1/2 significantly enhances the direct contribution  $\sim 5 \%$  at the expense of the fragmentation processes. Hence, we have used the region above 10 GeV – the control-region – to fix the scale-choice and the region below 10 GeV to perform the hypothesis test.

The  $\chi^2$ -test (as described e.g. in [112]) has been performed by taking the experimental values  $d\sigma_i^{\text{exp}}$  in each bin as estimators to the true values with uncertainty given by the uncorrelated statistical errors  $\epsilon_i$  (by that we have disregarded the systematical error of roughly the same magnitude, which is largely correlated between different  $p_T$ -bins [111]). Using the theoretical predictions  $d\sigma_i^{\text{theo}}$  for the cross section in each bin as the hypothesis that is to be tested, the residuals are given by

$$\chi^2 = \sum_{i=1}^{N_{\text{dof}}} \left( \frac{d\sigma_i^{\text{exp}} - d\sigma_i^{\text{theo}}}{\epsilon_i} \right)^2, \quad (4.3)$$

where the sum runs over the  $N_{\text{dof}}$  different  $p_T$ -bins. As the statistical errors on the experimental data points are expected to be Gaussian, the residuals are expected to follow a  $\chi^2$ -distribution  $\rho_{\chi^2}$  with  $N_{\text{dof}}$  degrees of freedom as long as the theory predictions

---

<sup>3</sup>By conservation of energy and momentum z-component in the CM frame one finds for a massless  $2 \rightarrow 2$  process  $x_{a,b} = x_T/2(e^{\pm y_1} + e^{\pm y_2})$ , which is  $x_T$  at central rapidity.

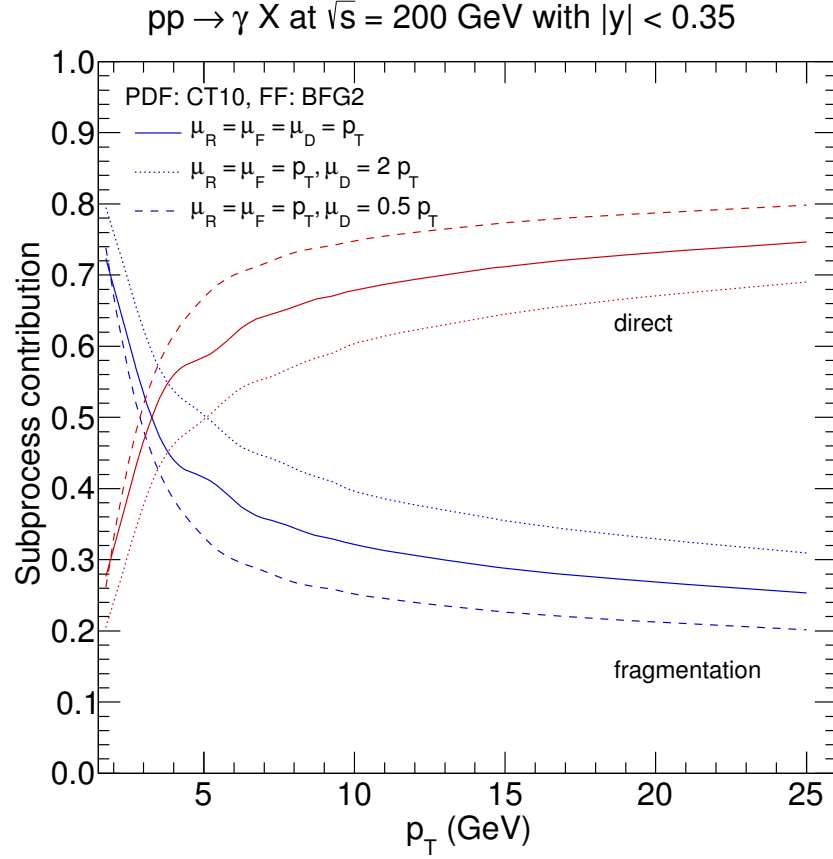


Figure 4.2: Fraction of the prompt photon cross section given by the direct and fragmentation subprocesses (as defined by the  $\overline{\text{MS}}$  factorization scheme). Uncertainties on the lines are scale variations in the fragmentation factorization scale  $\mu_D$ . As shown in [102].

$d\sigma_i^{\text{theo}}$  describe the experimental data correctly. By specifying a significance level  $\alpha$ , one defines that the  $(1 - \alpha)$ -quantile  $x_\alpha$ , given by

$$\int_0^{x_\alpha} dx \rho_{\chi^2}(x, N_{\text{dof}}) = 1 - \alpha,$$

is the largest acceptable value at which the residuals are believed to follow the  $\chi^2$ -distribution; at a larger value the hypothesis is rejected.

By varying the scales  $\mu_R$ ,  $\mu_F$  and  $\mu_D$  independently among the choices  $1/2p_T$ ,  $1p_T$  and  $2p_T$  and computing for each combination the residuals  $\chi^2$  for the bins with  $p_T > 10$  GeV, we have found that the minimal value of the residuals arises for the scale choice  $\mu_R = \mu_D = 1/2p_T$  and  $\mu_F = 2p_T$ . In that case,  $\chi^2/N_{\text{dof}} \approx 1.2$  for the BFG I and II FFs, while  $\chi^2/N_{\text{dof}} \approx 1.4$  for GRV NLO. Fixing the scales to this combination, which best reproduces the data in the control region, is a way to effectively reduce



the discrepancy between the perturbative NLO prediction and the true value, which is otherwise only approached by including corrections from higher orders. The PHENIX data and theoretical predictions with the scale choice found above are depicted in Fig. 4.3. Here, it is important to mention, that the BFG evolution starts at  $\mu_D = \sqrt{2} \text{ GeV}$ , which is why we froze the scales in case they otherwise would be dropping below that limit, as described in Sec. 3.5. Since we have done that for all FFs, it should affect them in a similar way, not impeding the discrimination between them.

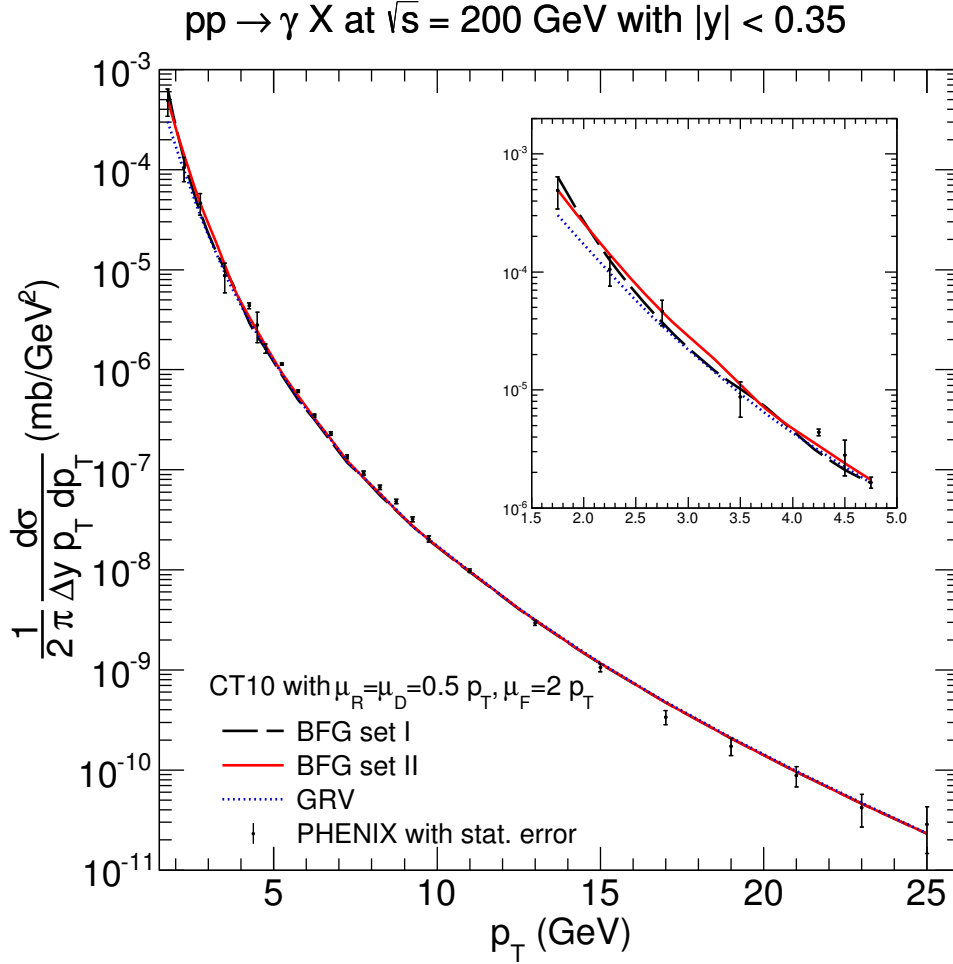


Figure 4.3: Invariant differential cross section as a function of  $p_T$  for BFG I, II and GRV NLO FFs with optimal scale choice compared to the PHENIX data with statistical errors. The enlarged low- $p_T$  region is shown extra. As shown in [102].

In the signal region  $p_T \leq 5 \text{ GeV}$  the residuals are such that it has been possible to reject the BFG I and GRV NLO hypothesis at a significance level  $\alpha = 1\%$ . We have found  $\chi^2/N_{\text{dof}}$  to be 2.3 for BFG II, 3.8 for BFG I and 3.3 for GRV NLO, while the

#### 4 Photon Fragmentation Functions

$(1-\alpha)$ -quantile is 2.6. However, these results strongly depend on one data point, namely, the exceptionally high point at  $p_T = 4.25$  GeV, which is the lowest point from the real photon measurement. Excluding that point from our analysis, we have found that none of the FFs can be rejected at  $\alpha = 1\%$ , where the quantile is now 2.8 and  $\chi^2/N_{\text{dof}}$  is 0.5 for BFG I, 0.6 for BFG II and 0.5 for GRV NLO.<sup>4</sup> By artificially decreasing the statistical errors on the extrapolated nearly-real photon data, we have estimated that a further reduction of the statistical error by at least a factor of 5 would be needed to favor one of the FFs with this type of hypothesis test.

---

<sup>4</sup>The results quoted in [102] are based on an exclusion of both real-photon points at  $p_T = 4.25$  GeV and  $p_T = 4.75$  GeV.

## 5 Heavy Ion Collisions

In Sec. 2.6 a short review of the phase structure of QCD has been given and lattice results on the existence of a Quark Gluon Plasma (QGP) have been quoted. This chapter serves to discuss some aspects of the exploration of the QGP through direct photon production in heavy ion collisions. First the terminology has to be made clear what “direct” photons in this context means. In the last chapter, the term “prompt” photons served to distinguish photons produced in hard (perturbatively calculable) processes from photons resulting from hadron decays. Furthermore, prompt photons fall into two (factorization scheme dependent) categories: “direct” and “fragmentation” photons, where for the description of the latter one has to resort to non-perturbative fragmentation functions. This last category “direct” has to be distinguished from the more general category of “direct photons” in the context of heavy ion collision. Here, it has the meaning of prompt photons plus “thermal photons” originating from thermal interactions, i.e. produced by the QGP or the hadron resonance gas (HRG) [113]. In fact, in the context of heavy ion collisions, it also means “all photons, except those from hadron decays”, keeping in mind that here one has other production mechanisms at work additionally to the hard scattering and hadron decays found for instance in  $e^+e^-$ -collision.

Sec. 5.1 serves to introduce the standard picture of a heavy ion collisions, whereby the collision can be divided into different stages. One of these stages corresponds to the hard scattering by which prompt photons can be produced. However, since one now deals with heavy ions instead of nucleons there are some initial state effects that have to be taken into account even for the description of the usual hard processes, as discussed in Sec. 5.2. In Sec. 5.3 the direct photon yield is compared to the prompt photon yield computed in NLO QCD and implications of a difference in prompt and direct photon yields are discussed.

### 5.1 Collision Stages

The collision of two highly energetic nuclei can in a first very crude approximation be split into “hard” and “soft” interactions [58]. At nearly the speed of light, interactions between the constituents will set in when the two nuclei start to overlap. Due to the relatively small hard process cross section, only a few high momentum transfer interactions between single partons take place at very short time scales  $\tau \ll 1/\Lambda_{\text{QCD}} \sim 1 \text{ fm } c^{-1}$ . On the other hand, the remaining constituents can interact over larger time and space scales, which, if the volume of the interaction region and density of constituents are large enough, may justify the use of a (quasi)macroscopic description of the system, characterized by temperature, density, pressure and transport coefficients, etc. This last point is what distinguishes the heavy ion collision from nucleon-nucleon collisions. Now,

## 5 Heavy Ion Collisions

if a macroscopic description of the system is allowed, then it may become feasible to compare the results for extended QCD matter from TFT calculations (cf. Sec. 2.6) to the system produced in heavy ion collisions.

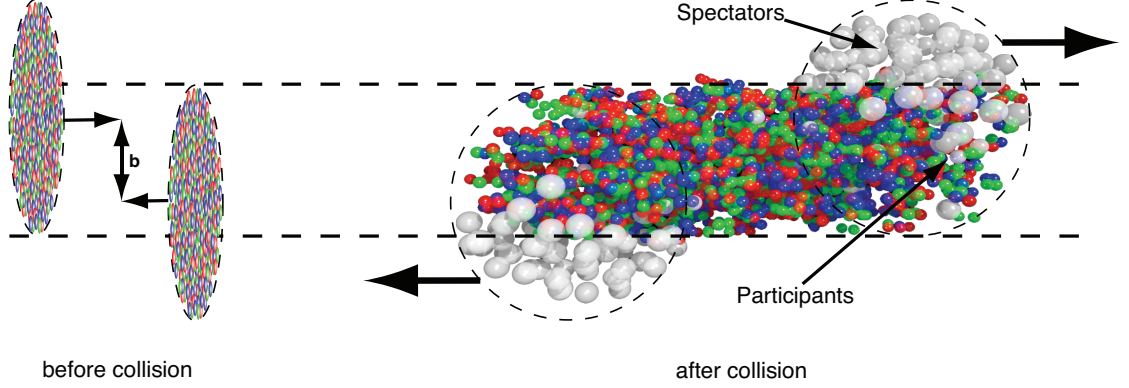


Figure 5.1: Two large nuclei traversing and creating a dense trail of particles; from [114].

A more refined model for the creation and evolution of a thermalized system in a heavy ion collision is the Bjorken scenario [115, 116]. In this model the two ions approach each other as highly contracted pancakes at nearly the speed of light and traverse each other while producing, through nucleon-nucleon collisions, secondary particles, as depicted in Fig. 5.1. The net baryon number carried by the incident ions is to be found in leading baryons near the beam axis after the collision while the secondary particles of zero net baryon number are left as a trail between the departing leading baryons.<sup>1</sup> Then, by assuming that the secondary particles have energies comparable to the secondaries produced in nucleon-nucleon collisions, one can estimate the initial energy density of the system depending on the number of nucleon-nucleon interactions (which depends on the impact parameter  $b$  in Fig. 5.1, i.e. on the centrality). For central collisions at RHIC (CM energy per nucleon  $\sqrt{s_{NN}} \lesssim 200$  MeV depending on the run) and LHC ( $\sqrt{s_{NN}} \lesssim 5.52$  TeV) the densities are estimated to be several times larger than the density of nuclear matter [50]

$$\begin{aligned}\epsilon_{\text{RHIC}} &\approx 5 \text{ GeV fm}^{-3}, \\ \epsilon_{\text{LHC}} &\approx 15 \text{ GeV fm}^{-3}.\end{aligned}$$

Particles in a trail with such an energy density are, at least near the beam axis, i.e. far away from the periphery of the trail, expected to interact with each other collectively, as long as the mean free path is much smaller than the size of the system, and will after some time  $\tau_0$  approach a thermal equilibrium with a temperature believed to lie above the QGP phase transition temperature  $T_c$ .<sup>2</sup> As depicted in Fig. 5.2, the thermalization

<sup>1</sup>This is the reason why heavy ion collision at sufficiently high energies probe the QCD phase diagram, Fig. 2.5, at zero baryochemical potential.

<sup>2</sup>An estimate of the temperature: If one were to take these energy densities as values for the system in equilibrium and if one would further interpret the numerical results of Fig. 2.6 as physical, these

time is usually given in terms of the proper time invariant under boosts in the beam direction

$$\tau^2 = t^2 - z^2,$$

in terms of which the initial collision takes place at  $\tau_{\text{coll}} \approx 0$  and the thermalization at points near the beam axis takes place at some  $\tau_0 \lesssim 1 \text{ fm } c^{-1}$ . For  $\tau \geq \tau_0$  the system is then locally thermalized and its expansion can be described by relativistic hydrodynamics [117] up to a time  $\tau_f \sim 20 \text{ fm } c^{-1}$  (at the LHC [50]) where the mean free path of the constituents exceeds the system size and it freezes out. The specifics of the hydrodynamic evolution depend on the fluid properties, especially the ratio of shear viscosity and entropy density  $\eta/s$  [118], and the equation of state of the locally thermalized cells, which ultimately contains the information on the type of matter, QGP or HRG, that has been created in the collision. If a QGP has been created, then at a time  $\tau_h \sim 10 \text{ fm } c^{-1} < \tau_f$  (at the LHC [50]) the system will additionally undergo a phase transition from QGP to HRG.

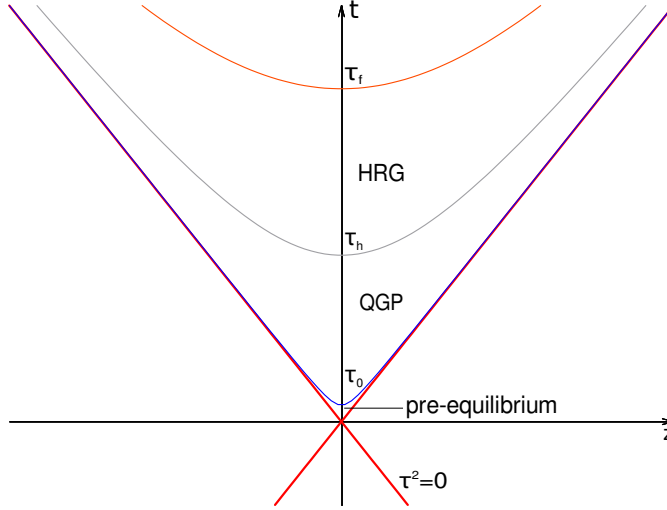


Figure 5.2: Evolution of the system created in a heavy ion collision. The light-cone is identified with the trajectory of the incident ions and receding leading baryons. Between the initial thermalization time  $\tau_0$  and the freeze out  $\tau_f$  the system is described by hydrodynamics. Cf. [58, 115, 50].

Unfortunately, the freeze out takes place long before the system reaches the detectors. That means a detector measures either particles created at the periphery or before the thermalization of the system, hard particles that were able to escape the system or the remnants of the freeze out. The latter should, in principle, give information on the flow, i.e. the collective expansion of the system, and thermal distribution of the particles just before the freeze out. The most notable example for a flow property is the so-called elliptic flow  $v_2$ , which emerges from pressure gradients in the trail of non-central

---

densities would correspond to temperatures  $T_{\text{RHIC}} \approx 240 \text{ MeV}$  and  $T_{\text{LHC}} \approx 310 \text{ MeV}$ , as can be seen by extracting the intersection of  $\epsilon_{\text{RHIC,LHC}}/T^4$  and the corresponding curve in Fig. 2.6.

collisions and a consequent azimuthal anisotropy in the expansion of the medium and its detected remnants. This observable is very sensitive to the equation of state and the fluid viscosity  $\eta/s$ , which gives a measure on how close the created QGP is to being a perfect fluid [114]. Hard probes, on the other hand, are interesting as they originate from hard scattering processes somewhere in the collision region and have enough energy to traverse the medium that is forming while they move through the collision region. Heavy quarks or jets, for example, would lose energy through interactions with the medium, resulting in the so-called heavy quark- or jet-quenching; a depression of the respective yield compared to nucleon-nucleon collisions in the vacuum. Electromagnetic probes, like photons or lepton pairs, on the other hand would ideally travel through the medium unaffected, as they do not interact strongly. If the electromagnetic probe is generated in conjunction with a jet, e.g. a photon and a parton back-to-back as in Fig. 5.3, then the energy-loss of the jet through medium interactions can, in a first approximation, be quantified by the ratio of jet- and photon-energies  $E_{\text{jet}}/E^\gamma < 1$ . If instead the electromagnetic particles originate from the thermalized medium, e.g. thermal photons, they carry direct information on the temperature inside. The role of perturbative QCD in this context is to provide a baseline with which the measurements can be compared, such that deviations from the baseline can be interpreted in terms of medium effects.

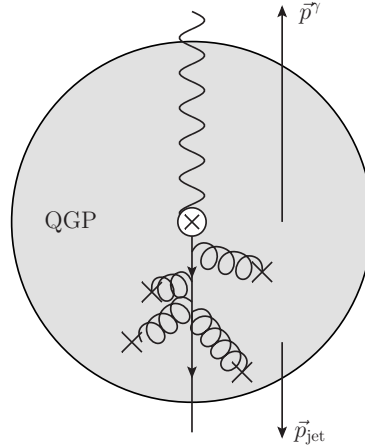


Figure 5.3: Hard photon-jet pair creation as viewed in beam direction. The surrounding medium decreases the jet-momentum while the photon travels through unhindered.

## 5.2 Initial State Effects

Disregarding, for the moment, the possibility of the creation of a medium and how it would affect observables, it is crucial to ask how hard scattering off a large nucleus compares to hard scattering off a nucleon. One especially has to answer the question if factorization is still working when one has large nuclei and probes relatively small values

of the longitudinal momentum fraction  $x$  and correspondingly large gluon densities.<sup>3</sup> Already for nucleons a breakdown of factorization due to large parton densities might become a problem, but the problem is most probably enhanced for large nuclei (since the parton densities are naively expected to scale roughly by the number of nucleons  $A$  whereas the transverse area of the Lorentz-contracted nucleus scales only with  $A^{2/3}$ ).

The results of Sec. 4 show that pQCD works well enough to describe prompt photon production in  $pp$ -collisions at  $\sqrt{s} = 200$  GeV with  $x$ -values of the order of  $10^{-2}$ . But the LHC probes, at low  $p_T$ ,  $x$ -values of at least  $10^{-4} - 10^{-3}$  at central rapidity and less for larger rapidities. Prompt photon data for  $pp$  at  $\sqrt{s} = 7$  TeV exist for isolated prompt photons of transverse momentum above 20 GeV (from ATLAS [104]). They are largely within the theoretical uncertainties of the NLO pQCD calculation, but show already significant deviations at the low  $p_T$  bound. However, this could be an effect related to the isolation (JETPHOX, for example, sometimes produces unphysical results for isolated photons at low  $p_T$ , like a larger direct component for isolated photons than for non-isolated photons [96]). From ALICE, measurements of inclusive direct photon spectra in  $pp$  collisions exist, but the prompt photon signal is buried in the uncertainties of the background while being consistent with pQCD predictions [119]. Preliminary results on low mass electron pairs, however, indicate an agreement between the inclusive direct photon yield in  $pp$  at for  $2 \text{ GeV} < p_T < 4 \text{ GeV}$  and NLO pQCD [120]. Additionally, it has been shown in [121] that a resummation of small- $x$  enhanced terms for prompt photons at the LHC has only marginal effects of the order of 1 % on the cross section at central rapidities. Insofar, one can hope to still apply NLO pQCD successfully at the  $x$ -values probed at central rapidity in  $pp$ -collisions.

From the assertion of the validity of NLO pQCD for  $pp$ -collisions, one has then to take a leap to large nuclei, which are made up of hundreds of nucleons. The question is then if the heavy ion  $A$  can, in a collision, be understood as bag of nucleons and if and how the known nucleon PDFs are affected by the nucleon being bound.

### 5.2.1 Glauber approach

In the geometrical Glauber approach to nucleon-nucleus  $NA$ - or nucleus-nucleus  $AB$ -collisions, as described in [122, 123], the nucleus is indeed understood as a collection of nucleons, quantified by the nuclear density  $\rho_A(\vec{x})$  (e.g. a Woods-Saxon potential) normalized to the number of nucleons

$$\int d^3x \rho_A(\vec{x}) = A. \quad (5.1)$$

Under the assumption that nucleons travel unhindered in straight lines – in this context also called optical or eikonal approximation – the number of collisions is, roughly said,

---

<sup>3</sup>As implied in Sec. 2.4.2, the factorization scale  $\mu_F$  can be interpreted as the inverse of the transverse resolution length, i.e.  $1/k_T$ , of partons in PDFs. When the number of partons at some value of  $x$ , quantified by  $xf_{i/A}(x, \mu_F)$ , becomes so large that the partons distributed over the area of the nucleus start to overlap, the parton model breaks down since one does no longer resolve individual partons. This breakdown of factorization is called “saturation” and is expected to apply to gluons, whose number diverges for  $x \rightarrow 0$  as indicated by the soft divergence in (2.37) [50].

determined by how many nucleons lie on a line parallel to the beam axis and by the nucleon-nucleon interaction cross section.

To be more specific, it is pedagogical to first consider  $NA$ -, i.e. nucleon-nucleus-collisions. For the nucleus  $A$  one can define a nuclear thickness function by integrating the nuclear density over the beam direction  $z$

$$T_A(\vec{b}) = \int dz \rho_A(\vec{b}, z). \quad (5.2)$$

This gives the nuclear areal density at a transverse distance  $\vec{b}$  from the center of the nucleus (this is the impact parameter in Fig. 5.1). From the geometrical interpretation of the total nucleon-nucleon cross section  $\sigma_{NN}^{\text{total}}(s)$  as the effective area of a nucleon in a scattering event at CM energy  $s$  follows that  $T_A(\vec{b})\sigma_{NN}^{\text{total}}(s)$  describes the occurrence of collisions if a nucleon strikes a nucleus at a distance  $\vec{b}$  from its center. The probability of having  $k$  collisions can then be modelled by a Poisson distribution,<sup>4</sup>

$$P_{\vec{b},s}(k) = \left( \sigma_{NN}^{\text{total}}(s) T_A(\vec{b}) \right)^k \frac{e^{-\sigma_{NN}^{\text{total}}(s) T_A(\vec{b})}}{k!}, \quad (5.3)$$

and the probability of any collision occurring is consequentially

$$P_{\vec{b},s}(k > 0) = 1 - e^{-\sigma_{NN}^{\text{total}}(s) T_A(\vec{b})}. \quad (5.4)$$

Integrating this over the impact parameter  $b$  (over a yet unspecified range) gives the nucleon-nucleus cross section

$$\sigma_{NA}^{\text{total}}(s) = \int d^2b \left[ 1 - e^{-\sigma_{NN}^{\text{total}}(s) T_A(\vec{b})} \right]. \quad (5.5)$$

Assuming this formula holds all the same when restricted to only hard (inelastic), differential nucleon-nucleon cross sections  $d\sigma_{NN}$  and acknowledging furthermore the smallness of  $d\sigma_{NN}$ , one simply has

$$d\sigma_{NA} \approx d\sigma_{NN} \int d^2b T_A(\vec{b}). \quad (5.6)$$

This means, given the  $NN$  cross section, the  $NA$  cross section is obtained via scaling with a geometrical factor that depends on the range that is allowed for the impact parameter. In a minimum bias measurement, i.e. a measurement not dismissing certain events due to some selection criteria, the impact parameter is unknown and one would have to integrate over all  $\vec{b}$  giving

$$d\sigma_{NA} \approx d\sigma_{NN} A.$$

---

<sup>4</sup>This is the approach underlying [122], whereas [123] describe the probability by a binomial distribution.

I take the Poisson approach simply for convenience; strictly speaking the binomial ansatz would be more correct. Though, in the end the results are the same, as long as one approximates the cross section to be small, which will be assumed here.



In the case of  $AB$  collisions one defines, additionally to the nuclear thickness functions  $T_A$  and  $T_B$ , a nuclear overlap function

$$T_{AB}(\vec{b}) = \int d^2s \, T_A(\vec{s}) T_B(\vec{b} - \vec{s}), \quad (5.7)$$

which is just the convolution of the nuclear thickness functions for the nuclei  $A$  and  $B$  and gives the areal density of nucleons in the overlap area. Following the same reasoning as before for  $NA$ -collisions, just with  $T_A$  replaced by  $T_{AB}$ , one has for the hard, differential  $AB$  cross section

$$d\sigma_{AB} \approx d\sigma_{NN} \int d^2b \, T_{AB}(\vec{b}). \quad (5.8)$$

For a certain observable, for instance the prompt photon cross section, one often gives the number of particles (photons) measured and normalized to the total number of inelastic scattering events, i.e.  $dN^\gamma/N_{\text{ev}}$ , which is related to the respective cross sections by expanding the fraction with the integrated luminosity

$$\frac{1}{N_{\text{ev}}} dN^\gamma = \frac{1}{\sigma_{\text{inel}}} d\sigma^\gamma.$$

For  $AB$ -collisions this means in terms of the nuclear overlap function

$$\frac{1}{N_{\text{ev}}} dN^\gamma = \frac{d\sigma_{NN}^\gamma \int d^2b \, T_{AB}(\vec{b})}{\int d^2b \left[ 1 - e^{-\sigma_{NN}^{\text{inel}}(s) T_{AB}(\vec{b})} \right]}, \quad (5.9)$$

where (5.5) and (5.8) have been used. Assuming rotational symmetry of the nucleus around the beam axis, the dependence on the vector  $\vec{b}$  reduces to a dependence on the distance  $b$ . Then (5.9) can be shortened by defining the mean nuclear overlap function for a centrality class  $c$ , i.e. for a specific range  $b \in [b_1, b_2]$ ,

$$\langle T_{AB} \rangle_c = \frac{\int_{b_1}^{b_2} db \, b \, T_{AB}(b)}{\int_{b_1}^{b_2} db \, b \left[ 1 - e^{-\sigma_{NN}^{\text{inel}}(s) T_{AB}(b)} \right]}. \quad (5.10)$$

For sophisticated models of the nucleus this quantity is computed by simulating heavy ion collisions in a Glauber Monte Carlo approach [123]. E.g. for the  $\sqrt{s_{NN}} = 2.76$  TeV Pb-Pb run at the LHC the mean overlap function at different centralities is tabulated in [124]. Thus, one has, depending on the centrality class, different scaling factors with which the nucleon-nucleon cross section is to be multiplied to get the yield of a hard probe, e.g.

$$\frac{1}{N_{\text{ev},c}} dN_c^\gamma = \langle T_{AB} \rangle_c d\sigma_{NN}^\gamma. \quad (5.11)$$

As explained in [124], the centrality classes are correlated with the yield of charged particles, such that by measuring the charged particle multiplicities in a heavy ion collision one can deduce the centrality of the collision and with that the mean nuclear overlap function, which in turn has to be used to scale the theoretical predictions for  $d\sigma_{NN}$  to get

the theoretical predictions for  $d\sigma_{AB}$ . This knowledge about the centrality of collisions is crucial for heavy ion collisions, especially as the formation of a thermalized medium is not expected for peripheral collisions; on the other hand, peripheral collisions can then be used to test the scaling hypothesis presented in this section.

At times, the definition (5.10) can be simplified, specifically, if one is concerned with small impact parameters  $b_1, b_2$ , where  $T_{AB}$  is rather large, and if the inelastic cross section is roughly of the same order as the inverse overlap function (e.g. in [124] one has roughly  $\sigma_{NN}^{\text{inel}}(s)T_{AB} \sim 200$  up to 40 % centrality). Then<sup>5</sup>

$$\langle T_{AB} \rangle_c \approx \frac{\int_{b_1}^{b_2} db \, b \, T_{AB}(\vec{b})}{\int_{b_1}^{b_2} db \, b}. \quad (5.12)$$

Using this, one can, for instance, readily extract  $\langle T_{AA} \rangle_{0\% - 40\%}$  for Pb-Pb-collisions at  $\sqrt{s_{NN}} = 2.76$  TeV from the results for  $\langle T_{AA} \rangle_{0\% - 5\%}$ ,  $\langle T_{AA} \rangle_{5\% - 10\%}$ ,  $\langle T_{AA} \rangle_{10\% - 20\%}$  and  $\langle T_{AA} \rangle_{20\% - 40\%}$  in Ref. [124] (the impact parameters corresponding to the centralities can be found there, too):

$$\begin{aligned} \langle T_{AA} \rangle_{0\% - 40\%} &= \left[ \int_{b(0\%)}^{b(40\%)} db \, b \right]^{-1} \left[ \int_{b(0\%)}^{b(5\%)} db \, b \, \langle T_{AA} \rangle_{0\% - 5\%} \right. \\ &\quad + \int_{b(5\%)}^{b(10\%)} db \, b \, \langle T_{AA} \rangle_{5\% - 10\%} \\ &\quad + \int_{b(10\%)}^{b(20\%)} db \, b \, \langle T_{AA} \rangle_{10\% - 20\%} \\ &\quad \left. + \int_{b(20\%)}^{b(40\%)} db \, b \, \langle T_{AA} \rangle_{20\% - 40\%} \right] \\ &= (12.8 \pm 1.3(\text{stat.}) \pm 0.2(\text{syst.})) \text{ mb}^{-1}, \end{aligned} \quad (5.13)$$

where the errors have been computed simply by adding them in quadrature. This result has been used for the results in the publication [125], which will be presented in Sec. 5.3.

### 5.2.2 Nuclear PDFs

In the last section,  $AB$ -collisions have been described in terms of  $NN$  cross sections scaled by a mean nuclear overlap function  $\langle T_{AB} \rangle_c$ . For the calculation of the cross section one usually has PDFs for the free proton available, which – assuming isospin symmetry – allow to construct the neutron PDFs by exchanging the  $u$ - and  $d$ -quark densities

$$f_{u/n}(x, \mu_F) = f_{d/p}(x, \mu_F), \quad (5.14)$$

$$f_{d/n}(x, \mu_F) = f_{u/p}(x, \mu_F), \quad (5.15)$$

<sup>5</sup>This relation is given as a definition of  $\langle T_{AB} \rangle_c$  in Ref. [122].

while keeping the remaining densities unchanged. This is correct as long as no electroweak effects are included in the PDFs (and the  $u$ -,  $d$ -quark masses are negligible). From the  $p$ - and  $n$ -PDFs one can now construct the PDF for an average nucleon  $\bar{N}$  of a certain nucleus  $A$  with  $Z$  protons and  $A - Z$  neutrons:

$$f_{u/\bar{N}}^{A,\text{free}}(x, \mu_F) = \frac{Z}{A} f_{u/p}(x, \mu_F) + \frac{A - Z}{A} f_{u/n}(x, \mu_F), \quad (5.16)$$

$$f_{d/\bar{N}}^{A,\text{free}}(x, \mu_F) = \frac{Z}{A} f_{d/p}(x, \mu_F) + \frac{A - Z}{A} f_{d/n}(x, \mu_F), \quad (5.17)$$

while, again, the other densities are assumed to be unchanged when going from protons and neutrons to the average nucleon in the nucleus  $A$ .

Up to this point, if one were to use the PDFs  $f_{i/\bar{N}}^{A,\text{free}}$  for the calculation of the hard process in (5.9), one would have only considered the nucleus as a collection of unbound, free nucleons, which would simply lead to scaled  $pp$  predictions incorporating isospin effects (disregarding isospin effects by simply scaling  $pp$  predictions can only be a viable ansatz for non-electroweak observables). Obviously, the nucleons are bound and one has to expect some modifications of the nucleon PDFs accommodating that fact.

Indeed, in the 1980s the EMC collaboration found, in comparing the structure functions from DIS on (calcium) nuclei and on deuterium (which is well-described by a free proton and a free neutron), that at small  $x \lesssim 0.1$  the ratio of nucleus and deuterium structure functions (which are directly related to the PDFs) is significantly smaller than unity, then it rises above unity at moderate  $x \gtrsim 0.1$ , only to fall again below unity at  $x \sim 0.3$  [126]. Further investigations of these effects have nowadays led to the picture in Fig. 5.4, which exemplifies the ratio of bound and free proton PDFs for a nucleus  $A$ , i.e. the nuclear modification function

$$R_{i/p}^A(x, \mu_F) = \frac{f_{i/p}^A(x, \mu_F)}{f_{i/p}(x, \mu_F)}. \quad (5.18)$$

As shown in Fig. 5.4, the enhanced and depleted regions have different names corresponding to different mechanisms believed to give an explanation of the behaviour. The shadowing effect is usually explained as the result of small- $x$  partons being delocalized beyond the bounds of their parent nucleon and recombining with small- $x$  partons from other nucleons nearby. The anti-shadowing region is then simply a result of momentum conservation, i.e.

$$\sum_i \int_0^1 dx x f_{i/p}(x, \mu_F) = 1,$$

requiring a compensation for the depletion in the shadowing region [113]. As the name suggests, the Fermi-motion effect is attributed to the intrinsic motion of the nucleons in the nucleus. Though, in the end, these are non-perturbative effects in the long-distance part of the scattering cross section. As such they are included in nuclear PDFs (nPDFs), i.e. PDFs that are measured by comparing factorized cross sections for some nucleus scattering process with experimental data.

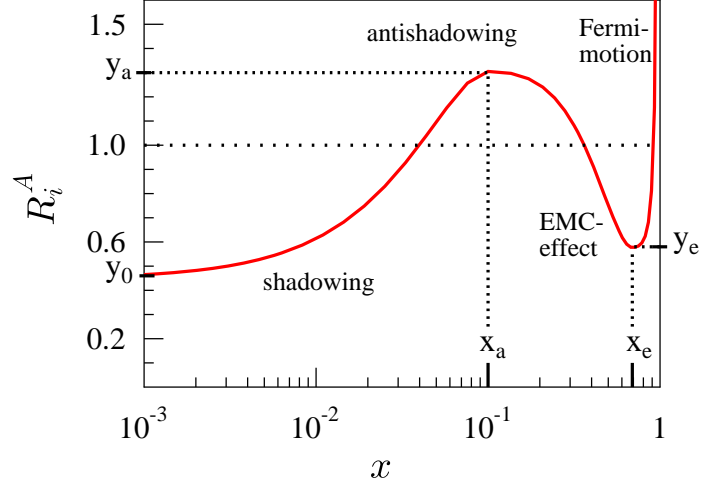


Figure 5.4: Illustrations of the different nuclear effects emerging in the ratio of PDFs of bound and free nucleons. Taken from [127].

There are several of such nPDF parametrizations, though far less than free proton PDFs. For instance, the NLO nPDFs we used in the publication [125] are the EPS09 [127], HKN07 [128], DSSZ [100] and nCTEQ [101]<sup>6</sup> parametrizations. The first three of those parametrizations are fits of the nuclear modification factor (5.18) w.r.t. the free proton PDFs CTEQ6.1M [130], MRST1998 [131] and MSTW2008 [132], respectively, while the nCTEQ parametrization does not depend on an underlying free proton PDF and instead parametrizes the average bound nucleon PDF depending on the type of nucleus.

To see how nPDFs including uncertainties and free proton PDFs compare, Fig. 5.5 shows an exemplary comparison of EPS09 and the widely used CT10nlo free proton PDF. The PDF errors, or more specific the upper and lower difference to the central set, have been computed by the master formula [133]

$$\Delta^+ f = \sqrt{\sum_i \left[ \max \left( f_i^{(+)} - f_0, f_i^{(-)} - f_0, 0 \right) \right]^2}, \quad (5.19)$$

$$\Delta^- f = \sqrt{\sum_i \left[ \max \left( f_0 - f_i^{(+)}, f_0 - f_i^{(-)}, 0 \right) \right]^2}, \quad (5.20)$$

where  $f$  may in general be any quantity computed with a certain PDF (or indeed the PDF itself): The zero subscript refers to the central PDF and the plus- and minus-superscripts correspond to the positive and negative eigendirections into which PDF

<sup>6</sup>These have since the publication of [125] been updated and officially published in [129].

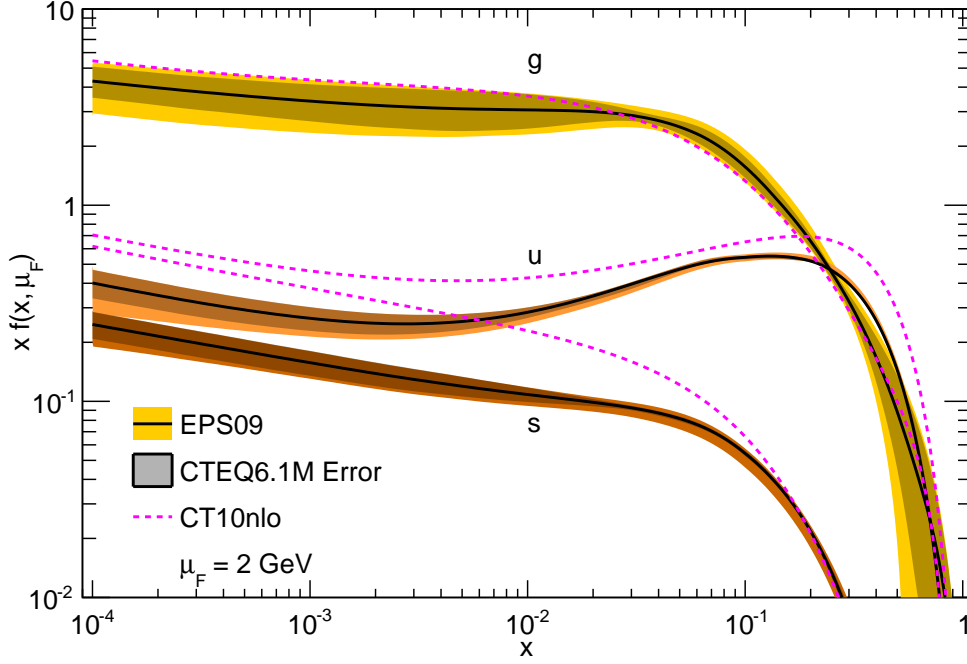


Figure 5.5: Comparison of the momentum distributions  $xf(x, \mu_F)$  for the free proton PDF CT10nlo (magenta) and the EPS09 nPDF (black); including nPDF error bands (yellow), as well as the CTEQ6.1M error band (shaded).  $d$ -quarks are not shown, since they follow the  $u$ -quark distribution, lying about a factor 2 below in the valence quark region  $x \gtrsim 0.1$ .

error sets are usually categorized. In Fig. 5.5 the EPS09 nPDF is plotted with error bands corresponding to the nuclear PDF uncertainty, as well as, in the shaded region, the uncertainty corresponding to the free proton PDF CTEQ6.1M that EPS09 is based on. The uncertainty due to the nuclear modification is considerably larger than the error band of the free proton PDF. Comparing EPS09 and CT10nlo, nuclear shadowing, anti-shadowing and EMC effects are visible in the gluon distribution, though not very prominent due to the large errors, whereas the two quark densities in the  $x$ -range displayed basically only show a strong shadowing suppression of up to a factor 1/2. Clearly, the gluon distribution dominates by an order of magnitude for  $x < 10^{-2}$  and has at the same time the largest absolute error, so that it is expected to have the largest impact on pQCD predictions for heavy ion collisions at the LHC at low  $p_T$ -values.

Fig. 5.6 shows a direct comparison of nPDFs at the same scale as in Fig. 5.5. Even the large uncertainty band of the EPS09 parametrization can not account for the differences to the other parametrizations over a large range of the longitudinal momentum fraction.

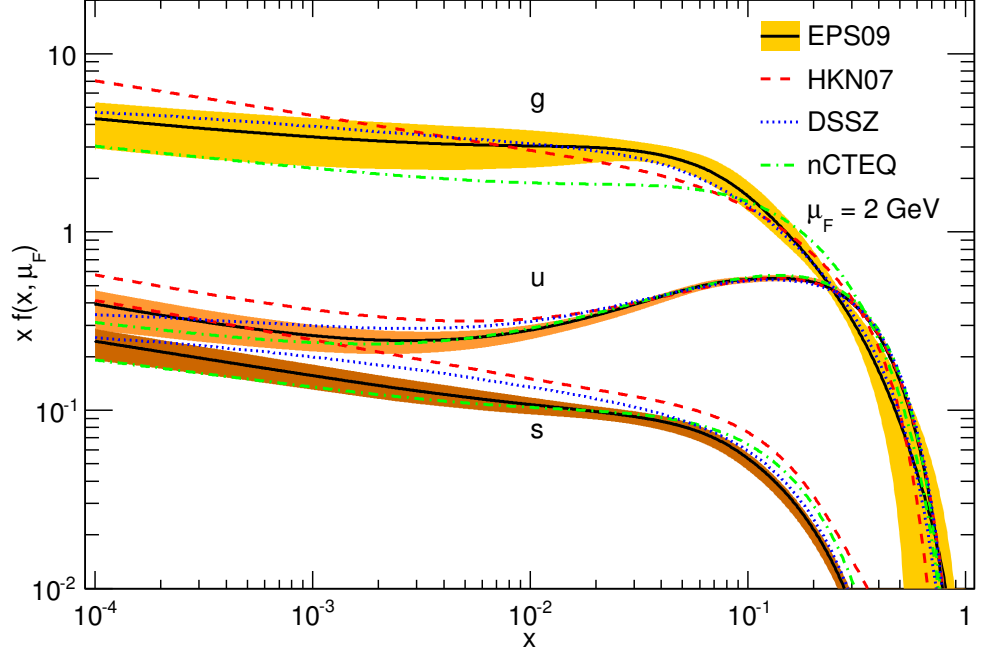


Figure 5.6: Comparison of the EPS09 (with errors), HKN07, DSSZ and nCTEQ nPDF sets at small factorization scale; as shown in [125].

Accordingly, as of now, nPDFs are, due to a lack of data, far less well-determined than their free proton equivalents.<sup>7</sup> Though, there is hope that especially the evaluation of  $pA$ -runs at the LHC will be able to conclusively improve the nPDF fits [135]. In [136] we have suggested that the  $p_T$ -spectrum of virtual photons, i.e. low-mass lepton pairs, produced in  $pA$ -collision at  $\sqrt{s} = 5.02$  TeV would allow for a good test of the especially problematic gluon distribution. The reason for this is that the process, starting at small but finite values of  $p_T$ , is dominated by the QCD Compton process, i.e. by a  $qg$  initial state, and significant differences of the order of  $\sim 10\%$  between the nPDFs become apparent in the  $p_T$ -spectrum. This channel is of course analog to the direct part of prompt photon production, but with the important difference, that for virtual photons there are no fragmentation effects obfuscating the interpretation of the data. However, in recent measurements of isolated prompt photons with transverse momenta larger than 20 GeV, where fragmentation should be significantly reduced by an isolation criterion, it has not even been possible to distinguish between scaled free proton PDFs and nPDFs [137]. In any case, a cleaner probe of nPDFs than in  $pA$ -collisions would be allowed by future  $eA$ -colliders, such as the proposed upgrade of the LHC by an electron accelerator, the LHeC, which would allow DIS at very low  $x$  [138].

<sup>7</sup>A short review of the technical differences between the shown parametrizations and open problems can be found in [134].

To conclude this section, it seems that, in general, pQCD predictions for hard probes have to incorporate nuclear effects through the use of nPDFs – at least to reflect the uncertainty that afflicts nPDF fits. This is of some importance to the subject of the next section.

### 5.3 Direct and Prompt Photon Production

In the search for the creation of a QGP in heavy ion collisions by means of direct photons, the extraction of a thermal photon signal can only be hoped for after measuring the inclusive photon yield. In particular, the photons have to be non-isolated as not to cut away a thermal photon signal, which is accompanied by a large background of uncorrelated hadrons. At  $p_T \gtrsim 1$  GeV the STAR [106] and PHENIX [107] experiments at RHIC and ALICE [109] at LHC were able to suppress the decay photon background sufficiently and extract the inclusive direct photon yield in  $\sqrt{s} = 200$  MeV AuAu and  $\sqrt{s} = 2.76$  TeV PbPb collisions, respectively – either directly or indirectly via low-invariant-mass  $e^+e^-$  pairs.

From the theory side, it has been expected that thermal photons are produced in a QGP at a significant rate with transverse momenta up to 10 GeV [113]. Thus, one expects a window  $1 \text{ GeV} \leq p_T \leq 10 \text{ GeV}$  for the extraction of a thermal photon signal by means of subtracting pQCD prompt photon predictions from the measured direct photons,

$$dN_\gamma^{\text{thermal}} = dN_\gamma^{\text{direct}} - dN_\gamma^{\text{prompt}}. \quad (5.21)$$

Naturally, this subtraction depends on the uncertainties of the prompt photon prediction. At  $\sqrt{s} = 2.76$  TeV the expected thermal photon  $p_T$ -range corresponds to  $x \sim 10^{-3}$  at central rapidity, which, as can be seen in Fig. 5.5, is affected by the shadowing effect, such that a reduction of the prompt photon yield w.r.t.  $pp$ -collisions might be expected. On the other hand, the dominating gluon distribution with its large errors is predestined to counteract the visibility of such an effect; this is one source of uncertainty in the pQCD calculation.

Furthermore, the results of Sec. 4 have shown that already at RHIC energies with  $\sqrt{s} = 200$  GeV the fragmentation contribution is comparable to or even dominates over the prompt-direct contribution. In that sense, the statement that photons “do not interact strongly”, that has been made in Sec. 5.1, calls for a qualification, namely that at low  $p_T$  prompt photons do, in fact to a large portion, interact strongly and by this the utility of the photon as an electromagnetic probe has to be re-examined. First, the uncertainties due to the FF have to be evaluated. The study in Sec. 4 has shown that the data from  $pp$  collision are not yet able to distinguish between different FF parametrization and in that sense, due to the given experimental accuracy, they are known to a high enough precision for RHIC. At the LHC, on the other hand, it is of course mandatory, due to the larger range of momentum fractions being probed, to perform calculations with different parametrizations to estimate the FF uncertainty – thereby constituting another source of theoretical uncertainty. Second, the medium might in effect modify the FF. Approaches to the modeling of parton energy loss before fragmentation have been suggested for

example in [139, 140]. There are though conflicting expectations about the effect of such a modification: An argument for the enhancement of bremsstrahlung photons through medium interactions has been given in [141]. In contradiction to that prediction, a 20 % decrease of the photon yield at RHIC has been calculated for  $p_T < 20$  GeV in [140]. Additionally, it would be natural, due to the larger quenching of strong probes at the LHC, e.g. the  $\pi^0$ -yield [142], to expect a larger fragmentation suppression, too. However, the RHIC AuAu data [143, 106] are (due to the large uncertainties) in good agreement with pQCD without FF modifications down to  $p_T \approx 4$  GeV, so that modifications of the photon-FF might become relevant only in case of a significant decrease of other uncertainties.

Additionally to the uncertainties mentioned, one has to keep in mind that a pQCD calculation depends on the choice of renormalization and fragmentation scales, which introduces a third type of uncertainty.

Certainly, the above-mentioned sources of uncertainties of the pQCD calculation decrease the room for the detection of a significant thermal photon signal in the direct photon yield.

### 5.3.1 Slope parameter

Thermal photons are produced through the whole space-time evolution of the medium, as soon as the medium is in local equilibrium and up to the point where it freezes out. That means that the thermal photon spectrum can not be simply understood as representing some kind of equilibrium temperature of the source. Furthermore, since the photons would interact only very weakly with the medium after the production, they themselves are not thermalized as in e.g. black body radiation. However, by comparing different scenarios for the production of thermal photons in the ever-expanding and cooling fireball with the actual measurement, one can still hope that the production of a QGP would leave an unequivocal signature in the photon spectrum, which distinguishes it from a pQCD or HRG photon spectrum.

The theoretical predictions for the thermal photon yield naturally depend on the initial conditions, such as formation time  $\tau_0$ , initial energy density and assumptions about the flow properties of the medium [144]. Hence, there are a many unknown or at least uncertain parameters that have to fit the thermal photon spectrum, while the main interest here lies in the initial temperature  $T_0$  and if  $T_0 > T_c$  (with  $T_c$  given in (2.87)). The authors of Ref. [145] suggest, that readily extracted information on the initial temperature of the medium can be found in the so-called inverse slope parameter (or sometimes effective temperature)  $T_{\text{eff}}$ , i.e. the parameter specifying the slope in an exponential fit

$$A \cdot \exp\left(-\frac{p_T}{T_{\text{eff}}}\right) \sim E \frac{dN_{\gamma}^{\text{thermal}}}{d^3p} \quad (5.22)$$

to the thermal photon spectrum ( $A$  is here just a normalization factor of no further relevance). In their simulations (for AuAu collisions at RHIC) they have found that the thermal photon signal dominates the direct photons for  $p_T \lesssim 4$  GeV and that  $T_{\text{eff}}$ , for fits in the range  $p_T \gtrsim 2$  GeV is positively correlated with  $T_0$ , such that  $T_{\text{eff}} \gtrsim 250$  MeV is



a clear signal for the creation of a QGP. Though, it has to be always kept in mind that the slope parameter is by no means identical to the temperature of the medium, nor is there a simple connection to be made without complete simulations of the evolution of the medium.

The result that there is a correlation of  $T_0$  and  $T_{\text{eff}}$  has since been carried over to the interpretation of the thermal photon signal measured at central rapidity  $|y| < 0.75$  by ALICE in PbPb collisions at  $\sqrt{s} = 2.76$  TeV in the 0% – 40% centrality class, as presented in [146]. There, an excess over the scaled prompt photon prediction begins to show for  $p_T < 4$  GeV, which has not been observed in the 40% – 80% centrality class. A fit to the (unsubtracted) direct photon signal in the transverse momentum range 0.8 GeV – 2.2 GeV returned an inverse slope parameter

$$T_{\text{eff}} = (304.0 \pm 5.1) \text{ MeV},$$

hinting at an initial temperature large enough for the formation of a QGP.

### 5.3.2 Effect of pQCD uncertainties

In [125] we have analyzed the direct photon data from [146] to answer the question if the apparent direct photon excess and especially the found inverse slope parameter survive the inclusion of theoretical uncertainties in the pQCD calculation and the subtraction of the prompt photon contribution. To compute the prompt photon yield at NLO, we made use of JETPHOX (modified as in Sec. 3.5). As presented at the end of Sec. 5.2.1, we have computed the nuclear overlap factor (5.13) for the centrality class of the ALICE data and use effectively

$$\langle T_{AA} \rangle_{0\% - 40\%} = 13 \text{ mb}^{-1}$$

to scale our nucleon-nucleon calculations to the full PbPb result (in the end this is just a normalization factor, whose exact errors will not affect the inverse slope parameter).

A comparison of the prompt photon yields as computed with the nPDFs mentioned in Sec. 5.2.2 for the ALICE setup at CM energy  $\sqrt{s} = 2.76$  TeV and rapidity range  $|y| < 0.75$  is shown in Fig. 5.7. The EPS09 nPDF parametrization can be seen to include the DSSZ and HKN07 parametrizations within its errors (which have been computed using (5.20) for the 30 EPS09 error sets). Only the nCTEQ parametrization lies below the lower error bound. For this reason we have taken EPS09 as our nPDF choice for the analysis, but noted that even the large EPS09 error seems to be too small.

The parametrizations of photon fragmentation functions have been discussed in Sec. 4 and we have chosen to use the BFG set II as the baseline for this publication and BFG set I as an estimator of the error implicit in the fragmentation function. To have an idea of the longitudinal momentum fraction  $z$  probed in the fragmentation process, we have modified JETPHOX to give for each generated fragmentation event the photon- $p_T$  and the  $z$ -value. By doing this we have found that mainly a  $z$ -range 0.01 – 0.1 is probed in the  $p_T$ -range of the ALICE data  $\sim 2 \text{ GeV} - 16 \text{ GeV}$ . Fig. 4.1 shows that, in this region, the gluon distribution is least constrained.<sup>8</sup> By activating only some subprocesses in

<sup>8</sup>At the time of the publication of [125] we did not have the GRV parametrization at hand, which can be seen to divert from the BFG parametrizations in the quark fragmentation for  $z \lesssim 0.3$ . However,

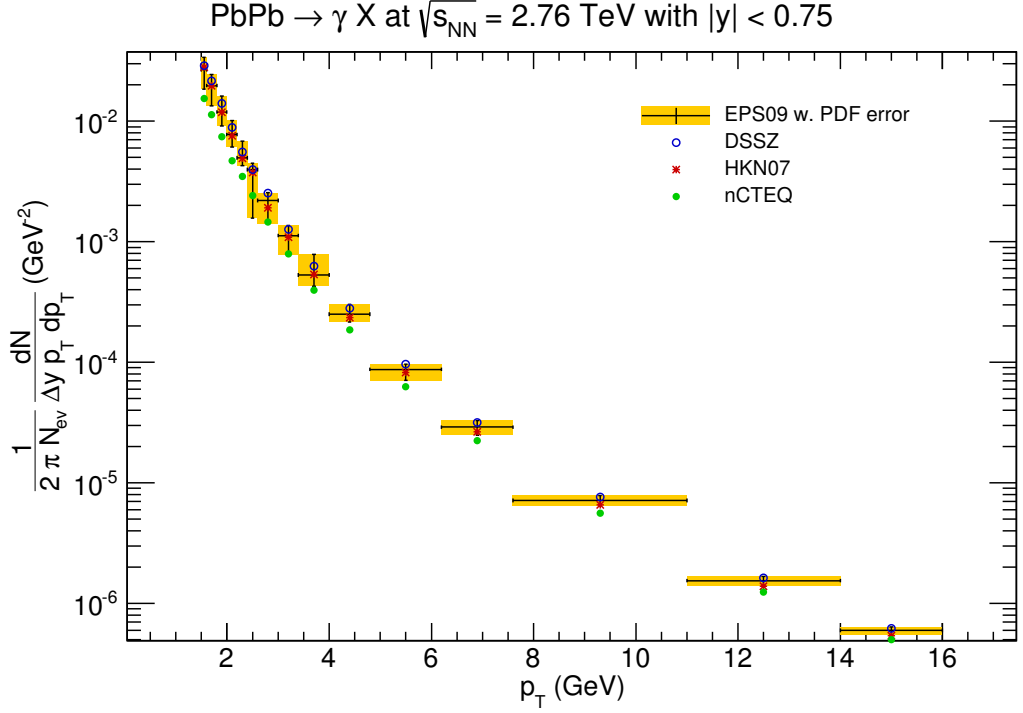


Figure 5.7: The invariant prompt photon yield in a  $p_T$ -range relevant to the ALICE thermal photon measurement, using the BFG set II fragmentation function. The nPDF errors have been computed with (5.20).

the JETPHOX calculation of the  $p_T$ -distribution, we have been able to break the invariant yield down into subprocess contributions, as depicted in Fig. 5.8. As noted earlier, the fragmentation contributions dominate in the low- $p_T$  region; here with the ALICE setup up to  $p_T \approx 12$  GeV. Furthermore, the process is clearly dominated by gluon initiated processes, indicating that there will be large errors due to the uncertainty of the gluon distribution in the nPDFs.

On the other hand, the assertion of a large impact of FF uncertainties is promoted further by examining the type of fragmentation processes, as depicted in Fig. 5.9. For  $p_T < 4$  GeV the leading fragmentation contribution comes from gluon-to-photon fragmentation, which, as noted above, is the least constrained. Clearly, it follows that the fragmentation uncertainties should not be ignored in the signal region extracted in [146].

Having motivated a closer look on the pQCD uncertainties by the conclusion that the least constraint processes dominate the thermal photon signal region, we have compared the data to the scaled JETPHOX calculation. Fig. 5.10 shows the invariant direct photon yield  $1/(2\pi N_{ev})dN/(\Delta y p_T dp_T)$  as measured by ALICE in comparison to our

---

below it is argued that the gluon distribution has the biggest impact on the error and the GRV gluon distribution lies between the BFG parametrizations. Thus, I expect that BFG sets I and II describe the FF error sufficiently.

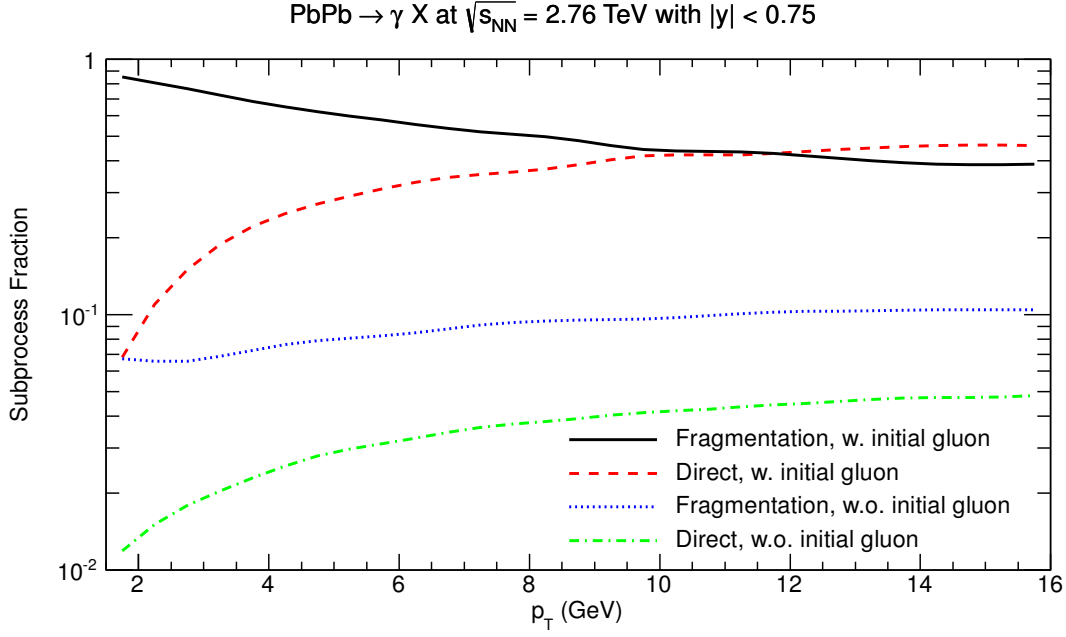


Figure 5.8: Comparison of the subprocess contributions to the invariant prompt photon yield for the ALICE setup mentioned in the text. The fragmentation and direct processes are subdivided into processes with and without an initial state gluon. As shown in [125].

equally binned calculation with EPS09 errors and scale uncertainties. The latter have been obtained by independently varying the renormalization, initial state factorization and fragmentation scales,  $\mu_R$ ,  $\mu_F$  and  $\mu_D$ , about  $p_T/2$ ,  $p_T$  and  $2p_T$ , as to give a rather generous, conservative estimate of the theoretical uncertainty. Of course, the definition of a scale error is in itself an arbitrary choice, though a variation about a factor of 2 is common practice to estimate the uncertainties involved in a truncation of the perturbation series. As explained in Sec. 3.5, the scales have been kept fixed if they were about to fall below  $\sqrt{2}$  GeV, which is why there is a drop in the scale uncertainty at  $p_T = 3$  GeV.

Taking only the nPDF errors in account, the data are, within their systematical and statistical errors, compatible with prompt photons down to  $p_T = 3.5$  GeV, with very good agreement only in the 8 GeV – 11 GeV bin. The scale error expands this range down to the drop in scale uncertainty, so that it is possible that the real scale error – if scales below  $\sqrt{2}$  GeV were allowed – extends up to the data points again. However, this point just shows, that the fixed order treatment and the scale error become questionable at such small  $p_T$  values.

The alternative calculation with BFG set I, shown in magenta, gives an estimate of the FF uncertainty, which can be up to a factor of three in the lowest bins. As expected, this large impact of the FF uncertainty is due to the dominance of the fragmentation contribution, in blue, over the direct contribution in green.

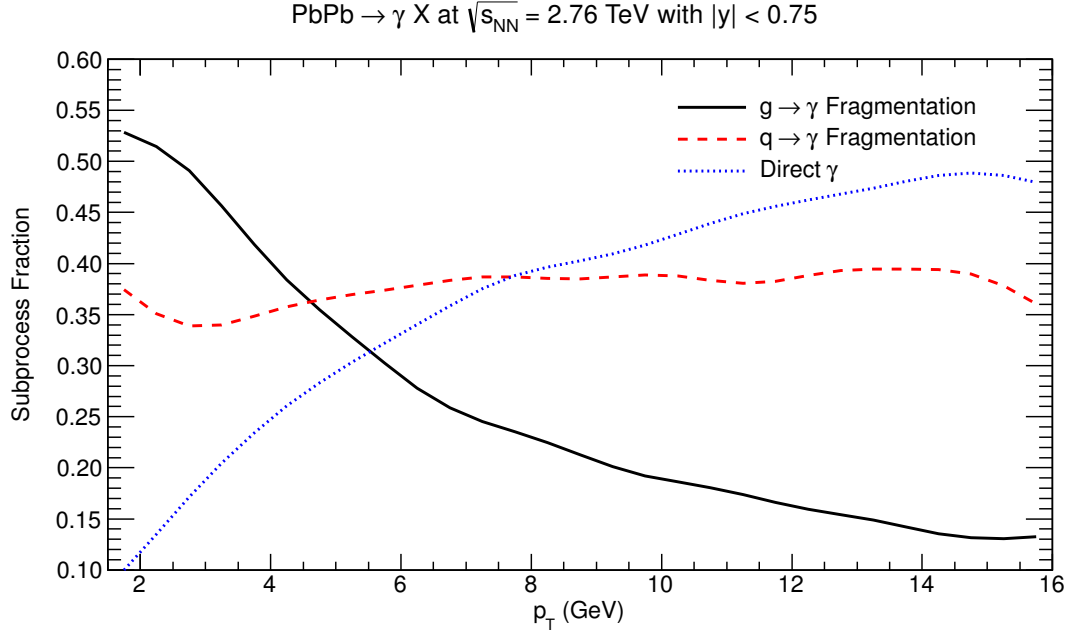


Figure 5.9: Relative contribution of the gluon-to-photon and quark-to-photon fragmentation and the direct processes. As shown in [125].

Fig. 5.10 furthermore includes a fit of  $A \exp(-p_T/T_{\text{eff}})$  to the experimentally measured direct photon spectrum for  $p_T < 2.2$  GeV, reproducing the ALICE result for the inverse slope parameter

$$T_{\text{eff}} = (304 \pm 58) \text{ MeV};$$

just with a slightly larger error, due to us simply adding the statistical and systematical errors in quadrature for the fit procedure. However, to get the inverse slope parameter of the thermal photon yield, we still had to subtract the prompt photon results.

Our calculations only reach down to bins with  $p_T > 1.5$  GeV, so that we had to exclude the data points at smaller  $p_T$  that have been used in the determination of the slope parameter before. In subtracting the theory predictions from the data, we have treated all errors, i.e. statistical and systematical uncertainties of the data and nPDF, scale uncertainties of our calculation, by adding them in quadrature. The result is shown in Fig. 5.11, depicting the data subtracted by the calculation with BFG set II in black and the subtraction with BFG set I in gray. For the latter no PDF and scale errors have been taken into account. In this way we have found a clear excess of direct photon data over the pQCD prompt photon prediction for  $p_T < 3.5$  GeV. Correspondingly, we have fitted the subtracted data with an exponential for the original range of  $p_T < 2.2$  GeV, like in [146], but also for the excess seen in Fig. 5.11, i.e. for  $p_T < 3.5$  GeV. Thus, we have found two inverse slope parameters for each range: For  $p_T < 2.2$  GeV the inverse slope parameter is  $(255 \pm 99)$  MeV if we use BFG set II and  $(263 \pm 96)$  MeV in case of BFG set I. For  $p_T < 3.5$  GeV we have found  $(309 \pm 64)$  MeV with BFG set II and  $(329 \pm 60)$  MeV

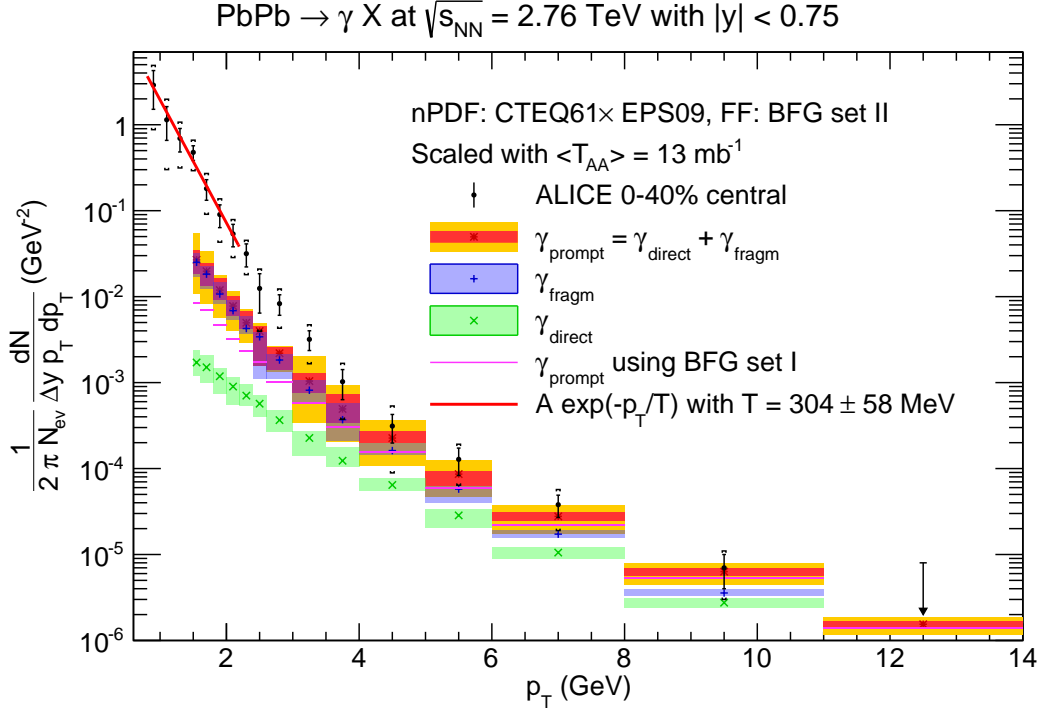


Figure 5.10: Comparison of ALICE direct photon data, with statistical (bars) and systematical uncertainties (horizontal brackets), and scaled JETPHOX predictions using BFG set II and EPS09 with nPDF (red) and scale uncertainties (yellow). Additionally the fragmentation and direct contributions with PDF errors are shown. A calculation with BFG set I is shown in magenta. As shown in [125].

in case of BFG set I. Not shown are further exponential fits to the whole range of data, giving an inverse slope parameter of  $(319 \pm 66)$  MeV, and to data subtracted by pQCD predictions where all scales have been varied simultaneously, resulting in an inverse slope parameter of  $(311 \pm 64)$  MeV. Due to the large uncertainties of the parameters, all results are compatible with the inverse slope parameter determined by ALICE. For the range  $p_T < 2.2$  GeV, the relative smallness of the parameters can be explained by the leverage of the data point in the 1.5 GeV – 1.6 GeV bin with its, in comparison to the other three points, small errors and which, as can be seen in Fig. 5.10, seems to have an unusually large value. In any case, looking at Fig. 5.11, there is no reason to restrict the fit range to  $p_T < 2.2$  GeV. On the contrary, following the discussion in Ref. [145] it is rather preferable to fit the yield at higher  $p_T$  values, so we have taken

$$T_{\text{eff}} = (309 \pm 64) \text{ MeV}$$

to be our main result for the inverse slope parameter.

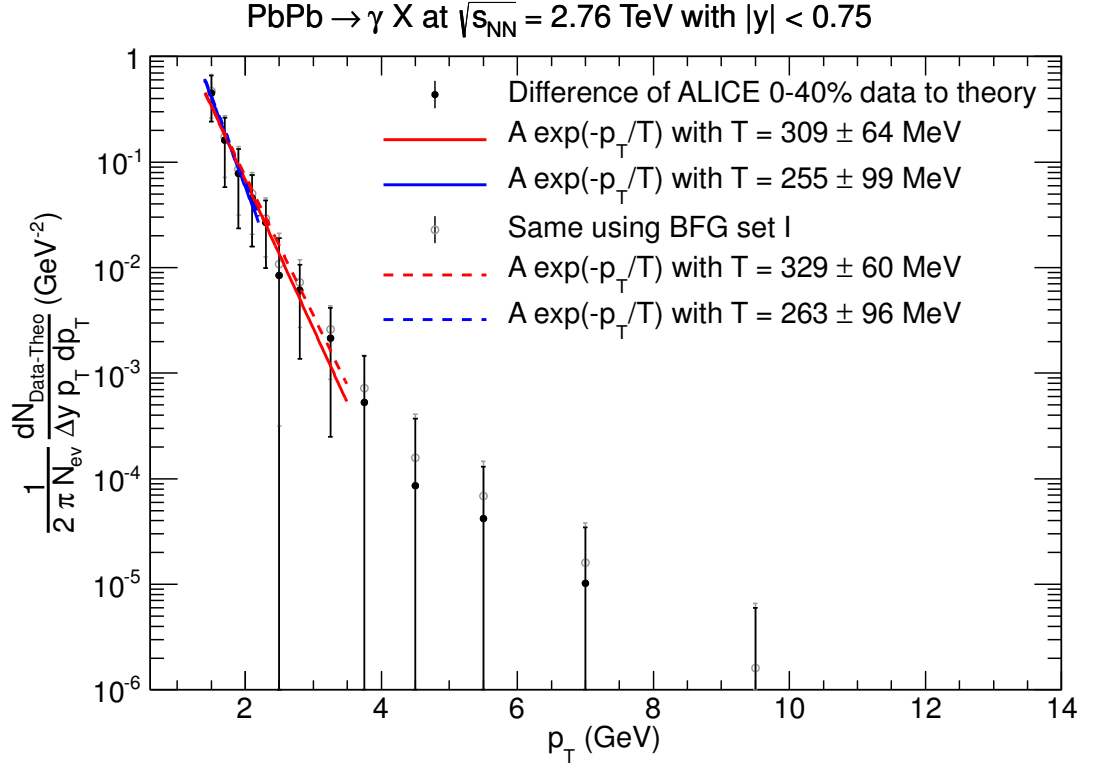


Figure 5.11: Subtracted direct photon, i.e. thermal photons yield. The subtraction of prompt photons computed with BFG set II is given by the full black circles, the gray open circles give the subtraction using BFG set I. As shown in [125].

Hence, we have found that the inclusion of the theoretical uncertainties leads to similar results as initially found by the ALICE collaboration. The reason for the relative stability of the results for the slope parameter w.r.t. each other, is the fact that the prompt photon yield makes up less than 20 % for  $p_T < 2.4$  GeV, as can be seen in Fig. 5.12. Since the fits are dominated by the points at low  $p_T$ , where the prompt photon yield is unimportant, the fit after employing the subtraction procedure does not contradict the fit to the unsubtracted data.

Since the publication of [125], the analysis of the ALICE thermal photon results has been finalized and published in [109]. The inverse slope parameter has been determined to be

$$T_{\text{ALICE}} = (297 \pm 12(\text{stat.}) \pm 41(\text{syst.})) \text{ MeV}$$

for the thermal photon yield in the 0 % – 20 % centrality class.

A similar analysis has been done before for PHENIX data, finding an inverse slope parameter [110]

$$T_{\text{RHIC}} = (221 \pm 19 \pm 19) \text{ MeV}.$$

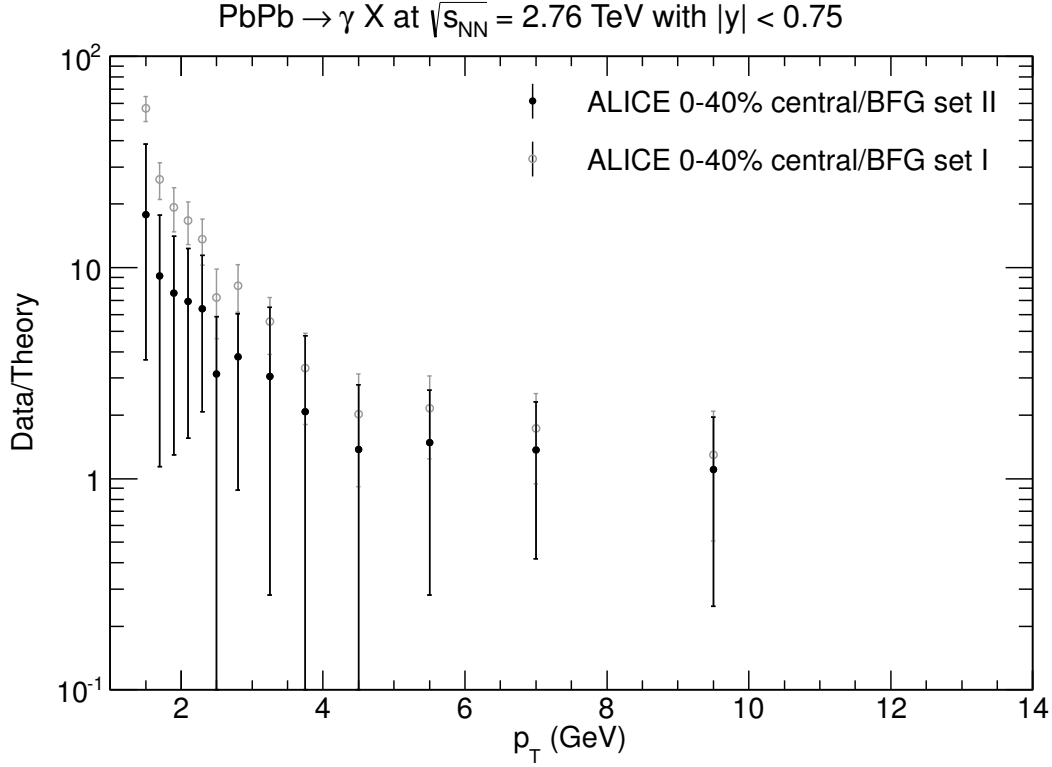


Figure 5.12: Ratio of experimental direct photon data to theoretical prompt photons prediction, again using full black circles for BFG set II, open gray circles for BFG set I and with all errors added in quadrature. As shown in [125].

These results add credibility to the claim that a QGP has been formed in heavy ion collisions at RHIC and LHC. As has been noted some sections before, there are several other observables – such as quenching of hard strongly interacting probes, multiplicity, elliptic flow – which, taken all together, point to the creation of the QGP [147].

However, besides the inverse slope parameter, another observable measured for photons is the elliptic flow of direct photons. Curiously, it has been found to be of a similar magnitude as the hadron elliptic flow [148, 149]. This constitutes the so-called photon puzzle: It has been expected that the photon elliptic flow would be smaller if the thermal photon yield were dominated by photons generated early in the evolution, i.e. in the QGP instead of the HRG (as the large inverse slope parameter suggests), where the flow should not have been build up yet [150]. Thus, even if the entirety of analyses point to the creation of the QGP, the interpretation of the thermal photon signal seems to be not yet completely consistent.

## 6 Parton Shower Matching

The results of the last chapters relied on fixed-order NLO calculations of the inclusive prompt photon cross section, where the focus was on photons of rather low transverse momentum. Even though there has been no glaring, unexpected inconsistency with the RHIC and LHC data at low  $p_T$ , this might in part be attributed to the relatively large errors in the measurement of the inclusive photon spectra in proton-proton collisions, as approximations to higher order corrections (NNLO) have been shown to be quite sizable – of the order of 10 % [121] – in this region. Nonetheless, the growing scale error in Fig. 5.10 could be interpreted as a call for higher order corrections, which should stabilize the scale dependence. Furthermore, it has already been mentioned that more exclusive measurements, such as isolated photons, which introduce new parameters, can lead to unphysical predictions for certain choices of these parameters, which can only be rectified by including higher order contributions [96]. These problems can be addressed by analytic resummation of the specific pathological terms.

Another approach is instead taken by general purpose event generators (GPEG), which essentially simulate the complete, fully exclusive event by adding to a hard partonic process at LO successive (soft and/or collinear) parton splittings – the parton shower – and by simulating the beam remnant interactions. At the end of this process the partons are combined into hadrons, using phenomenological hadronization models. The simulation of parton splitting processes amounts to a numerical resummation of the terms upon which the splitting probabilities are based, e.g. the logarithmically divergent collinear approximation; in many cases this improves the predictions (for example photon-jet correlations [151]). In addition, hadronization effects can lead to visible alterations and improvements for certain observables, too. As one ends up with an event comprised of hadrons, it is possible to then impose realistic selection criteria, such as isolation criteria or jet finding algorithms, and analyze the events in conjunction with detector-simulations. Prime examples of such GPEGs are PYTHIA [152, 153] and Herwig [154]; I will focus on the former.

As noted above, the parton shower adds radiation off partons to a hard partonic subprocess, and by that emulates a part of the higher order corrections. This leads to complications if one wants to base the whole procedure on hard partonic processes beyond the LO, since the real radiation contribution to the NLO process is also obtained by adding an additional parton to the LO subprocess: Adding a parton shower to an NLO process would double count the first radiation. For that reason, so-called matching<sup>1</sup>

---

<sup>1</sup>In the literature “matching” and “merging” are often used interchangeably. Here, I use the term “merging” only for procedures which deal only with tree-level corrections, while “matching” refers to the implementation of full higher order results.



schemes to bypass this problem have been defined, most notably MC@NLO [155] and POWHEG [45].

In GPEGs the prompt photon process entails usually only the direct LO contribution. This is due to the fact that the fragmentation function is an inclusive quantity, which only specifies if a particle fragments from a parton, but not what else happens: When a quark fragments into a photon something else has to carry the quark charges, but the FF gives no information on this, other than the momentum fraction  $1 - z$ . Thus one can not simply take the fragmentation contribution and apply a parton shower to it. But Ch. 3 has shown that the prompt photon production process profits tremendously from the inclusion of fragmentation contributions and corrections beyond LO. Especially, when it comes to the measurement of non-isolated low- $p_T$  photons, as in the last section, the LO direct result is simply not sufficient.

However, it turns out that the photon fragmentation contribution can be emulated by a QED shower [156], i.e. the simulation of photon radiation off partons. Furthermore, a NLO implementation in the POWHEG-framework for Herwig (for single and double prompt photon production) has already been presented in [157, 158], confirming the importance of NLO corrections to the parton shower. In this chapter an alternative implementation of single prompt photon production in the POWHEG BOX-framework, a GPEG-independent implementation of the POWHEG-method [46], is presented.

Sec. 6.1 discusses some of the parton shower/GPEG fundamentals, while Sec. 6.2 goes into some detail about the POWHEG method and the POWHEG BOX. Here, in the discussion of the general concepts I focus on final state radiation from a single emitter, to keep things simple. The implementation of prompt photon production is presented in Sec. 6.3, followed by a discussion of the results obtained with it.

## 6.1 Parton Showers

Parton showers are based on the IR divergence structure of partonic QCD amplitudes. It has already been exploited in Secs. 2.4.2 and 3.2, that, for kinematical configurations leading to singularities in only a subset of squared diagrams for a certain process, the complete squared amplitude for the process is obviously dominated by only this subset. If this subset of diagrams, in the region of interest, can be factorized into a squared amplitude of a process with less particles and some universal function, then the quantum mechanical probabilities for adding particles to a process have essentially become classical probabilities, as all interference effects are included in either the factorized parts or the subdominant diagrams. Consequently, one can again and again multiply with the squared amplitude for some  $n$ -particle process the universal, factorized function and construct by this a process with an arbitrary number of particles in the kinematical configuration that led to the divergences.

This is the case when some of the particles are soft or collinear. Squared diagrams in which these particles stem from the splitting off an external particle dominate, meaning that there is no interference of diagrams where these two particles have different origins (i.e. come from an internal propagator). In the collinear limit the splitting factorizes,

as in (2.33) and allows the radiation process to be described by a Born amplitude times a “classical” splitting probability, precisely because there is no interference of different splitting possibilities. Graphically, the repeated application of the splitting probability corresponds to a cut ladder diagram where the rungs do not cross. And as the collinear divergences are logarithmic, this procedure yields a leading log (LL) expression after regularizing the divergences. The soft limit, by comparison, is complicated by the fact that it involves colour-correlations, as in (2.50), but can be implemented by making use of something like the CS dipole formalism to construct splitting probabilities which reproduce the soft limit depending on two external particles of the hard process.

### 6.1.1 Branching probabilities

To be more specific about the statements just made, this section serves to give a heuristic derivation of branching probabilities, as motivated by the description in [159]. Focusing on final state radiation, the collinear splitting or branching probabilities can be derived from the factorization of final state collinear divergences (2.43).

To relate (2.43) to a branching probability, one first relates cross sections to probabilities.  $\sigma^{(n,r)}(Q^2)$  denotes the cross section for the production of  $n$  partons with a separation scale, e.g. relative  $k_T$ , of at least  $Q$  at  $r$ -th order in  $\alpha_s$ , where  $r \geq n$ . Since  $\sigma^{(n,r)}$  is only computed to order  $r$ , no statement can be made about the (non-)production of particles at higher orders and smaller scales; i.e.  $\sigma^{(n,r)}$  is a  $n$ -parton-inclusive cross section. The probability of producing  $n$  well-separated partons at  $r$ -th order is then given by

$$\mathcal{P}^{(n,r)}(Q^2) = \frac{\sigma^{(n,r)}(Q^2)}{\sum_{i=0}^r \sigma^{(i,r)}} = \frac{\sigma^{(n,r)}(Q^2)}{\sigma^{(\text{tot},r)}}. \quad (6.1)$$

If the perturbation series were convergent and one were able to compute  $\sigma^{(n,\infty)}(Q^2)$ , then  $\mathcal{P}^{(n,\infty)}(Q^2)$  would give an exclusive probability.

The LO probability for  $n$ -particle creation is  $\mathcal{P}^{(n,n)}(Q^2)$ . The goal is now to incorporate higher order corrections for scales below  $Q^2$ .  $\mathcal{P}^{(n,n)}(Q^2)$  stays constant when incorporating virtual and real higher order corrections for scales – i.e. loop momentum  $l$ , transverse momentum  $k_T$ , respectively – below  $Q^2$ , as long as the collinear and soft limits can be used, because then the virtual and real corrections cancel:

$$\begin{aligned} \sigma^{(n,n)}(Q^2) &\rightarrow \sigma^{(n,n)}(Q^2) + \sigma^{(n,n+1)}(Q^2, |l_{n+1}^2| < Q^2) + \sigma^{(n+1,n+1)}(Q^2, k_{Tn+1}^2 < Q^2) \\ &\approx \sigma^{(n,n)}(Q^2). \end{aligned}$$

To construct the probability for a  $n+1$ -th (or more) radiation to occur between the scales  $Q^2$  and  $Q^2 - \Delta Q^2$ , with  $\Delta Q^2$  small, one can then use the collinear limit (2.43). The approximate virtual corrections below  $Q^2 - \Delta Q^2$  are included by simply restricting the range of integration for  $k_T^2$  in (2.43) to  $[Q^2 - \Delta Q^2, Q^2]$ :

$$\sigma^{(n+1,n+1)}(Q^2, Q^2 - \Delta Q^2) \approx \sigma^{(n,n)}(Q^2) \frac{\alpha_s(Q^2)}{2\pi} \frac{\Delta Q^2}{Q^2} \int dz \hat{P}_{j[ij]}(z). \quad (6.2)$$

Boundaries for the  $z$ -integration are not given explicitly, but they can in principle be derived from momentum conservation for the Sudakov decomposition of a particle of virtuality  $< Q^2$  (cf. (D.7)). The renormalization scale has been set to  $Q$  as it is the defining hard scale of the process. Since the total cross section stays the same in this approximation, one has

$$\begin{aligned} \mathcal{P}^{(n(+1),n+1)}(Q^2, Q^2 - \Delta Q^2) / \mathcal{P}^{(n,n)}(Q^2) &\approx \frac{\alpha_s(Q^2)}{2\pi} \frac{\Delta Q^2}{Q^2} \int dz \hat{P}_{j[ij]}(z) \\ &\equiv \Delta \mathcal{P}_{\text{br}}(Q^2). \end{aligned} \quad (6.3)$$

This is the differential probability  $\Delta \mathcal{P}_{\text{br}}(Q^2)$  for a branching off an external leg in a tree-level result to occur just below the hard scale  $Q^2$  of the process, i.e. in a small range  $[Q^2 - \Delta Q^2, Q^2]$ .

With this it is possible to derive the all-orders probability to have no branching in a finite range of scales  $[q^2, Q^2]$ , called Sudakov factor  $\Delta(Q^2, q^2)$ . By considering the following, a differential equation for  $\Delta(Q^2, q^2)$  can be found: When slightly increasing the lower scale  $q^2$  to  $q^2 + \Delta q^2$ , the new no-branching probability  $\Delta(Q^2, q^2 + \Delta q^2)$  has to allow for anything to happen below  $q^2 + \Delta q^2$ . Thus, the no-branching probability at the new scale  $q^2 + \Delta q^2$  is given by a sum of the probability of no branching down to  $q^2$  and the combined probabilities of no branching down to  $q^2 + \Delta q^2$  and at least one branching afterwards:

$$\begin{aligned} \Delta(Q^2, q^2 + \Delta q^2) &= \Delta(Q^2, q^2) + \Delta(Q^2, q^2 + \Delta q^2) \Delta \mathcal{P}_{\text{br}}(q^2) \\ \rightarrow \frac{d\Delta(Q^2, q^2)}{dq^2} &= \Delta(Q^2, q^2) \frac{\alpha_s(q^2)}{2\pi} \frac{1}{q^2} \int dz \hat{P}_{j[ij]}(z) \quad \text{for } \Delta q^2 \rightarrow 0. \end{aligned} \quad (6.4)$$

The solution to this ODE is

$$\Delta(Q^2, q^2) = \exp \left( - \int_{q^2}^{Q^2} \frac{dk_{\text{T}}^2}{k_{\text{T}}^2} \int dz \frac{\alpha_s(k_{\text{T}}^2)}{2\pi} \hat{P}_{j[ij]}(z) \right), \quad (6.5)$$

with

$$\begin{aligned} \Delta(Q^2, Q^2) &= 1, \\ \Delta(Q^2, 0) &= 0. \end{aligned} \quad (6.6)$$

The first equality is a boundary condition to (6.4) and holds, since no radiation occurs if there is no phase space for it; the last equality holds because of the logarithmic divergence in the exponent of the solution. The latter will, however, practically never be used as the Sudakov factor and the considerations of this section make sense only in the perturbative region  $Q^2, q^2 > \Lambda_{\text{QCD}}^2$ . As an all-orders no-branching probability, the Sudakov factor resums the virtual corrections to a tree-level result between the scales  $Q^2$  and  $q^2$ , assuming the virtual corrections can be written as the negative real corrections.<sup>2</sup>

<sup>2</sup>Indeed, (6.5) can be derived by explicitly summing the virtual corrections between  $Q^2$  and  $q^2$  in the collinear limit [160].

Up to now the discussion was focused on final state radiation. Initial state radiation is somewhat more complicated, as one has to take the PDF evolution into account. One way to do this is by interpreting the DGLAP-equation as an equation for a branching probability. As long as the PDFs are positive definite – which is the case for LO PDFs (if positive definite at a starting scale  $Q_0$  they stay positive in LO evolution (2.42) due to positive definite splitting kernels) – they can be interpreted as parton densities. Accordingly, the DGLAP equation (2.42) can be interpreted as defining a branching probability, if the change in density is measured by the branching probability  $df_{j/A}(x, q) = f_{j/A}(x, q)d\mathcal{P}_{\text{br}}^{\text{IS}}(x, q^2)$  [161]

$$d\mathcal{P}_{\text{br}}^{\text{IS}}(x, q^2) = \frac{dq^2}{q^2} \frac{\alpha_s(q^2)}{2\pi} \int \frac{dz}{z} \frac{f_{a/A}(\frac{x}{z}, q)}{f_{j/A}(x, q)} P_{ja}(z). \quad (6.7)$$

From this, one can construct the no-branching probability analogously to the final state evolution, giving a version of (6.5) with  $d\mathcal{P}_{\text{br}}^{\text{IS}}(x, k_T^2)$  in the exponent. When starting the evolution at the hard scale  $Q^2$  of the LO process, the initial state Sudakov factor can be understood as the probability that an initial state parton did not originate from a branching between some scales  $Q^2$  and  $q^2$ .

Eq. (6.4), or the corresponding equation for the initial state, is not only the defining equation for the Sudakov factor, but also gives the probability for a branching to occur at  $q^2$  without branching between  $Q^2$  and  $q^2$ . A Monte Carlo parton shower generator uses this to compute scales  $q^2 < Q^2$  at which a branching occurs by generating a uniformly distributed random number  $r \in (0, 1)$  and solving

$$\Delta(Q^2, q^2) = r \quad (6.8)$$

for  $q^2$ . This is guaranteed to generate  $q$  following the distribution  $d\Delta(Q^2, q^2)/dq^2$  [162]. The event generator starts with a hard (LO) event at scale  $Q^2$ , generates a branching scale  $q^{(i)2}$  for each external leg  $i$ , then changes the particle content of the event by replacing the leg with the hardest branching scale  $q_0^2 = \max\{q^{(1)2}, \dots, q^{(n)2}\}$  by the two branched particles, and starts the process again for all external legs with a starting scale  $q_0^2$ , stopping only at some scale of order  $q_N^2 \approx \Lambda_{\text{QCD}}^2$ .<sup>3</sup> To ensure conservation of the four-momenta of all external particles, each radiation step has to be accompanied by a reshuffling of their momenta; for instance, one could use the kinematic mappings defined for CS dipoles, cf. Sec. 2.5.1, where the replacement of the (on-shell) pre-branching parton by two (on-shell) partons is compensated by a change of the momentum of a recoil parton, while keeping the remaining parton momenta fixed, or, for initial state branching, by boosting all other momenta (the implementation of a similar dipole-kinematics approach in PYTHIA is described in [161]). The whole algorithm constitutes an evolution of the event from a hard scale  $Q^2$  to the non-perturbative region, at which hadronization models construct hadrons from the final state parton configuration.

---

<sup>3</sup>A solution of (6.8) determines of course only a scale. To construct for each branching product the full four-momentum, the branching probability actually has to be understood as being differential in relative transverse momentum  $k_T$ , longitudinal momentum fraction  $z$  and azimuthal angle  $\phi$ .

In principle, a parton shower does not change the normalization of a process, i.e. approximating a two jet-cross section by a  $2 \rightarrow 2$  tree-level cross section will lead to the same total dijet cross section as the  $2 \rightarrow 2$  plus parton shower result. One can take gluon radiation off one quark leg as a simplified example to illustrate this: Each generated radiation results effectively in a multiplication of the cross section by the radiation probability, i.e. a factor  $d\Delta(Q^2, q^2)/dq^2$ . In a large enough sample, there will be cases where no radiation is generated between  $q_0^2 = Q^2$  and  $\Lambda_{\text{QCD}}$ , or only one radiation is generated at some scale  $q_1^2 < q_0^2$ , others with two radiations at some  $q_1^2$  and  $q_2^2$ , and so on, giving a factor

$$\begin{aligned}
& \Delta(Q^2, \Lambda_{\text{QCD}}^2) + \int_{\Lambda_{\text{QCD}}^2}^{Q^2} dq_1^2 \frac{d\Delta(Q^2, q_1^2)}{dq_1^2} \Delta(q_1^2, \Lambda_{\text{QCD}}^2) \\
& + \int_{\Lambda_{\text{QCD}}^2}^{Q^2} dq_1^2 \int_{\Lambda_{\text{QCD}}^2}^{q_1^2} dq_2^2 \frac{d\Delta(Q^2, q_1^2)}{dq_1^2} \frac{d\Delta(Q^2, q_2^2)}{dq_2^2} \Delta(q_2^2, \Lambda_{\text{QCD}}^2) + \dots \\
& = \sum_{i=0}^{\infty} \left( \prod_{j=0}^{i-1} \int_{\Lambda_{\text{QCD}}^2}^{q_j^2} dq_{j+1}^2 \frac{d\Delta(q_j^2, q_{j+1}^2)}{dq_{j+1}^2} \right) \Delta(q_i^2, \Lambda_{\text{QCD}}^2) \\
& = \Delta(Q^2, \Lambda_{\text{QCD}}^2) \sum_{i=0}^{\infty} \prod_{j=0}^{i-1} \int_{\Lambda_{\text{QCD}}^2}^{q_j^2} dq_{j+1}^2 \frac{d\mathcal{P}_{\text{br}}(q_{j+1}^2)}{dq_{j+1}^2} \\
& = \Delta(Q^2, \Lambda_{\text{QCD}}^2) \sum_{i=0}^{\infty} \frac{1}{i!} \left( \int_{\Lambda_{\text{QCD}}^2}^{Q^2} dq^2 \frac{d\mathcal{P}_{\text{br}}(q^2)}{dq^2} \right)^i \\
& = 1.
\end{aligned}$$

So in the end the inclusive cross section is multiplied with unity and unchanged. This is the unitarity of the parton shower, which, again, follows from the fact that in the approximation in use the virtual and real corrections cancel exactly.

Even if the normalization does not change, differential cross sections may greatly benefit from parton shower corrections. For example, dijets are in the LO approximation strictly separated by an azimuthal angle of  $\pi$ , i.e. the azimuthal correlation of the two jets is peaked at  $\phi = \pi$ . A parton shower will flesh out the two parton event with more partons, thus generating a realistic jet-shape, and, through momentum reshuffling, change the direction of the jets. An initial state splitting, for instance, could give the hard process a transverse momentum and, with this boost, narrow the azimuthal angle between the two jets and thus smear out the LO peak. For the purpose of this chapter, it is important to understand, that by a QCD shower also the kinematics of particles which are not allowed to participate in the actual QCD branching processes, e.g. electroweak particles, can be changed due to this momentum reshuffling.

### 6.1.2 Evolution variables

As noted in the last section, the parton shower is based on certain approximations to the real and virtual corrections. The one used in the last section was the collinear approxi-

mation, but one could use soft approximations or more complicated approximations like CS dipoles, which include both soft and collinear limits to the real and virtual contributions, to construct the branching probabilities. Naturally, different approximations improve different kinds of observables.

The collinear evolution algorithm sketched in the last section was strongly ordered in the successively generated  $k_T$ -scales of the collinear approximation:  $Q^2 > q_1^2 > \dots > q_N^2$ . This ordering can be seen a result of the fact that the hard event is actually made up of on-shell partons, but to allow those to split into two on-shell partons they have to be considered off-shell – which is a good approximation only for virtualities well-below the relative  $q^2 = k_T^2$  of the partons before splitting.

On the other hand it is possible to show that a parton shower based on the soft approximation (2.50) leads to an angular ordering. When disentangling the divergences in (2.50) due to  $p_i \cdot k$  and  $p_j \cdot k$  and looking at the part which contains the  $p_i \cdot k$  divergence, an azimuthal integration around the direction of  $p_i$ , for instance, leads to a zero result if the polar angle between the soft particle and the emitter  $p_i$  is greater than the opening angle between  $p_i$  and  $p_j$  [6]. That means that a parton shower generates only soft radiation off particle  $i$  in a cone around  $p_i$  with an opening angle smaller than the angle between  $p_i$  and  $p_j$ . Correspondingly, the next radiation would occur in a cone of an angle smaller than the angle between the new particles, and so on. A way to incorporate this coherence effect into the collinear branching of the last section is to simply replace the evolution variable  $k_T$  in (6.5) by the angle  $\theta \sim k_T$ . The result is then based on the collinear approximation, but uses angular ordering and thus reproduces the coherent branching effects of the soft limit. Similarly, one could also use the  $k_T$  evolution but at the same time check for every generated branching if it also respects angular ordering and otherwise discard the branching.

Another example for an evolution variable would be the virtuality, instead of relative transverse momentum or angle.

In the strict collinear limit all these choices are equivalent, but they have different effects in a parton shower generator, since it uses the collinear approximation not only for strictly collinear radiation [159]. In general, it depends on the GPEG which evolution variable is used; PYTHIA uses a type of  $k_T$ -ordered evolution [161, 153].

### 6.1.3 Large- $N_c$ limit

The soft limit for QCD radiation is strongly dependent on the colour structure of an event as indicated by the colour-correlations in (2.50). Furthermore, knowing the colour assignment of a process is crucial for GPEGs to hadronize the final state.<sup>4</sup> One way to unambiguously assign colours to partons is to combine the perturbative expansion in the strong coupling  $\alpha_s$  with an expansion in the inverse number of colours  $1/N_c$  and take the limit  $N_c \rightarrow \infty$  while  $\alpha_s N_c$  is held fixed – the so-called large- $N_c$  limit [164]. In the large- $N_c$  limit, gluons, which for  $N_c = 3$  carry the irreducible colour-octet representation **8**,

<sup>4</sup>For example, the colour lines stretching from colour to colour to anticolour can be interpreted as strings related to the string tension model of QCD confinement [8] and used for a phenomenological description of hadronization [163, 159].

can be replaced by a colour-anticolour-pair  $\mathbf{3} \otimes \bar{\mathbf{3}}$ , since the singlet state is negligible for large  $N_c$ . In graphical notation this means that a Feynman diagram can be replaced by a colour-flow diagram by interpreting the fermion lines as colour-flow lines and replacing gluon lines by two colour flow lines with opposite directions connected to the other colour lines of the diagram, e.g. Fig. 6.1.

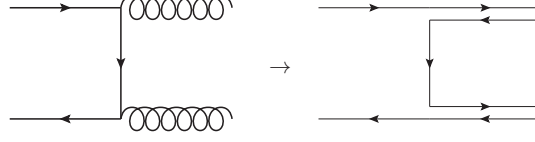


Figure 6.1: Example of colour flow for  $q\bar{q} \rightarrow gg$ .

A way to assign a definite colour-flow is then to find the different possible colour configurations of a process and chose a configuration with a probability proportional to the squared amplitude of each configuration, as described in [152, 165]. In the process  $q\bar{q} \rightarrow gg$ , for example, the colour structures found in the Feynman diagrams (before squaring) are either  $T_{ik}^a T_{kj}^b$  or  $T_{kj}^a T_{ik}^b$ , where the former corresponds to the  $t$ -channel colour flow depicted in Fig. 6.1, with  $i, k, j$  denoting the colours of the upper, internal and lower quark line, respectively, and the latter is an  $u$ -channel colour flow, where the initial quark lines are crossed. The squared coefficients of these colour structures give the probability with which a colour flow is to be chosen. For example, the coefficients of  $T_{ik}^a T_{kj}^b$  and  $T_{kj}^a T_{ik}^b$  are, after squaring, proportional to  $u/t - 2u^2/s^2$  and  $t/u - 2t^2/s^2$ , respectively, and the  $t$ -channel colour-flow is then chosen with a probability  $u^2/(t^2 + u^2)$  (this and more results for the  $2 \rightarrow 2$  processes relevant for this thesis can be found in [163]). By choosing one of the two colour structures with these probabilities, one disregards interference terms between different colour structures, which are included in the usual computation of squared Feynman diagrams (this can be seen by summing the kinematic terms quoted for the  $t$ - and  $u$ -channel and noting that the sum is not proportional to the squared amplitude of the process which is  $\propto (t^2 + u^2)/s^2 - 4/9(t/u + u/t)$ ). These colour interference terms would not allow for an unambiguous assignment of colours to external particles. However, they are of higher order in  $1/N_c$  and thus eliminated in the large- $N_c$  limit. Graphically, the higher orders in  $1/N_c$  can be interpreted as non-planar colour diagrams, in the sense that the colour lines of these interference diagrams can not be drawn on a two dimensional surface without intersections. For that reason leading terms in the large- $N_c$  limit are said to correspond to planar colour flows.

Now, if the shower Monte Carlo generates a hard event, then the planar colour flow leads to an unequivocal assignment of colours to the external legs. Additionally, the colour assignment in a branching is always planar as only three coloured particles are involved and different colour-assignments can not interfere. For instance, a final state quark line simply splits into a quark of another colour and a gluon carrying the colour of the parent quark and the anti-colour of the son. Thus, the colour flow of the whole event is unambiguous in the large- $N_c$  limit and colour-based models are readily employed.

## 6.2 NLO Matching

As described in the last sections, GPEGs are normally based on a LO approximation for the hard process, which is then dressed by a parton shower, and thus the normalization of the cross sections can be far off from higher order results. A way to compensate for this is the introduction of a  $K$ -factor and to simply scale the parton shower results with this factor. Another problem is the fact, that parton showers use approximations for a large range of scales, which would better be represented by full higher order calculations. If, for instance, the first radiation is generated at a large scale, only just below the scale of the hard process, it would be better to generate this radiation using the tree-level amplitude with one additional parton, instead of using the collinear approximation. This problem is solved by smoothly merging tree-level results with different numbers of partons and the parton shower. Another way to address both problems is to shower full NLO (or beyond) results, as this would improve the normalization of the total cross section and the distribution of the first radiation. Descriptions of this approach – matching – can be found in most up-to-date introductions to GPEGs, e.g. in [159, 166, 160].

### 6.2.1 MC@NLO

It has already been mentioned, that NLO accuracy can not simply be reached by using NLO instead of LO amplitudes for the hard process, as real and virtual corrections would partially be doubly counted. Since a NLO amplitude consists of a  $n$ - and  $n + 1$ -particle contribution, an event generator has to decide if a  $n$ - or  $n + 1$ -particle hard event is to be generated first. This can be done by choosing the hard event with a probability proportional to the respective contributions – after they have been subtracted to make them separately finite. Thus, using the notation introduced in Sec. 2.5, one could generate a  $n$ -event with a probability proportional to

$$\mathcal{B}(\Phi^{(n)}) + \mathcal{V}(\Phi^{(n)}) + \mathcal{I}(\Phi^{(n)})$$

and a  $n + 1$ -particle event according to

$$\mathcal{R}(\Phi^{(n+1)}) - \mathcal{D}(\Phi^{(n+1)}).$$

If a  $n$ -event is chosen, then the first radiation generated by the parton shower produces an event which could have also been generated by the  $n + 1$ -contribution. To calculate the error that is introduced by this double counting, one can expand the weight of the  $n$ -particle event with up to one parton shower generated radiation to NLO in the coupling:

$$\begin{aligned} & \left( \mathcal{B}(\Phi^{(n)}) + \mathcal{V}(\Phi^{(n)}) + \mathcal{I}(\Phi^{(n)}) \right) \Delta(Q^2(\Phi^{(n)}), \Lambda_{\text{QCD}}^2) \\ & + \left( \mathcal{B}(\bar{\Phi}^{(n)}) + \mathcal{V}(\bar{\Phi}^{(n)}) + \mathcal{I}(\bar{\Phi}^{(n)}) \right) \frac{d\Delta(Q^2(\Phi^{(n)}), q^2)}{dq^2} \\ & = \mathcal{B}(\Phi^{(n)}) \left( 1 - \int_{\Lambda_{\text{QCD}}^2}^{Q^2(\Phi^{(n)})} dq^2 \frac{d\mathcal{P}_{\text{br}}(q^2)}{dq^2} \right) \end{aligned} \quad (6.9)$$



$$+ \mathcal{B}(\bar{\Phi}^{(n)}) \frac{d\mathcal{P}_{\text{br}}(q^2)}{dq^2} \theta(q^2 - \Lambda_{\text{QCD}}^2) + \mathcal{V}(\Phi^{(n)}) + \mathcal{I}(\Phi^{(n)}) + \text{h.o.},$$

where the first line corresponds to an event with no parton shower generated radiation and the second line has one radiation at some scale  $q$ . The bars over the phase space variables indicate a momentum reshuffling to allow one of the  $n$  partons to branch at a scale  $q^2$ , and  $Q^2(\Phi^{(n)})$  indicates that the initial hard scale depends on the initial  $n$ -particle configuration. Problematic are the terms with  $d\mathcal{P}_{\text{br}}(q^2)/dq^2$  which spoil the NLO accuracy of the shower result:  $\mathcal{B}(\bar{\Phi}^{(n)})d\mathcal{P}_{\text{br}}(q^2)/dq^2$  competes with  $\mathcal{R} - \mathcal{D}$  for configurations

$$\Phi^{(n+1)} = \{\bar{\Phi}^{(n)}, \Phi_{\text{rad}}(q^2)\},$$

where the  $n+1$ -particle kinematics have been rewritten in terms of  $\bar{\Phi}^{(n)}$  and additional radiation variables depending the scale of the radiation  $q^2$ . For instance, the  $k_{\text{T}}$ -ordered shower described earlier, requires that  $\Phi_{\text{rad}}(q^2)$  selects configurations of  $\Phi^{(n+1)}$  where  $p_{n+1}$  is such that  $k_{\text{T},n+1}^2 = q^2$ .

A way to correct for this double counting error, is to subtract the problematic terms from the  $n$ - and  $n+1$ -contributions before selecting the hard event, so that  $n$ -events are generated according to

$$\mathcal{B}(\Phi^{(n)}) \left( 1 + \int_{\Lambda_{\text{QCD}}^2}^{Q^2(\Phi^{(n)})} dq^2 \frac{d\mathcal{P}_{\text{br}}(q^2)}{dq^2} \right) + \mathcal{V}(\Phi^{(n)}) + \mathcal{I}(\Phi^{(n)}) \quad (6.10)$$

and  $n+1$ -events according to

$$\mathcal{R}(\{\bar{\Phi}^{(n)}, \Phi_{\text{rad}}(q^2)\}) - \mathcal{D}(\{\bar{\Phi}^{(n)}, \Phi_{\text{rad}}(q^2)\}) - \mathcal{B}(\bar{\Phi}^{(n)}) \frac{d\mathcal{P}_{\text{br}}(q^2)}{dq^2} \theta(q^2 - \Lambda_{\text{QCD}}^2). \quad (6.11)$$

Reproducing (6.9) with (6.10) in place of  $\mathcal{B} + \mathcal{V} + \mathcal{I}$ , integrating over  $\Phi^{(n)}$  and adding (6.11) integrated over  $\Phi^{(n+1)}$  gives now the NLO result up to higher order terms, i.e. the first radiation has NLO accuracy.

The scale  $q^2$  is still restricted to values greater  $\Lambda_{\text{QCD}}$ , as the parton shower only generates events above that scale. However, one could ignore the restriction for (6.10) and (6.11), if one were to carefully shift the divergences such that both contributions are finite. For instance, if  $\mathcal{B}(\bar{\Phi}^{(n)})d\mathcal{P}_{\text{br}}(q^2)/dq^2$  reproduces all the divergences of  $\mathcal{R}$  for  $q^2 \rightarrow 0$ , then  $\mathcal{D}$  and correspondingly  $\mathcal{I}$  are not needed anymore and can be set to zero. Alternatively,  $-\mathcal{D}$  can be integrated over  $\Phi_{\text{rad}}(q)$  and shifted into (6.10), if one wants to use the known analytic form of  $\mathcal{I}$  to cancel the divergences of  $\mathcal{V}$ . This is, in a nutshell, the approach of MC@NLO [155].

A problem of this ansatz is that (6.10) and (6.11) could be negative<sup>5</sup>, which makes a probability interpretation impossible. This can be rectified by generating events with probabilities proportional to the absolute values of the two contributions and attach a negative weight to the events which would have had a negative probability. As long

<sup>5</sup>Indeed, the results of Sec. 3.4 show that the CS dipole subtracted real contribution is frequently negative.

as one is not interested in single events, but only in large samples of events, e.g. when computing some distribution, this poses no problem as the sum of both contributions is always positive (except when the NLO calculation fails). However, the `MC@NLO` method also has to be adapted for each GPEG anew, since most use different definitions of the branching probabilities  $d\mathcal{P}_{\text{br}}(q^2)/dq^2$  and evolution variables; as such (6.10) and (6.11) have to be recomputed for each GPEG.

### 6.2.2 POWHEG method

The problems with the modified subtraction procedure employed by `MC@NLO` are to some extent solved by the `POWHEG` method, which has been formulated in [167, 45]. Here, the main idea is not to first choose a  $n$ - or  $n+1$ -particle contribution, but start out with a  $n$ -particle contribution and generate the first emission by using a modified Sudakov factor, such that NLO accuracy is achieved. The parton shower is then allowed to generate radiation only below the scale to which `POWHEG` has evolved the first radiation, i.e. `POWHEG` always generates the hardest emission with NLO accuracy. Additionally, as long as the NLO cross section is positive, i.e. as long as the perturbative expansion works, the event is generated with a positive probability or rather has a positive weight. Accordingly, `POWHEG` stands for “positive weight hardest emission generator”.

As mentioned earlier, subtraction methods and the momentum reshuffling of parton showers in general imply a bijection of the  $n+1$ -particle phase space onto the  $n$ -particle phase space and some variables defining the radiation,

$$\Phi^{(n+1)} \leftrightarrow \{\bar{\Phi}^{(n)}, \Phi_{\text{rad}}\}.$$

Using such a map, one defines the weight of the  $n$ -particle contribution by

$$\begin{aligned} \bar{B}(\Phi^{(n)}) &= \mathcal{B}(\Phi^{(n)}) + \mathcal{V}(\Phi^{(n)}) + \mathcal{I}(\Phi^{(n)}) \\ &+ \left[ \int d\Phi_{\text{rad}} \left( \mathcal{R}(\Phi^{(n+1)}) - \mathcal{D}(\Phi^{(n+1)}) \right) \right]^{\bar{\Phi}^{(n)} = \Phi^{(n)}}, \end{aligned} \quad (6.12)$$

where the superscript on the square bracket indicates that the radiation variables are integrated out such that the momenta of the underlying (pre-splitting)  $n$  particles correspond to those specified by the configuration  $\Phi^{(n)}$  on the left hand side. Eq. (6.12) defines the probability with which an  $n$ -particle event (for which all radiation has been integrated out) is generated. Putting this into (6.9) instead of  $\mathcal{B} + \mathcal{V} - \mathcal{I}$  gives a hint that the `POWHEG` branching probability (corresponding to  $d\mathcal{P}_{\text{br}}(q^2)/dq^2$ ) has to be of the form  $\mathcal{R}/\mathcal{B}$ , which naturally reproduces the soft and collinear limiting expressions, to recreate the NLO cross section with the first parton shower generated radiation. In fact, the `POWHEG`-Sudakov factor is defined by

$$\Delta(\Phi^{(n)}, p_{\text{T}}) = \exp \left\{ - \int \frac{[d\Phi_{\text{rad}} \mathcal{R}(\Phi^{(n+1)}) \theta(k_{\text{T}}(\Phi^{(n+1)}) - p_{\text{T}})]^{\bar{\Phi}^{(n)} = \Phi^{(n)}}}{\mathcal{B}(\Phi^{(n)})} \right\} \quad (6.13)$$

and hence the differential **POWHEG** cross section, including  $n$ - and  $n + 1$ -particle contributions, is

$$\begin{aligned} d\sigma = \bar{B}(\Phi^{(n)})d\Phi^{(n)} & \left\{ \Delta(\Phi^{(n)}, p_T^{\min}) \right. \\ & \left. + \Delta(\Phi^{(n)}, k_T(\Phi^{(n+1)})) \frac{\mathcal{R}(\Phi^{(n+1)})}{\mathcal{B}(\Phi^{(n)})} \theta(k_T(\Phi^{(n+1)}) - p_T^{\min}) d\Phi_{\text{rad}} \right\} \bar{\Phi}^{(n)=\Phi^{(n)}} \quad (6.14) \end{aligned}$$

An expansion in the coupling to NLO shows that this gives the first radiation to NLO accuracy. Here, the rather general scale  $q$  from the last sections has again been replaced by  $k_T$  as **POWHEG** is explicitly based on a transverse momentum ordering. However, this means the **POWHEG** method is in fact not applicable to every parton shower generator; rather, the **GPEG** which further showers the event generated by the **POWHEG**-method has to have the ability to ensure that no radiation with a transverse momentum above  $k_T$  is generated. To do that, especially angular ordered parton showers have to employ a vetoing algorithm which allows to use angular ordering but forbids radiation above  $k_T$ .

### 6.2.3 POWHEG BOX

In the last section, the description focused on the general idea of the **POWHEG** method; a concrete implementation of the procedure is given by the **POWHEG BOX** [46].<sup>6</sup> The **POWHEG BOX** is a **FORTRAN**-code which can be run as a standalone program producing **POWHEG** events, corresponding to (6.14), which can then be further showered and evaluated in a **GPEG** of choice.

To be more concrete than in the last section, it has to be noted that in general there are several partonic subprocesses  $\mathcal{B}$  and several possibilities of adding radiation to a  $n$ -particle event, depending on the particle content of that event. Following the notation of Ref. [46] a  $n$ -particle event is hence assigned a Born flavour structure  $f_b$ , denoting the ordered set of external particles. Correspondingly, the **POWHEG** cross section (6.14) is in practice a sum over all flavour structures  $f_b$  which make up a process. For instance, in case of dijet production, a sum over  $f_b$  is a sum over all possible  $2 \rightarrow 2$  QCD processes. Real contributions, i.e.  $n + 1$ -particle processes, on the other hand, have flavour structures with one additional parton. For the **POWHEG** method only those real flavour structures are of interest, which can be reduced to a Born flavour structure  $f_b$  by replacing a final state parton and another parton by a parent parton, simply because these real flavour structures define a real radiation process.<sup>7</sup> They can be decomposed into singular regions, like the decomposition (2.68),

$$\mathcal{R} = \sum_{\alpha_r} \mathcal{R}^{\alpha_r}, \quad (6.15)$$

<sup>6</sup>Other implementations of the method are to be found for example in **Herwig**'s matchbox classes [154].

<sup>7</sup>Flavour structures which can not be reduced to some  $f_b$  are called regular flavour structures, since they in turn can not entail singular regions (which by the KLN theorem would have to be cancelled by a virtual corrections with a Born flavour structure). Regular contributions pose no problem in NLO matching since they can not be double-counted and will not be considered further.

where an index  $\alpha_r$  denotes the different singular regions. In fact, since the **POWHEG BOX** implements the FKS subtraction method, as described in Sec. 2.5.2, (2.68) and (6.15) are equivalent. That means the  $\mathcal{R}^{\alpha_r}$  are chosen such that, for some region of the real correction phase space where the configuration of two particles produces a collinear or soft singularity, only one  $\mathcal{R}^{\alpha_r}$  becomes singular, while all other  $\mathcal{R}^{\alpha_r}$  with  $\alpha_r \neq \alpha'_r$  vanish. Hence, every region  $\alpha_r$  corresponds to the  $f_b$  obtained by replacing the two particles in the singular configuration by the particle from which they emerged in a splitting process; thus defining a mapping  $\alpha_r \rightarrow f_b$ . Now, depending on the singular region  $\alpha_r$  a decomposition of the  $n+1$ -particle phase space  $\Phi^{(n+1)}$  into  $n$ -particle kinematics  $\bar{\Phi}^{(n)\alpha_r}$  and radiation variables  $\Phi_{\text{rad}}$  exists,<sup>8</sup> such that, in full generality, (6.14) is written as

$$\begin{aligned} d\sigma = \sum_{f_b} \bar{B}^{f_b}(\Phi^{(n)}) d\Phi^{(n)} & \left\{ \Delta^{f_b}(\Phi^{(n)}, p_T^{\min}) \right. \\ & \left. + \sum_{\alpha_r \in \{\alpha_r|f_b\}} \frac{[d\Phi_{\text{rad}} \theta(k_T - p_T^{\min}) \Delta^{f_b}(\Phi^{(n)}, k_T) R(\Phi^{(n+1)})]_{\alpha_r}^{\bar{\Phi}^{(n)\alpha_r} = \Phi^{(n)}}}{B^{f_b}(\Phi^{(n)})} \right\}, \end{aligned} \quad (6.16)$$

where the subscript on the square brackets indicates that everything in the square brackets is to be understood in terms of that singular region  $\alpha_r$ . In the **POWHEG BOX**  $\bar{B}^{f_b}$  is the FKS subtracted version of (6.12), where all radiative corrections from regions  $\alpha_r$  with underlying Born  $f_b$  – denoted by the set  $\{\alpha_r|f_b\}$  – have been integrated out,

$$\begin{aligned} \bar{B}^{f_b}(\Phi^{(n)}) &= B^{f_b}(\Phi^{(n)}) + V_{\text{sv}}^{f_b}(\Phi^{(n)}) \\ &+ \sum_{\alpha_r \in \{\alpha_r|f_b\}} \int [d\Phi_{\text{rad}} \{R(\Phi^{(n+1)}) - C(\Phi^{(n+1)})\}]_{\alpha_r}^{\bar{\Phi}^{(n)\alpha_r} = \Phi^{(n)}} \\ &+ \sum_{\alpha_{\oplus} \in \{\alpha_{\oplus}|f_b\}} \int \frac{dz}{z} G_{\oplus}^{\alpha_{\oplus}}(\Phi_{\oplus}^{(n)}) + \sum_{\alpha_{\ominus} \in \{\alpha_{\ominus}|f_b\}} \int \frac{dz}{z} G_{\ominus}^{\alpha_{\ominus}}(\Phi_{\ominus}^{(n)}). \end{aligned} \quad (6.17)$$

The terms  $V_{\text{sv}}$ ,  $G$  and  $R - C$  correspond directly to those finite terms itemized at the end of Sec. 2.5.2, namely to the soft-virtual subtracted contribution  $\mathcal{V}_{\text{sv}}$ , the collinear remnants  $\mathcal{G}$  for each incoming parton (here called  $\oplus$  and  $\ominus$  instead of  $a$  and  $b$ ), and the subtracted real contribution  $\sim \mathcal{R}$  (where the counterterm  $C$  is a representation of the plus-distributions in the FKS subtraction). That the collinear remnants depend on a  $n$ -particle phase space and additionally a longitudinal momentum fraction  $z$  is indicated by the  $\oplus$ -,  $\ominus$ -subscripts on  $\Phi^{(n)}$ ; similarly, the regions  $\alpha_{\oplus}$  and  $\alpha_{\ominus}$  indicate the regions associated with initial state radiation. The reason for the contributions being no longer denoted in calligraphic font is that now they are assumed to include the initial state PDFs, e.g.

$$B = f_{\oplus/A}(x_{\oplus}, \mu_F) f_{\ominus/B}(x_{\ominus}, \mu_F) \mathcal{B},$$

<sup>8</sup>The concrete map used in **POWHEG BOX** is given in [45].

following the notation of [45], to account for the initial state evolution. Correspondingly, the phase space measures  $d\Phi^{(n)}$  are now supposed to include the momentum fractions  $dx_{\oplus}dx_{\ominus}$ . In this more general notation, the POWHEG Sudakov factor (6.13) becomes

$$\Delta^{f_b}(\Phi^{(n)}, p_T) = \exp \left\{ - \sum_{\alpha_r \in \{\alpha_r | f_b\}} \int \frac{[d\Phi_{\text{rad}} R(\Phi^{(n+1)}) \theta(k_T(\Phi^{(n+1)}) - p_T)]_{\alpha_r}^{\bar{\Phi}^{(n)\alpha_r} = \Phi^{(n)}}}{B^{f_b}(\Phi^{(n)})} \right\}. \quad (6.18)$$

The POWHEG BOX code is modular in that it provides the main POWHEG functionality as a black box and allows a user to implement a new process by providing, as FORTRAN routines, the following contributions: The Born phase space in terms of four random numbers and the Born amplitudes  $4F\mathcal{B}^{f_b}$ , along with its colour-correlated relatives  $4F\mathcal{B}_{ij}$  as defined in (2.82), an assignment of colour structures as explained in Sec. 6.1.3, the finite part  $4F\mathcal{V}_{\text{fin}}$  of the virtual corrections (2.77), and the real correction amplitudes  $4F2\pi/\alpha_s\mathcal{R}$ . In addition, the spin-correlated Born amplitudes

$$4F\mathcal{B}_j^{\mu\nu} = \mathcal{N} \sum_{\substack{\text{spins} \\ \text{colours}}} \mathcal{M}_{\{s_k\}} \left( \mathcal{M}_{\{s_k\}}^\dagger \right)_{s_j \rightarrow s'_j} (\varepsilon_{s_j}^\mu)^* \varepsilon_{s'_j}^\nu, \quad (6.19)$$

where the index  $s_j$  represents the spin of the gluon on leg  $j$  and  $\varepsilon_{s_j}^\mu$  is a polarization vector for leg  $j$  (cf. Sec. 2.5.1), are required. From these the POWHEG BOX creates the collinear limit implicit in the plus-distributions of the subtracted real contribution  $R - C$ .<sup>9</sup>

These inputs are then linked against the core POWHEG BOX code, and the construction of soft-virtual contributions, the subtraction of the real amplitude and the collinear remnants are done automatically. To that end, the POWHEG BOX also identifies all the singular regions by comparing the Born and real flavour structures and tests if the soft and collinear limits constructed from the colour- and spin-correlated amplitudes and from the full real contributions agree; this constitutes a consistency check of the real contributions and the colour- and spin-correlated amplitudes provided by the user. PDFs for the event generation can be supplied by linking the code against LHAPDF.

The generation of events is divided into four steps [168]: First, a phase space sampling grid optimized to the inclusive cross section is created. Second, the inclusive cross section is integrated and an upper bounding function is assembled from step functions on the phase space grid from step one. Third, upper bounding functions for the POWHEG “splitting functions”  $R^{\alpha_r}/B^{f_b}$  are generated. In the fourth and last step, the events are generated using the results of the previous steps; the upper bounds are needed for the veto algorithm, as explained in the course of Sec. 6.3.5. Afterwards the events can be stored in Les Houches event files (LHEF), as standardized in the Les Houches Accords (LHA) [169, 170], which can then be read by any LHA compliant GPEG. Alternatively,

<sup>9</sup>The multiplication of the mentioned quantities with the flux factor  $4F$  stems from the fact that in [45], which I followed in Sec. 2.5, the functions  $\mathcal{B}$ ,  $\mathcal{V}$  and  $\mathcal{R}$  are defined including the flux factor, but the POWHEG BOX [46] requires only the squared amplitudes from the user.

the POWHEG BOX provides an interface to access the events at generation time in the HEPEUP format specified in [169], such that, if the GPEG provides a FORTRAN API which allows handing over hard events, each event can be showered and analyzed directly after its generation. In the code described in the following sections, I have only made use of the former possibility, as I wanted to use PYTHIA 8 [153], which is written in C++ (which would complicate the second approach). For the sake of generating enough events to have sufficient statistics it is of course preferable to run the POWHEG BOX in parallel. Even though it is not completely optimized to take hold of several CPUs in one process, it has the facility to be run with different seeds and to combine the results, as explained in detail in [168], so that in effect the event generation can be parallelized by the user.

## 6.3 Prompt Photon Production

### 6.3.1 POWHEG BOX implementation

As mentioned earlier, an implementation of NLO prompt photon production for parton showers making use of the POWHEG method has been reported in [157, 158] based on the idea that the fragmentation function can be modeled by a QED shower off QCD processes [156]. For an implementation into the POWHEG BOX framework I followed the approach of those references in that I have used amplitudes of the same order in the couplings  $\alpha$  and  $\alpha_s$ : Namely, the partial NLO approximation used for the `phoSec` code, as discussed in Sec. 3.4, with direct contributions (with one final state photon) of orders  $\alpha\alpha_s$  and  $\alpha\alpha_s^2$  as well as contributions of order  $\alpha_s^2$  (i.e.  $2 \rightarrow 2$  QCD amplitudes). Thus, using the notation of the last section, the Born flavour structures can be divided into QED,  $f_b^{\text{QED}}$ , and QCD,  $f_b^{\text{QCD}}$ , respectively. The latter then serve to simulate the fragmentation contribution arising from the QED radiation off partons.

In opposition to Refs. [157, 158], which employ a CS dipole based subtraction method, the computation of dipoles is not necessary for the POWHEG BOX implementation, since, as explained in the last section, the subtraction is handled automatically using the FKS method. However, the subtraction of QED singularities for photon radiation off quarks had been only partially implemented in the version my implementation is based on, Revision 3143. QED radiation off leptons, on the other hand, is handled completely automatically, as reported in [171], from POWHEG BOX v2 (Revision > 2334) on.<sup>10</sup> The consistent subtraction of singularities for photon radiation off quarks is one of the small modifications of the POWHEG BOX core code that has been necessary to consistently implement the prompt photon process. Among other things, the main problem is that the POWHEG BOX treats the massless particles democratically and expects an implementation of the following contributions

<sup>10</sup>In fact, the reason for the use of the CS dipole method in `phoSec` has been the assumption that the QED singularities would still have to be completely subtracted by the user. This became obsolete only with the release of the POWHEG BOX v2 mid-2013.

<b>Born</b>	$\mathcal{O}(\alpha\alpha_s)$		$\mathcal{O}(\alpha_s^2)$	
<b>Virtual</b>	$\mathcal{O}(\alpha\alpha_s) \cdot \mathcal{O}(\alpha)$	$\mathcal{O}(\alpha\alpha_s) \cdot \mathcal{O}(\alpha_s)$	$\mathcal{O}(\alpha_s^2) \cdot \mathcal{O}(\alpha)$	$\mathcal{O}(\alpha_s^2) \cdot \mathcal{O}(\alpha_s)$
<b>Real</b>	$\mathcal{O}(\alpha^2\alpha_s)$	$\mathcal{O}(\alpha\alpha_s^2)$		$\mathcal{O}(\alpha_s^3)$

whereas I wanted to implement only

<b>Born</b>	$\mathcal{O}(\alpha\alpha_s) = f_b^{\text{QED}}$		$\mathcal{O}(\alpha_s^2) = f_b^{\text{QCD}}$	
<b>Virtual</b>		$\mathcal{O}(\alpha\alpha_s) \cdot \mathcal{O}(\alpha_s)$		
<b>Real</b>		$\mathcal{O}(\alpha\alpha_s^2)$		

as in [157, 158] and `phoSec`. I will discuss these issues along with the tasks that a user has to complete to implement a new process.

**Subprocesses** The POWHEG BOX requires first a declaration of process parameters in the header file `nlegborn.h`, which the core code depends on via includes: The number of external particles is stored in parameters `nlegborn`, `nlegreal`, the dimension of the real phase space integral including momentum fractions, but without integration over the general azimuthal angle, in `ndiminteg` (which here is 6) and the maximum number of flavour structures in `maxprocborn`, `maxprocreal`, as well as the maximum number of singular regions  $\alpha_r$  in `maxalr`.

In a subroutine `init_processes` the different possible flavour structures of the process have to be specified in two-dimensional arrays `flst_born` and `flst_real` by assigning the PDG code [162] of the respective particles to the external legs (however, the gluon code is 0 instead of the standard 21). Here, the first index of the array denotes the leg of the process (in the order first initial, second initial, first final, second final, etc.), while the second index counts the flavour structures. The exact number of the latter has to be initialized in variables `flst_nborn`, `flst_nreal`. The flavour structures are assumed to be ordered in the final state particles, in the sense that the QCD partons come last, gluons always after quarks; for flavour structures which can be transformed into each other by permutation of the final state legs only one representation has to be included. In my implementation the photon is thus always on leg 3, the first final state leg (except for flavour structures  $f_b^{\text{QCD}}$  which do not include a photon, of course).

**Born amplitudes** Since the POWHEG BOX is a FORTRAN code like `phoSec`, the amplitudes implemented in `phoSec` can simply be transferred to the POWHEG BOX. To recapitulate, the  $f_b^{\text{QED}}$  Born amplitudes are given in App. C.1.1, the  $f_b^{\text{QCD}}$  Born amplitudes can be found in App. C.3. They have to be provided by a subroutine `setborn`, which has as input arguments two arrays specifying the four-momenta and the flavours of each external leg of the requested process and expect as output arguments the corresponding Born amplitude and two arrays with the colour- and spin-correlated amplitudes. Following the implementation of amplitudes in the dijet implementation of [172], I have implemented all the amplitudes in a standard ordered flavour structure with all legs outgoing and let the program derive the requested amplitude from the standard ordered amplitudes by crossing.

The colour-correlations  $4F\mathcal{B}_{ij}$  (cf. (2.82)) for  $f_b^{\text{QED}}$  are, up to a sign, identical to those for the CS dipoles given in Sec. C.2.5. Taking as a standard amplitude for example  $q\bar{q} \rightarrow \gamma g$ , one has

$$\mathcal{B}_{12} = \frac{2C_F - C_A}{2}\mathcal{B}, \quad (6.20)$$

$$\mathcal{B}_{14} = \mathcal{B}_{24} = \frac{C_A}{2}\mathcal{B}, \quad (6.21)$$

according to (C.87), (C.88) and (C.89). A check of the correctness of these results is that the  $\mathcal{B}_{ij}$  are symmetric under the exchange of  $i$  and  $j$  and thus fulfill colour conservation

$$\sum_{i,i \neq j} \mathcal{B}_{ij} = C_j \mathcal{B}. \quad (6.22)$$

Similarly, the spin correlations (6.19) are equal to those of the CS dipole formalism (C.90), i.e. for  $q\bar{q} \rightarrow \gamma g$

$$\mathcal{B}_4^{\mu\nu} = \frac{1}{2} \left( -g^{\mu\nu} + \frac{p_4^\mu \eta^\nu + p_4^\nu \eta^\mu}{p_4 \cdot \eta} \right) \mathcal{B}. \quad (6.23)$$

These obviously satisfy

$$g_{\mu\nu} \mathcal{B}_j^{\mu\nu} = -\mathcal{B}, \quad (6.24)$$

as expected from (6.19). As an unphysical vector,  $\eta$  will always drop out in the final physical results, nonetheless, it has to have a numerical value while processing the numerics. To that end, I have chosen

$$\eta^\mu = g^{\mu\mu} p_4^\mu,$$

i.e. setting  $\eta$  equal to the space inversion of the four-momentum of the gluon (in that way one can be sure that the two physical gluon polarizations, the momentum and  $\eta$  span the Minkowski space).

For the QCD flavour structures  $f_b^{\text{QCD}}$  both the colour- and spin-correlations are not needed. The reason for this is that  $\mathcal{O}(\alpha_s^3)$  corrections are not part of the implementation; therefore, there are no soft or collinear singularities which reduce the amplitude to colour- or spin-correlated  $f_b^{\text{QCD}}$  amplitudes. Furthermore, there is no need to compute the spin-correlations for photons since they are not allowed to split, i.e. real corrections with internal photon lines are not part of the implementation. Accordingly, I have set these contributions to zero, for cases where a  $f_b^{\text{QCD}}$  flavour structure is requested in `setborn`.

**Real amplitudes** The real corrections, cf. Sec. C.2.2, are to be implemented in a routine `setreal` in a way completely analogous to the `setborn` routine, except that no colour- or spin-correlations have to be returned.

For the real corrections one has to make sure, that the singular regions are correctly identified. To that end a variable `flst_lightpart` has to be set in `init_processes`, which determines the position in the flavour structures above which final state partons



are assumed to be massless and can be identified as sources of IR divergences. As in this implementation the photon is always on position 3 for the flavour structures  $f_b^{\text{QED}}$ , `flst_lightpart` is also set to 3 and thus the photon is treated as another massless parton (in comparison, in the implementation of  $Z$ -production, the  $Z$ -boson would always be on position 3 and `flst_lightpart` would be set to 4, so that the `POWHEG BOX` searches for singular regions by considering only partons on positions  $\geq 4$  as emitted particles). The `POWHEG BOX` then identifies and lists all singular regions  $\alpha_r$  of the real contributions and tests the singular limits. In the implementation at hand, these checks show that all singular limits, QCD and QED, soft and collinear, are correctly identified and computed, assuring the consistency of real contributions and colour- and spin-correlated amplitudes.

**Virtual amplitudes** Similar to the other amplitudes, the virtual corrections have to be accessible by a subroutine `setvirtual`, which has as input arguments the four-momenta and flavours, and expects as output the value of the finite virtual corrections as defined by  $4F\mathcal{V}_{\text{fin}}$  in the CDR scheme (2.77). However, here it is important to note, that  $\mathcal{V}_{\text{fin}}$  is not really the full finite contribution, since the other terms in (2.77) also include finite contributions due to  $\mathcal{B}$  and  $\mathcal{B}_{ij}$  being understood in  $D$  dimensions. On the other hand, `phoSec` is based on an implementation of virtual amplitudes of the form

$$\mathcal{V} = (4\pi)^\varepsilon \frac{\Gamma^2(1-\varepsilon)\Gamma(1+\varepsilon)}{\Gamma(1-2\varepsilon)} \left[ \frac{1}{\varepsilon^2} \mathcal{V}^{(-2)} + \frac{1}{\varepsilon} \mathcal{V}^{(-1)} + \mathcal{V}^{(0)} \right], \quad (6.25)$$

with all  $\varepsilon$ -dependence explicit. That means, that it has been necessary to compute from the actual finite result  $\mathcal{V}^{(0)}$  the “CDR-finite” result  $\mathcal{V}_{\text{fin}}$ . By expanding the Born amplitudes in  $\varepsilon$ ,

$$B = \mathcal{B}^{(0)} + \varepsilon \mathcal{B}^{(1)} + \varepsilon^2 \mathcal{B}^{(2)} + \mathcal{O}(\varepsilon^3), \quad (6.26)$$

and comparing (2.77) and (6.25), it is easy to see that the relation

$$\mathcal{V}_{\text{fin}} = \frac{2\pi}{\alpha_s} \mathcal{V}^{(0)} - c_{ij} \mathcal{B}_{ij}^{(1)} - a \mathcal{B}^{(2)} \quad (6.27)$$

holds (the  $\varepsilon$ -dependent prefactors of (2.77) and (6.25) are identical up to  $\mathcal{O}(\varepsilon^3)$ ). This has been implemented in the code by explicitly including the  $\varepsilon$ -expansion of the Born amplitude and using  $\mathcal{V}^{(0)}$  from the `phoSec`-code (which is why my `POWHEG BOX` implementation has to be linked against `LoopTools`).<sup>11</sup> The coefficients  $a$  and  $c_{ij}$  have already been given in (2.78), (2.79).

Using (6.27), I have implemented  $\mathcal{V}_{\text{fin}}$  for the virtual  $\mathcal{O}(\alpha_s)$  corrections to the photon production processes of  $\mathcal{O}(\alpha\alpha_s)$ , but have set it to zero for the  $\mathcal{O}(\alpha_s)$  corrections to the  $f_b^{\text{QCD}}$ , i.e.  $\mathcal{O}(\alpha_s^2)$  processes. This is consistent since real corrections of the same order,  $\mathcal{O}(\alpha_s^3)$ , are also not included. The  $\mathcal{O}(\alpha)$  corrections to  $\mathcal{O}(\alpha_s^2)$  are discussed consecutively.

<sup>11</sup>As mentioned in a footnote in Sec. 3.4, the virtual contributions have been tested in the form (6.27) against `MadLoop`, which also uses the CDR scheme, and were found to be correct.

**Subtraction remnants** The QED singularities of the real amplitudes are automatically subtracted in the FKS framework, i.e. by the fact that the `POWHEG BOX` implements the subtracted real amplitudes described in the last item of Sec. 2.5.2. But normally the FKS subtraction terms are cancelled by virtual corrections and, for initial state singularities, by PDF counterterms. The finite remnants of these cancellations have been collected in the other items in Sec. 2.5.2: The soft-virtual contribution  $\mathcal{V}_{\text{sv}}$  of (2.83) and the collinear remnants  $\mathcal{G}_{\oplus,\ominus}$  of (2.86). As already explained, the term  $\mathcal{V}_{\text{fin}}$  in (2.83) is implemented explicitly by the user, the other terms – the terms proportional to  $\mathcal{Q}$  and  $\mathcal{I}$  in (2.83) and  $\mathcal{G}_{\oplus,\ominus}$  – are part of the `POWHEG BOX` core, i.e. are computed fully automatically. And at this point the core code had to be modified, since the automatic calculation of these terms for all implemented flavour structures is inconsistent:

- If these terms are computed at  $\mathcal{O}(\alpha_s^3)$ , i.e. for QCD corrections to the  $f_b^{\text{QCD}}$  flavour structures, then one would include remnants for a subtraction of divergences which are present neither in the real correction nor in the virtual corrections of the approximation considered here.
- For QED these terms are only computed if a flag `flg_with_em` is set to `.true.` in the code, which I have done. However, now these terms are also computed automatically at  $\mathcal{O}(\alpha^2\alpha_s)$ , i.e. for virtual QED corrections to LO direct photon processes  $f_b^{\text{QED}}$ , which, again, are not part of the implementation at hand.

In my implementation these inconsistencies are solved by placing some if-clauses in the `btildecoll` and `btildevirt` routines, setting the  $\mathcal{Q}$ -,  $\mathcal{I}$ - and  $\mathcal{G}_{\oplus,\ominus}$ -terms to zero in the cases mentioned above.

However, there still is an ambiguity as to how to treat the finite remnants of the subtraction of QED singularities: Naively, one might expect that the user-controlled part of the virtual QED corrections to  $f_b^{\text{QCD}}$ , i.e.  $\mathcal{V}_{\text{fin}}^{f_b^{\text{QCD}}}$ , should be set to zero; but what about the corresponding finite  $\mathcal{Q}$ - and  $\mathcal{I}$ -terms? They include finite parts from the real corrections of  $\mathcal{O}(\alpha\alpha_s^2)$ , which are part of my implementation, as well as from the virtual QED corrections to  $f_b^{\text{QCD}}$ , which are not included, so it is not clear which contributions one would erase from the cross section if the  $\mathcal{Q}$ - and  $\mathcal{I}$ -terms were simply set to zero along with  $\mathcal{V}_{\text{fin}}^{f_b^{\text{QCD}}}$ . In analogy to a fixed order calculation, this freedom of choosing finite remnants to be included or excluded from the direct photon contribution amounts to a choice of a factorization scheme. Since in the fixed order calculation one usually uses the  $\overline{\text{MS}}$ -factorization scheme, I chose to emulate this scheme for the subtraction of the QED singularities. To recapitulate,  $\overline{\text{MS}}$ -factorization means that only terms proportional to  $(4\pi)^\varepsilon/\Gamma(1-\varepsilon)\varepsilon^{-2}$ ,  $(4\pi)^\varepsilon/\Gamma(1-\varepsilon)\varepsilon^{-1}$  have to be subtracted, i.e. I had to make sure, that only these poles are implemented for the virtual QED corrections  $\mathcal{V}_{\text{fin}}^{f_b^{\text{QCD}}}$ . But, of course, the poles are not explicitly implemented anywhere in the code. Instead, this is achieved by implementing

$$\mathcal{V}_{\text{fin}}^{f_b^{\text{QCD}}} = -c_{ij}^{\text{QED}} \mathcal{B}_{ij,\text{ch}}^{f_b^{\text{QCD}}(1)} - a^{\text{QED}} \mathcal{B}_b^{f_b^{\text{QCD}}(2)}, \quad (6.28)$$

which follows from the QED version of (6.27) by setting

$$\mathcal{V}_b^{f_b^{\text{QCD}}(0)} = 0,$$

instead of the naive choice

$$\mathcal{V}_{\text{fin}}^{f_b^{\text{QCD}}} = 0.$$

In that way only the  $\overline{\text{MS}}$  poles of the complete virtual QED corrections (6.25) to the  $f_b^{\text{QCD}}$  amplitudes are implemented. This is then effectively the same as having  $\overline{\text{MS}}$ -subtracted real contributions. However, it must be reiterated that this is still an arbitrary choice, as the parton shower generated fragmentation contribution can not in general be said to be in a certain scheme, like the FF of a fixed order calculation, which annuls the factorization scheme dependence of the complete result.

In summary, the soft-virtual term of the FKS subtraction procedure for the QED singularities, which is effectively employed by my implementation is

$$\begin{aligned} \mathcal{V}_{\text{sv}}^{f_b^{\text{QCD}}} = \frac{\alpha_s}{2\pi} & \left( \mathcal{Q}^{\text{QED}} \mathcal{B}_b^{f_b^{\text{QCD}}} + \sum_{ij} \mathcal{I}_{ij}^{\text{QED}} \mathcal{B}_{ij,\text{ch}}^{f_b^{\text{QCD}}} \right. \\ & \left. - a^{\text{QED}} \mathcal{B}_b^{f_b^{\text{QCD}}(2)} - c_{ij}^{\text{QED}} \mathcal{B}_{ij,\text{ch}}^{f_b^{\text{QCD}}(1)} \right). \end{aligned} \quad (6.29)$$

The coefficients with the QED superscript can, as usual, be derived from the known QCD counterparts (cf. (2.78) and (2.79))

$$a^{\text{QED}} = - \sum_i Q_i^2, \quad (6.30)$$

$$c_{ij}^{\text{QED}} = (1 - \delta_{ij}) \left[ -\frac{\gamma_i^{\text{QED}}}{Q_i^2} + \ln \left( \frac{2p_i \cdot p_j}{\mu_R^2} \right) \right]. \quad (6.31)$$

The  $\mathcal{I}$ -terms for QED (cf. (2.85)) were already included in the POWHEG BOX v2, but I still had to add the  $\mathcal{Q}$ -term for photon radiation off massless quarks to the subroutine `btildevirt` (cf. (2.84))

$$\begin{aligned} \mathcal{Q}^{\text{QED}} = \sum_i & \left[ \gamma_i^{\text{QED}'} - \ln \left( \frac{s}{\mu_R^2} \right) \left( \gamma_i^{\text{QED}} - 2Q_i^2 \ln \left( \frac{2E_i}{\xi_c \sqrt{s}} \right) \right) \right. \\ & \left. + 2Q_i^2 \left( \ln^2 \left( \frac{2E_i}{\sqrt{s}} \right) - \ln^2(\xi_c) \right) - 2\gamma_i^{\text{QED}} \ln \left( \frac{2E_i}{\sqrt{s}} \right) \right], \end{aligned} \quad (6.32)$$

where the sum is over all charged legs,  $Q_i$  is the charge of particle  $i$  and (cf. (2.80))

$$\gamma_i^{\text{QED}} = \frac{3}{2} Q_i^2, \quad (6.33)$$

$$\gamma_i^{\text{QED}'} = \left( \frac{13}{2} - \frac{2\pi^2}{3} \right) Q_i^2. \quad (6.34)$$

The charge-correlations (which were already present in the `POWHEG BOX v2`) are defined in analogy to (2.82)

$$\mathcal{B}_{ij,\text{ch}} = -\mathcal{B}Q_iQ_j(-1)^{\sigma_i+\sigma_j}, \quad (6.35)$$

where  $\sigma_i = 0$  if  $i$  is a (initial)final state (anti)particle and  $\sigma_i = 1$  if it is a (final)initial state (anti)particle (which is also equivalent up to a sign to the charge-correlations defined for the QED dipoles in Sec. C.2.6).

The PDF counterterms to QED singularities are in principle only present if one uses PDFs including QED corrections, such as the CT14qed sets [173]. From this point of view, in a consistent approach, one would have to use QED PDFs for this implementation. On the other hand, QED evolved PDFs are normally fitted making use of hard processes with full QED corrections, which I have not implemented (furthermore, it is known that the impact of QED improved PDFs on observables are rather negligible [171]). In any case, corresponding to the cancellation of singularities from the real contributions and from PDF IR counterterms, one has QED collinear remnants  $\mathcal{G}_{\oplus,\ominus}$  for each QED initial state singularity. These collinear remnants for QED were also already present in the `POWHEG BOX v2` and are actively used for the implementation at hand.

**Colour assignment** After the `POWHEG BOX` has decided on a Born configuration from which to start the shower, the external particles have to be assigned a definite colour before the event can be processed further. This is achieved by the user implementing a subroutine `borncolour_lh`, which includes a common block `HEPEUP`, as specified in [169], from which the user can access the event information. Based on the Born flavour structure of the event, one has to assign colours in the large- $N_c$  limit of Sec. 6.1.3 to the `icolup` array.

For the  $f_b^{\text{QED}}$  flavour structures this is rather straight-forward, as there is only one possible choice of colour flows: Different colours for each quark and the gluon is a combination of these colours. For the  $f_b^{\text{QCD}}$  processes this is more complicated, as one has competing colour flows for single subprocesses. However, as the  $f_b^{\text{QCD}}$  flavour structure are nothing else than the dijet Born flavour structures, it has been possible to simply use the existing implementation of colour assignments of the dijet code published in [172].

**Couplings** Couplings needed by the amplitudes – apart from the QCD coupling  $\alpha_s$ , which is handled by the `POWHEG BOX` core – can be defined in a subroutine `init_couplings`. In the case at hand, this entails the electromagnetic coupling `em_alpha`. Additionally, the number of light quarks for the QCD evolution of  $\alpha_s$  has to be specified in the variable `st_nlight`.

For the QED coupling to be passed also to the GPEG, one has to set the `HEPEUP` variable `AQEDUP` in the subroutine `finalize_lh`. This subroutine serves in general to set up all the information needed by the GPEG, which have not been automatically set by the `POWHEG BOX`.

**Born phase space** The momenta of the particles in a Born amplitude have to be set in a subroutine `born_pbsp`. This subroutine has as input arguments `ndiminteg-3` (i.e. in this case 3) random numbers, ranging from 0 to 1, corresponding to the integration variables of the Monte Carlo integrator, which have to be translated into the particle momenta, while keeping track of the Jacobian of the phase space integration. In principle, it would have been possible to take the phase space of the `phoSec` implementation with some modifications. However, since all particles are treated as massless, the Born phase space is the same for the prompt photon and dijet processes. Thus, it has been easiest to also use the phase space routines from the dijet code [172].

At the time of the generation of the Born kinematics, one also has to assign the values for the renormalization and factorization scales  $\mu_R$  and  $\mu_F$ . This is done in the subroutine `setfacrenscale` (also adopted from the dijet code), where I have set the scales for QCD and QED equal. Two possibilities for the choice of these scales are implemented. First, a fixed scale and, second, a running scale equal to the transverse momentum of the Born process. This last point is important to consider if one wants to compare the results of the `POWHEG BOX` and `phoSec` or `JETPHOX` implementations. The latter two can and do set the scales equal to the photon  $p_T$ , while the former can not: At the point at which the scales have to be assigned in the `POWHEG BOX` implementation, the photon  $p_T$  is not yet known, since it might not have been generated yet (as would be the case if a  $f_b^{\text{QCD}}$  flavour structure is selected to start the shower) or since its momentum might be reshuffled significantly by the first `POWHEG`-generated radiation. If the running scale is chosen for a run, then the scales are kept fixed at  $\mu_F = \mu_R = 1.5 \text{ GeV}$  if the Born  $k_T$  were to drop below this value (similar to the low- $p_T$  `JETPHOX` calculations of the previous chapters).

**Usage** By linking the user-generated files against the `POWHEG BOX` code and compiling, the main `POWHEG BOX` program `pwhg_main` for the process is generated. To start a run, one has to create a text file `powheg.input` including the process parameters, such as energies of the colliding beams, initial state PDFs, number of events to be generated and more technical parameters documented in [46].

In addition, the `POWHEG BOX` includes the possibility to use this file also for parameters specific to the user process implementation. This is achieved by using the function `powheginput`, which returns the value of some parameter, e.g. `param`, specified in `powheg.input`, e.g. as `param 1`, if invoked in the form `powheginput('#param')`. I have made use of this facility to read a parameter `emvirtual` by which the flag `flg_with_em` is set to `.true.` (1) or `.false.` (0) and, correspondingly, the contributions (6.29) are computed or not. The value of the inverse electromagnetic coupling can be set through the parameter `alfaem_inv`. Renormalization and factorization scales can be set to a fixed value by the parameter `fixedscale`; if this parameter is not present or negative, then the scales will be set equal to the transverse momentum of the underlying Born process of the event. Other important parameters are `bornktmin` and `bornsuppfact`, which are explained in the next section.

After a run terminated successfully, a file `pwgevents.lhe` containing the hard event information and several other files for diagnostic purposes have been placed in the directory where the program has been executed. `pwgevents.lhe` can then be read by PYTHIA (and other GPEGs) to use the events as a starting point for the shower generation. PYTHIA 8 provides the facilities to access all of the information provided in the LHEF file and automatically selects the starting scale of the shower from the `SCALUP` variable, the couplings from the `AQCDUP` and `AQEDUP` variables, etc. However, the user has, in any case, to take care of the normalization of the distributions that are to be created. Therefore it is important to note that the `XWGTUP` variable contains the weight of an event. If the value of this variable is equal for all events, then the events are unweighted, i.e. histograms filled with the events are yields and count the actual number of particles created in that bin. On the other hand, `XWGTUP` can also vary from event to event, as specified by the `IDWTUP` variable. In most applications of the POWHEG BOX `IDWTUP = -4` will be used, which means that `XWGTUP` varies from event to event, can be negative and gives the integrated cross section only when averaged over all events. Here, simply filling histograms with the events will not give physically sensible results. Instead the user must take care that the histograms are filled with events of the correct weight  $\text{XWGTUP}/N_{\text{ev}}$ , with  $N_{\text{ev}}$  the total number of events, which then reproduces the correct cross sections.

### 6.3.2 Born zero

Parton showers are usually generating hard events in the complete phase space of a process. The reason for this is that if one were to take only events from a slice of the phase space as starting point of the parton shower, then one can not in general know which part of the generated distribution after the shower is viable. If, for instance, one were to generate only hard events for a certain  $p_{\text{T}}$ -range and shower those, what  $p_{\text{T}}$ -range of the result can then be assumed to be correct? The relation between cuts before and after the shower is obfuscated by the momentum reshuffling of the parton shower; hence, a complete simulation of the phase space is necessary.

However, the amplitude of the hard event can have singularities, as is the case for prompt photon and dijet production at LO. These singularities are encountered for vanishing Born  $k_{\text{T}}$ , which is why these processes usually call for cuts on the transverse momentum. Indeed, the phase space generation of the prompt photon (and correspondingly dijet) process has to be restricted by a  $k_{\text{T}}^{\text{min}}$ -cut on the  $\overline{B}$  event generation, the value of which can be specified by the parameter `bornktmin`.

Alternatively, the dijet code includes a subroutine `born_suppression`, which has initially been introduced in [174] and serves to regulate the Born zero by reweighting the  $\overline{B}$  function with a factor that cancels the divergence – namely, the Born suppression factor

$$\mathcal{S}(k_{\text{T}}) = \left( \frac{k_{\text{T}}^2}{k_{\text{T}}^2 + k_{\text{T},\text{supp}}^2} \right)^3. \quad (6.36)$$

This feature is activated in the parameter file by setting the option `bornsuppfact` to a value for  $k_{\text{T},\text{supp}}$  and has the effect of replacing the functions  $\overline{B}^{f_b}(\Phi_n)$  in (6.16) with

$\mathcal{S}(k_T)\bar{B}^{f_b}(\Phi_n)$ . The Born zero divergence, which is  $\sim k_T^{-4}$ , is then cancelled out and no events will be generated at very low  $k_T$ . This change of the cross section is corrected for by weighting the generated events with the inverse of (6.36). Thus, if this feature is activated, one has to take care to fill the distributions one wishes to create with events of the weight specified in the **XWGTUP** variable of the LHEF file, which now automatically incorporates the additional weight, divided by the number of events.

The impact of both methods, **bornktmin** and **bornsuppfact**, on the  $p_T$ -spectra of dijets is documented in Ref. [172], where it has been found that **bornsuppfact** leads to a significantly better coverage of the  $p_T$  spectrum, and that for **bornktmin** the regions far above the cut are not influenced by the choice of the cut. However, these results can not directly be taken over to the prompt photon case, since here only a single particle, the photon, is of interest, whose  $p_T$ -distribution may not directly correspond to the Born  $k_T$ , while a jet may more or less resemble the hard  $\bar{B}$  event and the correspondence of Born  $k_T$ -cut and the jet  $p_T$ -spectrum is more direct.

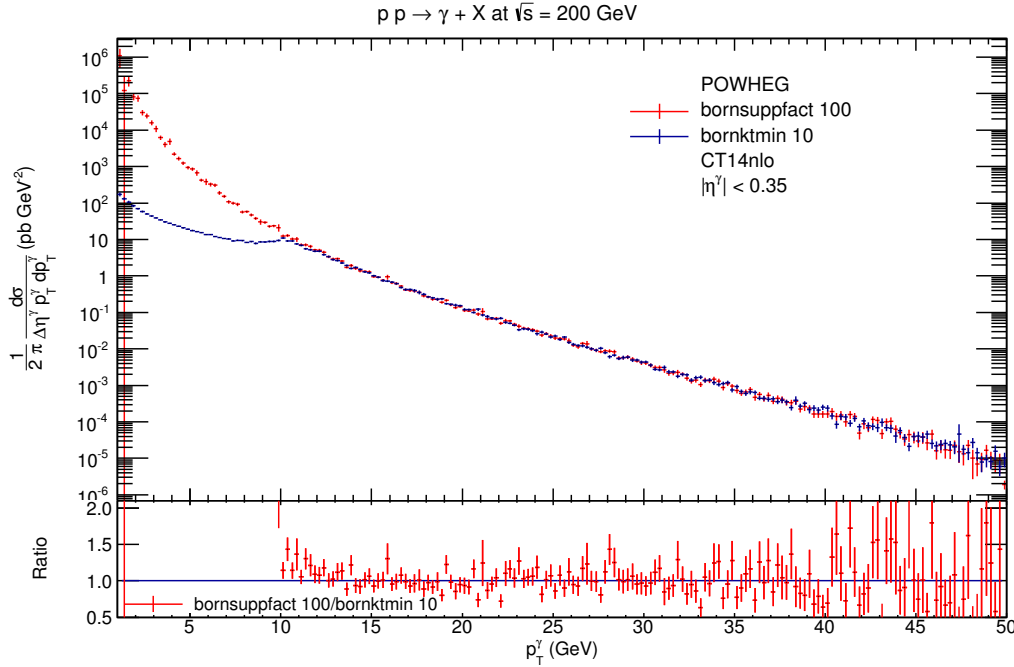


Figure 6.2: Comparison of the Born zero regularizations **bornktmin** = 10 and **bornsuppfact** = 100 via the POWHEG (pre-shower) prompt photon  $p_T$  spectrum. The error bars represent the statistical uncertainties.

The Figs. 6.2 and 6.3 show a comparison of the impact of **bornktmin** and **bornsuppfact** on the photon- $p_T$  spectrum at mid-range. **bornktmin** has been set to 10 GeV and

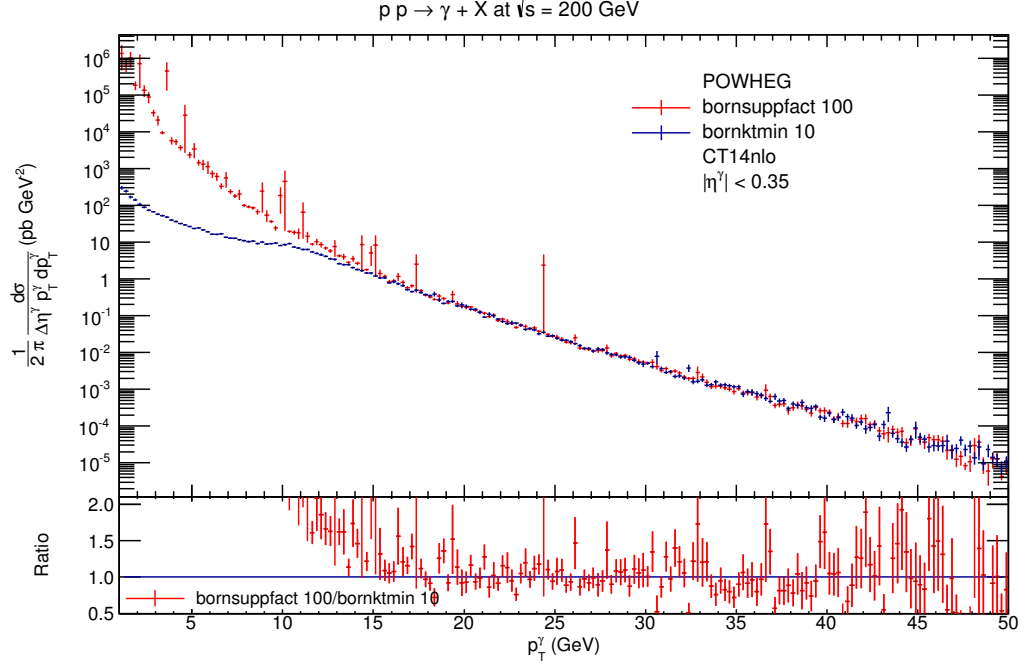


Figure 6.3: Same as Fig. 6.2, but after shower and hadronization with PYTHIA 8. From an event only the prompt photon with the hardest  $p_T$  w.r.t. the beam axis is counted (the details of the shower are described in Sec. 6.3.4).

**bornsuppfact** to 100 GeV for a PHENIX setup.<sup>12</sup> In the **bornktmin** plots the cut is clearly visible as a bump and a depopulation of events below 10 GeV w.r.t. to the **bornsuppfact** plots where the full Born  $k_T$  range is simulated but reweighted. However, as anticipated, there is still a significant amount of photons below 10 GeV, which are the result of radiation off  $f_b^{\text{QCD}}$  configurations with a Born  $k_T$  above 10 GeV. At roughly 20 GeV both options agree reasonably well. Though, as the plots are shown with a relatively fine binning, it can be seen that the **bornsuppfact** option introduces large peaks in single bins of the showered distribution, which, for a more reasonable, larger bin-width, would significantly increase the bin content. The origin of these peaks has been discussed in [175], where it was found that they also show up in jet- $p_T$ -distributions, if the **bornsuppfact** option is used.

The problem is that, with **bornsuppfact** in use, events at very low  $k_T$  are generated only very seldom, but if they are generated, they obtain a very large weight proportional to  $\mathcal{S}(k_T)^{-1}$ . In the POWHEG distributions these are not visible, i.e. the POWHEG distributions are smooth in any case. But if the photons in these single bins with large weight are, by means of the momentum reshuffling of the parton shower, shifted to higher  $p_T$ ,

<sup>12</sup>In addition, the data of these plots are based on runs with **enhancedradfac** 50 to boost the production of photons, as explained in Sec. 6.3.5.



then they will show up as large peaks. With other words: If the events would have been unweighted before the shower, the large number of events in the low- $p_T$  bins would be reshuffled more or less evenly over a larger  $p_T$  range, but as the low- $p_T$  bins in the **bornsuppfact**-approach might be constituted by one single event with a large weight, this one event will show up after the shower in another bin as a large peak.

In Ref. [175] a feature **doublefsr** has been introduced which changes the POWHEG BOXes internal definition of emitter and emitted – such that events for which the emitter would be softer than the emitted particle are produced rather with exchanged emitter-emitted-roles – and is found to largely solve the problem for dijet spectra. As can be seen in the showered result of Fig. 6.4, this feature clearly diminishes the appearance of these peaks also for the photon- $p_T$  spectrum. But additionally it significantly decreases the overall normalization of the spectrum by roughly 10 % – 20 %, as on display in the ratios on the bottom, which, by virtue of Ref. [175], should not happen. I have not been able to identify the reason for this.

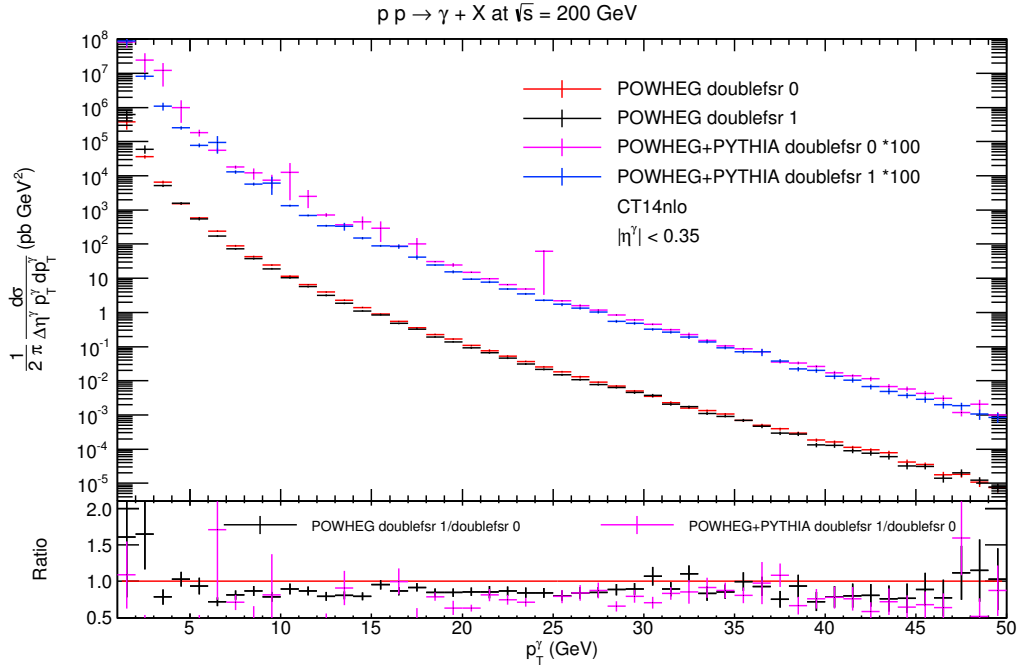


Figure 6.4: A comparison of the **bornsuppfact** = 100 plots shown in the previous figures with wider binning and additional data using the **doublefsr** option. The showered results are scaled by a factor 100 for visibility.

In the end, the Born zero constitutes the main remaining problem in the prompt photon implementation. Thus, in principle, one has to carefully inspect the impact of the choice of the parameters mentioned and either find a region which is not influenced by a reasonable change of these parameters or fit the spectrum to data. Since the main

region of interest of this work lies in the low- $p_T$  region, it follows that one has to make use of the `bornsuppfact` feature, as the region impacted by a `bornktmin` cut could be as large as the low- $p_T$  region itself. For the time being it is thus inevitable to accept the appearance of unphysical peaks in the spectrum, which can however clearly be identified as such as long as one uses a sufficiently finely grained binning.

### 6.3.3 Simulation of the fragmentation contribution

Apart from problems of the specific implementation or region of interest, it is not a trivial matter that the implementation recreates the physical photon spectrum at all. Why is it sensible to expect the parton shower to model the fragmentation function – a measured, non-perturbative quantity – without non-perturbative input?

Comparing the Sudakov factor (6.5) and the point-like component (3.16) of the photon FF, shows that the former is an exponentiation of the latter (barring the photon-FF boundary condition<sup>13</sup>). In the light of the known dominance of the anomalous contribution at large energies, discussed in Sec. 3.2, it is then natural to expect the QED Sudakov’s resummation of the anomalous, i.e. perturbative, photon fragmentation function to simulate the shape and evolution of the fragmentation contribution reasonably well. The normalization, on the other hand, i.e. the large difference between direct and direct plus fragmentation contributions documented in Sec. 3.4, is primarily not due to the normalization of the photon-FF, which is restricted by momentum sum rules, but due to the mere fact that a large set of new underlying processes, the pure QCD processes, has to be added to the direct contributions. Hence, it is also expected that the normalization of the parton shower-simulated fragmentation contribution is at least of the correct order of magnitude.

Sec. 4 has shown that the `JETPHOX` results give a good description of the data<sup>14</sup>, even in the low- $p_T$  region below 25 GeV. Fig. 6.5 shows a comparison of the full `JETPHOX`-generated  $p_T$  spectrum and the `POWHEG` spectrum. To highlight the low- $p_T$  region, the `bornsuppfact` option is set to 10 GeV. In the range 5 GeV – 17 GeV the agreement between `POWHEG` and `JETPHOX` is largely within statistical errors, though, again, a considerable impact of the `doublefsr` option is visible: The run with activated `doublefsr` underestimates, the other run overestimates the amount of photons. The deviations in the high  $p_T$  region can already be attributed to bad statistics, as only very few photon events, roughly 2 % of the  $72 \cdot 10^6$  events generated for this run, are generated in the sample, from which only about 10 % survive the PHENIX  $\eta^\gamma$ -cuts – the large majority of events consists of pure QCD configurations for which the QED shower has been evolved down to the lower cut-off scale and subsequent QED radiation is thus forbidden. This problem will be elaborated on in Sec. 6.3.5.

<sup>13</sup>For the NLO photon FFs, both the GRV [94] and BFG [99], have studied the impact of a zero boundary condition and found that it depends on the factorization scheme in use. In GRV’s  $\text{DIS}_\gamma$ -scheme the effect is only marginal.

<sup>14</sup>Though, here, the `JETPHOX` results have the scales simply set to  $p_T^\gamma$ . Furthermore, CT14nlo instead of CT10nlo is used; both agree within statistical errors for the `JETPHOX` photon spectrum.

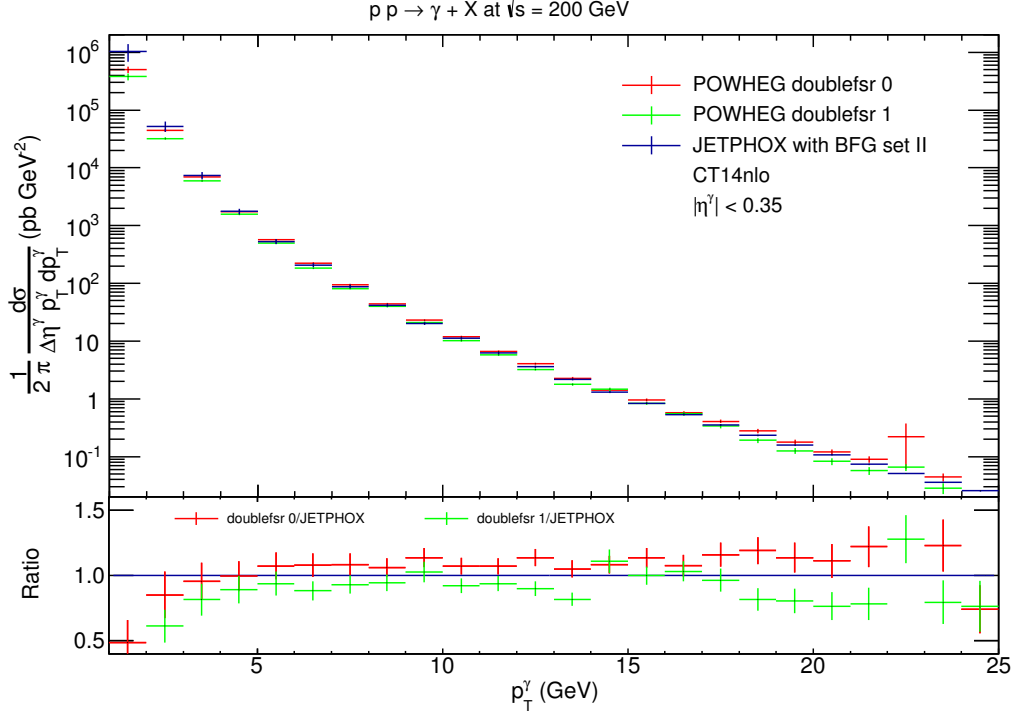


Figure 6.5: Comparison of POWHEG BOX and JETPHOX based on CT14nlo. JETPHOX uses BFG set II. The POWHEG results use `bornsuppfact` = 10 to increase statistical significance of the low- $p_T$  region.

From Fig. 4.2 it is known that the fragmentation contribution dominates the  $p_T$ -distribution below 4 GeV, while amounting to about 30 % over most of the shown  $p_T$ -range above 4 GeV. A 30 % difference to the JETPHOX results can not be observed for most of the statistically sound  $p_T$ -range of Fig. 6.5, indicating that the POWHEG radiation mimics the fragmentation function. Though, for  $p_T < 4$  GeV, where the FF dominates, both POWHEG predictions fall below the fixed order result. But it must be noted that the POWHEG-generated distributions are only partial results, as the shower has yet to be added. Thus this region could still be populated by the interplay of momentum reshuffling, QED shower, beam remnants and hadronization effects.

#### 6.3.4 Parton shower with PYTHIA 8

As mentioned earlier, PYTHIA 8 employs a transverse momentum ordered parton shower and can hence be used to shower POWHEG events. However, since the definitions of the relative transverse momentum of a shower-generated radiation differ for the POWHEG BOX and PYTHIA, this “hardness criterion” has to be translated from POWHEG to PYTHIA [153]. PYTHIA 8 provides the class `PowhegHooks` to manage the translation of definitions of the relative transverse momentum. Using this class, the preferred mode of usage is to have PYTHIA evolve the shower starting from the kinematical limit of the process, rather than

the scale passed by the `POWHEG BOX`, then translate the  $p_T$  of a shower-generated radiation from the `PYTHIA` definition to the `POWHEG BOX` definition and veto radiation harder than the hard `POWHEG` scale. In this way, one ensures the correct transverse momentum ordering intended by the `POWHEG` method. Though, there is still a considerable amount of freedom in the choice of scales that is mirrored in a multitude of optional definitions of relative transverse momentum implemented in the `PowhegHooks` class: Instead of taking the scale passed by the `POWHEG BOX` in the `SCALUP` variable of the LHEF event, it is also possible to define a new hardest scale by e.g. taking the smallest relative  $k_T$  of all the particle combinations of an event, or redefine the  $p_T$  of the `PYTHIA` emission, and more. Here I will not go into further detail about these settings.

In addition, there is, specifically for the prompt photon implementation, the question of how to handle the scales for QED and QCD radiation. The default would be to make no distinction and veto the evolution of QED and QCD radiation above the `POWHEG` scale, independently of the type of event. However, if a  $f_b^{\text{QCD}}$ -event is generated by the `POWHEG BOX` then, in the implementation presented here, only the next QED radiation is evolved by means of the `POWHEG` Sudakov (since its exponent is  $R/B f_b^{\text{QCD}} \propto \alpha$ ), the QCD shower is not evolved to a lower scale at all. If, on the other hand, an underlying event of  $f_b^{\text{QED}}$ -type is generated, then the `POWHEG` Sudakov only evolves the QCD shower (since  $R/B f_b^{\text{QED}} \propto \alpha_s$ ). This problem has been discussed in [158] and I followed the approach presented there, which suggests employing two different hard scales, one for the QED and one for the QCD shower. Further discussion of this approach and an approach which includes a competition between QED and QCD radiation already at the level of the `POWHEG` event (i.e. an implementation of  $R \sim \mathcal{O}(\alpha_s^3)$ ), such that both the QED and QCD Sudakov are evolved for each event by `POWHEG`, can be found in [176]. Following the nomenclature of the latter reference, I have used the “NC scheme”.

To allow for the distinctive treatment of QED and QCD radiation, the `POWHEG BOX` code has been modified to pass the CM energy of the underlying Born event, additionally to the scale of the first radiation, to `PYTHIA`. This Born scale<sup>15</sup> is then used by `PYTHIA` as the hard scale for QED radiation, if the underlying Born event includes a photon, i.e. for  $f_b^{\text{QED}}$  events. On the other hand, it is the hard scale for QCD radiation if the underlying Born event is a  $f_b^{\text{QCD}}$  event. The scale of the emission that is passed by the `POWHEG BOX` in the `SCALUP`-variable corresponds in those two cases to the hard scale for QCD and QED radiation, respectively. An additional modification of the `PowhegHooks` class ensures the correct vetoes: Every `PYTHIA` generated radiation is checked if it is a QED or QCD radiation and, depending on the underlying Born event, vetoed accordingly.<sup>16</sup>

In Fig. 6.6 a fully showered result in the PHENIX low- $p_T$  region is compared to the `POWHEG` and the `JETPHOX` spectra (in addition the PHENIX data from Sec. 4 are shown

<sup>15</sup>Actually, it is only half the CM scale which is used. `PYTHIA 8`’s dipole based parton shower kinematics define as the scale of a radiation the invariant dipole mass [161], which for 2 final state particles would amount to  $\hat{s}/2$ .

<sup>16</sup>Here, it is important to set the `POWHEG:vetoCount` option of the `PowhegHooks`-class to a high value  $\sim 50$  to be sure that the veto is enacted not only for the first radiation attempts. Contrary to a comment in the `PYTHIA 8` manual, this is crucial for the consistency of the prompt photon implementation and has visible effects.

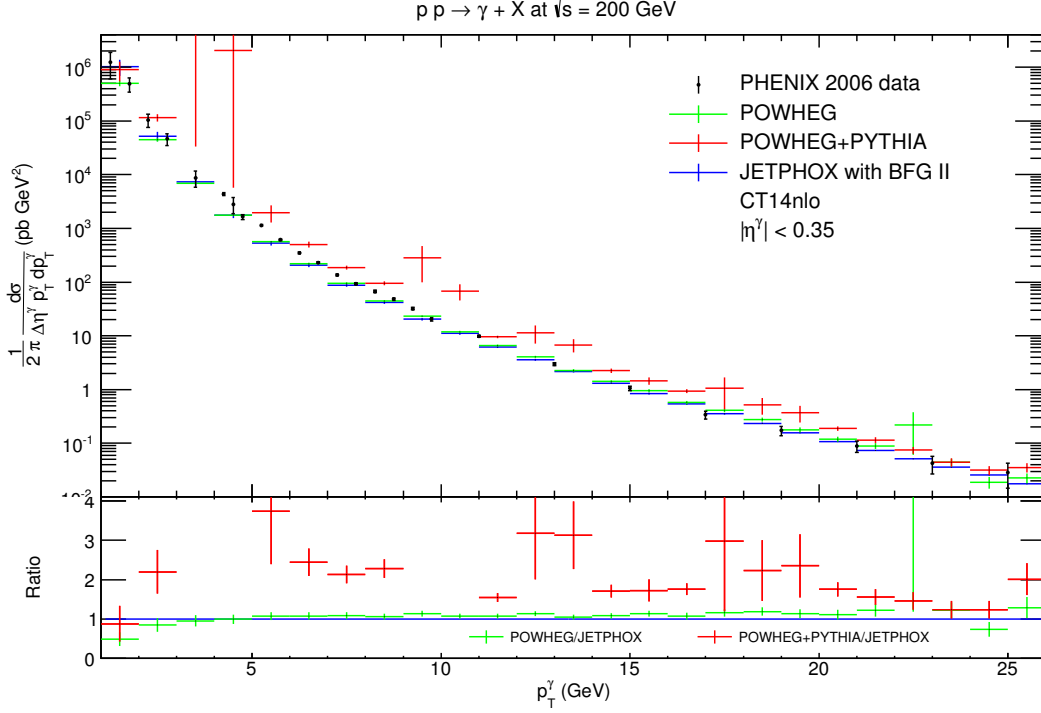


Figure 6.6: JETPHOX, POWHEG, and POWHEG with PYTHIA shower in comparison with PHENIX prompt photon data. POWHEG uses `bornsuppfact 10`.

for reference). It can be seen that the whole visible spectrum is significantly elevated by PYTHIA's event handling and clearly overshoots the JETPHOX reference. In addition, as already noted in Sec. 6.3.2, the spectrum is very uneven due to many peaks. Still, it must be stressed again that the peaks introducing the large fluctuations can be identified as outliers if the histograms are plotted with a finer binning, cf. Fig. 6.3. Using `doublefsr` the result is improved, as shown in Fig. 6.7. Apart from visible outliers, e.g. in the bins 9 GeV – 10 GeV, 12 GeV – 13 GeV and 14 GeV – 15 GeV, the spectrum is much smoother and in better agreement with JETPHOX as well as with the data. In the end, as speculated at the end of the last section, it is indeed found that the shower increases the photon count for  $p_T < 4$  GeV. However, it does so not only for  $p_T < 4$  GeV, but rather for the complete spectrum.

Fig. 6.8 shows a similar comparison based on a different run with the `bornsuppfact 100` option<sup>17</sup> to highlight the transverse momentum mid-range above 20 GeV. Here, the deviation of the showered results is much smaller than in Fig. 6.6, though with about 20 % still far from an acceptable agreement with JETPHOX. Activating the `doublefsr` option leads to the spectrum displayed in Fig. 6.9; now the shower shows nearly complete agreement within errors with the JETPHOX prediction.

<sup>17</sup>Again, using the `enhancedradfac 50` option of Sec. 6.3.5.

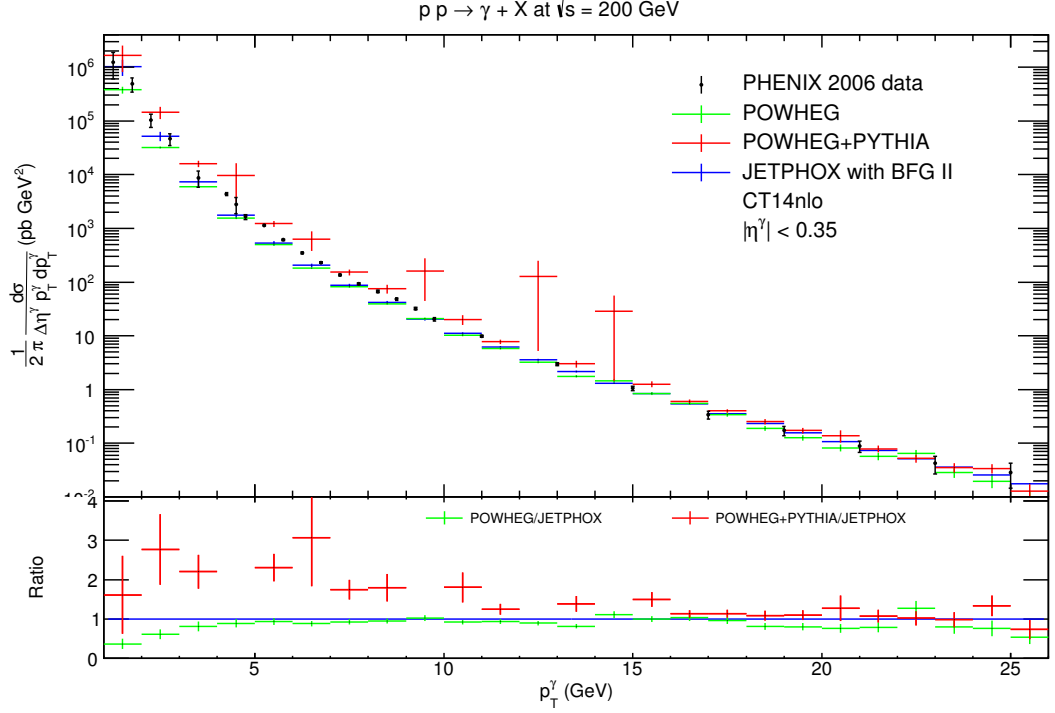


Figure 6.7: Same as Fig. 6.6, except that POWHEG uses `doublefsr`.

A crucial question is of course, how the additional photons in low- $p_T$  are generated. Initially, it has been assumed that the shower would basically just reshuffle those photons already generated by POWHEG – looking at the previous figures seems to undermine this argumentation, as there is a significant increase of the photon count in every bin (most importantly in all low- $p_T$  bins) when going from POWHEG to POWHEG plus PYTHIA. However, it must be noted that the PHENIX setup has a quite narrow  $\eta^\gamma$ -range and it is possible that the shower boosts photons into the central rapidity region, which, at POWHEG event level, lie out of this range. If this were the case, then a run with large  $\eta^\gamma$ -range should have some bins which are significantly depopulated when going from POWHEG to the showered results. But as Fig. 6.10 shows, this is not the case.<sup>18</sup> Instead the growth of the bin contents is similar to the central rapidity data; there are virtually no POWHEG+PYTHIA bins lying below the POWHEG results. As a side note, the `doublefsr` option can again be seen to increase the agreement of JETPHOX and the showered POWHEG results.

By incrementally activating the different event completion facilities of PYTHIA – these facilities being the final and initial state radiation, the multi-parton interactions and the beam remnant treatment – it can be seen, that indeed only the initial state radiation has the effect of increasing the prompt photon cross section, while the final state radiation has, as expected, no effect at all for this observable. The other facilities lead only to a minor reshuffling of events, not impacting the shape or normalization in general. Still,

<sup>18</sup>I have tested that one obtains the same result without  $\eta^\gamma$ -cuts.

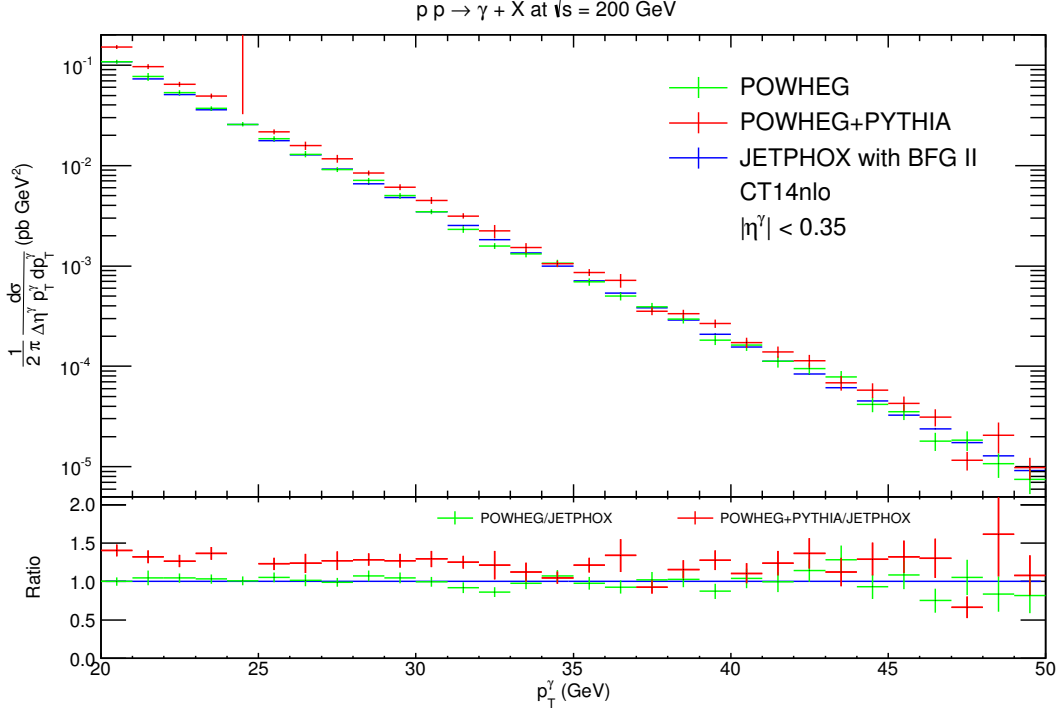


Figure 6.8: JETPHOX, POWHEG, and POWHEG with PYTHIA shower in comparison for the mid- $p_T$  range via `bornsuppfact 100`.

the problem persists, that, if the initial state shower only pushes some events from low- $p_T$  bins to higher  $p_T$ , then at least the lowest  $p_T$  bin should significantly decrease and furthermore, the integral over all bins should not change. Incidentally, by deactivating PYTHIA's QED shower exactly this behaviour can be seen: Using 1 GeV bins, the bin with the left edge at zero is significantly decreased while the rest of the spectrum is largely compatible within error bars with the full shower result. Furthermore, in this case the integrated cross sections of POWHEG and POWHEG+PYTHIA are equal, while the latter increases if the QED shower is active. That means, the assumption that the initial state shower boosts the photons to higher  $p_T$  is correct, but the lowest bin is refilled by photons from PYTHIA's QED shower. In a fully consistent approach, these photons should have been generated by POWHEG in the first place, but due to a slight mismatch in the lower cut-off scale of PYTHIA 8 and the POWHEG BOX there can be a considerable amount of additional low- $p_T$  photons. Setting POWHEG BOXes lower cut-off scale, controlled by the `powheg.input-parameter ptsqmin`, to  $p_T^{\min} = \sqrt{0.5} \text{ GeV}$  instead of  $\sqrt{0.8} \text{ GeV}$  has, however, led to very large negative results in the lowest  $p_T$ -bin, such that the integrated cross section becomes negative. This is most likely due to the fact that the QCD machinery, which depends crucially on `ptsqmin`, fails if  $p_T^{\min}$  is chosen as low as this value. This could only be circumvented by introducing separate cut-offs for QED and QCD radiation. As long as such a differentiation of lower cut-offs

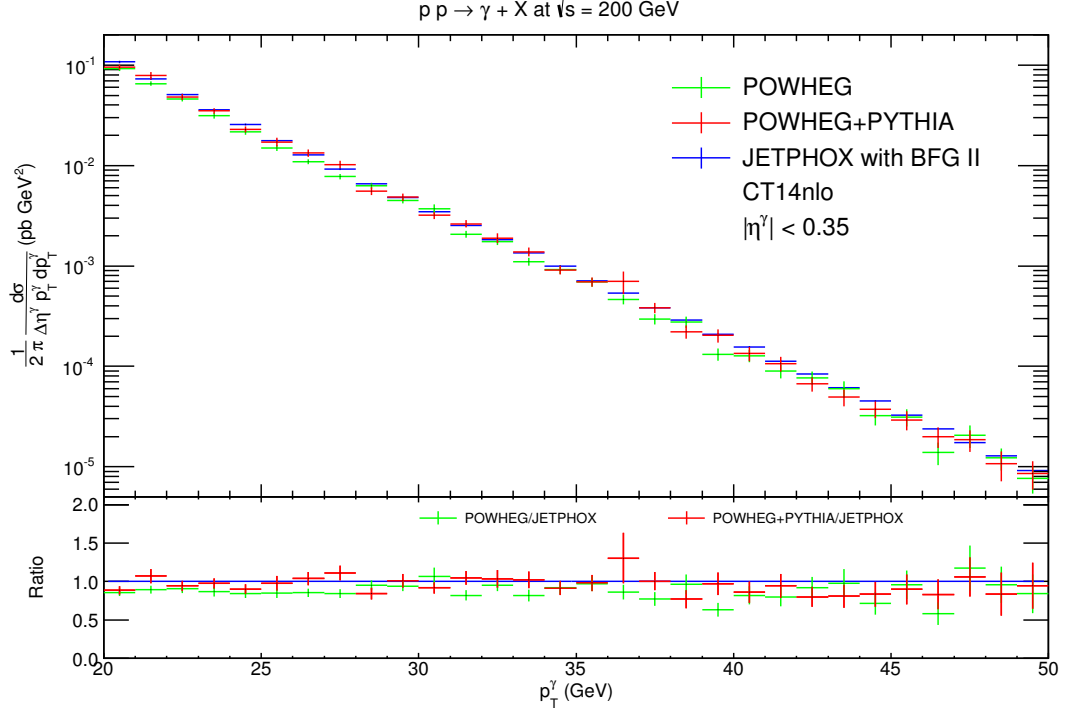


Figure 6.9: Same as Fig. 6.8, except that POWHEG uses `doublefsr`.

is not implemented, one has to accept that the photons of lowest  $p_T$  are produced by PYTHIA in the collinear limit approximation (which should, at such  $p_T$ -values, be a good approximation to the full NLO result) and that only after the shower the full fragmentation contribution, including  $p_T < 4$  GeV, has been generated.

As said earlier, there is a multitude of input parameters, which can be adjusted when applying the parton shower to POWHEG events. Fig. 6.11 shows a comparison of different PYTHIA setups, based on the same POWHEG events using CT10nlo.<sup>19</sup> The upper plot shows that the smallest deviation from JETPHOX is given by the “no hooks” histogram, which corresponds to not using the `PowhegHooks` class at all, while the disagreement is somewhat worse when the standard `PowhegHooks` class is used to veto radiation above the hard POWHEG scale and more so if different scales for QED and QCD radiation are used. However, in the first two cases, as discussed above, the shower leaves out large parts of the radiation phase space and is thus inconsistent. It is though obvious from the figure that the wider coverage of the phase space, and thus the additional amount of allowed radiation, increases the proliferation of peaks and consequentially the fluctuations of the bin contents. The lower plot shows a comparison of three tunes readily available in PYTHIA 8, where the “Monash” tune corresponds to the PYTHIA 8 standard. It has been noted in Ref. [153] that the introduction of NLO matched processes requires in principle a retuning of the free GPEG-parameters – and that such a retuning is, due to

<sup>19</sup>The effect of the PDF choice should in principle drop out of the ratio.



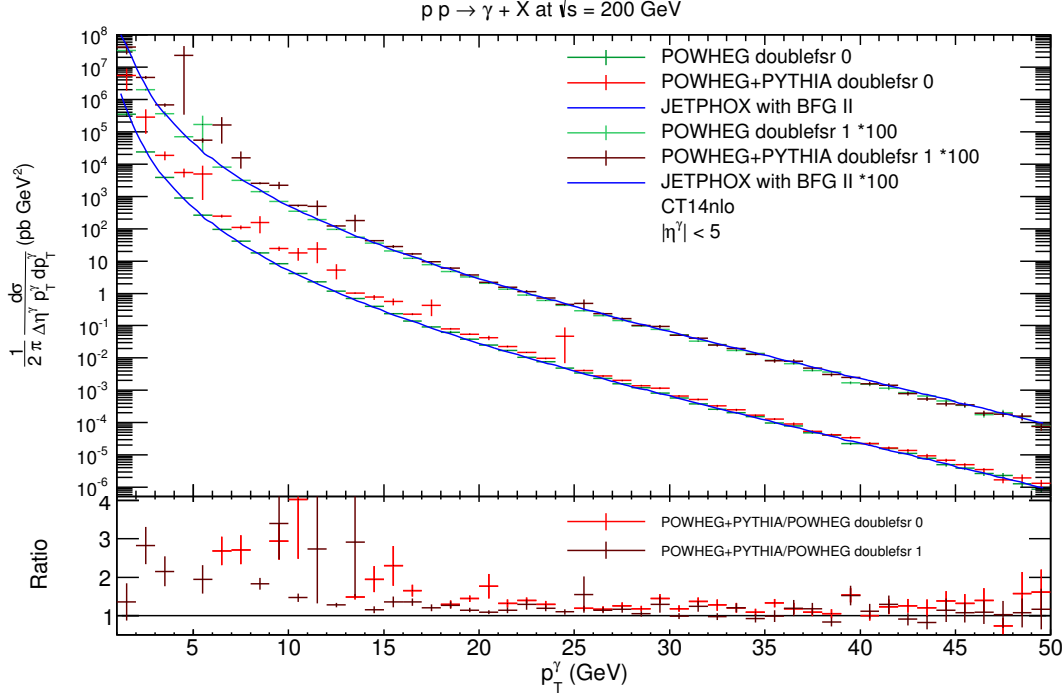


Figure 6.10: Photon  $p_T$  for larger rapidity range  $|\eta^\gamma| < 5$ . POWHEG and showered POWHEG results in comparison with JETPHOX (shown as a curve). Uses `bornsuppfact 100`, `doublefsr` is shown scaled by a factor 100.

the large number of parameters, usually only feasible for larger collaborations. However, in the comparison shown the different tunes do not impact the ratios strongly enough to significantly improve the outcome in the low- $p_T$  region. The change of the spectrum induced by using the POWHEG option `doublefsr` is considerably larger, so that considerations of new GPEG tunes should for now play no role in trying to improve the POWHEG BOX results.

### 6.3.5 Photon rate enhancement

As it stands, the implementation of single photon production in the POWHEG BOX framework described in the preceding sections leads to a very low photon production rate. As already mentioned in the last sections, a run at PHENIX energy  $\sqrt{s} = 200$  GeV with  $72 \cdot 10^6$  events, for instance, includes only about  $1.5 \cdot 10^6$  events with a photon, the remaining events are made up of QCD Born configurations, where the QED shower is evolved to the lower cut-off and thus no new photons will be generated (except in decay processes). In this special case the run has been distributed over 6 computing nodes with Intel Xeon Westmere X5650 processors with 12 cores at 2.67 GHz and 24 GB RAM and took 30 h to finish (these events then still have to be showered, which takes another day if done sequentially). The results of these runs are given in Figs. 6.5, where the

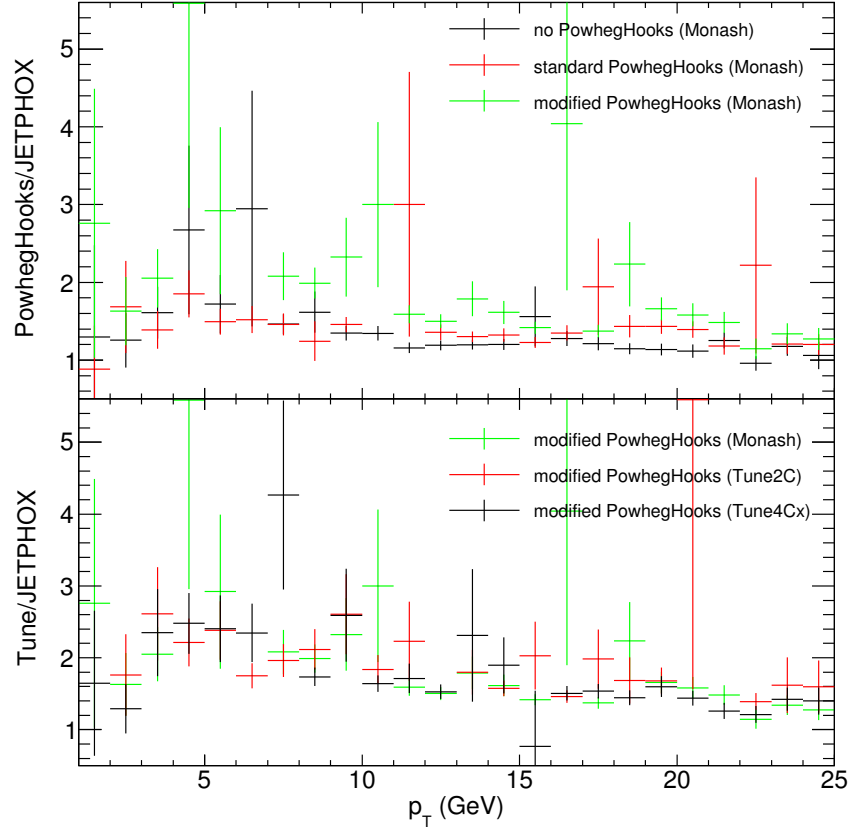


Figure 6.11: Ratio of fully evolved POWHEG BOX events and JETPHOX based on CT10nlo. JETPHOX uses BFG set II, POWHEG uses again `bornsuppfact` = 10. The upper plot shows a comparison of different setups of the `PowhegHooks`-class, the lower plot a comparison of different PYTHIA 8 tunes.

statistical fluctuations at least in the low  $p_T$  region are only just compensated by the error bars. It is obvious that for runs with a larger energy range, such as the LHC's, the duration of computations generating a sufficient photon yield becomes unacceptable.

The low production rate of photons is related to the smallness of the electromagnetic coupling  $\alpha$ , which results in a large no-branching probability (6.18), while additionally lowering the probability to generate a LO direct photon, i.e.  $f_b^{\text{QED}}$  event. Accordingly, a way to tackle this problem should be to artificially increase  $\alpha$  to make it comparable to  $\alpha_s$ . The POWHEG BOX v2 includes a reweighting feature that can be used for a fast recalculation of event weights in case of parameter changes which do not impede on the generation of the Born phase space or the generation of radiation, as described in [168]. However, a change of  $\alpha$  would precisely do that: First, it would change the relative weight of  $f_b^{\text{QCD}}$  and  $f_b^{\text{QED}}$  events. And second, it would change the amount of QED radiation

generated via POWHEG's Sudakov factor. Thus the given reweighting feature can not be used and, furthermore, using an increased coupling  $\alpha$  seems not to be feasible.

Alternatively, an approach to boosting the contribution of events with photon by changing the QED Sudakov factor's exponent has been described in [156] and a similar approach in [177]. Following these approaches, the exponent of the POWHEG Sudakov factor (6.18) for QED radiation, for now abbreviated by

$$f(\Phi_{\text{rad}}) \equiv \frac{R^{\alpha_r}(\Phi^{(n+1)})}{B^{f_{\text{QCD}}}(\Phi^{(n)})} \bigg|_{\bar{\Phi}^{(n)\alpha_r}=\Phi^{(n)}}, \quad (6.37)$$

is multiplied with a constant  $c > 1$ , thus decreasing the no-branching probability and generating more QED radiation. This has to be corrected for by reweighting the event. The weight necessary to do that can be obtained by modifying the POWHEG BOXes veto algorithm, as explained in the following.

In the POWHEG BOX (and, quite generally, in other parton shower generators), the  $p_T$  of a radiation is generated by first solving the equation

$$\ln \left( \Delta^{(U)}(p_T) \right) = \ln(r) \quad (6.38)$$

for a uniformly distributed random number  $r \in [0, 1]$ , where  $\Delta^{(U)}(p_T)$  is a lower bound for (6.18), obtained by replacing  $f(\Phi_{\text{rad}})$  by an upper bounding function  $U(\Phi_{\text{rad}}) \geq f(\Phi_{\text{rad}})$ . Afterwards, the generated  $p_T$  is accepted and a new branch added to the event record with a probability given by the ratio  $f/U$  or vetoed with a probability  $1 - f/U$ . In the latter case, (6.38) is solved again, but this time restricting  $p_T$  to values below the vetoed value. The whole procedure is then reiterated until a  $p_T$  is accepted or when a low- $p_T$  cutoff of the order of  $\Lambda_{\text{QCD}}$  is reached (the POWHEG BOX uses  $\sqrt{0.8} \text{ GeV}$ ).

That this creates the correct distribution, following the no-branching probability  $\Delta(p_T)$  rather than  $\Delta^{(U)}(p_T)$ , can be shown in the following way (the explicit  $\Phi^{(n)}$  dependence is suppressed for brevity): The probability density of a scale  $p_T$  is given, before the veto, by

$$\rho_{\text{rad}}^U(p_T) = \frac{d}{dp_T} \Delta^U(p_T) = \Delta^U(p_T) \int d\Phi_{\text{rad}} U(\Phi_{\text{rad}}) \delta(k_T(\Phi^{(n+1)}) - p_T) \quad (6.39)$$

or abbreviated

$$\rho_{\text{rad}}^U(p_T) = U(\Phi_{\text{rad}}) \big|_{k_T(\Phi^{(n+1)})=p_T} \Delta^U(p_T). \quad (6.40)$$

Afterwards, the  $p_T$  that has been generated is accepted with a probability

$$P_{\text{acc}}(p_T) = \frac{f(\Phi_{\text{rad}})}{U(\Phi_{\text{rad}})} \bigg|_{k_T(\Phi^{(n+1)})=p_T} \leq 1 \quad (6.41)$$

or rejected with  $1 - P_{\text{acc}}(p_T)$ . In case of a rejected  $p_T$ -value the scale is evolved downwards from  $p_T$  and a new  $p'_T \leq p_T$  is generated according to the density

$$\rho_{\text{rad}}^U(p'_T, p_T) = \frac{\partial}{\partial p'_T} \frac{\Delta^U(p'_T)}{\Delta^U(p_T)}, \quad (6.42)$$

## 6 Parton Shower Matching

which is then accepted with probability  $P_{\text{acc}}(p'_T)$  or rejected accordingly.

For a  $p_T$ -value that is accepted after  $n$  vetoes, one then has the distribution

$$\begin{aligned} \rho_n(p_T) = & P_{\text{acc}}(p_T) \\ & \cdot \int_{p_T}^{p_T^{\text{max}}} d\tau_1 \int_{p_T}^{\tau_1} d\tau_2 \cdots \int_{p_T}^{\tau_{n-1}} d\tau_n \rho_{\text{rad}}^U(p_T, \tau_n) \\ & \cdot (1 - P_{\text{acc}}(\tau_n)) \rho_{\text{rad}}^U(\tau_n, \tau_{n-1}) \cdots (1 - P_{\text{acc}}(\tau_1)) \rho_{\text{rad}}^U(\tau_1). \end{aligned} \quad (6.43)$$

Noting

$$(1 - P_{\text{acc}}(p_T)) \rho_{\text{rad}}^U(p_T) = (U(\Phi_{\text{rad}}) - f(\Phi_{\text{rad}}))|_{k_T(\Phi^{(n+1)})=p_T} \Delta^U(p_T) \quad (6.44)$$

and summing over all possible vetoes delivers a proof of the veto method:

$$\begin{aligned} \sum_{n=0}^{\infty} \rho_n(p_T) &= f(\Phi_{\text{rad}})|_{k_T(\Phi^{(n+1)})=p_T} \Delta^U(p_T) \\ &\cdot \sum_{n=0}^{\infty} \int_{p_T}^{p_T^{\text{max}}} d\tau_1 \cdots \int_{p_T}^{\tau_{n-1}} d\tau_n (U(\Phi_{\text{rad}}) - f(\Phi_{\text{rad}}))|_{k_T(\Phi^{(n+1)})=\tau_1} \\ &\cdots (U(\Phi_{\text{rad}}) - f(\Phi_{\text{rad}}))|_{k_T(\Phi^{(n+1)})=\tau_n} \\ &= f(\Phi_{\text{rad}})|_{k_T(\Phi^{(n+1)})=p_T} \Delta^U(p_T) \\ &\cdot \sum_{n=0}^{\infty} \frac{1}{n!} \left[ \int_{p_T}^{p_T^{\text{max}}} d\tau \int d\Phi_{\text{rad}} (U(\Phi_{\text{rad}}) - f(\Phi_{\text{rad}})) \delta(k_T(\Phi^{(n+1)}) - \tau) \right]^n \\ &= f(\Phi_{\text{rad}})|_{k_T(\Phi^{(n+1)})=p_T} \Delta(p_T), \end{aligned} \quad (6.45)$$

where in the last step the integral over  $\tau$  turns the  $\delta$ - into a  $\theta$ -distribution and the series representation of the exponential function has been used. But this is the  $p_T$ -derivative of (6.18), i.e. the veto method generates the correct distribution.

If now (6.38) is replaced by

$$\ln \left( \Delta^{(cU)}(p_T) \right) = \frac{\ln(r)}{c}, \quad (6.46)$$

for a constant  $c$ , then this has the same effect as multiplying both  $f$  and  $U$  by  $c$  and thus effectively decreases the no-branching probability.

Now, the distribution (6.43) for a radiation generated after  $n$  vetoes would be given by

$$\begin{aligned} \rho_n^{(c)}(p_T) = & P_{\text{acc}}(p_T) \\ & \cdot \int_{p_T}^{p_T^{\text{max}}} d\tau_1 \int_{p_T}^{\tau_1} d\tau_2 \cdots \int_{p_T}^{\tau_{n-1}} d\tau_n \rho_{\text{rad}}^{cU}(p_T, \tau_n) \\ & \cdot (1 - P_{\text{acc}}(\tau_n)) \rho_{\text{rad}}^{cU}(\tau_n, \tau_{n-1}) \cdots (1 - P_{\text{acc}}(\tau_1)) \rho_{\text{rad}}^{cU}(\tau_1). \end{aligned} \quad (6.47)$$

Following the derivation (6.45), this now generates a distribution  $d\Delta^{(cf)}(p_T)/dp_T$  instead of  $d\Delta(p_T)/dp_T$ . However, as proposed in [156], equipping the events generated by this distribution with a weight

$$w_n = \frac{1}{c} \prod_{i=1}^n \frac{1 - \frac{1}{c} P_{\text{acc}}(\tau_i)}{1 - P_{\text{acc}}(\tau_i)}, \quad (6.48)$$

where the product runs over all QED radiation vetoes, amounts to multiplying  $w_n$  to the integrand of (6.47). Since the weight (6.48) effectively replaces the probabilities  $P_{\text{acc}}(\tau_i)$  in (6.47) by

$$\frac{1}{c} P_{\text{acc}}(\tau_i) = \left. \frac{f(\Phi_{\text{rad}})}{c U(\Phi_{\text{rad}})} \right|_{k_T(\Phi^{(n+1)})=\tau_i},$$

the combination of the scale generation equation (6.46) and the event weight (6.48) produces the correct distribution  $d\Delta(p_T)/dp_T$  again. On the other hand, if no radiation is generated because the lower cut-off scale is reached first, then (6.48) without the prefactor  $1/c$  is the required event weight, reproducing the correct no-branching probability  $\Delta(p_T^{\text{min}})$ .

The implementation of this procedure into the POWHEG BOX code is accomplished by adding some lines of code to the routines `gen_radiation`, `gen_rad_isr` and `gen_rad_fsr`, which implement the vetoing procedure. First a flag is set, proclaiming if the underlying hard event is of  $f_b^{\text{QCD}}$  or  $f_b^{\text{QED}}$  type. Only in the former case, the reweighting procedure is activated, so that only QED radiation is enhanced. In that case, (6.38), which is implemented in `gen_rad_isr` and `gen_rad_fsr`, is replaced by (6.46). Then, for each vetoed  $p_T$  value  $\tau$ , the ratio

$$\frac{1 - \frac{1}{c} P_{\text{acc}}(\tau)}{1 - P_{\text{acc}}(\tau)}$$

is multiplied to a global (common block) variable `sudawgt`, which at the beginning of `gen_radiation` has been initialized to 1. Finally, if a  $p_T$  value is accepted, `sudawgt` is divided by the enhancement factor  $c$ . The constant  $c$  is itself accessible through a global variable `sudarwgtfac`. `sudawgt` is then equal to (6.48) (or the no-branching equivalent without prefactor  $1/c$ ) and has to be written to the LHEF file as additional event information, so that a GPEG can read it. This is done by modifying the `lhefwritev` subroutine, such that a tag `<wgt id='sudakovwgt'>` is written to the LHEF file for each event, containing (6.48). Combining, i.e. multiplying, the cross section weight `XWGTUP` and the `sudakovwgt` is then enough to correctly reweight the events.

The feature is activated by providing the option `enhancedradfac c` with  $c > 1$  in `powheg.input`. Furthermore, the parameters `lhrwgt_id` and `lhrwgt_descr` have to be set to some word and a description of the run enclosed in single quotes (this activates the tag-writing facilities of the POWHEG BOX needed to write the `sudakovwgt` tag to the LHEF file).

The influence of the `enhancedradfac` option on the number of generated photons is depicted in Fig. 6.12. Based on runs at  $\sqrt{s} = 200 \text{ GeV}$  with  $12 \cdot 10^6$  events, the number of photons is found to rise like a power of the constant  $c$  set by `enhancedradfac`. But of

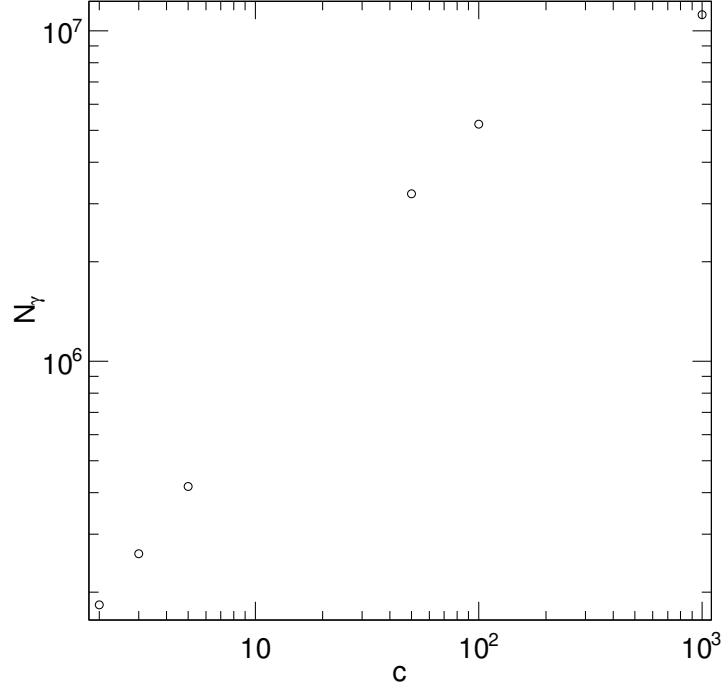


Figure 6.12: Number of photons produced in  $12 \cdot 10^6$  events for different enhancement factors  $c$ . The approximate linear dependence in a doubly-logarithmic plot is equivalent to a power-law relation.

course a high number of photons would be of no use if the distributions were skewed by the activation of this option. Fig. 6.13 shows a comparison of a high statistics run with  $72 \cdot 10^6$  events and a run with  $24 \cdot 10^6$  events using `enhancedradfac 50` and `bornsuppfact 10`. The ratio shows that for most of the displayed region the agreement is good, but the results start fluctuating and deviating from each other above 15 GeV.

Similar results have been obtained for other enhancement factors, with a tendency to more fluctuations for higher factors. Fig. 6.14 shows the ratio of `enhancedradfac 50` and `enhancedradfac 100` to a high statistics run using older data based on CT10nlo (other than that the settings are equivalent to the previous plot). Fits to the two ratios show that, within errors, the `enhancedradfac 50` is compatible with unity,  $0.98 \pm 0.03$ , while, due to the fluctuations, the `enhancedradfac 100` is not, giving  $0.96 \pm 0.02$ , when taking the full range into account. A fit to the latter is only compatible with unity if the fit is restricted to  $p_T \leq 16$  GeV. The reason for this might be that the weights (6.48) become numerically unstable for too large values of  $c$  and as a result (6.45) is in practice not reproduced by the sum over all events and radiation vetoes, only for small radiation scales (loosely corresponding to small  $p_T$ ) where a lot of vetoes have been enacted. The choice `enhancedradfac 50` has been the best compromise between agreement with high

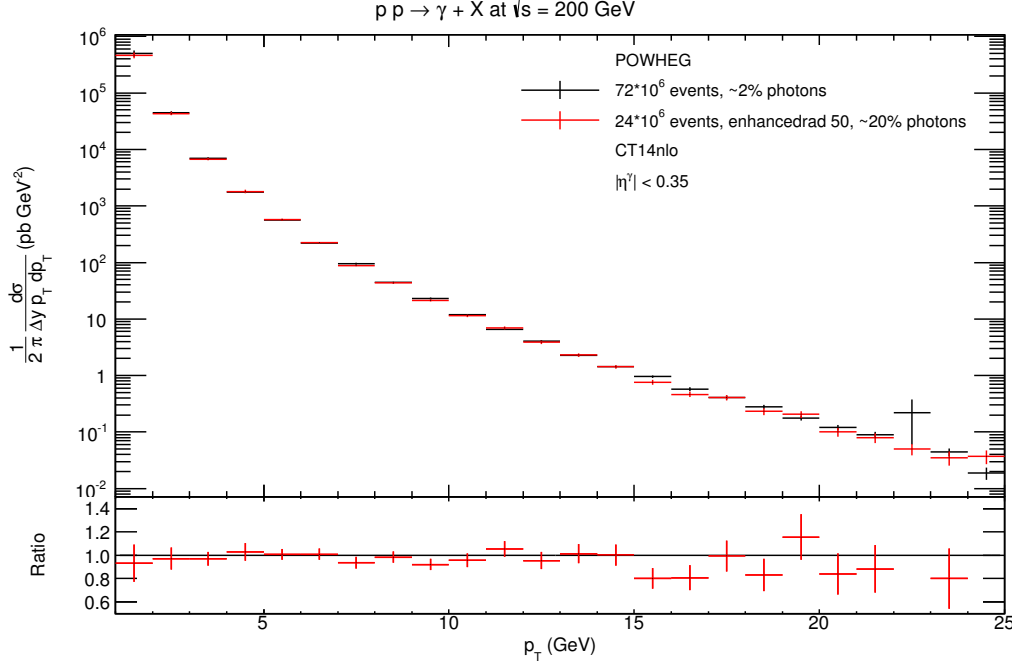


Figure 6.13: Comparison of POWHEG events from a high statistics run without enhanced QED radiation and a run with less events but **enhancedradfac** 50; again based on the PHENIX setup.

statistics run and increase of the number of photon events in the samples produced for the PHENIX setup.

As mentioned at the beginning of this section, a similar procedure has been described in [177]. This has been implemented and tested, too, giving similarly good results. Comparing the results of **enhancedradfac** 50 to the results presented in [177], which have overall higher statistics, a smaller enhancement factor and cover the same  $p_T$ -range but for a LEP run, one can see that the **enhancedradfac** 50 option works surprisingly well and that the shape of the fluctuations at larger  $p_T$  is very similar.

## 6.4 Comparison with LO and PHENIX Data

The PHENIX data on prompt photons, already used in Sec. 4, have been shown previously in Figs. 6.6 and 6.7. From these Figures it is clear, that an agreement between showered POWHEG results and data can only be reached with the **doublefsr** option activated. Figs. 6.7 and 6.10 reinforce this for an agreement between JETPHOX and POWHEG+PYTHIA for higher transverse momentum. The results of the following sections will thus all have **doublefsr** activated. Furthermore, to boost the creation of events with photons, the

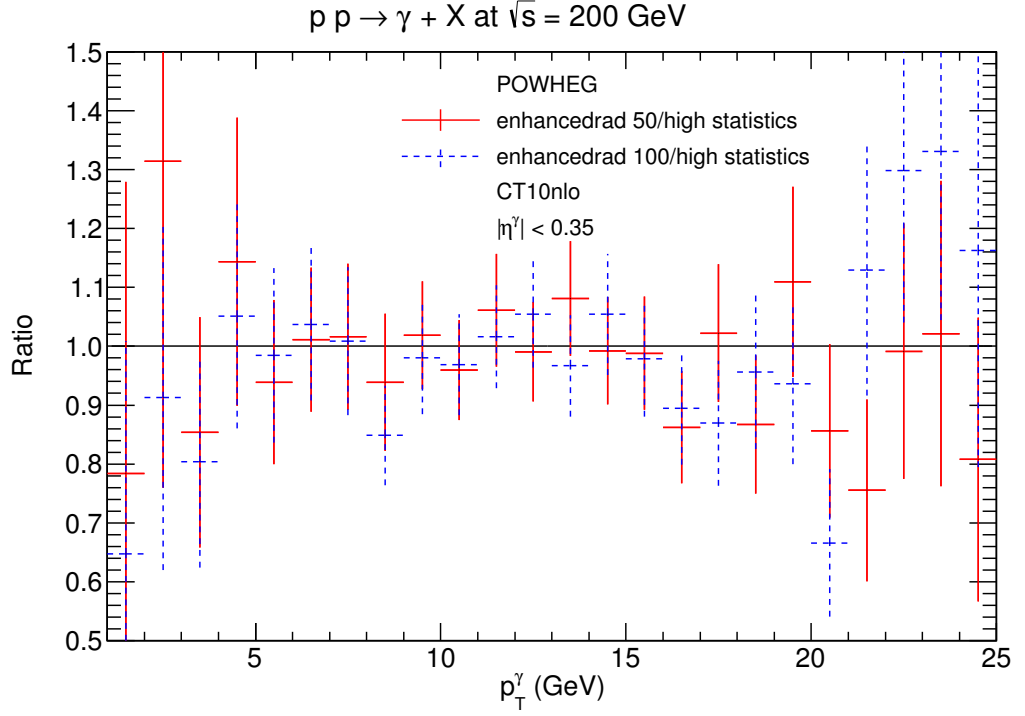


Figure 6.14: Ratio of `enhancedradfac 50` and `enhancedradfac 100` to a run with  $72 \cdot 10^6$  events and no `enhancedradfac` option activated. Using `bornsuppfact 10` and `CT10nlo`.

results here use `enhancedradfac 50`, as it has been shown that this does not impair the results over the interesting PHENIX  $p_T$  range.

It has earlier been mentioned that it might be more consistent to use PDFs which involve QED evolution. However, a comparison of POWHEG runs using `CT14qed_proton` with runs using `CT14nlo` (both with `bornsuppfact 10` and PHENIX setup) have shown that the two are compatible within statistical errors; a fit to the ratio of the runs in the range  $2 \text{ GeV} - 30 \text{ GeV}$  gives  $0.99 \pm 0.02$ . For that reason, the following results have been produced using `CT14nlo` for JETPHOX and POWHEG. PYTHIA is set to its standard PDF, NNPDF2.3 QCD+QED LO.

#### 6.4.1 Prompt photon transverse momentum spectrum

Figs. 6.15 and 6.16 show a comparison of PYTHIA (i.e. showered LO direct), JETPHOX (NLO) and POWHEG+PYTHIA (showered NLO) prompt photon spectra in a binning matching most of the PHENIX data (since the low-mass lepton and real photon data overlap, not all datapoints can be reproduced).

It can be seen that JETPHOX underestimates the data points below  $10 \text{ GeV}$ , as long as theoretical errors are not incorporated or the scales adjusted (as has been done in Sec. 4). The LO shower provided by PYTHIA clearly underestimates the whole region



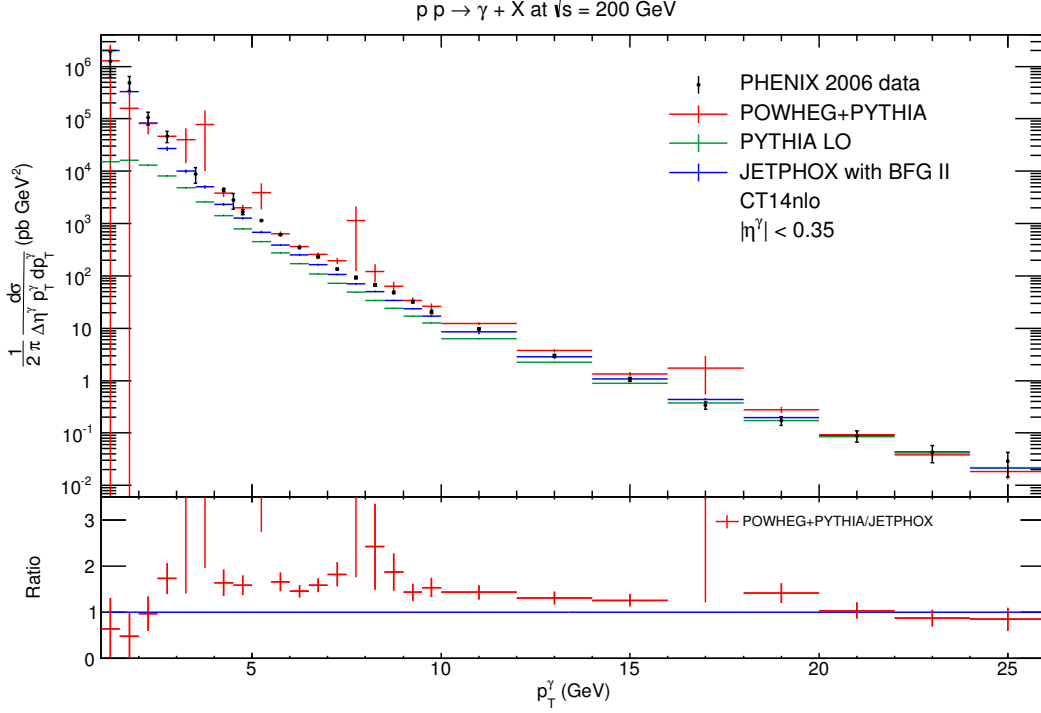
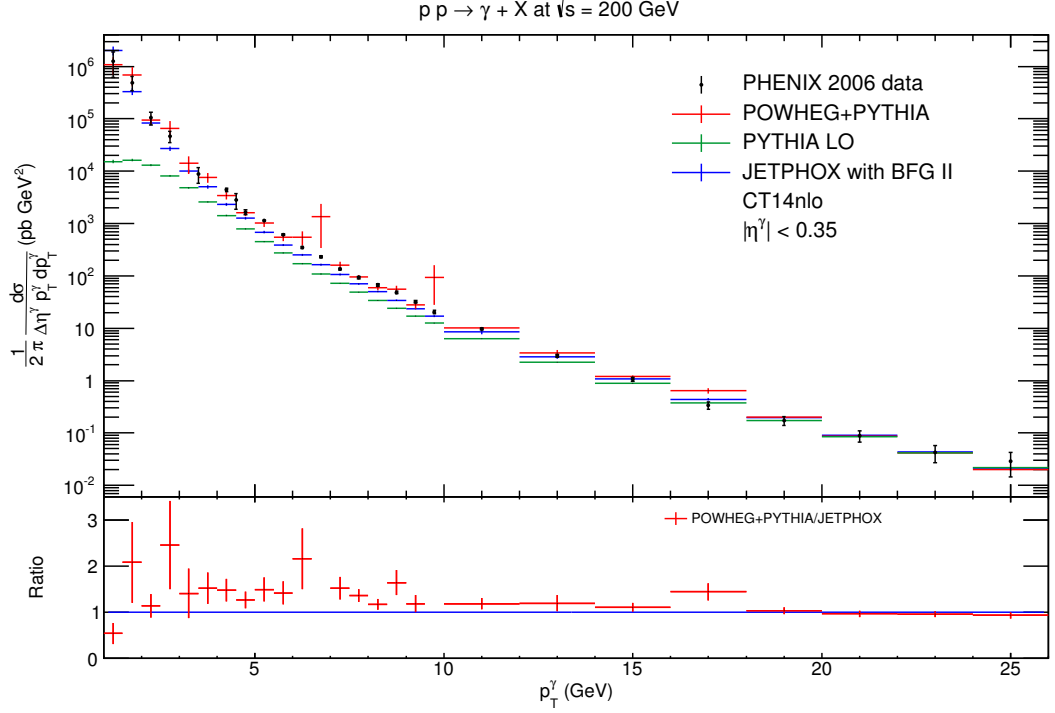


Figure 6.15: PYTHIA, JETPHOX and POWHEG+PYTHIA predictions compared to PHENIX prompt photon data. POWHEG uses `bornsuppfact` 10.

up to  $p_T = 14$  GeV;<sup>20</sup> the LO direct contribution is simply not sufficient for the correct normalization of the prompt photon cross section in this region. The showered POWHEG result in Fig. 6.15 improves both predictions below 10 GeV except for the pathological outliers between 3 GeV – 4 GeV and above 5 GeV and 7.5 GeV. Above 10 GeV the POWHEG+PYTHIA predictions perform worse than JETPHOX in the next five bins. It has been checked that this disagreement in the higher  $p_T$  region increases for `bornsuppfact` 5.

Using `bornsuppfact` 100, on the other hand, has been found to increase the overall agreement with the data (again apart from some peaks), as depicted in Fig. 6.16. The explanation for this behaviour is that, for the region above 10 GeV, the other values for `bornsuppfact` do not provide enough statistics as they strongly emphasize the range below 10 GeV. The better agreement of the `bornsuppfact` 100 with the data below 10 GeV is most likely due to the fact that the `bornsuppfact` 10 (and smaller) choice highlight too much of the unphysical, very low  $p_T$  region below 1 GeV, which results in a proliferation of peaks. As discussed earlier, this is inherently a problematic region for

<sup>20</sup>The turnover in the first two bins is due to an implicit  $p_T^{\min} = 1$  GeV cut on the hard process in PYTHIA and is not of a physical origin. In reference to what has been said about POWHEG's `bornktmin`, it must be noted though that this cut affects only the immediate neighbourhood of the cut, since for the LO direct contribution, the generation cut is directly linked to the photon  $p_T$ .

Figure 6.16: Same as Fig. 6.15 with `bornsuppfact` 100.

the perturbative hard process: A simple Born  $k_T$ -cut can not directly be translated into consequences for the photon  $p_T$ -spectrum at NLO (and even if it could, there would still be no definite fixed, physical value for this cut one would have to choose). Similarly, it is not known beforehand, what choice of `bornsuppfact` will reproduce the low  $p_T$  photon spectrum. In that sense, the results of Figs. 6.15, 6.16 can be seen as a fit of `bornsuppfact`. This problem can only be circumvented if a physical mechanism, for instance parton saturation, would be somehow employed to counteract the generation of hard events in unphysical regions.

To elaborate on the assessment of Sec. 6.3.3, that the fragmentation contribution is correctly simulated by the parton shower, a comparison of the photon  $p_T$ -spectrum and the transverse momentum of vector mesons is shown in Fig. 6.17. The vector mesons have been produced in PYTHIA via hard LO QCD processes, corresponding to the hard contributions underlying the LO fragmentation contribution in a fixed order calculation, and have been scaled by the ratio of electromagnetic coupling  $\alpha$  and squared meson decay constants  $f_V^2$ , as specified for the VMD (3.8). These decay constants can be found in [64]:

$$\begin{aligned} f_\rho^2 &= 2.02, \\ f_\omega^2 &= 23.2, \\ f_\phi^2 &= 13.96. \end{aligned}$$

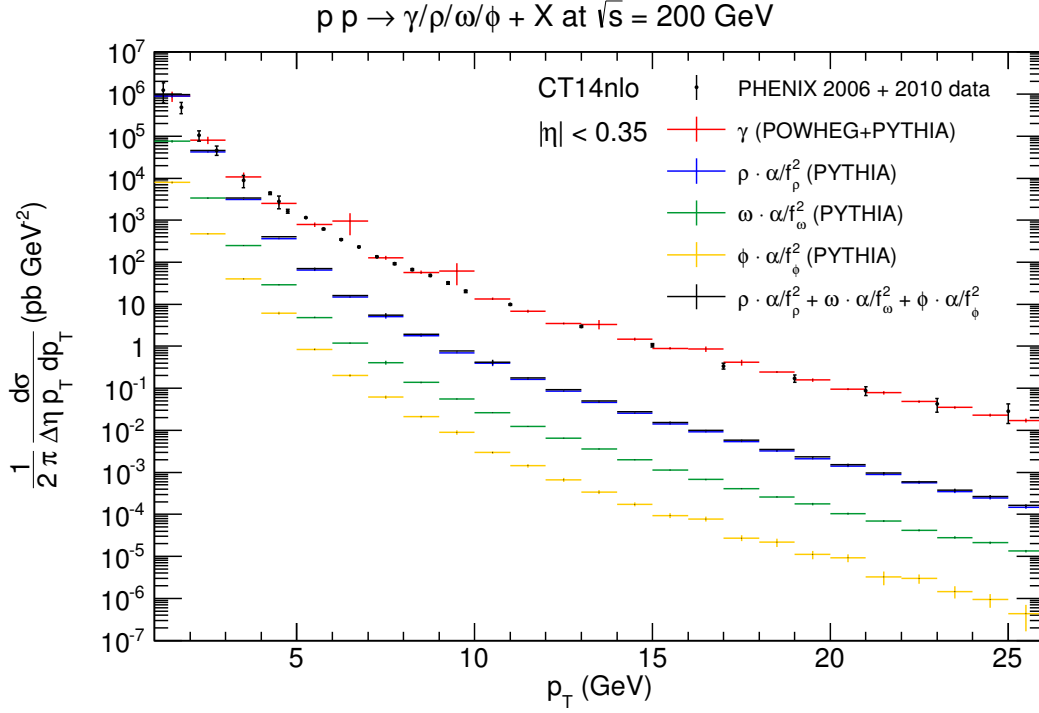


Figure 6.17: Hadronic input to the fragmentation contribution simulated by vector mesons according to the VMD. The sum of VMD contributions (in black) would have to be added to the photon spectrum to include the purely hadronic photon component.

As such, Fig. 6.17 gives a hint of the non-perturbative, hadronic input to the fragmentation function, which is not simulated by the `POWHEG BOX` implementation. These non-perturbative contributions are roughly of the same order as the data or showered `POWHEG` results only below 5 GeV and are completely dominated by the  $\rho$ -meson. If one were to add these contributions to the photon spectrum, the first two points of the `POWHEG` predictions would be roughly doubled, which would not increase the agreement of data and theory in this case. Thus it seems, that the hadronic input is not needed. Indeed, it has been argued before that the VMD input's influence on the fragmentation function strongly depends on the factorization scheme and it may thus be consistent to dispense with the VMD.

#### 6.4.2 Isolated photons

PHENIX data on the ratio of isolated to inclusive prompt photons have been published in [107]. As specified therein, an energy deposition of at most 10 % of the photon energy in a cone

$$R_{\text{isol}} = \sqrt{(\Delta\Phi)^2 + (\Delta\eta)^2} \leq 0.5$$

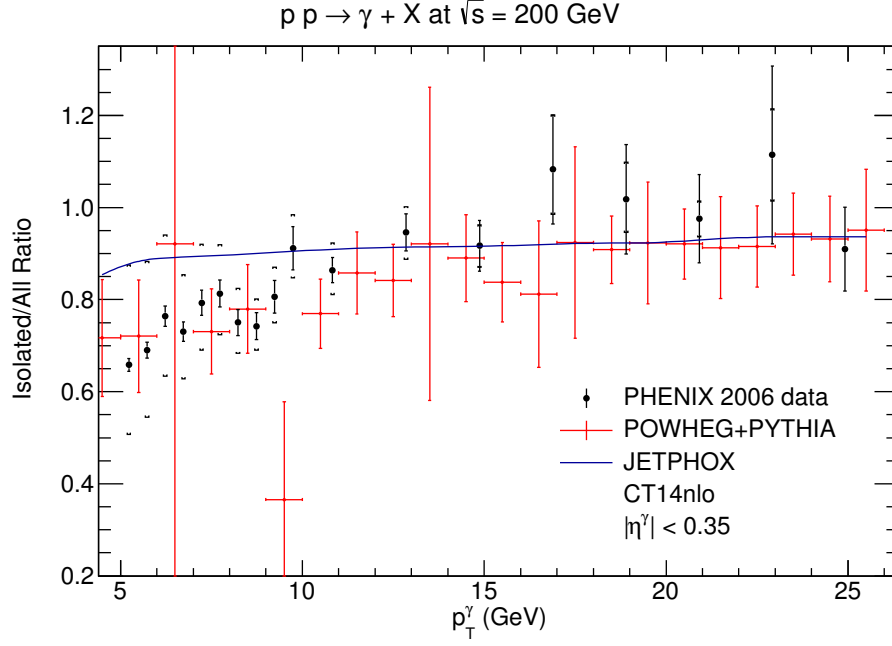


Figure 6.18: Ratio isolated to inclusive prompt photons as measured by PHENIX and predicted by JETPHOX and showered POWHEG using `bornsuppfact 100`. The data are shown with statistical (bars) and systematic (brackets) uncertainties.

around the photon momentum is allowed for the photon to be deemed isolated. This type of cut can be readily employed in JETPHOX, where it restricts the energy of the additional parton produced in the the real corrections. Such a cut is certainly even more realistic when applied to a fully showered and hadronized event, as produced by the POWHEG+PYTHIA combination. Here, in the analysis of the showered events, the energies of all final state particles in the allowed  $\eta$ -range which fall in the cone defined by  $R_{\text{isol}}$  (apart from the photon) are summed and compared to the photon energy to then apply the isolation cut.

The comparison of PHENIX data, JETPHOX and POWHEG+PYTHIA is depicted in Fig. 6.18. The fixed order result from JETPHOX follows the trend of the data in the low- $p_T$  region only slightly and can only be said to describe the data at the brim of the systematic uncertainties. In Ref. [107] scale variations of the NLO result are shown, too, and do not significantly improve the result, as they largely cancel out in the ratio. The POWHEG+PYTHIA prediction, on the other hand, follows the data more closely, reproducing the decrease in the ratio below 10 GeV and in general agreeing with the data when taking the statistical error bars of the theory prediction into account. Outliers, like the one at the 9 GeV bin, correspond to the peaks at the same places in Fig. 6.17 or Fig. 6.16 and are thus artifacts of the `bornsuppfact`-regularization.

Runs with other settings of `bornsuppfact`, with and without using `doublefsr`, have been tested, too, and found to follow the trend of the data. However, these results are struck by much stronger fluctuations, enhancing those seen in the corresponding photon  $p_T$ -spectra in the last sections.

### 6.4.3 Leading jet and charged hadron

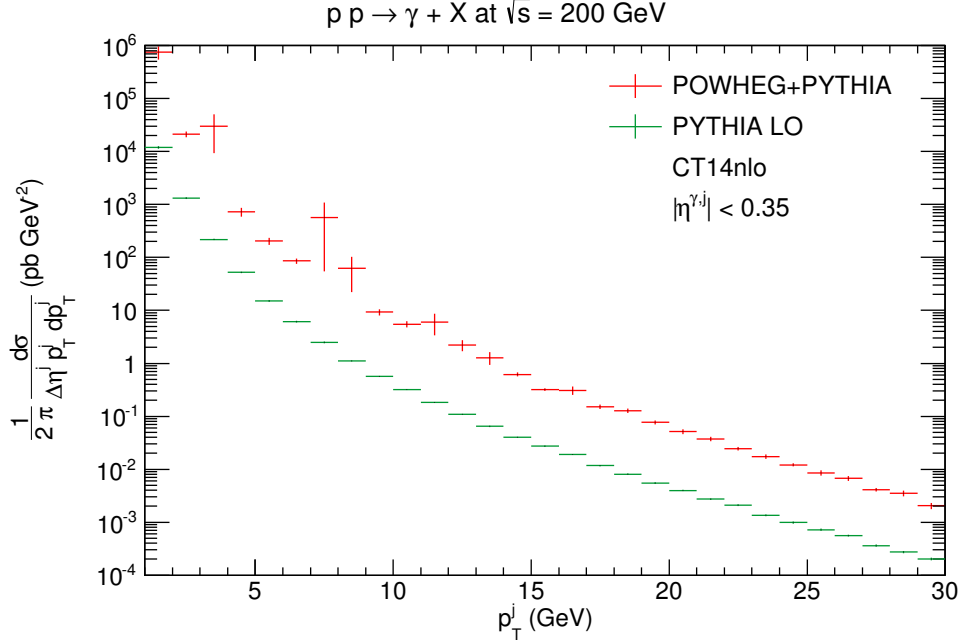


Figure 6.19: Transverse momentum distribution of the leading jet (comprised of charged hadrons) in events with a photon as predicted by PYTHIA, i.e. in LO, and POWHEG+PYTHIA at NLO.

As explained in the previous chapter, photons can be used in heavy ion collisions to gauge the quenching of an associated jet balancing the photon momentum. The picture of a photon exactly balancing the transverse momentum of an away-side jet holds though only in LO. Thus it is important to assess the impact of NLO corrections on the spectrum of the associated jet and on photon-jet-correlations (to be discussed in the following sections).

To identify the leading jet, `FastJet` [178] is employed to find the jet with the hardest  $p_T > 1$  GeV in events with a photon; using the anti- $k_T$  jet-finding algorithm [179] with a cone parameter  $R_{\text{jet}} = 0.4$  to assemble jets from the charged hadrons in the pseudorapidity-range  $|\eta^h| < 0.35$ .<sup>21</sup> Fig. 6.19 shows a comparison of showered LO and NLO via PYTHIA and showered POWHEG results, respectively. Through the NLO correc-

<sup>21</sup>The cone defined by  $R_{\text{jet}}$  actually exceeds the PHENIX pseudorapidity range, so that the jet is not localized in  $\eta$ .

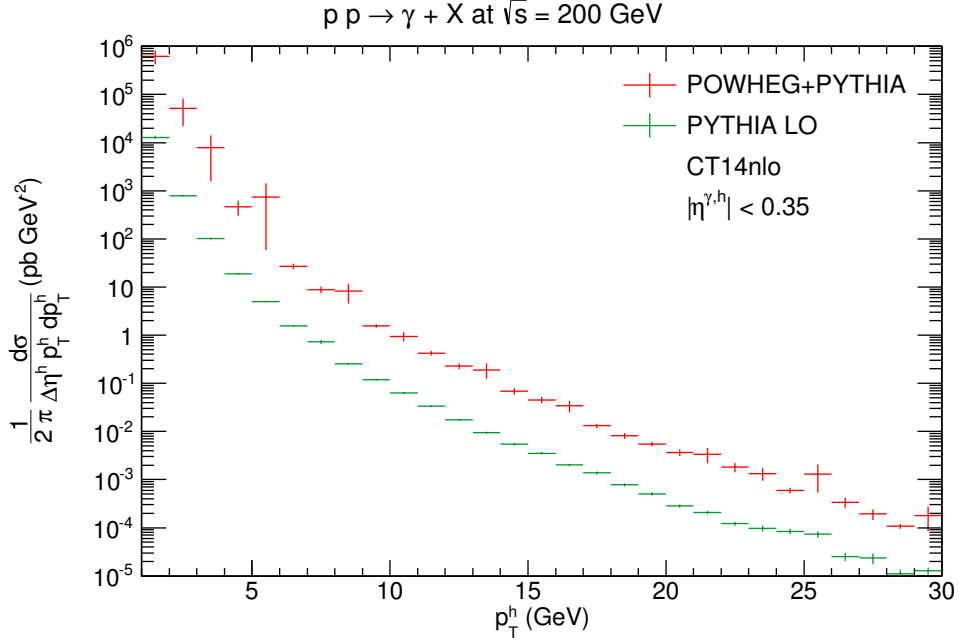


Figure 6.20: Transverse momentum distribution of the charged hadrons in events with a photon as predicted by PYTHIA and POWHEG+PYTHIA.

tions the normalization of the distribution is enhanced by an order of magnitude over the depicted  $p_T$ -range. In contrast to the photon- $p_T$  spectrum, Fig. 6.16, the LO and NLO results do not converge for large  $p_T$ . The reason for this is that PYTHIA includes only LO direct events, i.e. the photon is as hard as the balancing jet, whereas the POWHEG BOX implementation produces events where the photon is rather soft, while the jet can be balanced by another jet, via the fragmentation contribution. As the latter events are generated through photon radiation off  $f_b^{\text{QCD}}$  flavour structures, Fig. 6.19 basically amounts to a comparison of LO direct photon and LO dijet production.

In reality, PHENIX does not measure the leading jet but rather the charged hadrons in events with photons [143]. The transverse momentum distribution of these is shown in Fig. 6.20. Clearly, the result is very similar to the leading jet – the spectrum is falling slightly faster with increasing  $p_T$  – and the interpretation of the jet-result carries over since the underlying production mechanisms of both observables are the same.

#### 6.4.4 Transverse momentum of photon-jet and -hadron pairs

More interesting than the  $p_T$ -distribution of single photons, hadrons or jets are observables related to photon-hadron- or photon-jet-pairs, as correlations profit predominantly from parton shower corrections.

Figs. 6.21 and 6.22 show the  $p_T$ -distribution of pairs consisting of a photon and the leading jet (as defined in the last section) or a charged hadron, respectively (both are again required to have  $p_T > 1$  GeV). At fixed leading order (i.e. LO without shower) the

pair-momentum would be strictly zero, corresponding to a  $\delta$ -distribution in the pair- $p_T$ -differential cross section. Through the shower, the  $\delta$ -distribution is evidently smeared out in the PYTHIA predictions. Furthermore, since it is highly improbable that the hard process configuration is not reshuffled by the shower algorithm, there are virtually no events with pair- $p_T$  equal to zero, which in turn leads to the appearance of a turnover in the spectra at low  $p_T$ . In the figures this turnover is only suggested by a decrease in steepness in the low- $p_T$  bins, but it is fully visible with finer binning.

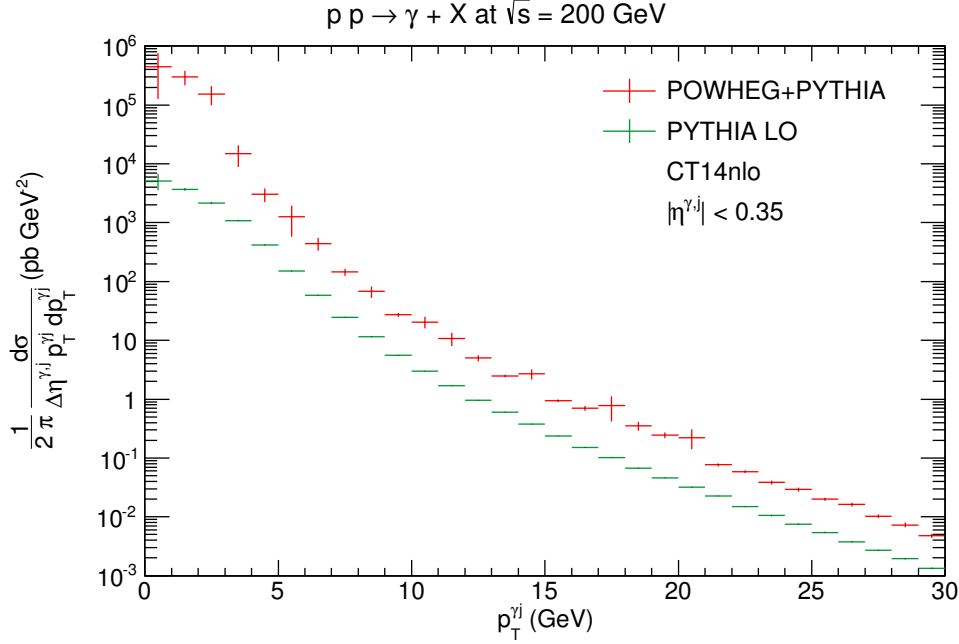


Figure 6.21: Transverse momentum distribution of the leading jet-photon-pair from PYTHIA and POWHEG+PYTHIA.

The POWHEG+PYTHIA results exhibit the same characteristic turnover in the spectrum, but at the same time improve the normalization. In both figures the largest NLO correction is to be found in the lowest  $p_T$  bins. It is interesting to note, however, that the POWHEG+PYTHIA results for the photon-jet-pair in Fig. 6.21 suggest a constant  $K$ -factor at larger  $p_T$ , while for the photon-hadron-pair in Fig. 6.22 the results of PYTHIA and POWHEG+PYTHIA converge. The difference in the photon-jet-pair spectrum is due to the fact that in PYTHIA it is improbable to produce a leading jet with a large  $p_T^{\gamma j}$ , while in POWHEG the leading jet can have a large  $p_T^{\gamma j}$  already before applying the shower, namely by means of the real radiation corrections. One would thus expect that also the pair- $p_T$  with the leading hadron exhibits a constant  $K$ -factor. However, the (not shown) leading hadron distribution rather resembles Fig. 6.22 than Fig. 6.21, which suggests that the hadrons which are part of a photon-hadron-pair with large  $p_T^{\gamma h}$  depend only weakly on the hard process parton configuration.

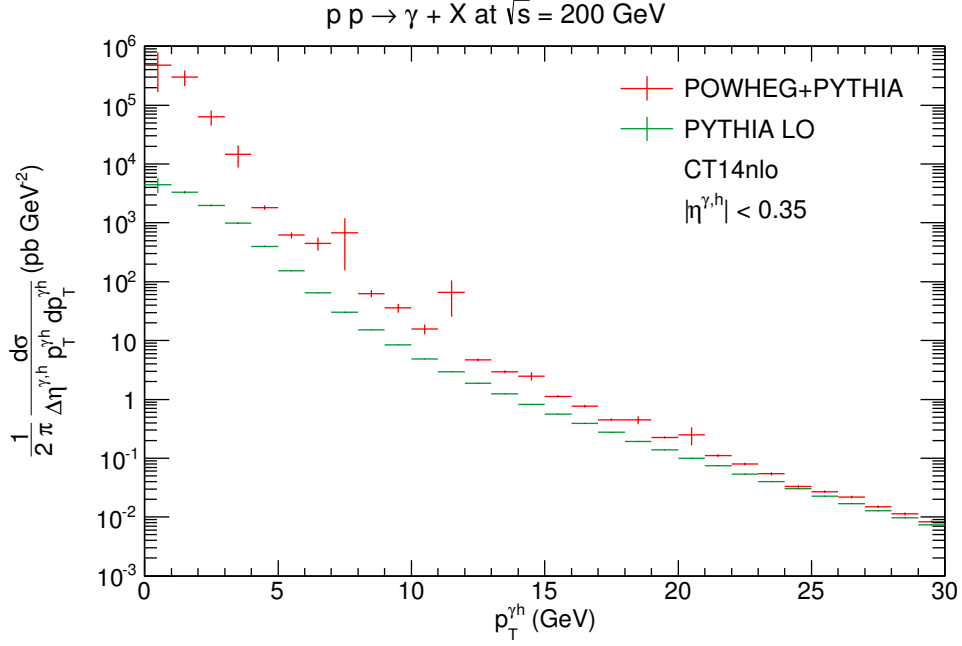


Figure 6.22: Transverse momentum distribution of the charged hadron-photon pairs from PYTHIA and POWHEG+PYTHIA.

In any case, jet- and hadron-correlations, it is mandatory to include the NLO corrections due to their largeness if one wants to establish a pQCD reference for possible medium modifications in a heavy ion setting.

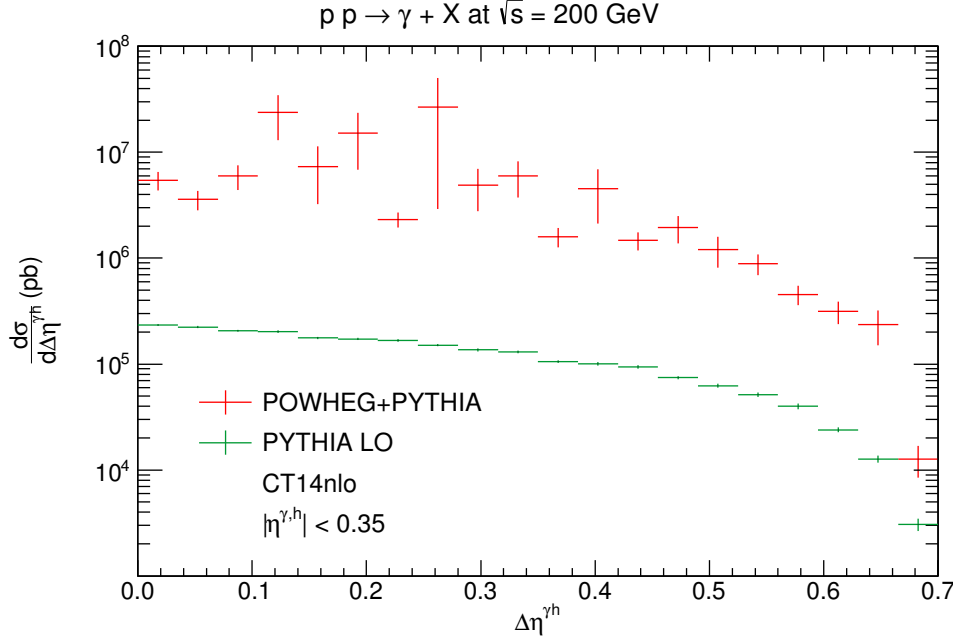
#### 6.4.5 Rapidity correlation of photon-hadron-pairs

An observable quantifying the separation of the pair-particles in beam direction is the rapidity difference  $\Delta\eta^{\gamma j} = |\eta^\gamma - \eta^j|$  or  $\Delta\eta^{\gamma h} = |\eta^\gamma - \eta^h|$  (in  $pp$ - or  $AA$ -collisions, definitions not taking the absolute value would of course be symmetric about  $\Delta\eta = 0$ ). If the jet or parton fragmenting into a hadron has to travel through a medium, it is expected that the  $\Delta\eta$ -distributions, i.e. the rapidity-correlations, are modified by the flow properties of the expanding fireball.<sup>22</sup>

Fig. 6.23 shows the  $\Delta\eta^{\gamma h}$ -distribution, where, similar to the last section, all hadrons with  $p_T > 1$  GeV in events with photons have been considered. The corresponding leading jet-correlation is nearly identical, only with slightly larger errors and falling somewhat faster at large  $\Delta\eta$ , which is why it is not reproduced here. Again, the pronounced feature of the NLO matched result is a larger normalization (and more statistical fluctuation).

<sup>22</sup>Usually, these types of “angular” correlations are measured as functions of both  $\Delta\eta$  and  $\Delta\phi$ , e.g. [180].



Figure 6.23:  $\Delta\eta^{\gamma h}$ -distribution in PYTHIA and POWHEG+PYTHIA.

#### 6.4.6 Azimuthal correlation of photon-hadron-pairs

The azimuthal angle is now the last missing component, after having obtained the pair  $p_T$  and the rapidity difference, if one aims at accessing the full three-dimensional orientation of the particle-pairs. As mentioned in the last chapter, the distribution of the azimuthal angle  $\Delta\phi$  between two particles in heavy ion collisions can be related to the elliptic flow of the fireball, and by that to the shear viscosity of the medium. As usual, it is important to have a correct assessment of the correlation in the vacuum as a benchmark.

Azimuthal photon-hadron-correlations have been measured by PHENIX [143] in  $pp$  and AuAu (in the 0%–20% centrality class) collisions. The latter exhibited a significant suppression of the correlation for the away-side, i.e. at large  $\Delta\phi$ , w.r.t. the former, indicating a medium induced suppression of the hadrons balancing the photon. The  $pp$ -data of that publication have been obtained by employing separate  $p_T$ -cuts on the photon- and hadron-momenta, namely

$$5 \text{ GeV} < p_T^\gamma < 7 \text{ GeV}$$

$$3 \text{ GeV} < p_T^h < 5 \text{ GeV}$$

while the setup is otherwise the same as in the last sections. In Fig. 6.24 PYTHIA and POWHEG+PYTHIA predictions are shown in comparison to said data. The distributions are shown in a ZYAM (zero yield at minimum) [181] representation, which for practical purposes here means that the PYTHIA and POWHEG+PYTHIA predictions are subtracted by their minimum in  $\Delta\Phi$  and normalized to the number of events with a photon (the trigger).

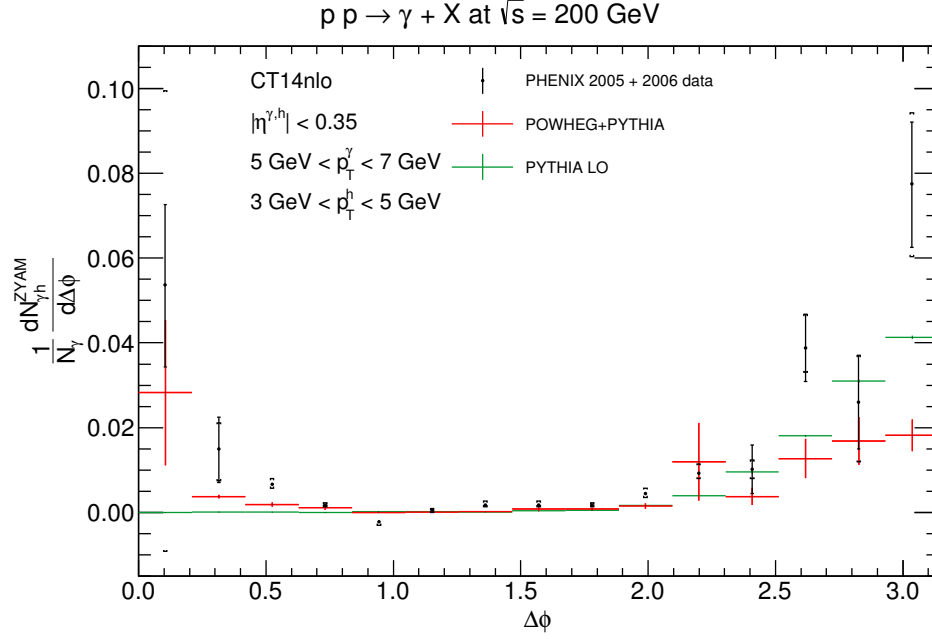


Figure 6.24: Azimuthal correlation in PYTHIA and POWHEG+PYTHIA compared to PHENIX data.

In a fixed order computation at LO the distribution would exhibit only a  $\delta$ -peak at  $\Delta\phi = \pi$ . The showered LO by PYTHIA can be seen to again smear out this peak over a finite range (roughly down to  $\Delta\phi = \pi/2$  in Fig. 6.24), following the experimental data – which are fluctuating – closely in the away-side region. However, PYTHIA is unable to predict the rise in the near-side region, since it does not include real radiation corrections and hence no fragmentation contributions. The showered POWHEG predictions, on the other hand, follow the data over the complete  $\Delta\phi$ -range; though, here, too, mostly lying below the data. That the PYTHIA results lie above POWHEG+PYTHIA at the away-side is an artifact of the ZYAM method, since the minimum in the POWHEG+PYTHIA distribution is roughly an order of magnitude larger than the PYTHIA minimum – clearly, at NLO there is a higher probability of producing a hadron at  $\pi/2$  w.r.t. to the photon than at LO.

An estimation of the fragmentation and direct contributions to the POWHEG+PYTHIA result is shown in Fig. 6.25 via the contributions from non-isolated and isolated photons to the azimuthal-correlation.<sup>23</sup> Here, the photon-isolation criterion from Sec. 6.4.2 has been used again. Fig. 6.25 has been rebinned (in comparison to Fig. 6.24) to tame the fluctuations. Additionally, the errors are not shown for better visibility of the general trend. The near-side is dominated by non-isolated photons – as expected – which include

<sup>23</sup>Of course, the fragmentation contribution of a fixed order calculation is not equal to the non-isolated contribution shown here, but, at this CM energy, the former is almost completely included in the latter.

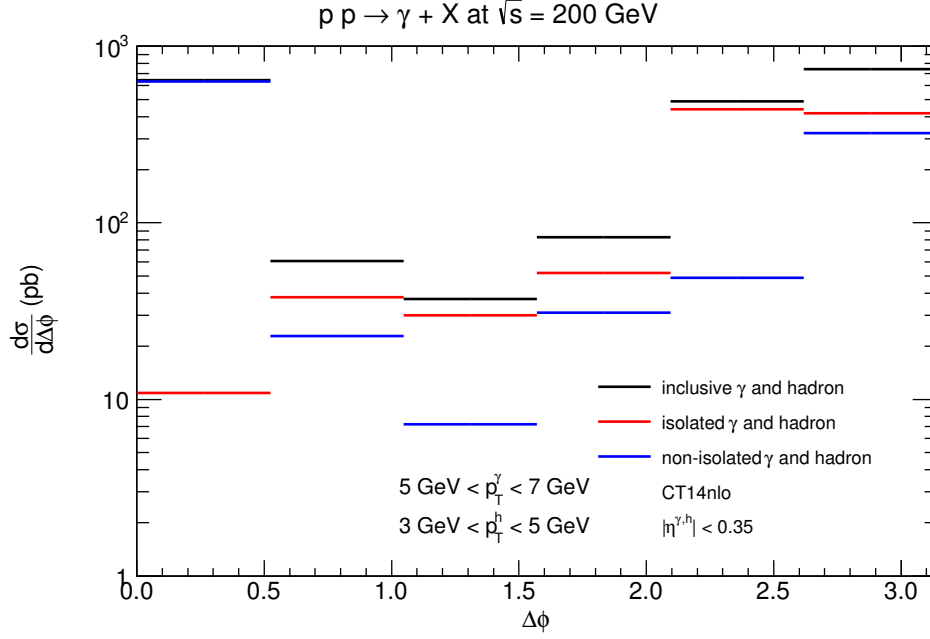


Figure 6.25:  $\Delta\phi$ -differential cross section for the POWHEG+PYTHIA result in Fig. 6.24 broken down into contributions from isolated and non-isolated photons.

the fragmentation contribution, while the isolated photon contribution outweighs them for the rest of the  $\Delta\phi$ -range. However, even at the away-side the non-isolated photons contribute roughly 40 %, which is why PYTHIA (not shown here) would not be able to provide the correct normalization even in this region.

All in all, the results of the last section have shown that the prompt photon predictions of the parton shower matched NLO implementation are – in principle – superior to both the fixed order and the simple parton shower predictions. In practice, the shown results, while reproducing the given experimental data, exhibit a lack of accuracy and have to be improved by further increasing the statistics and optimizing the parameters of the POWHEG BOX and PYTHIA to generate high precision predictions.

## 7 Conclusion and Outlook

In the preceding chapters, detailed calculations and predictions for prompt photon production at NLO and NLO matched to a parton shower have been described. A fixed order calculation based on the Catani-Seymour dipole formalism and its implementation in a FORTRAN code, named `phoSec`, has been presented and shown to reproduce results obtained with `JETPHOX`. This laid the groundwork for a `POWHEG BOX` implementation of the process.

`JETPHOX`, on the other hand, has been modified slightly to examine low- $p_T$  photons in the region measured by experiments committed to the exploration of the creation of the quark-gluon-plasma. It has been shown that, in the signal region for thermal photons, the photon fragmentation contribution can not be neglected – rather that it dominates over the direct component. Due to this fact, an evaluation of new PHENIX prompt photon data with higher statistics has been found to have the potential to improve one of the major sources of theoretical uncertainty, namely the photon fragmentation function.

Furthermore, by comparing `JETPHOX` results for heavy ion collisions, incorporating initial state effects via nPDFs, to ALICE direct photon measurements, it has been possible to verify that the impact of theoretical pQCD uncertainties on the inverse slope parameter, which is an indicator of the fireball temperature, is rather insignificant. However, by subtracting the NLO prompt photon predictions from the direct photon signal, a larger  $p_T$ -range for the thermal photon signal than used in the initial analysis has been made visible.

To improve on the fixed order results, an implementation of prompt photon production at NLO into the `POWHEG BOX` framework has been presented. First results have been compared to PHENIX data and showed an improvement over both `PYTHIA`'s showered LO and `JETPHOX`'s fixed order NLO, albeit struck by unphysical peaks in the spectrum.

The work presented here is of course not the endpoint of the development of the `POWHEG BOX` prompt photon implementation. Indeed, there are several questions that might be worth of further investigation. Do the `POWHEG` predictions improve if, for the real radiation processes, a full competition between pure QCD and QED processes is employed, i.e. by including NLO fragmentation processes of  $\mathcal{O}(\alpha_s^3)$ ? Certainly, statistical problems would get worse in that case, due to the dominance of pure QCD processes, and it has to be considered if the effort needed for overcoming this problem is justified compared to the expected improvement. Furthermore, what is the effect of the inclusion of QED virtual corrections? Comparing QED evolved and normal PDFs has not led to a significant difference in the  $p_T$  spectra, such that including full virtual QED corrections (as the hard process counterpart to QED PDFs) is also not expected to give

a large contribution. Nonetheless, it would erase a momentum of arbitrariness in the implementation presented here.

Some technicalities which might be improved in the `POWHEG BOX` itself, are, for instance, that the upper bounding functions for QED radiation (`iupperfsr` and `iupperisr`) are both based on  $\alpha_s$  evolution (as can be seen in the `pt2solve` function and App. C,D of Ref. [46]). Maybe the effectiveness of the generation of QED radiation could be improved slightly by implementing extra bounds for QED. In addition, differing lower cut-off scales  $p_T^{\min}$  for QED and QCD radiation could erase the problem that the GPEG, instead of `POWHEG`, generates the hardest photon at very low scales. These are, however, by no means pressing issues.

More important is a detailed analysis of `POWHEG` prompt photon predictions at LHC energies, which, depending on the  $p_T$ -range considered, requires computational efforts beyond those undertaken in this work to reach acceptable statistics. It must also be noted, that at this point a lot of free parameters at the interface between `POWHEG BOX` and `PYTHIA 8`, namely those of the `PowhegHooks` class, have not yet been systematically studied for different observables. It may well turn out that, for instance, a different definition of the hard scale improves the predictions considerably.

In the simulation of the fragmentation function by the parton shower and subsequent GPEG event handling, it would be interesting to see if there is a way to incorporate the non-perturbative, hadronic inputs – as long as the precision of the predictions is at some point high enough to expose a need for these contributions. However, this kind of “hadronization into photons” would certainly need a retuning of the phenomenological GPEG machinery. An exploration of GPEG tunes for NLO matching might, in general, at some point increase the accuracy and reliability of `POWHEG` predictions.

Since quite some results on analytically resummed prompt photon production are available it would also be interesting to see, how predictions of the `POWHEG BOX` implementation compare to these theoretical predictions.

Further down the road, a combination of the `POWHEG BOX` implementation with in-medium simulations might become feasible and enable simulations of the medium-modifications of the FF and the quenching of the jet balancing a photon in heavy ion collisions.

# A Conventions

As is common practice in particle physics, natural units

$$\hbar = c = 1$$

are used throughout this thesis.

Where not stated differently in the text, the following conventions hold for indices: Latin indices are used for general degrees of freedom, such as colours

$$i, j, \dots = 1, \dots, N_c,$$

$SU(N_c)$ -generators/gluons

$$a, b, \dots = 1, \dots, N_c^2 - 1$$

or quark flavours

$$f = 1, \dots, N_f.$$

Greek indices are used exclusively to label coordinates of Minkowski space, e.g.

$$\mu, \nu, \dots = 0, \dots, D - 1,$$

with  $D$  the dimension of space-time, and can be lowered and raised with the Bjorken-Drell metric

$$g_{\mu\nu} = \begin{cases} 1 & \text{if } \mu = \nu = 0, \\ -1 & \text{if } \mu = \nu = 1, \dots, D - 1, \\ 0 & \text{else.} \end{cases}$$

Einstein's summation convention is used for pairs of one upper and an identical lower Greek index and for repeating either upper or lower Latin indices. A dot is used for inner products of Minkowski space, i.e. for two four-vectors

$$p \cdot k = p^\mu k_\mu = g_{\mu\nu} p^\mu k^\nu.$$

The notation  $p^2$  is meant to be the square of the four-vector,  $p^2 = p_\mu p^\mu$ , if not specified otherwise in the context.

Furthermore, the Feynman slash notation is used to denote contractions of four-vectors with Dirac matrices

$$\not{p} = p_\mu \gamma^\mu.$$

Arbitrary dimensions of Minkowski space are given as a deviation from 4 dimensions via

$$D = 4 - 2\varepsilon,$$

such that the Standard Model couplings attain momentum dimension  $\varepsilon$ .

The Lie-algebra of  $SU(N_c)$  is defined through the commutation relation

$$\left[T^a, T^b\right] = \mathrm{i}f^{abc}T^c.$$

In the fundamental representation the generators are normalized as

$$\mathrm{tr}\left[T^a T^b\right] = \frac{1}{2}\delta^{ab},$$

and the adjoint representation is defined by

$$(T_{\mathrm{adj}}^a)_{bc} = -\mathrm{i}f^{abc}.$$

Traces over Dirac-matrices are denoted by  $\mathrm{Tr}[\dots]$ , colour-traces by  $\mathrm{tr}[\dots]$ .

When it comes to discussing cross sections, I will often use differentials  $\mathrm{d}\sigma$ . They have to be understood as shorthand for differential cross sections or cross sections integrated over some part of the phase space. For instance, writing “ $\mathrm{d}\sigma$  is small” means that a corresponding  $\sigma$  integrated over some part of the phase space, or totally differential cross section, etc. is small.

## B Feynman Rules

**External Fermions** (colour vector in fundamental representation implicit)

	$u_s(p)$		$\overline{v_s(p)}$
	$\overline{u_s(p)}$		$v_s(p)$

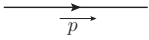
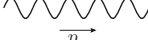
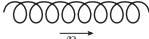
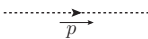
**External Photons**

	$\varepsilon_\mu^\lambda(p)$		$\varepsilon_\mu^{\lambda*}(p)$
---	------------------------------	--	---------------------------------

**External Gluons** (colour vector in adjoint representation implicit)

	$\varepsilon_\mu^\lambda(p)$		$\varepsilon_\mu^{\lambda*}(p)$
---	------------------------------	--	---------------------------------

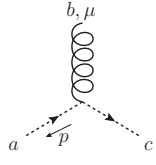
**Propagators** (colour-diagonal)

	$\frac{i(\not{p}+m)}{p^2-m^2+i\epsilon}$		$\frac{-ig_{\mu\nu}}{p^2+i\epsilon}$
	$\frac{-i\left(g_{\mu\nu}-(1-\xi)\frac{p_\mu p_\nu}{p^2}\right)}{p^2+i\epsilon}$		$\frac{i}{p^2+i\epsilon}$

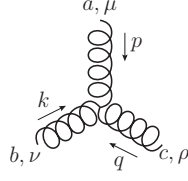
**Vertices**

	$iQ_f e \gamma^\mu$		$ig_s \gamma^\mu T^a$
---	---------------------	--	-----------------------

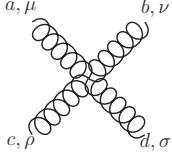




$$-g_s f^{abc} p^\mu$$



$$g_s f^{abc} [g^{\mu\nu} (p - k)^\rho + g^{\nu\rho} (k - q)^\mu + g^{\rho\mu} (q - p)^\nu]$$



$$-ig_s^2 \left[ f^{abe} f^{cde} (g^{\mu\rho} g^{\nu\sigma} - g^{\mu\sigma} g^{\nu\rho}) + f^{ace} f^{bde} (g^{\mu\nu} g^{\rho\sigma} - g^{\mu\sigma} g^{\nu\rho}) + f^{ade} f^{bce} (g^{\mu\nu} g^{\rho\sigma} - g^{\mu\rho} g^{\nu\sigma}) \right]$$

## Counterterms



$$i(\delta Z_\Psi \not{p} - \delta Z_m m)$$



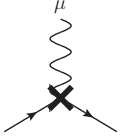
$$i\delta Z_\eta p^2$$



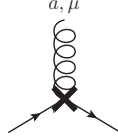
$$-i\delta Z_A^{\text{QED}} (g^{\mu\nu} p^2 - p^\mu p^\nu)$$



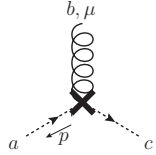
$$-i\delta Z_A (p^2 g^{\mu\nu} - p^\mu p^\nu)$$



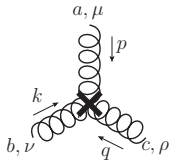
$$iQ_f e \gamma^\mu \delta Z_e$$



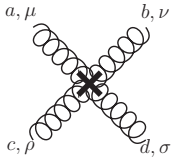
$$i\delta Z_g g_s \gamma^\mu T^a$$



$$-\delta Z_{g\eta} g_s f^{abc} p^\mu$$



$$g_s \delta Z_{g3} f^{abc} [g^{\mu\nu} (p - k)^\rho + g^{\nu\rho} (k - q)^\mu + g^{\rho\mu} (q - p)^\nu]$$



$$-ig_s^2 \delta Z_{g4} \left[ f^{abe} f^{cde} (g^{\mu\rho} g^{\nu\sigma} - g^{\mu\sigma} g^{\nu\rho}) + f^{ace} f^{bde} (g^{\mu\nu} g^{\rho\sigma} - g^{\mu\sigma} g^{\nu\rho}) + f^{ade} f^{bce} (g^{\mu\nu} g^{\rho\sigma} - g^{\mu\rho} g^{\nu\sigma}) \right]$$

# C Prompt Photon Production Cross Section

## C.1 Leading Order Direct

### C.1.1 Matrix elements

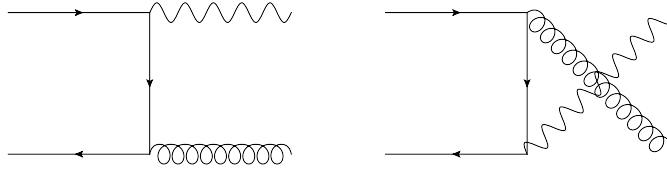


Figure C.1: Feynman diagrams for  $q\bar{q} \rightarrow \gamma g$  at LO.

The production of one on-shell photon via QCD-partons at leading order is given by only two  $2 \rightarrow 2$ -diagram topologies. Considering for example  $q\bar{q} \rightarrow \gamma g$ , one has a  $t$ - and an  $u$ -channel topology, see Fig. C.1, corresponding to the matrix element

$$\mathcal{M}_{q\bar{q} \rightarrow \gamma g} = \mathcal{M}^{(t)} + \mathcal{M}^{(u)}.$$

Now, the cross section, as a measure of the probability for the process to happen, is related to the squared amplitude

$$|\mathcal{M}_{q\bar{q} \rightarrow \gamma g}|^2 = |\mathcal{M}^{(t)}|^2 + |\mathcal{M}^{(u)}|^2 + 2 \operatorname{Re} \left( \mathcal{M}^{(t)} \mathcal{M}^{(u)*} \right).$$

A graphical representation is given by the cut notation, e.g. Fig. C.2, where the left side of the cut corresponds to some  $\mathcal{M}^{(u,t)}$  and the right side to some Hermitian adjoint  $\mathcal{M}^{(u,t)\dagger}$ .

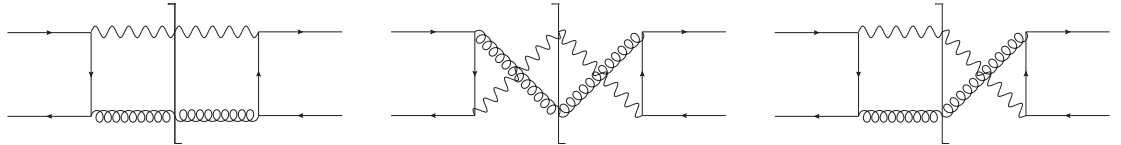


Figure C.2: The LO squared amplitudes for  $q\bar{q} \rightarrow \gamma g$  in cut notation.

After a short calculation, making use of the Feynman rules from App. B, and computing the fermion and colour traces, one finds the spin- and colour-averaged amplitudes for the diagrams in Fig. C.2

$$\overline{|\mathcal{M}^{(t)}|^2} = \frac{32\pi^2\alpha\alpha_s C_F Q^2}{N_C}(\varepsilon - 1)^2 \frac{\hat{u}}{\hat{t}} \quad (\text{C.1})$$

$$\overline{|\mathcal{M}^{(u)}|^2} = \frac{32\pi^2\alpha\alpha_s C_F Q^2}{N_C}(\varepsilon - 1)^2 \frac{\hat{t}}{\hat{u}} \quad (\text{C.2})$$

$$\overline{\mathcal{M}^{(t)}\mathcal{M}^{(u)\dagger}} = \frac{32\pi^2\alpha\alpha_s C_F Q^2}{N_C}(\varepsilon - 1)\varepsilon \quad (\text{C.3})$$

and thus the process to be given by

$$\overline{|\mathcal{M}_{q\bar{q}\rightarrow\gamma g}|^2} = \frac{32\pi^2\alpha\alpha_s C_F Q^2}{N_C}(\varepsilon - 1) \frac{((\varepsilon - 1)\hat{t}^2 + (\varepsilon - 1)\hat{u}^2 + 2\varepsilon\hat{t}\hat{u})}{\hat{t}\hat{u}}, \quad (\text{C.4})$$

where all particles are treated as massless and the computation has been carried through in  $D = 4 - 2\varepsilon$  dimensions for later reference. This result can of course be found in the literature [6] or automatically generated by FormCalc [89] and similar programs. Here, the Mandelstam variables have been defined as

$$\begin{aligned} \hat{s} &= (p_a + p_b)^2 = (p_1 + p_2)^2, \\ \hat{t} &= (p_a - p_1)^2 = (p_b - p_2)^2, \\ \hat{u} &= (p_a - p_2)^2 = (p_b - p_1)^2, \end{aligned} \quad (\text{C.5})$$

while assigning the four-momenta  $p_a, p_b, p_1, p_2$  to  $q, \bar{q}, \gamma$ , and  $g$  respectively.

All LO photon production processes – i.e.

$$\begin{array}{ll} q\bar{q} \rightarrow \gamma g & \bar{q}q \rightarrow \gamma g \\ qg \rightarrow \gamma q & \bar{q}g \rightarrow \gamma \bar{q} \\ gq \rightarrow \gamma q & g\bar{q} \rightarrow \gamma \bar{q} \end{array}$$

– are related to  $q\bar{q} \rightarrow \gamma g$  via crossing symmetry; e.g.  $qg \rightarrow \gamma q$  is obtained by taking the results above and exchanging  $p_b \leftrightarrow -p_2$ , i.e.  $s \leftrightarrow u$ , and supplying an extra factor of  $-1$  to the resulting amplitude accounting for the flip of an external fermion line (this is due to the exchange of particle and antiparticle in Feynman diagrams of averaged amplitudes translating to an exchange of factors  $(\not{p} + m)$  and  $(\not{p} - m)$  in the fermion traces).

### C.1.2 Phase space

The invariant phase space for  $n$  final state particles, produced by initial state particles with momenta  $p_a$  and  $p_b$ , is given by

$$d\Phi^{(n)}(p_a, p_b) = (2\pi)^4 \delta^{(4)}\left(p_a + p_b - \sum_{i=1}^n p_i\right) \prod_{i=1}^n \frac{d^3 p_i}{(2\pi)^3 2E_i}. \quad (\text{C.6})$$

For a huge class of processes of interest this can be simplified to one free variable, namely for  $n = 2$ , massless, spin-averaged processes (whose amplitudes are thus symmetric in the plane perpendicular to the beam direction). It is understood that in the following the equality is meant as holding in case of an integration of a test function.

$$\begin{aligned}
 d\Phi^{(2)} &= (2\pi)^4 \delta^{(4)}(p_a + p_b - p_1 - p_2) \frac{d^3 p_1}{(2\pi)^3 2E_1} \frac{d^4 p_2}{(2\pi)^3} \delta(p_2^2) \theta(E_2) \\
 &= \frac{1}{2(2\pi)^2} \frac{d^3 p_1}{E_1} \delta((p_a + p_b - p_1)^2) \theta(E_a + E_b - E_1) \\
 &= \frac{1}{2(2\pi)^2} \frac{d^3 p_1}{E_1} \delta(\hat{s} - 2p_1 \cdot (p_a + p_b)) \theta(E_a + E_b - E_1)
 \end{aligned} \tag{C.7}$$

At this point it is easiest to chose the center of mass (CM) frame

$$\vec{p}_a + \vec{p}_b = 0$$

with

$$E_a = E_b = \frac{\sqrt{\hat{s}}}{2}.$$

One has

$$\begin{aligned}
 \hat{t} &= -2p_a \cdot p_1 = -2E_a E_1 (1 - \cos(\vartheta)) \\
 d\Omega &= d\varphi d\cos(\vartheta) = \frac{4\pi}{\hat{s}} d\hat{t}
 \end{aligned}$$

with the polar and azimuthal angles  $\vartheta$  and  $\varphi$  and thus obtains

$$\begin{aligned}
 d\Phi^{(2)} &= \frac{1}{2(2\pi)^2} \frac{dE_1 E_1^2 d\Omega}{E_1} \delta(\hat{s} - 2E_1 \sqrt{\hat{s}}) \theta(\sqrt{\hat{s}} - E_1) \\
 &= \frac{d\hat{t}}{8\pi \hat{s}}.
 \end{aligned} \tag{C.8}$$

Alternatively and especially useful in case of jet- or photon-production is the parametrization in terms of the photon's transverse momentum  $p_T$  and rapidity  $y$  w.r.t. the beam axis in the 3-direction, since these are the quantities usually measured [72] (NB: Rapidity  $y$  and the experimentally readily accessible pseudo-rapidity  $\eta$  are interchangeable for massless particles [6]). Since one has to assume a finite  $p_T$  – otherwise the amplitude diverges – one can in general write

$$p = p_T (\cosh(y), \cos(\varphi), \sin(\varphi), \sinh(y)) \tag{C.9}$$

for the four-momentum of a final state particle. Going back to the last line of (C.7) and using

$$d^3 p_1 = dp_T p_T E d\varphi dy \tag{C.10}$$

(where again  $\vartheta$  and  $\varphi$  are the polar and azimuthal angle w.r.t. the beam direction) one finds

$$d\Phi^{(2)} = \frac{1}{4\pi} dp_T dy p_T \delta(\hat{s} - 2p_1 \cdot (p_a + p_b)) \theta(E_a + E_b - E_1). \tag{C.11}$$

To simplify this further, the integral over the momentum fractions of the initial state particles and the parton distribution functions (PDF) have to be considered.

### C.1.3 Cross section

To arrive at the LO cross section the flux factor  $1/(4F)$ , accounting for the flux of initial state partons with momenta  $p_a = x_a p_A$ ,  $p_b = x_b p_B$ , with

$$F(p_a, p_b) = \sqrt{(p_a \cdot p_b)^2 - p_a^2 p_b^2} = x_a x_b \frac{s}{2}, \quad (\text{C.12})$$

where

$$s = (p_A + p_B)^2$$

is the hadronic CM energy squared, and the PDFs have to be included in the calculation. Following the parton model (see Sec. 2.1) the cross section for hadrons  $A$ ,  $B$  producing  $n$  particles  $\{i\}$  and unspecified remnants  $X$  is given as

$$\begin{aligned} d\sigma_{AB \rightarrow \{i\}X}(p_A, p_B) \\ = \sum_{a,b} \int_0^1 dx_a \int_0^1 dx_b f_{a/A}(x_a) f_{b/B}(x_b) \frac{1}{2x_a x_b s} \overline{|\mathcal{M}_{ab \rightarrow \{i\}}|^2} d\Phi^{(n)}(x_a p_A, x_b p_B). \end{aligned} \quad (\text{C.13})$$

Here,  $\overline{|\mathcal{M}_{ab \rightarrow \{i\}}|^2}$  depends on the momenta of the initial state partons  $p_a$  and  $p_b$ . The sum is taken over all partons  $q$ ,  $\bar{q}$  and  $g$ .

To be more specific to photon production in hadron-hadron-collisions, taking (C.13) and inserting (C.11) leads to

$$\begin{aligned} d\sigma_{AB \rightarrow \gamma X}^{(\text{direct})}(p_A, p_B) &= \sum_{a,b,c} \int_0^1 dx_a \int_0^1 dx_b f_{a/A}(x_a) f_{b/B}(x_b) \frac{1}{2x_a x_b s} \overline{|\mathcal{M}_{ab \rightarrow \gamma c}|^2} d\Phi^{(2)} \\ &= \sum_{a,b,c} \int_{x_{\min}}^1 dx_a f_{a/A}(x_a) f_{b/B}(x_b) \frac{1}{8\pi x_a x_b s} \overline{|\mathcal{M}_{ab \rightarrow \gamma c}|^2} dp_T dy \\ &\quad \cdot \frac{x_b e^y}{x_a \sqrt{s}} \theta \left( (x_a + x_b) \frac{\sqrt{s}}{2} - p_T \cosh(y) \right) \end{aligned} \quad (\text{C.14})$$

in the hadron-CM with

$$x_b = \frac{x_a p_T e^{-y}}{x_a \sqrt{s} - p_T e^y}$$

and

$$x_{\min} = \frac{p_T e^y}{\sqrt{s} - p_T e^{-y}}.$$

In the form (C.14), cuts on the photon's transverse momentum and rapidity are easily implemented in the CM frame by restricting the ranges of integration of the variables  $p_T$  and  $y$ .

When using these variables for integration, the relations to the partonic Mandelstam variables may be useful:

$$\hat{s} = x_a x_b s, \quad (\text{C.15})$$

$$\hat{t} = -x_a \sqrt{s} p_T e^{-y}, \quad (\text{C.16})$$

$$\hat{u} = -x_a \sqrt{s} p_T e^y. \quad (\text{C.17})$$

## C.2 Next to Leading Order Direct

### C.2.1 Virtual corrections

The virtual corrections at NLO in  $\alpha_s$  are given by the squared amplitudes of  $\mathcal{O}(\alpha_{\text{em}}\alpha_s^2)$  with one internal (i.e. uncut), closed loop. Since only one closed loop is allowed, the squared amplitudes evidently have to be constructed as interference diagrams of a LO diagram  $\mathcal{M}^{(u,t)}$  on one side of the cut and a loop diagram on the other side. Clearly, there can then be no other partonic processes than those allowed at LO and it is again convenient to compute only  $q\bar{q} \rightarrow \gamma g$  and obtain the other partonic processes via crossing.

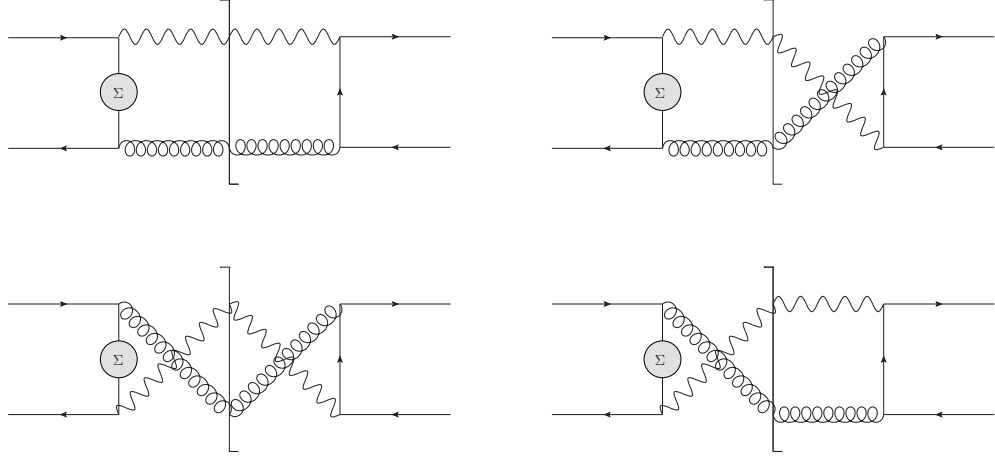


Figure C.3: Skeletons for the internal self energy corrections.

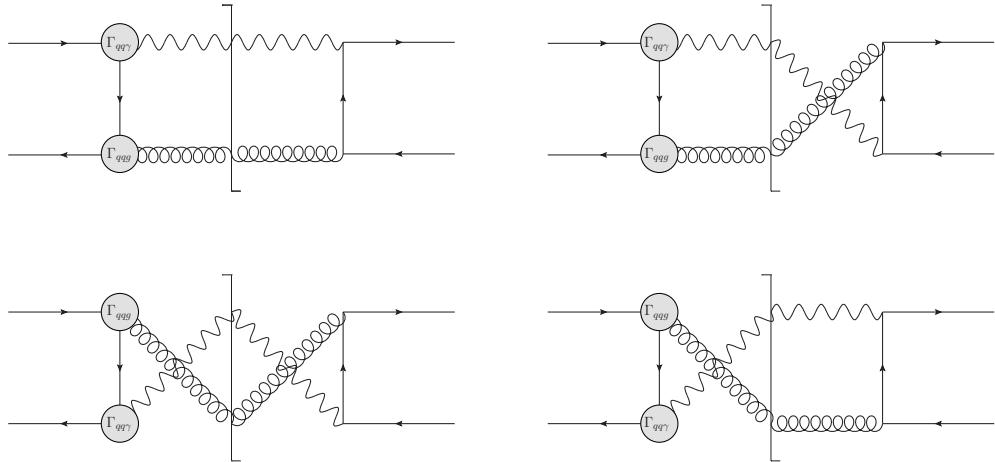


Figure C.4: Skeletons for the virtual vertex corrections. One of the blobs in each skeleton is a placeholder for the virtual correction, while the other blob represents the LO vertex.

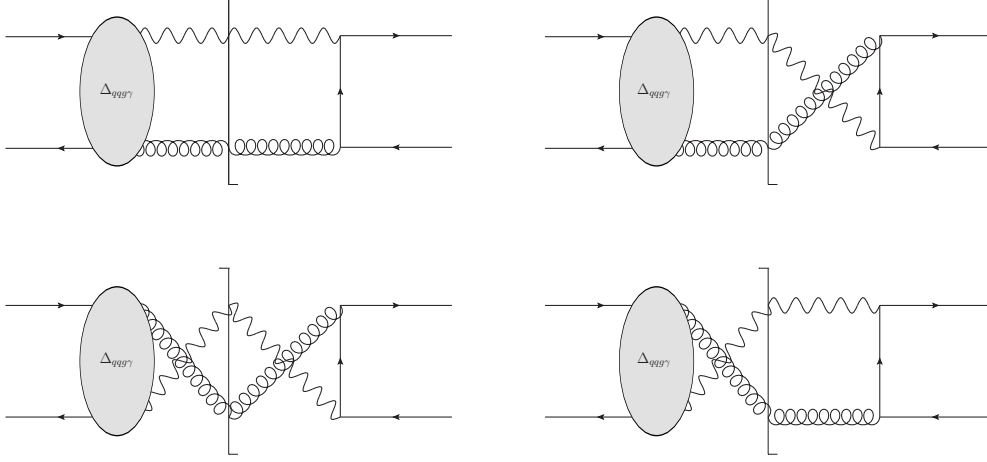


Figure C.5: Skeletons for the virtual box corrections.

There are three types of loop corrections relevant for this process: self-energy, vertex and box corrections. Tadpole corrections, i.e. additional gluon lines ending in a loop, are allowed, too, but vanish, since they entail the trace of a single  $SU(3)_c$  generator in the fundamental or adjoint representation. The self-energy corrections can further be subdivided into self-energy corrections of internal and external propagators. The internal self-energy, vertex and box corrections are shown in Figs. C.3, C.4 and C.5 as “skeletons”, with blobs representing the spots where the amputated (one particle irreducible) loop-diagrams can be plugged in. Not depicted are the self-energy corrections of the external propagators, which I have computed by means of the LSZ formula. In the following, the results for amputated loops will be presented, but not the full results for the amplitude. The latter have been computed by using **FORM** to plug the loop-results into the expressions for the skeleton diagrams, and the results are quite lengthy.

To regularize the UV and IR divergences appearing in the integration over the loop momenta, dimensional regularization is used, i.e. the calculations are carried out in  $D = 4 - 2\varepsilon$  dimensions with  $\varepsilon \neq 0$ , such that a divergence manifests itself as a pole in  $\varepsilon$  for  $\varepsilon \rightarrow 0$ . To be more precise: The UV divergences are regularized by  $\varepsilon > 0$ , IR divergences by  $\varepsilon < 0$ . However, there is no need to go into the specifics of the integration, as the integrals can be reduced to known standard integrals by means of the Passarino-Veltman reduction [36]. The results of these integrals are available analytically and in several numerical libraries, e.g. **QCDLoop** [182] or **LoopTools** [89]. For this work the **LoopTools** library has been used.

The standard tensor integrals are defined (sticking to the **LoopTools** conventions) as

$$\begin{aligned}
 T_{\mu_1, \dots, \mu_M}^N(p_1, \dots, p_N, m_1, \dots, m_N) \\
 = \frac{\mu^{4-D}}{i\pi^{D/2} r_\Gamma} \int d^D l \frac{l_{\mu_1} \cdots l_{\mu_M}}{(l^2 - m_0^2 + i\epsilon) \cdots ((l + \sum_{i=1}^{N-1} p_i)^2 - m_N^2 + i\epsilon)}
 \end{aligned} \tag{C.18}$$

with

$$r_\Gamma = \frac{\Gamma^2(1-\varepsilon)\Gamma(1+\varepsilon)}{\Gamma(1-2\varepsilon)}. \quad (\text{C.19})$$

Here, the momenta  $p_i$  are the external momenta connected to the loop, the masses  $m_i$  are the masses of the particles in the loop, see Fig. C.6. One of the momentum-arguments is of course redundant, due to the implicit momentum conservation.

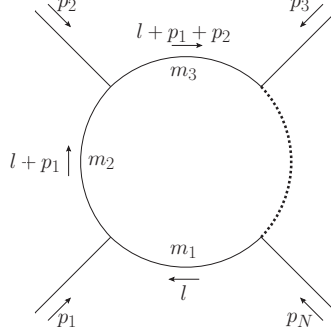


Figure C.6: Assignment of loop momenta.

Instead of  $T^N$ , it is customary to use  $A \equiv T^1$ ,  $B \equiv T^2$ ,  $C \equiv T^3$ ,  $D \equiv T^4$ , and so on. The tensor integrals are then, through a decomposition in Lorentz tensors, related to the scalar integrals (which are provided by `LoopTools`):

$$B^\mu(p, m_1, m_2) = p^\mu B_1(p^2, m_1^2, m_2^2), \quad (\text{C.20})$$

$$B^{\mu\nu}(p, m_1, m_2) = g^{\mu\nu} B_{00}(p^2, m_1^2, m_2^2) + p^\mu p^\nu B_{11}(p^2, m_1^2, m_2^2), \quad (\text{C.21})$$

$$C^\mu(p_1, p_2, p_3, m_1, m_2, m_3) = \sum_{i=1}^2 k_i^\mu C_i(p_1^2, p_2^2, p_3^2, m_1^2, m_2^2, m_3^2), \quad (\text{C.22})$$

$$C^{\mu\nu}(p_1, p_2, p_3, m_1, m_2, m_3) = g^{\mu\nu} C_{00}(p_1^2, p_2^2, p_3^2, m_1^2, m_2^2, m_3^2) + \sum_{i,j=1}^2 k_i^\mu k_j^\nu C_{ij}(p_1^2, p_2^2, p_3^2, m_1^2, m_2^2, m_3^2), \quad (\text{C.23})$$

$$D^\mu(p_1, p_2, p_3, p_4, m_1, m_2, m_3, m_4) = \sum_{i=1}^3 k_i^\mu D_i(p_1^2, p_2^2, p_3^2, p_4^2, m_1^2, m_2^2, m_3^2, m_4^2), \quad (\text{C.24})$$

$$D^{\mu\nu}(p_1, p_2, p_3, p_4, m_1, m_2, m_3, m_4) = g^{\mu\nu} D_{00}(p_1^2, p_2^2, p_3^2, p_4^2, m_1^2, m_2^2, m_3^2, m_4^2) + \sum_{i,j=1}^3 k_i^\mu k_j^\nu D_{ij}(p_1^2, p_2^2, p_3^2, p_4^2, m_1^2, m_2^2, m_3^2, m_4^2), \quad (\text{C.25})$$

$$D^{\mu\nu\rho}(p_1, p_2, p_3, p_4, m_1, m_2, m_3, m_4)$$



$$\begin{aligned}
&= \sum_{i=1}^3 (g^{\mu\nu} k_i^\rho + g^{\nu\rho} k_i^\mu + g^{\rho\mu} k_i^\nu) D_{00i}(p_1^2, p_2^2, p_3^2, p_4^2, m_1^2, m_2^2, m_3^2, m_4^2) \\
&\quad + \sum_{i,j,l=1}^3 k_i^\mu k_j^\nu k_l^\rho D_{ijl}(p_1^2, p_2^2, p_3^2, p_4^2, m_1^2, m_2^2, m_3^2, m_4^2), \tag{C.26}
\end{aligned}$$

where

$$k_j = \sum_{i=1}^j p_i \tag{C.27}$$

has been used in the decomposition (these definitions are chosen such that the scalar functions are totally symmetric in their indices).

To renormalize the loop corrections, the UV-divergences have to be absorbed into the corresponding counterterms. The de facto standard in QCD is the modified minimal subtraction or  $\overline{\text{MS}}$ -scheme. This scheme is defined by the condition that the pole and some finite terms that arise from the  $D$ -dimensional integration over the momentum, along with some factors accompanying them, are absorbed into the counterterms. For example, every  $D$ -dimensional integration of a loop-momentum comes with a factor  $(2\pi)^{-D}$  from the measure and a factor  $2\pi^{D/2}/\Gamma(D/2)$  from the integration over the solid angle. The  $\varepsilon$ -dependence of the latter is included in the factor in front of the integral in (C.18). Due to this definition, the tensor integrals  $T^N$  in the expressions for the loop diagrams are always accompanied by a factor  $\pi^{D/2} r_\Gamma / (2\pi)^D$ . Consequentially, the poles of the functions  $T^N$  result in terms

$$\frac{1}{\varepsilon} \frac{\pi^{D/2} r_\Gamma}{(2\pi)^D} = \frac{1}{16\pi^2} \left( \frac{1}{\varepsilon} - \gamma_E + \ln(4\pi) \right) + \mathcal{O}(\varepsilon) = \frac{1}{16\pi^2} \Delta + \mathcal{O}(\varepsilon). \tag{C.28}$$

In the  $\overline{\text{MS}}$ -scheme, the terms proportional to  $\Delta$  are to be absorbed into the counterterms.

### Fermion self-energy

The diagrams for the renormalized fermion self-energy are shown in Fig. C.7. After amputating the external propagators carrying colours  $i$  and  $j$  and translating the diagram into its algebraic expression with the Feynman rules from Sec. B (using the Feynman gauge  $\xi = 1$ ), I rewrite the integral over the loop momentum  $l$  as a sum of integrals of the form (C.18):

$$\begin{aligned}
-i\Sigma_{ij}(p) &= ig_s \mu^\varepsilon T_{jk}^b \gamma^\nu \int \frac{d^D l}{(2\pi)^D} \frac{i(\not{p} + \not{l})}{(p+l)^2 + i\epsilon} ig_s \mu^\varepsilon T_{ki}^a \gamma^\mu \frac{-ig_{\mu\nu} \delta^{ab}}{l^2 + i\epsilon} \\
&\quad + i\delta_{ij} \delta Z_\Psi \not{p} \\
&= -g_s^2 \mu^{2\varepsilon} C_F \delta_{ij} (2-D) \gamma_\rho \int \frac{d^D l}{(2\pi)^D} \frac{p^\rho + l^\rho}{(p+l)^2 + i\epsilon} \frac{1}{l^2 + i\epsilon} \\
&\quad + i\delta_{ij} \delta Z_\Psi \not{p} \\
&= -\frac{g_s^2 \mu^{2\varepsilon}}{(2\pi)^D} C_F \delta_{ij} (2-D) \gamma_\rho \frac{i\pi^{D/2} r_\Gamma}{\mu^{4-D}} [p^\rho B_0(p^2, 0, 0) + B^\rho(p, 0, 0)]
\end{aligned}$$

$$\begin{aligned}
& + i\delta_{ij}\delta Z_\Psi \not{p} \\
& = -i\delta_{ij}C_F \frac{\alpha_s}{4\pi} (4\pi)^\varepsilon r_\Gamma 2(\varepsilon - 1) \not{p} [B_0(p^2, 0, 0) + B_1(p^2, 0, 0)] \\
& + i\delta_{ij} \delta Z_\Psi \not{p}.
\end{aligned} \tag{C.29}$$

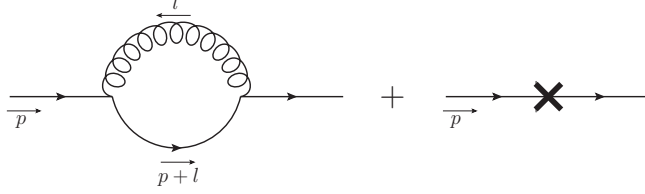


Figure C.7: Diagrams for the renormalized fermion self-energy.

The UV poles of the  $B$ -function can be read off the analytical results given in [36]:

$$\lim_{\varepsilon \rightarrow 0} \varepsilon B_0(p^2, 0, 0) = 1, \tag{C.30}$$

$$\lim_{\varepsilon \rightarrow 0} \varepsilon B_1(p^2, 0, 0) = -\frac{1}{2}. \tag{C.31}$$

Replacing the  $B$ -functions in (C.29) by these poles gives then

$$-i\Sigma_{ij}(p)|_{\text{div}} = i\delta_{ij}\not{p} \left\{ C_F \frac{\alpha_s}{4\pi} [\Delta + \mathcal{O}(\varepsilon)] + \delta Z_\Psi \right\}. \tag{C.32}$$

Since this is the “ $\overline{\text{MS}}$  divergence” of the renormalized self-energy, it has to vanish (apart from the finite terms denoted by  $\mathcal{O}(\varepsilon)$ ). Hence, the wave function renormalization constant in the  $\overline{\text{MS}}$ -scheme is given by

$$Z_\Psi = 1 + \delta Z_\Psi = 1 - \frac{\alpha_s}{4\pi} C_F \Delta. \tag{C.33}$$

To use the LSZ formula for the correction of external legs, one has to know the residue of the on-shell propagator. The residue is computed by multiplying the full propagator by the inverse of the free propagator and taking the on-shell limit  $p^2 \rightarrow 0$  (suppressing the small imaginary parts  $i\epsilon$  and the colour indices for now):

$$\begin{aligned}
N_\Psi^2 &= \lim_{p^2 \rightarrow 0} -i\not{p} \left\{ \frac{i\not{p}}{p^2} + \frac{i\not{p}}{p^2} (-i\Sigma(p)) \frac{i\not{p}}{p^2} + \mathcal{O}(\alpha_s^2) \right\} \\
&= \lim_{p^2 \rightarrow 0} \left\{ 1 + C_F \frac{\alpha_s}{4\pi} (4\pi)^\varepsilon r_\Gamma 2(\varepsilon - 1) [B_0(p^2, 0, 0) + B_1(p^2, 0, 0)] - \delta Z_\Psi \right\} \\
&= 1 - \delta Z_\Psi.
\end{aligned} \tag{C.34}$$

The last step requires some explanation. Of course the residue has to be UV finite, since it is the residue of the renormalized propagator. Indeed, the  $\varepsilon$ -pole in  $\delta Z_\Psi$  is to

be interpreted as an IR pole in (C.34). This follows from the property of dimensional regularization that integrals of  $l^{2k}$  for any integer  $k$  are defined to vanish [183]. For example one has

$$\begin{aligned}
B_0(0,0,0) &= \frac{\mu^{4-D}}{i\pi^{D/2}r_\Gamma} \int d^D l (l^2 + i\epsilon)^{-2} = \frac{\mu^{4-D}}{\pi^{D/2}r_\Gamma} \int d^D l_E l_E^{-4} \\
&= \frac{\mu^{4-D}}{\pi^{D/2}r_\Gamma} \int d\Omega_D \int_0^\infty dl_E l_E^{D-5} \\
&= \frac{2\mu^{4-D}\Gamma(D/2)}{r_\Gamma} \int_0^\infty dl_E l_E^{D-5} \\
&= \frac{2\mu^{4-D}\Gamma(D/2)}{r_\Gamma} \left( \int_0^\Lambda dl_E l_E^{-1-2\varepsilon_{\text{IR}}} + \int_\Lambda^\infty dl_E l_E^{-1-2\varepsilon_{\text{UV}}} \right) \\
&= \frac{2\mu^{4-D}\Gamma(D/2)}{r_\Gamma} \left( \frac{\Lambda^{-2\varepsilon_{\text{IR}}}}{-2\varepsilon_{\text{IR}}} - \frac{\Lambda^{-2\varepsilon_{\text{UV}}}}{-2\varepsilon_{\text{UV}}} \right), \tag{C.35}
\end{aligned}$$

where a Wick-rotation (with Euclidean momentum  $l_E = (\vec{l}, il^0)$ ) has been performed in the second step and with  $\varepsilon_{\text{IR}} \rightarrow 0^-$  and  $\varepsilon_{\text{UV}} \rightarrow 0^+$ . Defining such results to be zero by an identification  $\varepsilon_{\text{IR}} = \varepsilon_{\text{UV}}$ , one has

$$B_0(0,0,0) = 0, \tag{C.36}$$

$$B_1(0,0,0) = 0, \tag{C.37}$$

since

$$B_1(p^2, 0, 0) = -\frac{1}{2}B_0(p^2, 0, 0) \tag{C.38}$$

from [36]. This means, that, by usage of these identities, the pole in  $\delta Z_\Psi$  in (C.34) has effectively been “turned” into an IR pole.

### Gluon self-energy

The diagrams for the gluon self-energy corrections are depicted in Fig. C.8. In the following, the open Lorentz and colour indices corresponding to the amputated propagators are  $\mu$  and  $a$  on the left vertex and  $\nu$  and  $b$  on the right vertex, respectively.

The fermion-loop with  $N_f$  massless fermions (keeping in mind that a closed loop of particles described by Grassmann fields gives an extra minus sign) is given by

$$\begin{aligned}
i\Pi_{\text{fermion}}^{\mu\nu,ab}(p) &= -i\delta^{ab}\frac{\alpha_s}{4\pi}(4\pi)^\varepsilon r_\Gamma 2N_f \left\{ p^\mu B^\nu(p,0,0) + p^\nu B^\mu(p,0,0) \right. \\
&\quad \left. + 2B^{\mu\nu}(p,0,0) + \frac{1}{2}p^2 g^{\mu\nu} B_0(p^2,0,0) \right\}. \tag{C.39}
\end{aligned}$$

Since I use the Feynman rules in a Lorentz gauge, there is a ghost loop, too, which subtracts unphysical degrees of freedom from the gluon loops and which, again, has to be endowed with an extra minus sign:

$$i\Pi_{\text{ghost}}^{\mu\nu,ab}(p) = -i\delta^{ab}\frac{\alpha_s}{4\pi}(4\pi)^\varepsilon r_\Gamma C_A \{ p^\mu B^\nu(p,0,0) + B^{\mu\nu}(p,0,0) \}. \tag{C.40}$$

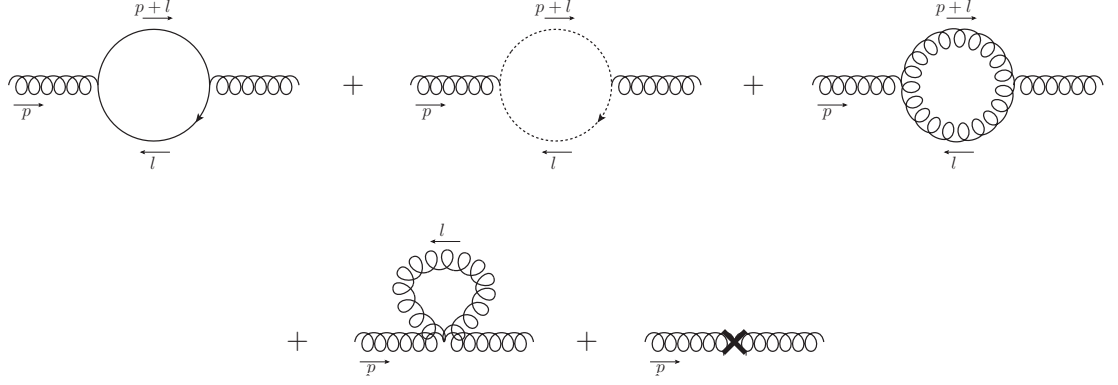


Figure C.8: Diagrams for the renormalized gluon self-energy.

The next diagram is the gluon loop with cubic gluon interactions. Here, some attention has to be paid to the symmetry factor of the diagram. The Feynman rule for the cubic gluon interaction, as given in App. B, is derived by contracting three gluon fields at different positions in all possible ways with the three gluon fields in the term  $-g_s f^{abc} A^{b\mu}(x) A^{c\nu}(x) \partial_\mu A_\nu^a(x)$  of the Lagrangian (2.2), i.e. implying  $3!$  contractions. Hence, a blind application of the Feynman rule for this graph would imply a factor  $(3!)^2$ . But there are just  $3! \cdot 3$  distinct contractions of the fields in the two cubic interactions with two external fields. Therefore the graph has to be multiplied by a symmetry factor  $1/2$ , giving

$$\begin{aligned} i\Pi_{3g}^{\mu\nu,ab}(p) = i\delta^{ab} \frac{\alpha_s}{4\pi} (4\pi)^\varepsilon r_\Gamma \frac{C_A}{2} \Big\{ & [5g^{\mu\nu} p^2 + (D-6)p^\mu p^\nu] B_0(p^2, 0, 0) \\ & + (2D-3) [p^\mu B^\nu(p, 0, 0) + p^\nu B^\mu(p, 0, 0)] \\ & + 2g^{\mu\nu} p_\rho B^\rho(p, 0, 0) + (4D-6) B^{\mu\nu}(p, 0, 0) \Big\}. \end{aligned} \quad (C.41)$$

The gluon loop with the quartic interaction vanishes, since it involves a scaleless integral:

$$i\Pi_{4g}^{\mu\nu,ab}(p) \propto A(0) = 0. \quad (C.42)$$

The sum of all diagrams, including the counterterm, and using the relations (C.20), (C.21), is then

$$\begin{aligned} i\Pi^{\mu\nu,ab}(p) = i\delta^{ab} \frac{\alpha_s}{4\pi} (4\pi)^\varepsilon r_\Gamma \Big\{ & -2N_f \left[ \frac{1}{2} g^{\mu\nu} p^2 B_0(p^2, 0, 0) + 2p^\mu p^\nu B_1(p^2, 0, 0) \right. \\ & \left. + 2g^{\mu\nu} B_{00}(p^2, 0, 0) + 2p^\mu p^\nu B_{11}(p^2, 0, 0) \right] \\ & + \frac{C_A}{2} \left[ (5g^{\mu\nu} p^2 - 2(1+\varepsilon)p^\mu p^\nu) B_0(p^2, 0, 0) \right. \\ & + (8(1-\varepsilon)p^\mu p^\nu + 2g^{\mu\nu} p^2) B_1(p^2, 0, 0) \\ & \left. + 8(1-\varepsilon)g^{\mu\nu} B_{00}(p^2, 0, 0) \right] \end{aligned}$$

$$\begin{aligned}
& + 8(1 - \varepsilon) p^\mu p^\nu B_{11}(p^2, 0, 0) \Big] \Big\} \\
& - i \delta^{ab} \delta Z_A \left( g^{\mu\nu} - \frac{p^\mu p^\nu}{p^2} \right) p^2.
\end{aligned} \tag{C.43}$$

This result can be simplified by a decomposition into a transverse and longitudinal part

$$\Pi^{\mu\nu,ab}(p) = \left( g^{\mu\nu} - \frac{p^\mu p^\nu}{p^2} \right) \Pi_T^{ab}(p) + \frac{p^\mu p^\nu}{p^2} \Pi_L^{ab}(p) \tag{C.44}$$

since the longitudinal part has to vanish due to a Slavnov-Taylor identity [8]. Indeed, this can be checked contracting (C.43) with  $p^\mu$  and using (again from [36])

$$p^2 B_{11}(p^2, 0, 0) + B_{00}(p^2, 0, 0) = -\frac{1}{2} p^2 B_1(p^2, 0, 0), \tag{C.45}$$

and (C.38). One then has

$$\begin{aligned}
i \Pi^{\mu\nu,ab}(p) &= \left( g^{\mu\nu} - \frac{p^\mu p^\nu}{p^2} \right) \Pi_T^{ab}(p) \\
&= i \delta^{ab} \frac{\alpha_s}{4\pi} (4\pi)^\varepsilon r_\Gamma \left( g^{\mu\nu} - \frac{p^\mu p^\nu}{p^2} \right) \\
&\quad \left\{ -2N_f \left[ \frac{p^2}{2} B_0(p^2, 0, 0) + 2B_{00}(p^2, 0, 0) \right] \right. \\
&\quad \left. + \frac{C_A}{2} [5p^2 B_0(p^2, 0, 0) + 2p^2 B_1(p^2, 0, 0) + 8(1 - \varepsilon) B_{00}(p^2, 0, 0)] \right\} \\
&\quad - i \delta^{ab} \delta Z_A \left( g^{\mu\nu} - \frac{p^\mu p^\nu}{p^2} \right) p^2,
\end{aligned} \tag{C.46}$$

which can be further simplified to

$$\begin{aligned}
i \Pi^{\mu\nu,ab}(p) &= i \delta^{ab} \frac{\alpha_s}{4\pi} (4\pi)^\varepsilon r_\Gamma \left( g^{\mu\nu} - \frac{p^\mu p^\nu}{p^2} \right) p^2 B_0(p^2, 0, 0) \\
&\quad \cdot \left\{ N_f \left( \frac{4 - 2\varepsilon}{3 - 2\varepsilon} - 2 \right) + C_A \left[ 2 + (1 - \varepsilon) \left( 1 - \frac{4 - 2\varepsilon}{3 - 2\varepsilon} \right) \right] \right\} \\
&\quad - i \delta^{ab} \delta Z_A \left( g^{\mu\nu} - \frac{p^\mu p^\nu}{p^2} \right) p^2.
\end{aligned} \tag{C.47}$$

The last equation can be derived from (C.46) by use of (C.38), (C.45) and the following identity:

$$p^2 B_{00}(p^2, 0, 0) + B_{11}(p^2, 0, 0) = \frac{1}{4} B_0(p^2, 0, 0), \tag{C.48}$$

which is obtained by contracting (C.21) with  $p^\mu p^\nu$ .

Knowing the pole of  $B_0$ , (C.30), one finds in the  $\overline{\text{MS}}$ -scheme

$$Z_A = 1 + \frac{\alpha_s}{4\pi} \left( \frac{5}{3} C_A - \frac{2}{3} N_f \right) \Delta. \tag{C.49}$$

The residue of the propagator is given by

$$\begin{aligned}
N_A^2 g_\tau^\nu &= \lim_{p^2 \rightarrow 0} i g_{\tau\mu} p^2 \left\{ \frac{-i g^{\mu\nu}}{p^2} + \frac{-i g^{\mu\rho}}{p^2} i \Pi_{\rho\sigma} \frac{-i g^{\sigma\nu}}{p^2} \right\} \\
&= \lim_{p^2 \rightarrow 0} \left\{ g_\tau^\nu + g_\tau^\rho \frac{\alpha_s}{4\pi} (4\pi)^\varepsilon r_\Gamma \left( g_{\rho\sigma} - \frac{p_\rho p_\sigma}{p^2} \right) p^2 B_0(p^2, 0, 0) \right. \\
&\quad \cdot \left\{ N_f \left( \frac{4-2\varepsilon}{3-2\varepsilon} - 2 \right) + C_A \left[ 2 + (1-\varepsilon) \left( 1 - \frac{4-2\varepsilon}{3-2\varepsilon} \right) \right] \right\} \frac{-i g^{\sigma\nu}}{p^2} \\
&\quad \left. + g_\tau^\rho i \delta Z_A \left( g_{\rho\sigma} - \frac{p_\rho p_\sigma}{p^2} \right) p^2 \frac{-i g^{\sigma\nu}}{p^2} \right\}.
\end{aligned}$$

As a result of a Ward-Takahashi identity, QCD matrix elements are orthogonal to the four-momenta of gluons, i.e. they vanish if a gluon polarization vector gets replaced by its momentum four-vector, as long as at most one of them is off-shell [184]. Since, in this work, all external particles are on-shell, one can then neglect all terms  $\propto p_\rho p_\sigma$  in the residue as they would be contracted with an on-shell matrix element. Thus, using (C.36) gives

$$N_A^2 = 1 - \delta Z_A, \quad (\text{C.50})$$

which has the same structure as (C.34) and where similarly the pole in  $\delta Z_A$  is to be interpreted as an IR pole.

### Fermion-photon triangle

The  $\mathcal{O}(\alpha_s)$  correction to the fermion-photon vertex is shown in Fig. C.9. After amputating the legs, the diagrams have two open color indices  $i$  and  $j$  for the quark and antiquark, respectively, as well as an uncontracted Lorentz index  $\mu$  for the photon. The momenta are chosen such that the sum of the external momenta gives zero. Translating the integral in  $C$ -functions gives

$$\begin{aligned}
\Gamma_{ij}^\mu(p_1, p_2) &= i \delta_{ij} Q_f e \mu^\varepsilon \frac{\alpha_s}{4\pi} (4\pi)^\varepsilon r_\Gamma C_F \gamma^\nu \gamma_\rho \gamma^\mu \gamma_\sigma \gamma_\nu [C^{\rho\sigma}(p_1, p_2, p_3, 0, 0, 0) \\
&\quad + p_1^\sigma C^\rho(p_1, p_2, p_3, 0, 0, 0) + (p_1 + p_2)^\rho C^\sigma(p_1, p_2, p_3, 0, 0, 0) \\
&\quad + (p_1 + p_2)^\rho p_1^\sigma C_0(p_1^2, p_2^2, p_3^2, 0, 0, 0)] \\
&\quad + i Q_f e \gamma^\mu \delta Z_e \\
&= i \delta_{ij} Q_f e \mu^\varepsilon \frac{\alpha_s}{4\pi} (4\pi)^\varepsilon r_\Gamma C_F \gamma^\nu \gamma_\rho \gamma^\mu \gamma_\sigma \gamma_\nu [p_1^\sigma (p_1 + p_2)^\rho C_0 \\
&\quad + (2p_1 + p_2)^\rho p_1^\sigma C_1 + (p_1 + p_2)^\rho (2p_1 + p_2)^\sigma C_2 \\
&\quad + g^{\rho\sigma} C_{00} + p_1^\rho p_1^\sigma C_{11} + (p_1^\sigma p_2^\rho + p_1^\rho (2p_1 + p_2)^\sigma) C_{12} \\
&\quad + (p_1 + p_2)^\rho (p_1 + p_2)^\sigma C_{22}] \\
&\quad + i Q_f e \gamma^\mu \delta Z_e. \quad (\text{C.51})
\end{aligned}$$

In the last result the arguments of the scalar  $C$ -functions are suppressed; they are identically  $p_1^2, p_2^2, p_3^2, 0, 0, 0$ . This is both UV and IR divergent. Since the IR divergences are

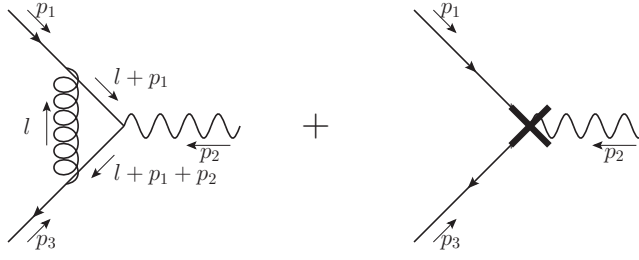


Figure C.9: Diagrams for the renormalized fermion-photon vertex.

mass divergences, one can examine the UV pole separately by setting the mass-arguments to some finite values  $m_1, m_2, m_3$ . The UV divergence is included in  $C_{00}$  [185]

$$\lim_{\varepsilon \rightarrow 0} \varepsilon C_{00}(p_1^2, p_2^2, p_3^2, m_1^2, m_2^2, m_3^2) = \frac{1}{4}. \quad (\text{C.52})$$

Thus, replacing the square-bracket by  $g^{\rho\sigma}/(4\varepsilon)$ , contracting the Dirac matrices and requiring a cancellation of the pole and the counterterm in the  $\overline{\text{MS}}$ -scheme gives

$$Z_e = 1 - \frac{\alpha_s}{4\pi} C_F \Delta. \quad (\text{C.53})$$

As expected from the comment in Sec. 3.1 this is equal to (C.33).

### Fermion-gluon triangle

The two  $\mathcal{O}(\alpha_s)$  corrections to the fermion-gluon vertex are depicted in Fig. C.10. For the amputated diagrams I have chosen the open indices completely analogous to the correction of the fermion-photon vertex: Colours  $i$  and  $j$  for the quark and antiquark, and a Lorentz index  $\mu$  plus a gluon index  $a$  for the amputated gluon leg.

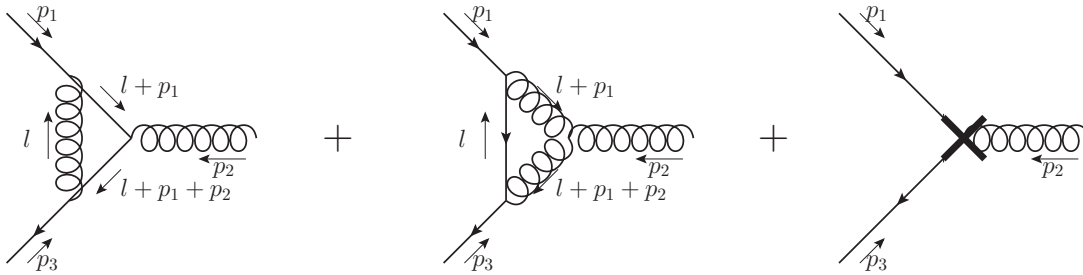


Figure C.10: Diagrams for the renormalized fermion-gluon vertex.

## C Prompt Photon Production Cross Section

Apart from the colour-algebra, the first diagram is identical to the fermion-photon vertex correction:

$$\begin{aligned}\Gamma_{ij}^{(1)\mu a}(p_1, p_2) = & \text{i}g_s\mu^\varepsilon \frac{\alpha_s}{4\pi}(4\pi)^\varepsilon r_\Gamma \left( C_F - \frac{C_A}{2} \right) T_{ji}^a \gamma^\nu \gamma_\rho \gamma^\mu \gamma_\sigma \gamma_\nu [p_1^\sigma (p_1 + p_2)^\rho C_0 \\ & + (2p_1 + p_2)^\rho p_1^\sigma C_1 + (p_1 + p_2)^\rho (2p_1 + p_2)^\sigma C_2 \\ & + g^{\rho\sigma} C_{00} + p_1^\rho p_1^\sigma C_{11} + (p_1^\sigma p_2^\rho + p_1^\rho (2p_1 + p_2)^\sigma) C_{12} \\ & + (p_1 + p_2)^\rho (p_1 + p_2)^\sigma C_{22}] .\end{aligned}\quad (\text{C.54})$$

Of course, the second diagram has no Abelian counterpart and is given by

$$\begin{aligned}\Gamma_{ij}^{(2)\mu a}(p_1, p_2) = & g_s\mu^\varepsilon \frac{\alpha_s}{4\pi}(4\pi)^\varepsilon r_\Gamma \left( -\frac{\text{i}}{2} C_A \right) T_{ji}^a \gamma^\nu \gamma_\sigma \gamma^\rho \\ & \cdot [g^\mu{}_\rho ((p_2 - p_1)_\nu C^\sigma - C^\sigma{}_\nu) \\ & + g_{\rho\nu} (2C^{\sigma\mu} + (2p_1 + p_2)^\mu C^\sigma) \\ & - g_\nu{}^\mu (C^\sigma{}_\rho + (p_1 + 2p_2)_\rho C^\sigma)] ,\end{aligned}$$

with the arguments of the  $C$ -tensor-functions given by  $p_1, p_2, p_3$  and all masses identically zero. This can be reduced to

$$\begin{aligned}\Gamma_{ij}^{(2)\mu a}(p_1, p_2) = & -\text{i}g_s\mu^\varepsilon \frac{\alpha_s}{4\pi}(4\pi)^\varepsilon r_\Gamma \frac{C_A}{2} T_{ji}^a \gamma^\nu \gamma_\sigma \gamma^\rho \\ & \cdot [C_1 p_1^\sigma (g_{\nu\rho} (2p_1 + p_2)^\mu + g^\mu{}_\rho (p_2 - p_1)_\nu - g^\mu{}_\nu (p_1 + 2p_2)_\rho) \\ & + C_2 (p_1 + p_2)^\sigma (g_{\nu\rho} (2p_1 + p_2)^\mu + g^\mu{}_\rho (p_2 - p_1)_\nu - g^\mu{}_\nu (p_1 + 2p_2)_\rho) \\ & + C_{00} (2g^{\mu\sigma} g_{\nu\rho} - g^\mu{}_\rho g_\nu{}^\sigma - g^\mu{}_\nu g_\rho{}^\sigma) \\ & + C_{11} p_1^\sigma (2p_1^\mu g_{\nu\rho} - g^\mu{}_\rho p_{1\nu} - g^\mu{}_\nu p_{1\rho}) \\ & + C_{22} (p_1 + p_2)^\sigma (2(p_1 + p_2)^\mu g_{\nu\rho} - g^\mu{}_\rho (p_1 + p_2)_\nu - g^\mu{}_\nu (p_1 + p_2)_\rho) \\ & + C_{12} (2g_{\nu\rho} (p_2^\mu p_1^\sigma + p_1^\mu (2p_1 + p_2)^\sigma) \\ & - g^\mu{}_\rho ((2p_1 + p_2)_\nu p_1^\sigma + p_{1\nu} p_2^\sigma) \\ & - g^\mu{}_\nu ((2p_1 + p_2)_\rho p_1^\sigma + p_{1\rho} p_2^\sigma))] ,\end{aligned}\quad (\text{C.55})$$

where the arguments of the  $C$ -functions are again  $p_1^2, p_2^2, p_3^2, 0, 0, 0$ .

The full correction is

$$\Gamma_{ij}^{\mu a}(p_1, p_2) = \Gamma_{ij}^{(1)\mu a}(p_1, p_2) + \Gamma_{ij}^{(2)\mu a}(p_1, p_2) + \text{i}\delta Z_g g_s \gamma^\mu T_{ji}^a .\quad (\text{C.56})$$

As is the case for the fermion-photon vertex, the UV divergence is entirely contained in the  $C_{00}$  function. The renormalization constant for the fermion-gluon interaction is then in the  $\overline{\text{MS}}$ -scheme

$$Z_g = 1 - \frac{\alpha_s}{4\pi} (C_F + C_A) \Delta \quad (\text{C.57})$$



### Fermion-fermion-photon-gluon box

The one-particle irreducible corrections to the process  $q\bar{q} \rightarrow \gamma g$  are also termed box corrections, since the amputated diagrams constitute boxes, as can be seen in Fig. C.11. Through analysis of the superficial degree of divergence  $d$ , it is clear that these diagrams do not entail any UV divergence, since  $d = -1$  and hence the integrals for large momenta behave like  $d\kappa \kappa^{-2}$ . Renormalization is then not necessary (and even more, it would not be possible in the standard model, due to the absence of a  $q\bar{q}\gamma g$ -counterterm). For these diagrams the results are given only in terms of the tensor integral functions owing to the length of the reduced expressions.

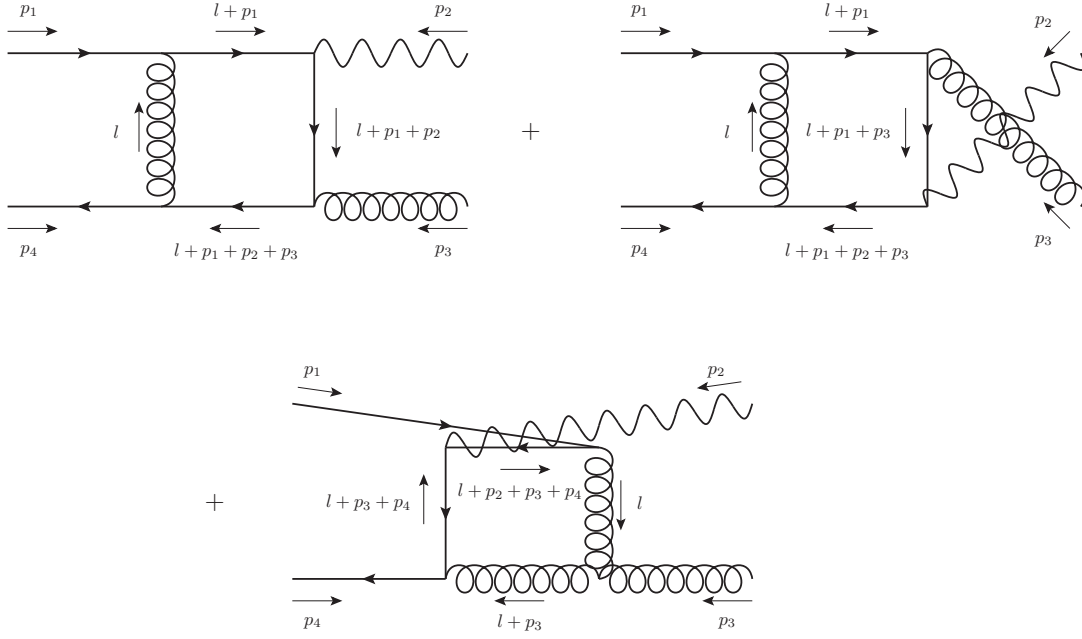


Figure C.11: Diagrams for box corrections to  $q\bar{q} \rightarrow \gamma g$ .

Amputating the external propagators, the expressions for the diagrams have two open colour indices  $i, j$  – again for the quark and antiquark, respectively – a Lorentz index  $\mu$  for the photon and similarly an index  $\nu$  for the gluon, plus a gluon colour index  $a$ . The first diagram gives

$$\begin{aligned} \Delta_{ij}^{(1)\mu\nu a}(p_1, p_2, p_3) = & -ig_s Q_f e \mu^{2\epsilon} \frac{\alpha_s}{4\pi} (4\pi)^\epsilon r_\Gamma \left( C_F - \frac{C_A}{2} \right) T_{ji}^a \gamma^\rho \gamma_\sigma \gamma^\nu \gamma_\tau \gamma^\mu \gamma_\omega \gamma_\rho \\ & \cdot [D^{\sigma\tau\omega} + p_1^\omega D^{\sigma\tau} + (p_1 + p_2)^\tau D^{\sigma\omega} + (p_1 + p_2)^\tau p_1^\omega D^\sigma \\ & + (p_1 + p_2 + p_3)^\sigma (D^{\tau\omega} + p_1^\omega D^\tau \\ & + (p_1 + p_2)^\tau D^\omega + (p_1 + p_2)^\tau p_1^\omega D_0)] , \end{aligned} \quad (\text{C.58})$$

with  $p_1, p_2, p_3, p_4, 0, 0, 0, 0$  as suppressed arguments of the  $D$ -functions.

## C Prompt Photon Production Cross Section

Fairly similar to the first, the second diagram gives

$$\begin{aligned} \Delta_{ij}^{(2)\mu\nu a}(p_1, p_2, p_3) = & -ig_s Q_f e \mu^{2\varepsilon} \frac{\alpha_s}{4\pi} (4\pi)^\varepsilon r_\Gamma \left( C_F - \frac{C_A}{2} \right) T_{ji}^a \gamma^\rho \gamma_\sigma \gamma^\mu \gamma_\tau \gamma^\nu \gamma_\omega \gamma_\rho \\ & \cdot [D^{\sigma\tau\omega} + p_1^\omega D^{\sigma\tau} + (p_1 + p_3)^\tau D^{\sigma\omega} + (p_1 + p_3)^\tau p_1^\omega D^\sigma \\ & + (p_1 + p_2 + p_3)^\sigma (D^{\tau\omega} + p_1^\omega D^\tau \\ & + (p_1 + p_3)^\tau D^\omega + (p_1 + p_3)^\tau p_1^\omega D_0)] , \quad (\text{C.59}) \end{aligned}$$

where the argument of the  $D$ -functions are now  $p_1, p_3, p_2, p_4, 0, 0, 0, 0$ .

Finally, the expression for the third diagram with the cubic gluon interaction is

$$\begin{aligned} \Delta_{ij}^{(3)\mu\nu a}(p_1, p_2, p_3) = & g_s Q_f e \mu^{2\varepsilon} \frac{\alpha_s}{4\pi} (4\pi)^\varepsilon r_\Gamma \left( -\frac{i}{2} C_A \right) T_{ji}^a \gamma^\sigma \gamma_\tau \gamma^\mu \gamma_\omega \gamma^\rho \\ & \cdot [(-g^\nu_\rho g_{\alpha\sigma} + 2g_{\rho\sigma} g_\alpha{}^\nu - g_\sigma{}^\nu g_{\alpha\rho}) \\ & \cdot (D^{\alpha\tau\omega} + (p_2 + p_3 + p_4)^\omega D^{\alpha\tau} + (p_3 + p_4)^\tau D^{\alpha\omega} \\ & + (p_3 + p_4)^\tau (p_2 + p_3 + p_4)^\omega D^\alpha) \\ & + p_3^\alpha (g^\nu_\rho g_{\alpha\sigma} + g_{\rho\sigma} g_\alpha{}^\nu - 2g_\sigma{}^\nu g_{\alpha\rho}) \\ & \cdot (D^{\tau\omega} + (p_2 + p_3 + p_4)^\omega D^\tau + (p_3 + p_4)^\tau D^\omega \\ & + (p_3 + p_4)^\tau (p_2 + p_3 + p_4)^\omega D_0)] , \quad (\text{C.60}) \end{aligned}$$

with  $D$ -function-arguments  $p_3, p_4, p_2, p_1, 0, 0, 0, 0$ .

### Corrections on external legs

Self-energy corrections on external legs are computed using the LSZ reduction formula, which relates correlation functions of fields to matrix elements of particles created by these fields, e.g.

$$\int dx_1 \cdots \int dx_n e^{-i\sum_i p_i x_i} \langle 0 | \Phi(x_1) \cdots \Phi^\dagger(x_n) | 0 \rangle \sim \langle \dots, p_n | p_1, \dots \rangle .$$

The correlation function can be computed as a series of Feynman diagrams with external propagators. To transform the result of the correlation function into the corresponding matrix element between on-shell states, one has to put the external legs on-shell and replace the full external propagators with the wave function

$$\langle 0 | \Phi(0) | p, s \rangle$$

for incoming (or the adjoint for outgoing) particles. In a free-field theory (or in the Born approximation) the wave functions are just the coefficients of the field expansion in plane waves, e.g.  $u_s(p)$ ,  $\varepsilon^\mu(p)$ , etc. However, in general, one has to include a normalization constant  $N$ , e.g.

$$\langle 0 | \Psi(0) | p, s \rangle = N_\Psi u_s(p) , \quad (\text{C.61})$$

owing to the interactions of the field. Analyzing the form of a general on-shell propagator, it can be shown (e.g. [82]) that these normalization constants  $N_i$  are equal to the square roots of the residues.

Now it is straight-forward to use the Born results to construct the external corrections: The S-matrix elements in the Born approximation can be interpreted as correlation functions which include corrections only on external legs, but with the full external propagators truncated and substituted by the wave function coefficients  $u_s$ ,  $\varepsilon^\mu$ , and so on. The difference to the LSZ prescription is that the normalization factors  $N$  are missing. Multiplying each external leg of the Born results by  $N$  then gives the correct matrix element incorporating external corrections.

The residues in (C.34) and (C.50) are of the form

$$N_i^2 = 1 - \delta Z_i ,$$

giving

$$N_i = 1 - \frac{1}{2}\delta Z_i + \mathcal{O}(\delta Z_i^2) . \quad (\text{C.62})$$

That means multiplying every external leg (left and right of the cut) in Fig. C.2 with  $N_i$  gives the  $\mathcal{O}(\alpha_s)$  loop corrections on external legs as

$$\overline{|\mathcal{M}_{q\bar{q} \rightarrow \gamma g}^{(1 \text{ ext})}|^2} = -(2\delta Z_\Psi + \delta Z_A) \overline{|\mathcal{M}_{q\bar{q} \rightarrow \gamma g}|^2} . \quad (\text{C.63})$$

Again, the poles that appear here through the renormalization constants are, in this context, to be interpreted as IR poles. Since these poles are present, the Born amplitude  $\overline{|\mathcal{M}_{q\bar{q} \rightarrow \gamma g}|^2}$  has to be given in  $D$  dimensions, i.e. (C.4), to correctly generate the finite terms arising through a cancellation of poles and terms proportional to  $\varepsilon$ .

### Corrections on internal propagators

The diagrams in Fig. C.3 are also easily obtained using the results for the squared tree-level diagrams. Since the internal propagator of the process in question is always a quark propagator and the corresponding self-energy correction (C.29) is of the form

$$-i\Sigma(p) = -i\not{p}\Sigma_s(p^2) , \quad (\text{C.64})$$

the correction of the propagator is just a multiplication with a function, i.e.

$$\frac{i\not{p}}{p^2} (-i\Sigma(p)) \frac{i\not{p}}{p^2} = \Sigma_s(p^2) \frac{i\not{p}}{p^2} . \quad (\text{C.65})$$

Hence, the internal self-energy corrections are given by

$$\begin{aligned} \overline{|\mathcal{M}_{q\bar{q} \rightarrow \gamma g}^{(1 \text{ int})}|^2} = 2 \operatorname{Re} \left[ \Sigma_s(t) \left( \overline{|\mathcal{M}^{(t)}|^2} + \overline{\mathcal{M}^{(t)} \mathcal{M}^{(u)\dagger}} \right) \right. \\ \left. + \Sigma_s(u) \left( \overline{|\mathcal{M}^{(u)}|^2} + \overline{\mathcal{M}^{(u)} \mathcal{M}^{(t)\dagger}} \right) \right] , \end{aligned} \quad (\text{C.66})$$

using the results (C.1), (C.2), and (C.3).

### C.2.2 Real corrections

To get the real corrections – i.e. all  $2 \rightarrow 3$  processes with a single final state photon

$$\begin{array}{llll}
 q\bar{q} \rightarrow \gamma gg & \bar{q}q \rightarrow \gamma gg & q\bar{q} \rightarrow \gamma q\bar{q} & \bar{q}q \rightarrow \gamma q\bar{q} \\
 q\bar{q} \rightarrow \gamma q'\bar{q}' & \bar{q}q \rightarrow \gamma q'\bar{q}' & qq \rightarrow \gamma qq & qq' \rightarrow \gamma qq' \\
 \bar{q}\bar{q} \rightarrow \gamma \bar{q}\bar{q} & \bar{q}\bar{q}' \rightarrow \gamma \bar{q}\bar{q}' & q\bar{q}' \rightarrow \gamma q\bar{q}' & \bar{q}q' \rightarrow \gamma q'\bar{q} \\
 qg \rightarrow \gamma qg & \bar{q}g \rightarrow \gamma \bar{q}g & gq \rightarrow \gamma qg & g\bar{q} \rightarrow \gamma \bar{q}g \\
 gg \rightarrow \gamma q\bar{q} & & & 
 \end{array}$$

– one has to compute three new matrix elements from which all other real corrections can be obtained by using crossing. I take these three processes to be  $q\bar{q} \rightarrow \gamma gg$ ,  $qq' \rightarrow \gamma qq'$ , and  $qq \rightarrow \gamma qq$ . The diagrams for the process  $q\bar{q} \rightarrow \gamma gg$  are depicted in Fig. C.12. Fig. C.13 shows the diagrams for  $qq' \rightarrow \gamma qq'$  with  $q' \neq q$ . For the process  $qq \rightarrow \gamma qq$  one has to compute all the diagrams of Figs. C.13 and C.14, i.e. the difference to the process with  $q' \neq q$  are the diagrams with crossing quark lines.

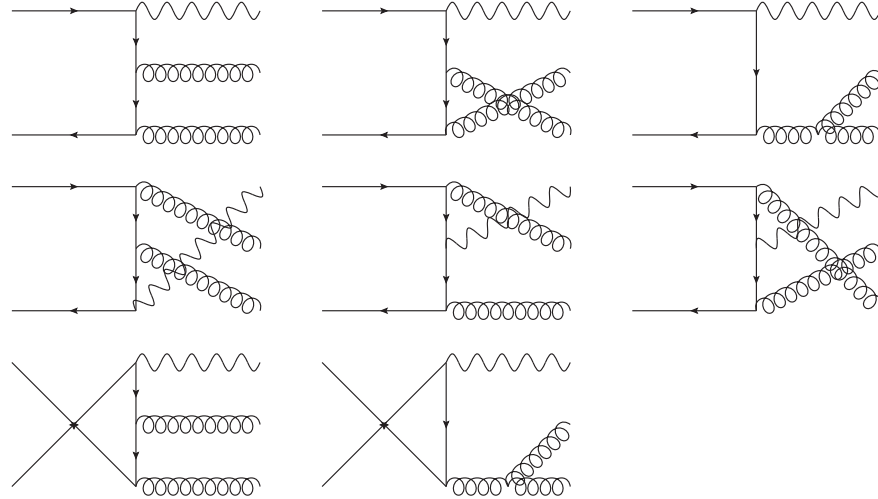


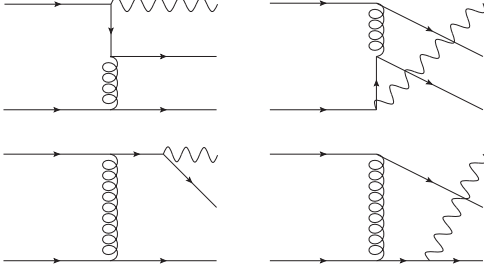
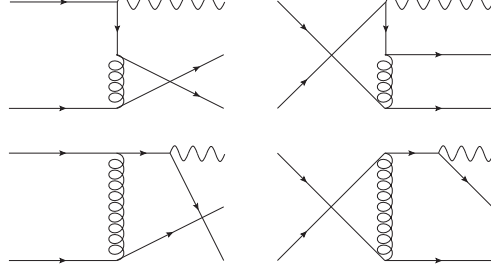
Figure C.12: Diagrams for  $q\bar{q} \rightarrow \gamma gg$ .

To compute the amplitudes for these processes I have used **FormCalc** [89]. A set of linearly independent Mandelstam variables suitable for these  $2 \rightarrow 3$  processes is defined by<sup>1</sup>

$$s_{12} = (p_1 + p_2)^2, \quad (\text{C.67})$$

$$s_{ab} = (p_a + p_b)^2, \quad (\text{C.68})$$

<sup>1</sup>For  $N$  particles involved in the scattering, there are  $3N$  momentum components, 4 of which are determined by momentum conservation, while 6 are determined by the Lorentz-transformation properties of the amplitude under the 6 generators of  $SO(3, 1)$ . Hence, here, 5 independent variables are needed.


 Figure C.13: Diagrams for  $qq' \rightarrow \gamma qq'$ .

 Figure C.14: Additional diagrams for  $qq \rightarrow \gamma qq$ .

$$t_{a1} = (p_a - p_1)^2, \quad (C.69)$$

$$t_{a2} = (p_a - p_2)^2, \quad (C.70)$$

$$t_{b1} = (p_b - p_1)^2, \quad (C.71)$$

where the incoming momenta  $p_a, p_b$  and outgoing momenta  $p_1, p_2, p_3$  are assigned from top to bottom to the external legs of the diagrams. The results are given by:

$$\begin{aligned} \overline{|\mathcal{M}_{q\bar{q} \rightarrow \gamma gg}|^2} = & -64\pi^3 \alpha \alpha_s^2 \frac{N_c^2 - 1}{N_c^3} Q^2 \{ s_{12}^2 (s_{ab} + 2t_{a1}) + s_{12} t_{a1} (2s_{ab} + 3t_{a1} + 2t_{a2}) \\ & + s_{12} t_{b1} (t_{a1} - 2t_{a2}) + s_{ab} t_{a1}^2 + (t_{a1} + t_{b1}) [t_{a1} (t_{a1} + t_{a2}) - t_{a2} t_{b1}] \} \\ & \cdot \{ N_c [s_{12}^3 (s_{ab} + t_{a1} + 2t_{a2}) + 3s_{12}^2 (s_{ab}^2 + s_{ab} (2(t_{a1} + t_{a2}) + t_{b1}) \\ & + (t_{a1} + t_{a2})(t_{a1} + 2t_{a2} + t_{b1})) + s_{12} (6s_{ab}^3 + 8s_{ab}^2 (2(t_{a1} + t_{a2}) + t_{b1}) \\ & + s_{ab} (5t_{a1} + 6t_{a2} + 2t_{b1}) (3t_{a1} + 2(t_{a2} + t_{b1})) + 5t_{a1}^3 + 17t_{a1}^2 t_{a2} \\ & + 18t_{a1} t_{a2}^2 + t_{b1}^2 (4t_{a1} + 5t_{a2}) + 2t_{b1} (2t_{a1} + t_{a2}) (2t_{a1} + 3t_{a2}) + 8t_{a2}^3) \\ & + 4s_{ab}^4 + 2s_{ab}^3 (7t_{a1} + 6t_{a2} + 4t_{b1}) \\ & + s_{ab}^2 (19t_{a1}^2 + 34t_{a1} t_{a2} + 22t_{a1} t_{b1} + 16t_{a2}^2 + 18t_{a2} t_{b1} + 6t_{b1}^2) \\ & + s_{ab} (12t_{a1}^3 + t_{a1}^2 (32t_{a2} + 21t_{b1}) + 4t_{a1} (7t_{a2}^2 + 9t_{a2} t_{b1} + 3t_{b1}^2) \\ & + 2(t_{a2} + t_{b1}) (2t_{a2} + t_{b1})^2) + (t_{a1} + t_{a2}) (t_{a1} + 2t_{a2} + t_{b1}) \\ & \cdot (3t_{a1}^2 + 3t_{a1} t_{a2} + 4t_{a1} t_{b1} + 2t_{a2}^2 + t_{a2} t_{b1} + 2t_{b1}^2)] \\ & + [2s_{ab}^2 + 2s_{ab} (t_{a1} + t_{b1}) + (t_{a1} + t_{b1})^2] \\ & \cdot [s_{12} (s_{ab} + t_{a1} + 2t_{a2}) + (t_{a1} + 2t_{a2}) (s_{ab} + t_{a1} + t_{a2}) \\ & + t_{b1} (t_{a1} + t_{a2})] \} \\ & / [s_{12} t_{a1} t_{a2} t_{b1} (s_{12} + t_{a1} + t_{a2}) (s_{12} + t_{a1} + t_{b1}) (s_{ab} + t_{a1} + t_{a2}) \\ & (s_{12} + s_{ab} + t_{a1} + t_{a2} + t_{b1})], \end{aligned} \quad (C.72)$$

$$\begin{aligned}
|\overline{\mathcal{M}_{qq' \rightarrow \gamma qq'}}|^2 = & -64\pi^3 \alpha \alpha_s^2 \frac{N_c^2 - 1}{N_c^2} \left\{ s_{12}^2 + 2s_{12}(s_{ab} + t_{a1} + t_{a2} + t_{b1}) + 4s_{ab}^2 \right. \\
& + 2t_{b1}(2(s_{ab} + t_{a1}) + t_{a2}) + 6s_{ab}t_{a1} + 4s_{ab}t_{a2} + 3t_{a1}^2 \\
& + 4t_{a1}t_{a2} + 2t_{a2}^2 + 2t_{b1}^2 \} \\
& \cdot \{ Q'^2 s_{12}t_{a1}(s_{12} + t_{a1} + t_{a2}) \\
& + Q'Q[(s_{12} + t_{a1})((s_{12} + t_{a1})(s_{ab} + t_{a1}) + t_{a1}t_{a2}) \\
& + t_{b1}(s_{12}(t_{a1} - t_{a2}) + t_{a1}(t_{a1} + t_{a2}))] \\
& - Q^2 t_{a2}t_{b1}(s_{12} + t_{a1} + t_{b1}) \} \\
& / [s_{12}t_{a1}t_{a2}t_{b1}(s_{12} + t_{a1} + t_{a2})(s_{12} + t_{a1} + t_{b1})] ,
\end{aligned} \tag{C.73}$$

$$\begin{aligned}
|\overline{\mathcal{M}_{qq \rightarrow \gamma qq}}|^2 = & -64\pi^3 \alpha \alpha_s^2 \frac{N_c^2 - 1}{N_c^3} Q^2 \{ s_{12}^2(s_{ab} + 2t_{a1}) + s_{12}t_{a1}(2s_{ab} + 3t_{a1} + 2t_{a2}) \\
& + s_{12}t_{b1}(t_{a1} - 2t_{a2}) + s_{ab}t_{a1}^2 + (t_{a1} + t_{b1})[t_{a1}(t_{a1} + t_{a2}) - t_{a2}t_{b1}] \} \\
& \cdot \{ N_c [s_{12}^3(s_{ab} + t_{a1} + 2t_{a2}) + 3s_{12}^2(s_{ab}^2 + s_{ab}(2(t_{a1} + t_{a2}) + t_{b1}) \\
& + (t_{a1} + t_{a2})(t_{a1} + 2t_{a2} + t_{b1})) \\
& + s_{12}(6s_{ab}^3 + 8s_{ab}^2(2(t_{a1} + t_{a2}) + t_{b1}) \\
& + s_{ab}(5t_{a1} + 6t_{a2} + 2t_{b1})(3t_{a1} + 2(t_{a2} + t_{b1})) + 5t_{a1}^3 t_{a2} \\
& + 17t_{a1}^2 + 18t_{a1}t_{a2}^2 + t_{b1}^2(4t_{a1} + 5t_{a2}) \\
& + 2t_{b1}(2t_{a1} + t_{a2})(2t_{a1} + 3t_{a2}) + 8t_{a2}^3) \\
& + 4s_{ab}^4 + 2s_{ab}^3(7t_{a1} + 6t_{a2} + 4t_{b1}) \\
& + s_{ab}^2(19t_{a1}^2 + 34t_{a1}t_{a2} + 22t_{a1}t_{b1} + 16t_{a2}^2 + 18t_{a2}t_{b1} + 6t_{b1}^2) \\
& + s_{ab}(12t_{a1}^3 + t_{a1}^2(32t_{a2} + 21t_{b1}) + 4t_{a1}(7t_{a2}^2 + 9t_{a2}t_{b1} + 3t_{b1}^2) \\
& + 2(t_{a2} + t_{b1})(2t_{a2} + t_{b1})^2) \\
& + (t_{a1} + t_{a2})(t_{a1} + 2t_{a2} + t_{b1}) \\
& \cdot (3t_{a1}^2 + 3t_{a1}t_{a2} + 4t_{a1}t_{b1} + 2t_{a2}^2 + t_{a2}t_{b1} + 2t_{b1}^2)] \\
& + [2s_{ab}^2 + 2s_{ab}(t_{a1} + t_{b1}) + (t_{a1} + t_{b1})^2] \\
& \cdot [s_{12}(s_{ab} + t_{a1} + 2t_{a2}) + (t_{a1} + 2t_{a2})(s_{ab} + t_{a1} + t_{a2}) \\
& + t_{b1}(t_{a1} + t_{a2})] \} \\
& / [s_{12}t_{a1}t_{a2}t_{b1}(s_{12} + t_{a1} + t_{a2})(s_{12} + t_{a1} + t_{b1})(s_{ab} + t_{a1} + t_{a2}) \\
& \cdot (s_{12} + s_{ab} + t_{a1} + t_{a2} + t_{b1})] .
\end{aligned} \tag{C.74}$$

The vanishing of some of the invariants leads to soft, collinear or soft-collinear divergences. For instance, a photon that is soft and/or collinear to the initial state parton corresponds to

$$t_{a1} = -2p_a \cdot p_1 = -2E_a E_1 (1 - \cos(\theta_{a1})) \rightarrow 0 ,$$

which, in the first three diagrams of Fig. C.12, where the photon radiates off the quark, leads to a divergence in (C.72).

### C.2.3 Real phase space

For the 3-particle phase space one again starts with (C.6) and integrates out one of the momenta, e.g.  $p_3$ ,

$$d\Phi^{(3)} = \frac{1}{4(2\pi)^5} \frac{d^3p_1 d^3p_2}{p_1^0 p_2^0} \theta(p^0 - p_1^0 - p_2^0) \delta([p - p_1 - p_2]^2) \quad (C.75)$$

with  $p = p_a + p_b$ . Using the definition (C.9) for  $p_1$  and  $p_2$  in the CM frame, one has

$$p \cdot p_i = \sqrt{s_{ab}} p_{Ti} \cosh(y_i) \quad (C.76)$$

and

$$p_1 \cdot p_2 = p_{T1} p_{T2} [\cosh(y_1) \cosh(y_2) - \cos(\varphi_2) - \sinh(y_1) \sinh(y_2)] \quad (C.77)$$

if the azimuthal angles are defined with respect to the direction of the transverse momentum of the first particle

$$p_1 = p_{T1} (\cosh(y_1), 1, 0, \sinh(y_1)) .$$

The measures can be rewritten in terms of transverse momentum and rapidity according to (C.10). As long as the integrand depends only on the invariants  $p_i \cdot p_j$ , it is without a preferred direction and  $\varphi_1$  can be integrated out, giving a factor  $2\pi$ . Furthermore, it is then a function of  $c_\varphi \equiv \cos(\varphi_2)$ , so it is best to write

$$\int_0^{2\pi} d\varphi_2 \dots = 2 \int_{-1}^1 dc_\varphi \frac{\dots}{\sqrt{1 - c_\varphi^2}} . \quad (C.78)$$

For brevity (and in case of an unrestricted rapidity range also for the sake of numerical integrability) I also rewrite the integration over the rapidities via

$$\begin{aligned} \cosh(y_i) &= \gamma_i , \\ \sinh(y_i) &= \beta_i \gamma_i , \end{aligned}$$

with the velocities along the beam direction,  $\beta_i \equiv \tanh(y_i)$ , and the Lorentz factors  $\gamma_i \equiv \sqrt{1 - \beta_i^2}^{-1}$ , giving

$$\int_{-\infty}^{\infty} dy_i \dots = \int_{-1}^1 d\beta_i \gamma_i^2 \dots \quad (C.79)$$

The phase space is then

$$\begin{aligned} d\Phi^{(3)} &= \frac{1}{2(2\pi)^4} dp_{T1} dp_{T2} d\beta_1 d\beta_2 dc_\varphi \frac{p_{T1} \gamma_1^2 p_{T2} \gamma_2^2}{\sqrt{1 - c_\varphi^2}} \theta(\sqrt{s_{ab}} - p_{T1} \gamma_1 - p_{T2} \gamma_2) \\ &\quad \cdot \delta(s_{ab} - 2\sqrt{s_{ab}}(p_{T1} \gamma_1 + p_{T2} \gamma_2) + 2p_{T1} p_{T2} (\gamma_1 \gamma_2 - \gamma_1 \beta_1 \gamma_2 \beta_2 - c_\varphi)) . \end{aligned} \quad (C.80)$$

## C Prompt Photon Production Cross Section

One can then eliminate the  $\delta$ -distribution by the  $c_\varphi$  integration

$$\begin{aligned} & \int_{-1}^1 dc_\varphi \delta(s_{ab} - 2\sqrt{s_{ab}}(p_{T1}\gamma_1 + p_{T2}\gamma_2) + 2p_{T1}p_{T2}(\gamma_1\gamma_2 - \gamma_1\beta_1\gamma_2\beta_2 - c_\varphi)) \dots \\ &= \theta\left(1 \pm \left[\frac{s_{ab}}{2p_{T1}p_{T2}} - \sqrt{s_{ab}}\left(\frac{\gamma_1}{p_{T2}} + \frac{\gamma_2}{p_{T1}}\right) + \gamma_1\gamma_2(1 - \beta_1\beta_2)\right]\right) \frac{1}{2p_{T1}p_{T2}} \dots \end{aligned}$$

Here, I defined

$$\theta(1 \pm c_\varphi) \equiv \theta(1 + c_\varphi) \theta(1 - c_\varphi)$$

and from now on I will write  $c_\varphi$  as a shortcut for the expression in the square brackets. On the other hand, the  $\theta$ -distribution in (C.80) gives a bound on the  $p_{T2}$  integration

$$p_{T2} \leq p_{T2}^{\max} \equiv \frac{\sqrt{s_{ab}} - p_{T1}\gamma_1}{\gamma_2} \quad (\text{C.81})$$

and, since  $p_{T2} \geq 0$ , also an upper bound on  $p_{T1}$

$$p_{T1} \leq p_{T1}^{\max} \equiv \frac{\sqrt{s_{ab}}}{\gamma_1}, \quad (\text{C.82})$$

such that the phase space integration can be written

$$\begin{aligned} & \int d\Phi^{(3)} \dots \\ &= \frac{1}{64\pi^4} \int_{-1}^1 d\beta_1 \int_{-1}^1 d\beta_2 \int_0^{p_{T1}^{\max}} dp_{T1} \int_0^{p_{T2}^{\max}} dp_{T2} \frac{\gamma_1^2 \gamma_2^2}{\sqrt{1 - c_\varphi^2}} \theta(1 \pm c_\varphi) \dots \end{aligned} \quad (\text{C.83})$$

### C.2.4 NLO cross section

The complete cross section at NLO is now given by the  $2 \rightarrow 2$  contributions of the form (C.14), where the matrix element now includes the virtual corrections,

$$|\overline{\mathcal{M}_{q\bar{q} \rightarrow \gamma g}}|^2 = |\overline{\mathcal{M}_{q\bar{q} \rightarrow \gamma g}^{(0)}}|^2 + |\overline{\mathcal{M}_{q\bar{q} \rightarrow \gamma g}^{(1)}}|^2, \quad (\text{C.84})$$

plus the  $2 \rightarrow 3$  contributions, so all in all:

$$\begin{aligned} \int d\sigma_{AB \rightarrow \gamma X}^{(\text{direct})}(p_A, p_B) &= \sum_{a,b} \int_0^1 dx_a \int_0^1 dx_b f_{a/A}(x_a) f_{b/B}(x_b) \\ &\cdot \frac{1}{4F(x_a p_A, x_b p_B)} \left[ \sum_c \int d\Phi^{(2)} |\overline{\mathcal{M}_{ab \rightarrow \gamma c}}|^2 \right. \\ &\quad \left. + \sum_{c,d} \int d\Phi^{(3)} |\overline{\mathcal{M}_{ab \rightarrow \gamma cd}}|^2 \right] \theta(p_1 \dots). \end{aligned} \quad (\text{C.85})$$



For the sake of brevity,  $\theta$ -distributions implementing for instance  $p_T$  and rapidity cuts on the photon have only been indicated.

As noted before, the QCD divergences cancel between the two contributions, up to collinear divergences that are implicitly absorbed into the PDFs. On the other hand, the IR divergences related to the photon can not be cancelled at this point, since the fragmentation contribution is missing. To enable numerical integration of the cross section the divergences related to pure QCD, i.e. disregarding the photon for the moment, can be made visible and cancelled by using CS dipoles, as described in Sec. 2.5.1. To this end, (C.85) has to be rewritten using a jet-defining function  $F_J$ , as in (2.45),(2.46). The jet-defining function can only be given by the  $\theta$ -distributions defining the photon-cuts. Thus, for rapidity and  $p_T$  cuts on the photon momentum  $p_1$ , (3.20) is used which is valid for both the LO and NLO contributions and thus fulfills (2.30). Then, (C.85) becomes

$$\begin{aligned} \int d\sigma_{AB \rightarrow \gamma X}^{(\text{direct})}(p_A, p_B) &= \sum_{a,b} \int_0^1 dx_a \int_0^1 dx_b f_{a/A}(x_a) f_{b/B}(x_b) \\ &\cdot \frac{1}{4F} \left[ \sum_c \int d\Phi^{(2)} |\overline{\mathcal{M}_{ab \rightarrow \gamma c}}|^2 \right. \\ &\quad \left. + \sum_{c,d} \int d\Phi^{(3)} |\overline{\mathcal{M}_{ab \rightarrow \gamma cd}}|^2 \right] F_J(p_1). \end{aligned} \quad (\text{C.86})$$

It is crucial to notice that, while the dipoles themselves take no note of the presence of non-QCD particles (in the sense that uncoloured particles can not be emitter, emitted or spectator), the jet-defining function might depend on momenta of non-QCD particles, as is here the case with the dependence on the photon momentum – crucial, because the prescription for the dipole subtraction formalism encompasses not only the calculation and subtraction of the dipoles, but also a modification of the jet-defining function!

As the process then includes two identified initial state partons and no identified final state parton, all relevant formulae for the construction of dipoles are found in Ch. 10 of Ref. [29]. The types of dipoles to compute all either have an initial state spectator or emitter:  $\mathcal{D}_{cd}^a$ ,  $\mathcal{D}_{cd}^b$ ,  $\mathcal{D}_d^{ac}$ ,  $\mathcal{D}_c^{ad}$ ,  $\mathcal{D}_d^{bc}$ ,  $\mathcal{D}_c^{bd}$ .

### C.2.5 QCD Dipoles

Instead of giving all the dipoles necessary to counter the divergences of all real correction processes, I will just exemplify how the dipoles for the processes  $q\bar{q} \rightarrow \gamma gg$  are computed. Afterwards, I give the results for the integrated dipoles needed to cancel the IR divergences in the virtual corrections and comment on the collinear remnants.

By removing the radiated gluon on the right side of Fig. C.15, it is clear that the underlying Born process is  $q\bar{q} \rightarrow \gamma g$ , i.e. the colour- and spin-correlated amplitudes have to be computed for the ket-vector

$$|g(p_2); q(p_a), \bar{q}(p_b)\rangle$$

(the photon is not explicitly denoted as it is not coloured).

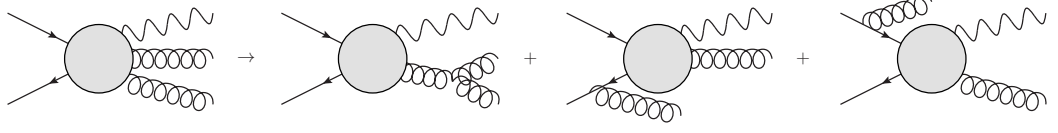


Figure C.15: Diagram structures that lead to singularities for  $q\bar{q} \rightarrow \gamma gg$ . The three diagrams on the right correspond to the dipoles  $(\mathcal{D}_{gg}^q + \mathcal{D}_{gg}^{\bar{q}})$ ,  $(\mathcal{D}^{qg,\bar{q}} + \mathcal{D}_g^{qg})$  and  $(\mathcal{D}^{\bar{q}g,q} + \mathcal{D}_g^{\bar{q}g})$ .

### Colour-correlations

Colour-conservation (2.57) makes it easy to compute the colour-correlations, since in case of only three coloured particles the products  $\mathbf{T}_i \cdot \mathbf{T}_j$  reduce to a sum of Casimir operators  $\mathbf{T}_k^2 = C_k$  (see App. A of Ref. [29]):

$$\begin{aligned} \mathbf{T}_1 + \mathbf{T}_2 + \mathbf{T}_3 |1, 2, 3\rangle &= 0 \\ (\mathbf{T}_1 + \mathbf{T}_2 + \mathbf{T}_3)^2 |1, 2, 3\rangle &= 0 \\ 2\mathbf{T}_2 \cdot \mathbf{T}_3 |1, 2, 3\rangle &= (\mathbf{T}_1^2 - \mathbf{T}_2^2 - \mathbf{T}_3^2) |1, 2, 3\rangle. \end{aligned}$$

Thus, with

$$\mathbf{T}_q \cdot \mathbf{T}_{\bar{q}} |g; q, \bar{q}\rangle = \frac{C_A - 2C_F}{2} |g; q, \bar{q}\rangle, \quad (\text{C.87})$$

$$\mathbf{T}_g \cdot \mathbf{T}_q |g; q, \bar{q}\rangle = -\frac{C_A}{2} |g; q, \bar{q}\rangle, \quad (\text{C.88})$$

$$\mathbf{T}_g \cdot \mathbf{T}_{\bar{q}} |g; q, \bar{q}\rangle = -\frac{C_A}{2} |g; q, \bar{q}\rangle, \quad (\text{C.89})$$

all colour-correlations are known – even for all permutations of  $g$ ,  $q$  and  $\bar{q}$  since the Casimir operators do not differentiate between incoming, outgoing or particle, antiparticle.

### Spin-correlations

Furthermore, there is only one spin-correlated amplitude, since the Born process has only one gluon. Hence, it can be computed by considering the matrix element of  $q\bar{q} \rightarrow \gamma g$  and replacing the polarization tensor of the gluon,  $\varepsilon_\lambda^{*\mu}$ , by the polarization sum (2.60):

$$\begin{aligned} &\langle g(p_2); q(p_a), \bar{q}(p_b) | \nu \rangle \langle \mu | g(p_2); q(p_a), \bar{q}(p_b) \rangle \\ &= -(Q_f e)^2 g_s^2 C_F N_c \left\{ \frac{1}{((p_a - p_1)^2)^2} \text{Tr} \left[ \not{p}_a \gamma_\tau (\not{p}_a - \not{p}_1) \gamma^{\nu'} \not{p}_b \gamma^{\mu'} (\not{p}_a - \not{p}_1) \gamma^\tau \right] \right. \\ &\quad + \frac{1}{((p_a - p_2)^2)^2} \text{Tr} \left[ \not{p}_a \gamma^{\nu'} (\not{p}_a - \not{p}_2) \gamma_\tau \not{p}_b \gamma^\tau (\not{p}_a - \not{p}_2) \gamma^{\mu'} \right] \\ &\quad \left. + \frac{1}{(p_a - p_1)^2 (p_a - p_2)^2} \left[ \text{Tr} \left[ \not{p}_a \gamma^{\nu'} (\not{p}_a - \not{p}_2) \gamma_\tau \not{p}_b \gamma^{\mu'} (\not{p}_a - \not{p}_1) \gamma_\tau \right] \right. \right. \end{aligned}$$

$$\begin{aligned}
& + \text{Tr} \left[ \not{p}_a \gamma_\tau (\not{p}_a - \not{p}_1) \gamma^{\nu'} \not{p}_b \gamma^\tau (\not{p}_a - \not{p}_2) \gamma^{\mu'} \right] \Big\} \\
& \cdot \left( -g_{\mu'\mu} + \frac{p_{2\mu'} \eta_\mu + p_{2\mu} \eta_{\mu'}}{p_2 \cdot \eta} \right) \left( -g_{\nu'\nu} + \frac{p_{2\nu'} \eta_\nu + p_{2\nu} \eta_{\nu'}}{p_2 \cdot \eta} \right).
\end{aligned}$$

Using `FORM` to reduce this, I finally find the simple result

$$\begin{aligned}
& \langle g(p_2); q(p_a), \bar{q}(p_b) | \nu \rangle \langle \mu | g(p_2); q(p_a), \bar{q}(p_b) \rangle \\
& = \frac{1}{2} \left( -g_{\mu\nu} + \frac{p_{2\mu} \eta_\nu + p_{2\nu} \eta_\mu}{p_2 \cdot \eta} \right) \sum_{\substack{\text{spins} \\ \text{colours}}} |\mathcal{M}_{q\bar{q} \rightarrow \gamma g}|^2,
\end{aligned} \tag{C.90}$$

i.e. the spin-correlation factorizes. This result holds via crossing for all Born processes.<sup>2</sup> It turns out that the unphysical vector  $\eta$  drops out in all dipoles; though, this might have been expected, as the dipoles reproduce limits to physical results.

### $\mathcal{D}_{gg}^q$

With these results it is possible to tackle the calculation of the dipoles. Eqs. (5.36)-(5.38) and (5.40) of Ref. [29] lead to

$$\begin{aligned}
& \mathcal{D}_{gg}^q(p_a, p_b, p_1, p_2, p_3) \\
& = -\frac{1}{2p_2 \cdot p_3} \frac{1}{x_{23,a}} \left( -\frac{1}{2} \right) \langle \mu | \mathbf{V}_{gg}^q | \nu \rangle \frac{1}{2} \left( -g_{\mu\nu} + \frac{\tilde{p}_{23\mu} \eta_\nu + \tilde{p}_{23\nu} \eta_\mu}{\tilde{p}_{23} \cdot \eta} \right) \\
& \cdot \sum_{\substack{\text{spins} \\ \text{colours}}} |\mathcal{M}_{q\bar{q} \rightarrow \gamma g}(\tilde{p}_a, p_b, p_1, \tilde{p}_{23})|^2.
\end{aligned} \tag{C.91}$$

In fact all dipoles have this form: a kinematic prefactor, a factor from the colour-correlations, a factor from spin-correlation tensor and  $\mathbf{V}$  operator, and the Born amplitude with modified kinematics. It is hence unproblematic to compute these parts separately in a numerical code; a major simplification of this particular process compared to processes with more gluons, where the spin-correlation might not factorize. Using `FORM` to perform the tensor-algebra and simplifying the final expression with `Mathematica` I find

$$\begin{aligned}
& \langle \mu | \mathbf{V}_{gg}^q | \nu \rangle \frac{1}{2} \left( -g_{\mu\nu} + \frac{\tilde{p}_{23\mu} \eta_\nu + \tilde{p}_{23\nu} \eta_\mu}{\tilde{p}_{23} \cdot \eta} \right) \\
& = 16\pi\alpha_s C_A \left( \frac{(s_{ab} + t_{a1})^3}{s_{ab} + t_{a1} - t_{a2} + t_{b1}} + \frac{(s_{ab} + t_{a1})^3}{2s_{ab} + 2t_{a1} + t_{a2} + t_{b1}} \right. \\
& \quad \left. - t_{a2}(s_{ab} + t_{a1}) - 2(s_{ab} + t_{a1})^2 - t_{a2}^2 \right) / (s_{ab} + t_{a1})^2
\end{aligned} \tag{C.92}$$

<sup>2</sup>The results for colour- and spin-correlations have also been obtained in [186] by explicit calculation of the amplitudes. However, in that thesis the prescription for the spin-correlation is interpreted as leaving out the polarization tensor instead of replacing it with a polarization sum.

## C Prompt Photon Production Cross Section

and

$$x_{23,a} = \frac{-t_{b1}}{s_{ab} + t_{a1}} \quad (C.93)$$

in terms of the Mandelstam variables (C.67)-(C.71). As the Born amplitude is also usually written in terms of Mandelstam variables, I use

$$|\mathcal{M}_{q\bar{q} \rightarrow \gamma g}(\tilde{p}_a, p_b, p_1, \tilde{p}_{23})|^2 = |\mathcal{M}_{q\bar{q} \rightarrow \gamma g}|^2(\tilde{s}, \tilde{t}, \tilde{u}) \quad (C.94)$$

with

$$\tilde{s} = 2\tilde{p}_a \cdot p_b = -\frac{s_{ab}t_{b1}}{s_{ab} + t_{a1}}, \quad (C.95)$$

$$\tilde{t} = -2\tilde{p}_a \cdot p_1 = -\frac{t_{a1}t_{b1}}{s_{ab} + t_{a1}}, \quad (C.96)$$

$$\tilde{u} = -2\tilde{p}_a \cdot \tilde{p}_{23} = t_{b1}. \quad (C.97)$$

Since momentum conservation is implemented by the dipole formalism,

$$\tilde{s} + \tilde{t} + \tilde{u} = 0$$

evidently holds.

The complete result is

$$\begin{aligned} \mathcal{D}_{gg}^q(p_a, p_b, p_1, p_2, p_3) &= \frac{4096}{9} \pi^3 \alpha_s^2 C_A C_F N_c \frac{\left( \frac{t_{a1}^2}{(s_{ab} + t_{a1})^2} + 1 \right)}{t_{a1} t_{b1} (s_{ab} + t_{a1} + t_{b1})} \\ &\cdot \left( \frac{(s_{ab} + t_{a1})^3}{s_{ab} + t_{a1} - t_{a2} + t_{b1}} + \frac{(s_{ab} + t_{a1})^3}{2s_{ab} + 2t_{a1} + t_{a2} + t_{b1}} \right. \\ &\quad \left. - t_{a2}(s_{ab} + t_{a1}) - 2(s_{ab} + t_{a1})^2 - t_{a2}^2 \right). \end{aligned} \quad (C.98)$$

$\mathcal{D}_{gg}^{\bar{q}}$

The dipole with spectator  $\bar{q}$  is obtained completely analogous to the previous dipole. As long as initial and final states are not interchanged, a crossing symmetry holds, i.e. only the kinematics have to be modified from  $(\tilde{p}_a, p_b)$  to  $(p_a, \tilde{p}_b)$ , or equivalently  $p_a \leftrightarrow p_b$ , giving finally

$$\begin{aligned} \mathcal{D}_{gg}^{\bar{q}}(p_a, p_b, p_1, p_2, p_3) &= \mathcal{D}_{gg}^q(p_b, p_a, p_1, p_2, p_3) \\ &= \frac{2048}{9} \pi^3 \alpha_s^2 C_A C_F N_c \frac{(s_{ab} + t_{b1})^2 \left( \frac{t_{b1}^2}{(s_{ab} + t_{b1})^2} + 1 \right)}{t_{a1} t_{b1} (s_{ab} + t_{a1} + t_{b1})} \\ &\cdot \left( -\frac{2(s_{12} + t_{a1} + t_{a2})^2}{(s_{ab} + t_{b1})^2} - \frac{2(s_{12} + t_{a1} + t_{a2})}{s_{ab} + t_{b1}} \right. \\ &\quad \left. - \frac{s_{12} + 2t_{a1} + t_{a2}}{s_{12} + 2s_{ab} + 2t_{a1} + t_{a2} + 2t_{b1}} + \frac{2(s_{12} + t_{a2})}{-s_{12} + s_{ab} - t_{a2} + t_{b1}} - 1 \right). \end{aligned} \quad (C.99)$$

$\mathcal{D}_g^{qg}$ 

These are actually two dipoles, one where the splitting gluon is the gluon with momentum  $p_2$ ,  $\mathcal{D}_{g_3}^{qg_2}$ , one where it is the gluon with momentum  $p_3$ ,  $\mathcal{D}_{g_2}^{qg_3}$ . For the former, I give just the final result. With Eqs. (5.61)-(5.64) and (5.65) of Ref. [29] I find

$$\mathcal{D}_{g_2}^{qg_3} = -\frac{1}{2p_a \cdot p_3} \frac{1}{x_{23,a}} \left( -\frac{C_A}{2C_F} \right) V_{g_2}^{qg_3} \sum_{\substack{\text{spins} \\ \text{colours}}} |\mathcal{M}_{q\bar{q} \rightarrow \gamma g}(\tilde{p}_{a3}, p_b, p_1, \tilde{p}_2)|^2 \quad (\text{C.100})$$

with

$$V_{g_2}^{qg_3} = 8\pi\alpha_s C_F \frac{t_{b1}(s_{ab} + t_{a1} + t_{a2}) - t_{a2}(s_{ab} + t_{a1}) + t_{b1}^2}{(s_{ab} + t_{a1})(2s_{ab} + 2t_{a1} + t_{a2} + t_{b1})} \quad (\text{C.101})$$

and  $x_{23,a}$ ,  $\tilde{s}$ ,  $\tilde{t}$ ,  $\tilde{u}$  coincidentally as before.

Assembling all ingredients gives

$$\begin{aligned} & \mathcal{D}_{g_2}^{qg_3}(p_a, p_b, p_1, p_2, p_3) \\ &= -\frac{2048}{9} \pi^3 \alpha_s^2 C_A C_F N_c (s_{ab}^2 + 2s_{ab}t_{a1} + 2t_{a1}^2) \\ & \quad \cdot \frac{(-t_{b1}(s_{ab} + t_{a1} + t_{a2}) + t_{a2}(s_{ab} + t_{a1}) - t_{b1}^2)}{t_{a1}t_{b1}(s_{ab} + t_{a1})(s_{ab} + t_{a1} + t_{a2})(2s_{ab} + 2t_{a1} + t_{a2} + t_{b1})} \end{aligned} \quad (\text{C.102})$$

and in case of the radiation of the other gluon

$$\begin{aligned} & \mathcal{D}_{g_3}^{qg_2}(p_a, p_b, p_1, p_2, p_3) \\ &= \frac{2048}{9} \pi^3 \alpha_s^2 C_A C_F N_c (s_{ab}^2 + 2s_{ab}t_{a1} + 2t_{a1}^2) \\ & \quad \cdot \frac{((s_{ab} + t_{a1})(-s_{ab} - t_{a1} - t_{a2}) + t_{a2}t_{b1} - t_{b1}^2)}{t_{a1}t_{a2}t_{b1}(s_{ab} + t_{a1})(s_{ab} + t_{a1} - t_{a2} + t_{b1})} \end{aligned} \quad (\text{C.103})$$

 $\mathcal{D}_g^{\bar{q}g}$ 

This is again obtained similarly to the previous dipole, by exchanging  $\tilde{p}_{a3}, p_b$  with  $p_a, \tilde{p}_{b3}$ , etc. The results are

$$\begin{aligned} & \mathcal{D}_{g_2}^{\bar{q}g_3}(p_a, p_b, p_1, p_2, p_3) \\ &= -\frac{2048}{9} \pi^3 \alpha_s^2 C_A C_F N_c \frac{(s_{ab}^2 + 2s_{ab}t_{b1} + 2t_{b1}^2)}{t_{a1}t_{b1}(s_{ab} + t_{b1})} \\ & \quad \cdot \frac{((s_{ab} + t_{b1})(-s_{12} - s_{ab} - t_{a1} - t_{a2} - t_{b1}) - t_{a1}(-s_{12} - t_{a1} - t_{a2}) - t_{a1}^2)}{(-s_{12} - t_{a1} - t_{a2})(-s_{12} + s_{ab} - t_{a2} + t_{b1})} \end{aligned} \quad (\text{C.104})$$

and

$$\begin{aligned} & \mathcal{D}_{g_3}^{\bar{q}g_2}(p_a, p_b, p_1, p_2, p_3) \\ &= -\frac{2048}{9} \pi^3 \alpha_s^2 C_A C_F N_c \frac{(s_{ab}^2 + 2s_{ab}t_{b1} + 2t_{b1}^2)}{t_{a1}t_{b1}(s_{ab} + t_{b1})} \\ & \quad \cdot \frac{(-t_{a1}(s_{12} + s_{ab} + t_{a1} + t_{a2} + t_{b1}) + (s_{ab} + t_{b1})(s_{12} + t_{a1} + t_{a2}) - t_{a1}^2)}{(s_{12} + s_{ab} + t_{a1} + t_{a2} + t_{b1})(s_{12} + 2s_{ab} + 2t_{a1} + t_{a2} + 2t_{b1})} \end{aligned} \quad (\text{C.105})$$

$\mathcal{D}^{qg,\bar{q}}$

The initial state splitting-initial state spectator dipoles are computed via Eqs. (5.136)-(5.139) of Ref. [29], in this case in combination with Eq. (5.145). Taking the gluon with momentum  $p_3$  to partake in the splitting, I find

$$\mathcal{D}^{qg3,\bar{q}} = -\frac{1}{2p_a \cdot p_3} \frac{1}{x_{3,ab}} \left( \frac{1}{2} \frac{C_A - 2C_F}{C_F} \right) V^{qg3,\bar{q}} \sum_{\substack{\text{spins} \\ \text{colours}}} |\mathcal{M}_{q\bar{q} \rightarrow \gamma g}(\tilde{p}_{a3}, p_b, \tilde{p}_1, \tilde{p}_2)|^2 \quad (\text{C.106})$$

with

$$V^{qg3,\bar{q}} = -8\pi\alpha_s C_F \frac{s_{12}^2 + s_{ab}^2}{s_{ab}(s_{12} - s_{ab})} \quad (\text{C.107})$$

and

$$x_{3,ab} = \frac{s_{12}}{s_{ab}}, \quad (\text{C.108})$$

$$\tilde{s} = s_{12}, \quad (\text{C.109})$$

$$\tilde{t} = \frac{s_{12}t_{b1}(-s_{ab} + t_{a1} + t_{a2}) - s_{12}(s_{ab} - t_{a1})(2s_{12} + s_{ab} + t_{a1} + t_{a2})}{s_{12}(3s_{ab} - t_{a1} - t_{a2}) + s_{ab}(s_{ab} + t_{a1} + t_{a2})}, \quad (\text{C.110})$$

$$\tilde{u} = -\tilde{s} - \tilde{t}. \quad (\text{C.111})$$

Assembling everything, I get the final results

$$\begin{aligned} & \mathcal{D}^{qg3,\bar{q}}(p_a, p_b, p_1, p_2, p_3) \\ &= -\frac{2048}{9} \pi^3 \alpha_s^2 C_F N_c (C_A - 2C_F) \frac{(s_{12}^2 + s_{ab}^2)}{s_{12}^2(s_{12} - s_{ab})(s_{ab} + t_{a1} + t_{a2})} \\ & \quad \cdot (s_{12}^2(s_{12}(s_{ab} + t_{a1} - t_{a2}) + s_{ab}(t_{a1} - t_{b1}) + (t_{a1} + t_{a2})(t_{a1} + t_{b1}))^2 \\ & \quad + (s_{12}(s_{ab} - t_{a1})(2s_{12} + s_{ab} + t_{a1} + t_{a2}) - s_{12}t_{b1}(-s_{ab} + t_{a1} + t_{a2}))^2) \\ & \quad / ((s_{12}t_{b1}(-s_{ab} + t_{a1} + t_{a2}) - s_{12}(s_{ab} - t_{a1})(2s_{12} + s_{ab} + t_{a1} + t_{a2})) \\ & \quad \cdot (s_{12}(s_{ab} + t_{a1} - t_{a2}) + s_{ab}(t_{a1} - t_{b1}) + (t_{a1} + t_{a2})(t_{a1} + t_{b1}))) \end{aligned} \quad (\text{C.112})$$

and

$$\begin{aligned} & \mathcal{D}^{qg2,\bar{q}}(p_a, p_b, p_1, p_2, p_3) \\ &= \frac{2048}{9} \pi^3 \alpha_s^2 C_F N_c (C_A - 2C_F) \frac{((s_{12} + t_{a1} + t_{b1})^2 + s_{ab}^2)}{t_{a2}(s_{12} + t_{a1} + t_{b1})(s_{12} + s_{ab} + t_{a1} + t_{b1})} \\ & \quad \cdot (s_{12}^2(8(s_{ab}^2 + t_{a1}^2) + 4t_{a2}(s_{ab} + t_{a1}) + t_{a2}^2) + 4s_{12}(s_{ab}^2(4t_{a1} + t_{a2} + 4t_{b1}) \\ & \quad + s_{ab}(t_{a1}t_{a2} + 4t_{a1}t_{b1} + 3t_{a2}t_{b1}) + (2t_{a1} + t_{a2})^2(t_{a1} + t_{b1})) \\ & \quad + s_{ab}^2(8t_{a1}^2 + 4t_{a1}(t_{a2} + 4t_{b1}) + t_{a2}^2 + 16t_{b1}^2) \\ & \quad + 2s_{ab}(t_{a1} + t_{b1})(8t_{b1}(t_{a1} + t_{a2}) - t_{a2}^2) \\ & \quad + (8t_{a1}^2 + 12t_{a1}t_{a2} + 5t_{a2}^2)(t_{a1} + t_{b1})^2) \\ & \quad / ((2s_{12}(t_{a1} - s_{ab}) + (2t_{a1} + t_{a2})(-s_{ab} + t_{a1} + t_{b1})) \\ & \quad \cdot (s_{12}(2(s_{ab} + t_{a1}) + t_{a2}) + 2s_{ab}(t_{a1} + 2t_{b1}) + 2(t_{a1} + t_{a2})(t_{a1} + t_{b1}))) \end{aligned} \quad (\text{C.113})$$

$\mathcal{D}^{\bar{q}g,q}$ 

These are again two dipoles; one for the splitting gluon having momentum  $p_2$ ,  $\mathcal{D}^{\bar{q}g_2,q}$ , one with  $p_3$ ,  $\mathcal{D}^{\bar{q}g_3,q}$ . The latter is obtained similarly to the previous dipole by exchanging  $\tilde{p}_{a3}, p_b$  with  $p_a, \tilde{p}_{b3}$ , etc. Thus, for the final dipoles, I find

$$\begin{aligned}
& \mathcal{D}^{\bar{q}g_3,q}(p_a, p_b, p_1, p_2, p_3) \\
&= -\frac{2048}{9}\pi^3\alpha\alpha_s^2C_F N_c(C_A - 2C_F)\frac{(s_{12}^2 + s_{ab}^2)}{s_{12}(s_{12} - s_{ab})(s_{12} + t_{a1} + t_{a2})} \\
&\quad \cdot \left( (s_{12}^2 + s_{12}(2s_{ab} + t_{a2} + t_{b1}) - 2s_{ab}t_{a1} - (t_{a1} + t_{a2})(t_{a1} + t_{b1}))^2 \right. \\
&\quad \left. + (s_{12}(s_{ab} + t_{a1} - t_{b1}) + s_{ab}(t_{a1} - t_{a2}) + (t_{a1} + t_{a2})(t_{a1} + t_{b1}))^2 \right) \\
&\quad / ((s_{12}(s_{ab} + t_{a1} - t_{b1}) + s_{ab}(t_{a1} - t_{a2}) + (t_{a1} + t_{a2})(t_{a1} + t_{b1})) \\
&\quad \cdot (s_{12}^2 + s_{12}(2s_{ab} + t_{a2} + t_{b1}) - 2s_{ab}t_{a1} - (t_{a1} + t_{a2})(t_{a1} + t_{b1}))) \quad (C.114)
\end{aligned}$$

and

$$\begin{aligned}
& \mathcal{D}^{\bar{q}g_2,q}(p_a, p_b, p_1, p_2, p_3) \\
&= -\frac{2048}{9}\pi^3\alpha\alpha_s^2C_F N_c(C_A - 2C_F)\frac{((s_{12} + t_{a1} + t_{b1})^2 + s_{ab}^2)}{(s_{12} + t_{a1} + t_{b1})(s_{12} + s_{ab} + t_{a1} + t_{b1})} \\
&\quad \cdot ((s_{12}(s_{ab} + t_{a1} - t_{b1}) - (s_{ab} - t_{a1} - t_{b1})(s_{ab} + t_{a1} + t_{a2} - t_{b1}))^2 \\
&\quad + ((s_{12} + 2t_{a1})(s_{12} - s_{ab} + t_{a1} + t_{a2}) + t_{b1}(s_{12} + 2(t_{a1} + t_{a2}))))^2) \\
&\quad / ((s_{12}(s_{ab} + t_{a1} - t_{b1}) - (s_{ab} - t_{a1} - t_{b1})(s_{ab} + t_{a1} + t_{a2} - t_{b1})) \\
&\quad \cdot (s_{12} + s_{ab} + t_{a1} + t_{a2} + t_{b1}) \\
&\quad \cdot ((s_{12} + 2t_{a1})(s_{12} - s_{ab} + t_{a1} + t_{a2}) + t_{b1}(s_{12} + 2(t_{a1} + t_{a2})))) \quad (C.115)
\end{aligned}$$

**Dipole-subtracted  $q\bar{q} \rightarrow \gamma gg$**

Now, the subtracted cross section for the real radiation process  $q\bar{q} \rightarrow \gamma gg$  can be computed; taking note of (2.61) and (C.86), I find it to be given by

$$\begin{aligned}
 & \int_0^1 dx_a \int_0^1 dx_b f_{q/A}(x_a, \mu_F) f_{\bar{q}/B}(x_b, \mu_F) \\
 & \cdot \int d\Phi^{(3)} \frac{1}{4F} \frac{1}{2} \left\{ F_J(p_1) \left[ \overline{|\mathcal{M}_{q\bar{q} \rightarrow \gamma gg}(x_a p_A, x_b p_B, p_1, p_2)|^2} \right. \right. \\
 & \quad - \mathcal{N} \left( \mathcal{D}_{gg}^q(x_a p_A, x_b p_B, p_1, p_2, p_3) \right. \\
 & \quad \quad + \mathcal{D}_{gg}^{\bar{q}}(x_a p_A, x_b p_B, p_1, p_2, p_3) \\
 & \quad \quad + \mathcal{D}_{g_3}^{qg_2}(x_a p_A, x_b p_B, p_1, p_2, p_3) \\
 & \quad \quad + \mathcal{D}_{g_2}^{qg_3}(x_a p_A, x_b p_B, p_1, p_2, p_3) \\
 & \quad \quad + \mathcal{D}_{g_3}^{\bar{q}g_2}(x_a p_A, x_b p_B, p_1, p_2, p_3) \\
 & \quad \quad \left. \left. + \mathcal{D}_{g_2}^{\bar{q}g_3}(x_a p_A, x_b p_B, p_1, p_2, p_3) \right) \right] \\
 & \quad - F_J(\tilde{p}_1) \mathcal{N} \left[ \mathcal{D}^{qg_2, \bar{q}}(x_a p_A, x_b p_B, p_1, p_2, p_3) \right. \\
 & \quad \quad + \mathcal{D}^{qg_3, \bar{q}}(x_a p_A, x_b p_B, p_1, p_2, p_3) \\
 & \quad \quad + \mathcal{D}^{\bar{q}g_2, q}(x_a p_A, x_b p_B, p_1, p_2, p_3) \\
 & \quad \quad \left. \left. + \mathcal{D}^{\bar{q}g_3, q}(x_a p_A, x_b p_B, p_1, p_2, p_3) \right] \right\}. \tag{C.116}
 \end{aligned}$$

The factor  $1/2$  is the symmetry factor for identical final state gluons and

$$\mathcal{N} = \frac{1}{4N_c^2}$$

is the averaging factor for initial state spins and colours.

It is again of utter importance to note, that the initial state correlated dipoles have to be integrated over a modified range. The jet-defining function depends on the photon momentum  $p_1$ , which for these dipoles has to be shifted to  $\tilde{p}_1$ , cf. Eq. (10.4) of Ref. [29]. To illustrate this, one can take as an example the prescription to compute  $\mathcal{D}^{qg_3, \bar{q}}$  in (C.106), where – with Eq. (5.139) of Ref. [29] –  $\tilde{p}_1$  is given by

$$\begin{aligned}
 \tilde{p}_1^\mu &= 2 \frac{s_{12}(2s_{ab} - t_{a2}) + s_{ab}(s_{ab} + t_{a1} + t_{a2} + t_{b1})}{s_{12}(3s_{ab} - t_{a1} - t_{a2}) + s_{ab}(s_{ab} + t_{a1} + t_{a2})} p_1^\mu \\
 &+ \frac{s_{12}(s_{ab} + t_{a1} - t_{a2}) + s_{ab}(s_{ab} + t_{a1} + t_{a2} + 2t_{b1})}{s_{12}(3s_{ab} - t_{a1} - t_{a2}) + s_{ab}(s_{ab} + t_{a1} + t_{a2})} p_2^\mu \\
 &+ \frac{s_{12}(2s_{ab} - t_{a2}) + s_{ab}(s_{ab} + t_{a1} + t_{a2} + t_{b1})}{s_{12}(3s_{ab} - t_{a1} - t_{a2}) + s_{ab}(s_{ab} + t_{a1} + t_{a2})} \left[ p_3^\mu + \left( \frac{s_{12}}{s_{ab}} - 1 \right) p_a^\mu \right]. \tag{C.117}
 \end{aligned}$$

This vanishes in the soft limit  $p_2 \rightarrow 0$  (which is included in the integration over  $\Phi^{(3)}$ ) as can be seen by setting

$$s_{12} = t_{a2} = s_{ab} + t_{a2} + t_{b1} = 0$$



(the last equality is just  $s_{23} = 0$ ). Thus, since  $|\mathcal{M}_{q\bar{q} \rightarrow \gamma g}(\tilde{p}_{a3}, p_b, \tilde{p}_1, \tilde{p}_2)|^2$  diverges in the zero-momentum limit,  $\mathcal{D}^{qg3, \bar{q}}$  does so too and would introduce an additional soft divergence in (C.116), if the jet-defining function  $F_J$  were not adjusted to depend on  $\tilde{p}_1$  instead of  $p_1$ .

There is another problem if the scales of the process  $\mu_R$  and  $\mu_F$  are related to  $p_1$  in the real process  $|\mathcal{M}_{q\bar{q} \rightarrow \gamma gg}|^2$ . Then in the initial state correlated dipoles  $\mu_R$  and  $\mu_F$  have to be related to  $\tilde{p}_1$ , since now, with  $F_J$  depending on  $\tilde{p}_1$ , there is no protection against  $p_1 \rightarrow 0$ , which would lead to undefined quantities  $\alpha_s(\mu_R = 0)$  and  $f_{i/H}(x, \mu_F = 0)$ . Unfortunately, the scales in [29] are kept fixed throughout the discussion, so that the authors do not comment on this issue. However, tracing their derivation of the integrated dipoles in Sec. 5.5 of [29], one can infer that the prescription of the dipole subtraction with running scales  $\mu_R = \mu_F = h(p_1)$ , with  $h$  some function of some final state momentum  $p_1$ , has to include: In every term of the subtracted real contribution (like (C.116)) where  $p_1$  is transformed to  $\tilde{p}_1$ , also the scales have to be transformed to  $\mu_R = \mu_F = h(\tilde{p}_1)$ . Otherwise the integration over the radiated particle's momentum in Eq. (5.152) of [29] could not be done, as it would encompass an integration over  $\alpha_s$  and the PDFs.

Hence, to make perfectly clear the prescription for the dipole subtraction, I assume  $\mu_R = \mu_F = p_{T1}$ , such that (C.116) becomes

$$\begin{aligned}
& \int_0^1 dx_a \int_0^1 dx_b \int d\Phi^{(3)} \frac{1}{4F} \frac{1}{2} \\
& \cdot \left\{ f_{q/A}(x_a, p_{T1}) f_{\bar{q}/B}(x_b, p_{T1}) F_J(p_1) \right. \\
& \cdot \left[ \overline{|\mathcal{M}_{q\bar{q} \rightarrow \gamma g}(x_a p_A, x_b p_B, p_1, p_2, \mu_R = p_{T1})|^2} \right. \\
& \quad - \mathcal{N} \left( \mathcal{D}_{gg}^q(x_a p_A, x_b p_B, p_1, p_2, p_3, \mu_R = p_{T1}) \right. \\
& \quad + \mathcal{D}_{gg}^{\bar{q}}(x_a p_A, x_b p_B, p_1, p_2, p_3, \mu_R = p_{T1}) \\
& \quad + \mathcal{D}_{g3}^{qg2}(x_a p_A, x_b p_B, p_1, p_2, p_3, \mu_R = p_{T1}) \\
& \quad + \mathcal{D}_{g2}^{qg3}(x_a p_A, x_b p_B, p_1, p_2, p_3, \mu_R = p_{T1}) \\
& \quad + \mathcal{D}_{g3}^{\bar{q}g2}(x_a p_A, x_b p_B, p_1, p_2, p_3, \mu_R = p_{T1}) \\
& \quad \left. \left. + \mathcal{D}_{g2}^{\bar{q}g3}(x_a p_A, x_b p_B, p_1, p_2, p_3, \mu_R = p_{T1}) \right) \right] \\
& \quad - f_{q/A}(x_a, \widetilde{p_{T1}}) f_{\bar{q}/B}(x_b, \widetilde{p_{T1}}) F_J(\tilde{p}_1) \mathcal{N} \\
& \quad \cdot \left[ \mathcal{D}^{qg2, \bar{q}}(x_a p_A, x_b p_B, p_1, p_2, p_3, \mu_R = \widetilde{p_{T1}}) \right. \\
& \quad + \mathcal{D}^{qg3, \bar{q}}(x_a p_A, x_b p_B, p_1, p_2, p_3, \mu_R = \widetilde{p_{T1}}) \\
& \quad + \mathcal{D}^{\bar{q}g2, q}(x_a p_A, x_b p_B, p_1, p_2, p_3, \mu_R = \widetilde{p_{T1}}) \\
& \quad \left. \left. + \mathcal{D}^{\bar{q}g3, q}(x_a p_A, x_b p_B, p_1, p_2, p_3, \mu_R = \widetilde{p_{T1}}) \right] \right\}. \tag{C.118}
\end{aligned}$$

This is now fit for a numerical integration, as it does not include divergences.

**Integrated dipoles: Insertion operators  $\mathbf{I}(\varepsilon)$ ,  $\mathbf{K}$ ,  $\mathbf{P}$**

The operators  $\mathbf{I}$ ,  $\mathbf{K}$  and  $\mathbf{P}$  (given respectively in Eqs. (10.15), (10.24) and (10.25) of Ref. [29]) reproduce, when inserted into some Born amplitude, the integration over the sum of all dipoles which have that same Born process as an underlying process. The necessary  $\mathbf{I}$ -insertions are computed using Eqs. (10.15), (7.21), (7.22) and (5.32)-(5.34) of Ref. [29]:

$$\begin{aligned}
 & \langle g(p_2); q(p_a), \bar{q}(p_b) | \mathbf{I}(\varepsilon) | g(p_2); q(p_a), \bar{q}(p_b) \rangle \\
 &= -\alpha_s \frac{(\varepsilon-1)(4\pi)^{\varepsilon-1} \Gamma(1-\varepsilon)^2}{\varepsilon^2(2\varepsilon-3)(3\varepsilon-1)\Gamma(1-3\varepsilon)} \left\{ 2C_F(2\varepsilon^2-7\varepsilon+6) \left( \frac{\mu_R^2}{\hat{s}} \right)^\varepsilon \right. \\
 & \quad + N_c \left[ \varepsilon^2 \left( -2 \left( \frac{\mu_R^2}{\hat{s}} \right)^\varepsilon + \left( -\frac{\mu_R^2}{\hat{t}} \right)^\varepsilon + \left( -\frac{\mu_R^2}{\hat{u}} \right)^\varepsilon \right) \right. \\
 & \quad \quad + \varepsilon \left( 7 \left( \frac{\mu_R^2}{\hat{s}} \right)^\varepsilon - 6 \left( -\frac{\mu_R^2}{\hat{t}} \right)^\varepsilon - 6 \left( -\frac{\mu_R^2}{\hat{u}} \right)^\varepsilon \right) \\
 & \quad \quad \left. + 6 \left( -\left( \frac{\mu_R^2}{\hat{s}} \right)^\varepsilon + \left( -\frac{\mu_R^2}{\hat{t}} \right)^\varepsilon + \left( -\frac{\mu_R^2}{\hat{u}} \right)^\varepsilon \right) \right] \\
 & \quad \left. - \varepsilon N_f \left( \left( -\frac{\mu_R^2}{\hat{t}} \right)^\varepsilon + \left( -\frac{\mu_R^2}{\hat{u}} \right)^\varepsilon \right) \right\} |\mathcal{M}_{q\bar{q} \rightarrow \gamma g}|^2(\hat{s}, \hat{t}, \hat{u}), \tag{C.119}
 \end{aligned}$$

$$\begin{aligned}
 & \langle q(p_2); g(p_a), q(p_b) | \mathbf{I}(\varepsilon) | q(p_2); g(p_a), q(p_b) \rangle \\
 &= \langle \bar{q}(p_2); g(p_a), \bar{q}(p_b) | \mathbf{I}(\varepsilon) | \bar{q}(p_2); g(p_a), \bar{q}(p_b) \rangle \\
 &= -\alpha_s \frac{(\varepsilon-1)(4\pi)^{\varepsilon-1} \Gamma(1-\varepsilon)^2}{\varepsilon^2(2\varepsilon-3)(3\varepsilon-1)\Gamma(1-3\varepsilon)} \left\{ 4C_F(\varepsilon^2-3) \left( -\frac{\mu_R^2}{\hat{t}} \right)^\varepsilon \right. \\
 & \quad - \varepsilon \left[ 14C_F \left( -\frac{\mu_R^2}{\hat{t}} \right)^\varepsilon + N_f \left( \left( \frac{\mu_R^2}{\hat{s}} \right)^\varepsilon + \left( -\frac{\mu_R^2}{\hat{u}} \right)^\varepsilon \right) \right] \\
 & \quad + N_c \left[ \varepsilon^2 \left( \left( \frac{\mu_R^2}{\hat{s}} \right)^\varepsilon - 2 \left( -\frac{\mu_R^2}{\hat{t}} \right)^\varepsilon + \left( -\frac{\mu_R^2}{\hat{u}} \right)^\varepsilon \right) \right. \\
 & \quad \quad + \varepsilon \left( -6 \left( \frac{\mu_R^2}{\hat{s}} \right)^\varepsilon + 7 \left( -\frac{\mu_R^2}{\hat{t}} \right)^\varepsilon - 6 \left( -\frac{\mu_R^2}{\hat{u}} \right)^\varepsilon \right) \\
 & \quad \quad \left. + 6 \left( \left( \frac{\mu_R^2}{\hat{s}} \right)^\varepsilon - \left( -\frac{\mu_R^2}{\hat{t}} \right)^\varepsilon + \left( -\frac{\mu_R^2}{\hat{u}} \right)^\varepsilon \right) \right] \right\} |\mathcal{M}_{gq \rightarrow \gamma q}|^2(\hat{s}, \hat{t}, \hat{u}), \tag{C.120}
 \end{aligned}$$

where the matrix element is given by the unaveraged version of (C.4) or the respective crossed result. By exchanging  $p_a \leftrightarrow p_b$ , these results determine all the  $\mathbf{I}$ -insertions needed.

I refrain from giving the expression for the insertions of  $\mathbf{K}$  and  $\mathbf{P}$  due to their length. From Eqs. (10.29), (10.30) of Ref. [29] it follows that the complete subtracted  $q\bar{q} \rightarrow \gamma g$  process is

$$\begin{aligned}
& \sum_{a,b} \int_0^1 dx_a \int_0^1 dx_b f_{q/A}(x_a, p_{T1}) f_{\bar{q}/B}(x_b, p_{T1}) F_J(p_1) \\
& \cdot \left\{ \int d\Phi^{(2)}(x_a p_A, x_b p_B) \frac{1}{4F(x_a p_A, x_b p_B)} \left( \overline{|\mathcal{M}_{q\bar{q} \rightarrow \gamma g}(x_a p_A, x_b p_B, p_1, p_2, \mu_R = p_{T1})|^2} \right. \right. \\
& \quad \left. \left. + \mathcal{N}\langle g(p_2); q(x_a p_A), \bar{q}(x_b p_B) | \mathbf{I}(\varepsilon) | g(p_2); q(x_a p_A), \bar{q}(x_b p_B) \rangle \right) \right. \\
& \quad + \int_0^1 dz \int d\Phi^{(2)}(z x_a p_A, x_b p_B) \frac{\mathcal{N}}{4F(z x_a p_A, x_b p_B)} \langle g(p_2); q(z x_a p_A), \bar{q}(x_b p_B) | \\
& \quad \quad \mathbf{K}^{q,q}(z) + \mathbf{P}^{q,q}(z x_a p_A, z; \mu_F^2 = p_{T1}^2) | g(p_2); q(z x_a p_A), \bar{q}(x_b p_B) \rangle \\
& \quad + \int_0^1 dz \int d\Phi^{(2)}(x_a p_A, z x_b p_B) \frac{\mathcal{N}}{4F(x_a p_A, z x_b p_B)} \langle g(p_2); q(x_a p_A), \bar{q}(z x_b p_B) | \\
& \quad \quad \left. \left. \mathbf{K}^{\bar{q},\bar{q}}(z) + \mathbf{P}^{\bar{q},\bar{q}}(z x_b p_B, z; \mu_F^2 = p_{T1}^2) | g(p_2); q(x_a p_A), \bar{q}(z x_b p_B) \rangle \right) \right\}, \tag{C.121}
\end{aligned}$$

where  $\overline{|\mathcal{M}_{q\bar{q} \rightarrow \gamma g}|^2}$  includes the virtual corrections. The cancellation of divergences occurs in

$$\begin{aligned}
& \overline{|\mathcal{M}_{q\bar{q} \rightarrow \gamma g}(x_a p_A, x_b p_B, p_1, p_2, \mu_R = p_{T1})|^2} \\
& + \mathcal{N}\langle g(p_2); q(x_a p_A), \bar{q}(x_b p_B) | \mathbf{I}(\varepsilon) | g(p_2); q(x_a p_A), \bar{q}(x_b p_B) \rangle,
\end{aligned}$$

which can be checked by computing the coefficients of  $\varepsilon^{-2}$  and  $\varepsilon^{-1}$ ; they vanish and only the finite contribution, i.e. the coefficient of  $\varepsilon^0$ , has to be implemented in a numerical code.

I want to stress that the  $\mathbf{K}$ - and  $\mathbf{P}$ -terms include in their definition plus- and  $\delta$ -distributions in the momentum fraction  $z$ . Naturally, these can not be implemented in a numerical code as distributions. Instead the contributions have to be disentangled and integrated separately. The collinear remnant can generally be written in the form

$$\int_0^1 dz \int d\Phi^{(2)}(z, \dots) f(z, \dots) g(z, \dots),$$

where only the  $z$  dependence is explicitly shown and  $f$  might be a specific matrix element of the  $\mathbf{K}$ - or  $\mathbf{P}$ -operator and  $g$  a collection of the other factors (e.g.  $F_J$ ) that make up the collinear remnant contribution. Then  $f$  can be written as a sum of regular,  $\delta$ -distribution and plus-distribution contributions

$$f(z, \dots) = f^f(z, \dots) + f^d(z, \dots) \delta(1 - z) + f^p(z, \dots) h_+(z)$$

and the integral decomposes into

$$\int d\Phi^{(2)}(1, \dots) f^d(1, \dots) g(1, \dots)$$

and

$$\int_0^1 dz \left[ \int d\Phi^{(2)}(z, \dots) (f^r(z, \dots)g(z, \dots) + f^p(z, \dots)h(z)g(z, \dots)) - \int d\Phi^{(2)}(1, \dots) f^p(1, \dots)h(z)g(1, \dots) \right].$$

That means the collinear remnant has contributions that have to be integrated w.r.t. the simple Born phase space and some which are actually integrated over  $z$ . Even though it might look like the second contribution can be further subdivided into an integral over  $d\Phi^{(2)}(z, \dots)$  and an integral over  $d\Phi^{(2)}(1, \dots)$ , care has to be taken that those two contribution are handled in the same integration step, as a cancellation of divergences in  $z$  takes place between these two contributions. It is this complicated structure of the collinear remnants that constitutes the trickiest component of the practical application of the CS dipole method.

### C.2.6 QED Dipoles

Up to this point, I have discussed only the dipoles for the subtraction of QCD divergences. The QED divergences, on the other hand, have to be cancelled by dipoles adapted to QED. In Sec. 3.3, I have described shortly how to transform the expressions for the QCD dipoles to QED dipoles by exchanging the non-Abelian colour-generators with Abelian charge-generators. Furthermore, one has to realize that the photon is an identified particle and one has to use the formulae in [29] for dipoles with two identified initial state partons and one identified final state parton, i.e. the multi-particle correlation formulae of Sec. 11 of Ref. [29].

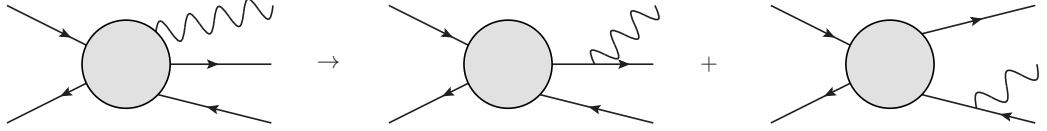


Figure C.16: Diagram structures that lead to QED singularities for  $q\bar{q} \rightarrow \gamma q' \bar{q}'$ . The two diagrams on the right correspond to the dipoles  $(\mathcal{D}_{\gamma q', \bar{q}'} + \mathcal{D}_{\gamma q'}^{(n)q} + \mathcal{D}_{\gamma \bar{q}'}^{(n)\bar{q}})$  and  $(\mathcal{D}_{\gamma \bar{q}', q'} + \mathcal{D}_{\gamma \bar{q}'}^{(n)q} + \mathcal{D}_{\gamma q'}^{(n)\bar{q}})$ .

To exemplify the calculation, I discuss the process  $q\bar{q} \rightarrow \gamma q' \bar{q}'$  where the photon can be in two singular configurations: Collinear to  $q'$  or to  $\bar{q}'$ .<sup>3</sup> As detailed in Sec. 11 of Ref. [29], these divergences are countered by the dipoles  $\mathcal{D}_{\gamma q', \bar{q}'}$ ,  $\mathcal{D}_{\gamma \bar{q}', q'}$ ,  $\mathcal{D}_{\gamma q'}^{(n)q}$ ,  $\mathcal{D}_{\gamma \bar{q}'}^{(n)\bar{q}}$ ,  $\mathcal{D}_{\gamma q'}^{(n)\bar{q}}$ ,  $\mathcal{D}_{\gamma \bar{q}'}^{(n)q}$ , where the latter denote the multi-particle correlated dipoles. Obviously, the underlying Born process to these dipoles is the pure QCD process  $q\bar{q} \rightarrow q' \bar{q}'$ , or in ket-notation

$$|q'(p_1), \bar{q}'(p_2); q(p_a), \bar{q}(p_b)\rangle.$$

<sup>3</sup>As a reminder: Soft photon divergences and initial state collinear photon divergences for processes with initial state quarks are forbidden by a mandatory low- $p_T$ -cut imposed through  $F_J$ .

In general, all the  $2 \rightarrow 2$  QCD tree-level amplitudes involving quarks are needed to compute the dipoles; as they are also a prerequisite for the fragmentation contribution, they are discussed in Sec. C.3.

### Charge correlations

With the substitution (3.21) it is rather easy to compute the charge correlations:

$$\mathbf{T}_{q'} \cdot \mathbf{T}_{\bar{q}'} |q', \bar{q}'; q, \bar{q}\rangle = -Q_{f_{q'}} Q_{f_{\bar{q}'}} |q', \bar{q}'; q, \bar{q}\rangle, \quad (\text{C.122})$$

$$\mathbf{T}_{q'} \cdot \mathbf{T}_q |q', \bar{q}'; q, \bar{q}\rangle = -Q_{f_{q'}} Q_{f_q} |q', \bar{q}'; q, \bar{q}\rangle, \quad (\text{C.123})$$

$$\mathbf{T}_{q'} \cdot \mathbf{T}_{\bar{q}} |q', \bar{q}'; q, \bar{q}\rangle = Q_{f_{q'}} Q_{f_{\bar{q}}} |q', \bar{q}'; q, \bar{q}\rangle, \quad (\text{C.124})$$

$$\mathbf{T}_{\bar{q}'} \cdot \mathbf{T}_q |q', \bar{q}'; q, \bar{q}\rangle = Q_{f_{\bar{q}'}} Q_{f_q} |q', \bar{q}'; q, \bar{q}\rangle, \quad (\text{C.125})$$

$$\mathbf{T}_{\bar{q}'} \cdot \mathbf{T}_{\bar{q}} |q', \bar{q}'; q, \bar{q}\rangle = -Q_{f_{\bar{q}'}} Q_{f_{\bar{q}}} |q', \bar{q}'; q, \bar{q}\rangle. \quad (\text{C.126})$$

### Spin correlations

Spin-correlations for the QED dipoles would only be needed if splittings of photons into fermion-antifermion pairs were relevant to the processes in question. Since the photon is not present as an internal particle they do not have to be considered here.

### $\mathcal{D}_{\gamma q', \bar{q}'}$

The final state correlated dipoles with an identified final state particle are defined in Eqs. (5.114)-(5.116) of Ref. [29]. With Eq. (5.118) of Ref. [29], the substitutions (3.21)-(3.25) and (C.122) I find

$$\mathcal{D}_{\gamma q', \bar{q}'}(p_a, p_b, p_1, p_2, p_3) = -\frac{1}{2p_1 \cdot p_2} (-1) V_{\gamma q', \bar{q}'} \sum_{\substack{\text{spins} \\ \text{colours}}} |\mathcal{M}_{q\bar{q} \rightarrow q' \bar{q}'}(\tilde{s}, \tilde{t}, \tilde{u})|^2 \quad (\text{C.127})$$

with

$$\tilde{s} = s_{ab}, \quad (\text{C.128})$$

$$\tilde{t} = -2p_a \cdot \tilde{p}_{12} = -\frac{s_{ab} t_{a1}}{t_{a1} + t_{b1}}, \quad (\text{C.129})$$

$$\tilde{u} = -2p_a \cdot \tilde{p}_3 = -\frac{s_{ab} t_{b1}}{t_{a1} + t_{b1}} \quad (\text{C.130})$$

and

$$V_{\gamma q', \bar{q}'} = -8\pi\alpha Q_{f'}^2 \frac{2s_{ab}^2 + 2s_{ab}(t_{a1} + t_{b1}) + (t_{a1} + t_{b1})^2}{s_{ab}(t_{a1} + t_{b1})}. \quad (\text{C.131})$$

The full result in terms of Mandelstam variables is

$$\begin{aligned} & \mathcal{D}_{\gamma q', \bar{q}'}(p_a, p_b, p_1, p_2, p_3) \\ &= -256\pi^3 \alpha \alpha_s^2 (N_c^2 - 1) Q_{f'}^2 \frac{(t_{a1}^2 + t_{b1}^2) (2s_{ab}^2 + 2s_{ab}(t_{a1} + t_{b1}) + (t_{a1} + t_{b1})^2)}{s_{12} s_{ab} (t_{a1} + t_{b1})^3}. \end{aligned} \quad (\text{C.132})$$

### $\mathcal{D}_{\gamma\bar{q}',q'}$

This is completely analog to the previous calculation, just with the final momenta exchanged. Here, I define the Mandelstam variables  $\tilde{s}$ ,  $\tilde{t}$  and  $\tilde{u}$  such that the emitter with momentum  $\tilde{p}_{13}$ , i.e. in this case  $\bar{q}'$ , is the particle corresponding to the first position in the underlying Born. That means the underlying process here is  $|\mathcal{M}_{q\bar{q}\rightarrow\bar{q}'q'}|^2$  instead of  $|\mathcal{M}_{q\bar{q}\rightarrow q'\bar{q}'}|^2$ . This choice simplifies the integration of the dipoles later on. Furthermore, it turns out that now

$$\mathcal{D}_{\gamma\bar{q}',q'}(p_a, p_b, p_1, p_2, p_3) = \mathcal{D}_{\gamma q',\bar{q}'}(p_a, p_b, p_1, p_2, p_3). \quad (\text{C.133})$$

### $\mathcal{D}_{\gamma q'}^{(n)q}$

The prescription for the dipoles with correlations of identified particles are given in Eqs. (5.180)-(5.182) and Eqs. (5.162)-(5.164) of Ref. [29]. Here the momenta of the identified particles are left unchanged, whereas (similar to the initial state correlated dipoles used in the last section) all other momenta have to be transformed. As these dipoles depend not only on the momenta of the emitter, emitted and spectator particle, but also on the momentum sum  $n$  of the unidentified particles, they are not dipoles in the strict sense. I have

$$\mathcal{D}_{\gamma q'}^{(n)q}(p_a, p_b, p_1, p_2, p_3) = -\frac{1}{2p_1 \cdot p_2} \frac{-Q_f}{Q_{f'}} V_{\gamma q'}^{(n)q} \sum_{\substack{\text{spins} \\ \text{colours}}} |\mathcal{M}_{q\bar{q}\rightarrow q'\bar{q}'}(\tilde{s}, \tilde{t}, \tilde{u})|^2, \quad (\text{C.134})$$

coincidentally with the same  $2 \rightarrow 2$  Mandelstam variable as for  $\mathcal{D}_{\gamma q',\bar{q}'}$  and

$$V_{\gamma q'}^{(n)q} = -8\pi\alpha Q_{f'}^2 \frac{2s_{ab}^2 + 2s_{ab}(t_{a1} + t_{b1}) + (t_{a1} + t_{b1})^2}{s_{ab}(t_{a1} + t_{b1})}, \quad (\text{C.135})$$

giving finally

$$\begin{aligned} & \mathcal{D}_{\gamma q'}^{(n)q}(p_a, p_b, p_1, p_2, p_3) \\ &= -256\pi^3 \alpha \alpha_s^2 (N_c^2 - 1) Q_f Q_{f'} \\ & \quad \cdot \frac{(t_{a1}^2 + t_{b1}^2) (2s_{ab}^2 + 2s_{ab}(t_{a1} + t_{b1}) + (t_{a1} + t_{b1})^2)}{s_{12}s_{ab}(t_{a1} + t_{b1})^3}, \end{aligned} \quad (\text{C.136})$$

which differs from the other results only through the charges  $Q_f$ ,  $Q_{f'}$ .

### $\mathcal{D}_{\gamma\bar{q}'}^{(n)q}$

The following dipoles are computed similarly to the previous dipole. The final results differ only through the sign of the charge correlations.

$$\mathcal{D}_{\gamma\bar{q}'}^{(n)q}(p_a, p_b, p_1, p_2, p_3) = -\mathcal{D}_{\gamma q'}^{(n)q}(p_a, p_b, p_1, p_2, p_3) \quad (\text{C.137})$$

$$\mathcal{D}_{\gamma q'}^{(n)\bar{q}}$$

$$\mathcal{D}_{\gamma q'}^{(n)\bar{q}}(p_a, p_b, p_1, p_2, p_3) = -\mathcal{D}_{\gamma q'}^{(n)q}(p_a, p_b, p_1, p_2, p_3) \quad (\text{C.138})$$

$$\mathcal{D}_{\gamma \bar{q}'}^{(n)\bar{q}}$$

$$\mathcal{D}_{\gamma \bar{q}'}^{(n)\bar{q}}(p_a, p_b, p_1, p_2, p_3) = \mathcal{D}_{\gamma q'}^{(n)q}(p_a, p_b, p_1, p_2, p_3) \quad (\text{C.139})$$

### Integrated dipoles

For an identified final state particle of momentum  $p^\gamma$ , the formulae in Sec. 11 of Ref. [29] refer to the partonic invariant differential cross section, i.e. the kernel of the invariant photon-differential cross section

$$\begin{aligned} (2\pi)^3 2p^{\gamma 0} \frac{d\sigma}{d^3 p^\gamma}(p_A, p_B, p^\gamma) &= \sum_{a,b,c} \int_0^1 dx_a \int_0^1 dx_b \int_0^1 dz f_{a/A}(x_A, \mu_F) f_{a/B}(x_B, \mu_F) \\ &\quad \cdot (2\pi)^3 2p^{\gamma 0} \frac{d\hat{\sigma}_{ab \rightarrow cx}}{d^3 p^\gamma} \left( x_a p_A, x_b p_B, \frac{p_\gamma}{z}, \mu_F \right) D_{\gamma/c}(z, \mu_F) \\ &= \sum_{a,b,c} \int_0^1 dx_a \int_0^1 dx_b \int_0^1 \frac{dz}{z^2} f_{a/A}(x_A, \mu_F) f_{a/B}(x_B, \mu_F) \\ &\quad \cdot (2\pi)^3 2 \frac{p^{\gamma 0}}{z} \frac{d\hat{\sigma}_{ab \rightarrow cx}}{d^3 \frac{p^\gamma}{z}} \left( x_a p_A, x_b p_B, \frac{p_\gamma}{z}, \mu_F \right) D_{\gamma/c}(z, \mu_F) \end{aligned}$$

(cf. (3.9)). Hence, in this section I will discuss first and foremost the differential partonic cross section

$$(2\pi)^3 2p_1^0 \frac{d\hat{\sigma}_{ab \rightarrow cx}}{d^3 p_1}(x_a p_A, x_b p_B, p_1, \mu_F)$$

which is to be multiplied by the photon-jet-defining function  $F_J(p^\gamma)$ , i.e. the cuts on the photon in terms of  $\theta$ -distributions, and integrated over the photon momentum  $p^\gamma$  afterwards. In Ref. [29], there is also a jet-defining function included in the definition of  $(2\pi)^3 2p_1^0 d\hat{\sigma}_{ab \rightarrow cx}/d^3 p_1$ ; in the case at hand this jet-defining function is simply set to unity, as the other partons are integrated out anyway (though it would pose no problem to carry out the following calculation with some general jet-defining function).

The  $D$ -dimensional phase space measure for the integration over two particles with momenta  $p_i, p_k$  and a particle of momentum  $p_1$  being identified (and left unintegrated) is denoted by

$$d\Phi(p_i, p_k; Q - p_1) = (2\pi)^D \delta^{(D)}(Q - p_1 - p_i - p_k) \frac{d^{D-1} p_i}{(2\pi)^{D-1} 2p_i^0} \frac{d^{D-1} p_k}{(2\pi)^{D-1} 2p_k^0}. \quad (\text{C.140})$$

with

$$Q = p_a + p_b.$$

Hence, the dipole subtracted  $2 \rightarrow 3$ -contribution of the differential partonic cross section is given by

$$\begin{aligned}
 & (2\pi)^3 2p_1^0 \frac{d\hat{\sigma}_{ab \rightarrow cx}}{d^3p_1}(x_a p_A, x_b p_B, p_1, \mu_F) \\
 &= \int d\Phi(p_2, p_3; Q - p_1) \frac{1}{4F} \left\{ \overline{|\mathcal{M}_{ab \rightarrow cde}(p_a, p_b, p_1, p_2, p_3)|^2} \right. \\
 &\quad \left. - \mathcal{N} \sum_{\substack{i,k=2 \\ i \neq k}}^3 \mathcal{D}_{1i,k}(p_a, p_b, p_1, p_2, p_3) \right. \\
 &\quad \left. - \mathcal{N} \sum_{i=2}^3 \sum_{k=a,b} \mathcal{D}_{1i}^{(n)k}(p_a, p_b, p_1, p_2, p_3) \right\}. \tag{C.141}
 \end{aligned}$$

In my case  $c = \gamma$  since I only consider  $2 \rightarrow 3$  processes of the type  $ab \rightarrow \gamma de$ . The dipoles  $\mathcal{D}_{1i,k}$  and  $\mathcal{D}_{1i}^{(n)k}$  then correspond to those described in the previous section.

The ultimate goal is now to integrate the dipoles over the particle  $i$  and thus obtain the integrated dipoles that have to be added to the  $2 \rightarrow 2$  contribution. Focusing first on the final state correlated dipoles, one has

$$\begin{aligned}
 & \int d\Phi(p_2, p_3; Q - p_1) \sum_{\substack{i,k=2 \\ i \neq k}}^3 \mathcal{D}_{1i,k}(p_a, p_b, p_1, p_2, p_3) \\
 &= \sum_{\substack{i,k=2 \\ i \neq k}}^3 \int d\Phi(p_i, p_k; Q - p_1) \mathcal{D}_{1i,k}(p_a, p_b, p_1, p_2, p_3) \tag{C.142}
 \end{aligned}$$

$$= \sum_{\substack{i,k=2 \\ i \neq k}}^3 \int_0^1 \frac{d\eta}{\eta^{2-2\varepsilon}} \int d\Phi(\tilde{p}_k; Q - \frac{p_1}{\eta}) dp_i(\tilde{p}_k, p_a; \eta) \mathcal{D}_{1i,k}(p_a, p_b, p_1, p_2, p_3) \tag{C.143}$$

$$\begin{aligned}
 &= \sum_{\substack{i,k=2 \\ i \neq k}}^3 \int_0^1 \frac{d\eta}{\eta^{2-2\varepsilon}} \int d\Phi(\tilde{p}_k; Q - \frac{p_1}{\eta}) dp_i(\tilde{p}_k, p_a; \eta) \\
 &\quad \cdot \frac{-1}{2p_1 \cdot p_i} \langle \tilde{1}_i, \tilde{k}, \dots; \dots | \frac{\mathbf{T}_k \cdot \mathbf{T}_{1i}}{\mathbf{T}_{1i}^2} | \tilde{1}_i, \tilde{k}, \dots; \dots \rangle \langle V_{1i,k} \rangle \tag{C.144}
 \end{aligned}$$

$$\begin{aligned}
 &= - \sum_{\substack{i,k=2 \\ i \neq k}}^3 \int_0^1 \frac{d\eta}{\eta^{2-2\varepsilon}} \int d\Phi(\tilde{p}_k; Q - \frac{p_1}{\eta}) \\
 &\quad \cdot \langle \tilde{1}_i, \tilde{k}, \dots; \dots | \frac{\mathbf{T}_k \cdot \mathbf{T}_{1i}}{\mathbf{T}_{1i}^2} | \tilde{1}_i, \tilde{k}, \dots; \dots \rangle \frac{\alpha}{2\pi} \frac{1}{\Gamma(1-\varepsilon)} \left( \frac{4\pi\mu_R^2}{2\tilde{p}_k \cdot p_1} \right)^\varepsilon \mathcal{V}_{1i,1}(\eta, \varepsilon), \tag{C.145}
 \end{aligned}$$



using the definition of the dipole, the phase space factorization Eqs. (5.122), (5.123), the discussion after (5.22), and Eq. (5.125) of Ref. [29].  $\widetilde{1i}$  is the particle that splits into particle 1, i.e. the photon  $\gamma$ , and particle  $i$ , i.e. some quark, and has the momentum  $p_1/\eta$  in the last line (after the integration over  $p_i$ ). The functions  $\mathcal{V}_{1i,1}(\eta, \varepsilon)$  include the divergences as a pole in  $\varepsilon$ . Here, I need  $\mathcal{V}_{1i,1}(\eta, \varepsilon) = \mathcal{V}_{\gamma i, \gamma}(\eta, \varepsilon)$  – the QED version of Eq. (5.131) of Ref. [29]:

$$\mathcal{V}_{\gamma i, \gamma}(\eta, \varepsilon) = -\frac{1}{\varepsilon} P_{\gamma i}(\eta) + P_{\gamma i}(\eta) \ln(1 - \eta) + Q_i^2 \eta + \mathcal{O}(\varepsilon) \quad (\text{C.146})$$

with  $P_{\gamma q}$  given in (3.13).

Expanding the  $\varepsilon$ -dependent terms in (C.145) up to  $\mathcal{O}(\varepsilon)$ , I find that they can be rewritten

$$\begin{aligned} & \frac{1}{\eta^{2-2\varepsilon}} \frac{1}{\Gamma(1-\varepsilon)} \left( \frac{4\pi\mu_R^2}{2\widetilde{p}_k \cdot p_1} \right)^\varepsilon \mathcal{V}_{1i,1}(\eta, \varepsilon) \\ &= \frac{1}{\eta^2} \left\{ \frac{1}{\Gamma(1-\varepsilon)} \left( \frac{4\pi\mu_R^2}{\mu_F^2} \right)^\varepsilon \left( -\frac{1}{\varepsilon} P_{\gamma i}(\eta) \right) + R_i(\eta, \widetilde{p}_k \cdot p_1, \mu_F) \right\} + \mathcal{O}(\varepsilon) \end{aligned}$$

with

$$R_i(\eta, \widetilde{p}_k \cdot p_1, \mu_F) \equiv P_{\gamma i}(\eta) \left[ \ln \left( \frac{1-\eta}{\eta} \right) - \ln \left( \frac{\mu_F^2}{2\widetilde{p}_k \cdot p_1} \right) \right] + Q_i^2 \eta. \quad (\text{C.147})$$

Thus, the divergence in (C.145) is

$$\begin{aligned} & \sum_{\substack{i,k=2 \\ i \neq k}}^3 \int_0^1 \frac{d\eta}{\eta^2} \int d\Phi(p_k; Q - \frac{p_1}{\eta}) \\ & \cdot \langle \widetilde{1i}, \widetilde{k}, \dots; \dots | \frac{\mathbf{T}_k \cdot \mathbf{T}_{1i}}{\mathbf{T}_{1i}^2} | \widetilde{1i}, \widetilde{k}, \dots; \dots \rangle \frac{\alpha}{2\pi} \frac{1}{\Gamma(1-\varepsilon)} \left( \frac{4\pi\mu_R^2}{\mu_F^2} \right)^\varepsilon \frac{1}{\varepsilon} P_{\gamma i}(\eta). \end{aligned}$$

It is this divergence that will be completely absorbed into the fragmentation functions. On the other hand, the function  $R_i$  that has been defined above is the collinear remnant, i.e. the left-over from this absorption.

Turning now to the integration of the initial state correlated dipole (the last line in (C.141)), I find with Eqs. (5.180), (5.187) and (5.190) of Ref. [29]

$$\begin{aligned} & \int d\Phi(p_2, p_3; Q - p_1) \sum_{i=2}^3 \sum_{k=a,b} \mathcal{D}_{1i}^{(n)k}(p_a, p_b, p_1, p_2, p_3) \\ &= \sum_{i=2}^3 \sum_{k=a,b} \int d\Phi(p_i, p_j; Q - p_1) \mathcal{D}_{1i}^{(n)k}(p_a, p_b, p_1, p_2, p_3) \\ &= \sum_{i=2}^3 \sum_{k=a,b} \int_0^1 \frac{d\eta}{\eta^{2-2\varepsilon}} \int d\Phi(\widetilde{p}_j; Q - \frac{p_1}{\eta}) dp_i (n = Q - p_1; p_1, \eta) \end{aligned} \quad (\text{C.148})$$

$$\begin{aligned} & \cdot \mathcal{D}_{1i}^{(n)k}(p_a, p_b, p_1, p_2, p_3) \\ &= \sum_{i=2}^3 \sum_{k=a,b} \int_0^1 \frac{d\eta}{\eta^{2-2\varepsilon}} \int d\Phi(\tilde{p}_j; Q - \frac{p_1}{\eta}) dp_i (n = Q - p_1; p_1, \eta) \end{aligned} \quad (\text{C.149})$$

$$\begin{aligned} & \cdot \frac{-1}{2p_1 \cdot p_i} \langle \tilde{1}i, \tilde{j}, \dots; \dots | \frac{\mathbf{T}_k \cdot \mathbf{T}_{1i}}{\mathbf{T}_{1i}^2} | \tilde{1}i, \tilde{j}, \dots; \dots \rangle \langle V_{1i}^{(n)k} \rangle \end{aligned} \quad (\text{C.150})$$

$$\begin{aligned} &= - \sum_{i=2}^3 \sum_{k=a,b} \int_0^1 \frac{d\eta}{\eta^{2-2\varepsilon}} \int d\Phi(\tilde{p}_j; Q - \frac{p_1}{\eta}) \\ & \cdot \langle \tilde{1}i, \tilde{j}, \dots; \dots | \frac{\mathbf{T}_k \cdot \mathbf{T}_{1i}}{\mathbf{T}_{1i}^2} | \tilde{1}i, \tilde{j}, \dots; \dots \rangle \\ & \cdot \frac{\alpha}{2\pi} \frac{1}{\Gamma(1-\varepsilon)} \left( \frac{4\pi\mu_R^2}{2p_k \cdot p_1} \right)^\varepsilon \bar{\mathcal{V}}_{1i,1}(\eta; \varepsilon; p_1, p_k, n). \end{aligned} \quad (\text{C.151})$$

Again, the momentum of particle  $\tilde{1}i$  in the last line is  $p_1/\eta$ . The function

$$\bar{\mathcal{V}}_{1i,1}(\eta; \varepsilon; p_1, p_k, n) = \bar{\mathcal{V}}_{\gamma i, \gamma}(\eta; \varepsilon; p_1, p_k, n)$$

is the QED version of Eq. (5.192) of Ref. [29]:

$$\begin{aligned} \bar{\mathcal{V}}_{\gamma i, \gamma}(\eta; \varepsilon; p_1, p_k, n) &= -\frac{1}{\varepsilon} P_{\gamma i}(\eta) + 2P_{\gamma i}(\eta) \ln(1-\eta) + Q_i^2 \eta \\ & - P_{\gamma i}(\eta) \ln \left( \frac{n^2(p_1 \cdot p_k)}{2(p_1 \cdot n)^2} \right) + \mathcal{O}(\varepsilon), \end{aligned} \quad (\text{C.152})$$

with

$$n = p_a + p_b - p_1.$$

Investigating the  $\varepsilon$ -dependent terms gives

$$\begin{aligned} & \frac{1}{\eta^{2-2\varepsilon}} \frac{1}{\Gamma(1-\varepsilon)} \left( \frac{4\pi\mu_R^2}{2p_k \cdot p_1} \right)^\varepsilon \bar{\mathcal{V}}_{1i,1}(\eta; \varepsilon; p_1, p_k, n) \\ &= \frac{1}{\eta^2} \left\{ \frac{1}{\Gamma(1-\varepsilon)} \left( \frac{4\pi\mu_R^2}{\mu_F^2} \right)^\varepsilon \left( -\frac{1}{\varepsilon} P_{\gamma i}(\eta) \right) + R'_i(\eta, p_1, p_k, n, \mu_F) \right\} + \mathcal{O}(\varepsilon) \end{aligned}$$

with

$$\begin{aligned} & R'_i(\eta, p_1, p_k, n, \mu_F) \\ & \equiv P_{\gamma i}(\eta) \left[ 2 \ln \left( \frac{1-\eta}{\eta} \right) - \ln \left( \frac{\mu_F^2}{2p_k \cdot p_1} \right) - \ln \left( \frac{n^2(p_1 \cdot p_k)}{2(p_1 \cdot n)^2} \right) \right] + Q_i^2 \eta \\ & = P_{\gamma i}(\eta) \left[ 2 \ln \left( \frac{1-\eta}{\eta} \right) - \ln \left( \frac{\mu_F^2 n^2}{4(p_1 \cdot n)^2} \right) \right] + Q_i^2 \eta. \end{aligned} \quad (\text{C.153})$$

Correspondingly, the divergence in (C.151) is

$$\sum_{i=2}^3 \sum_{k=a,b} \int_0^1 \frac{d\eta}{\eta^2} \int d\Phi(\tilde{p}_j; Q - \frac{p_1}{\eta}) \cdot \langle \tilde{1}i, \tilde{j}, \dots; \dots | \frac{\mathbf{T}_k \cdot \mathbf{T}_{1i}}{\mathbf{T}_{1i}^2} | \tilde{1}i, \tilde{j}, \dots; \dots \rangle \frac{\alpha}{2\pi} \frac{1}{\Gamma(1-\varepsilon)} \left( \frac{4\pi\mu_R^2}{\mu_F^2} \right)^\varepsilon \frac{1}{\varepsilon} P_{\gamma i}(\eta).$$

That means, finally, the sum of the divergences of (C.145) and (C.151) is given by (renaming the integration variables)

$$\sum_{i=2}^3 \sum_{\substack{k=a,b,2,3 \\ k \neq i}} \int_0^1 \frac{d\eta}{\eta^2} \int d\Phi(p_2; Q - \frac{p_1}{\eta}) \cdot \langle \tilde{1}i, \dots; \dots | \frac{\mathbf{T}_k \cdot \mathbf{T}_{1i}}{\mathbf{T}_{1i}^2} | \tilde{1}i, \dots; \dots \rangle \frac{\alpha}{2\pi} \frac{1}{\Gamma(1-\varepsilon)} \left( \frac{4\pi\mu_R^2}{\mu_F^2} \right)^\varepsilon \frac{1}{\varepsilon} P_{\gamma i}(\eta). \quad (\text{C.154})$$

But

$$\sum_{\substack{k=a,b,2,3 \\ k \neq i}} \langle \tilde{1}i, \dots; \dots | \frac{\mathbf{T}_k \cdot \mathbf{T}_{1i}}{\mathbf{T}_{1i}^2} | \tilde{1}i, \dots; \dots \rangle = -\langle \tilde{1}i, \dots; \dots | \tilde{1}i, \dots; \dots \rangle$$

by charge conservation, (3.22), and thus the divergences become

$$\begin{aligned} & - \sum_{i=2}^3 \int_0^1 \frac{d\eta}{\eta^2} \int d\Phi(p_2; Q - \frac{p_1}{\eta}) \cdot \langle \tilde{1}i, \dots; \dots | \tilde{1}i, \dots; \dots \rangle \frac{\alpha}{2\pi} \frac{1}{\Gamma(1-\varepsilon)} \left( \frac{4\pi\mu_R^2}{\mu_F^2} \right)^\varepsilon \frac{1}{\varepsilon} P_{\gamma i}(\eta) \\ & = - \sum_{i=2}^3 \int_0^1 \frac{d\eta}{\eta^2} \int d\Phi(p_2; Q - \frac{p_1}{\eta}) \cdot \frac{\alpha}{2\pi} \frac{1}{\Gamma(1-\varepsilon)} \left( \frac{4\pi\mu_R^2}{\mu_F^2} \right)^\varepsilon \frac{1}{\varepsilon} P_{\gamma i}(\eta) \sum_{\substack{\text{spins} \\ \text{colours}}} |\mathcal{M}_{ab \rightarrow [\gamma i]c}(p_a, p_b, \frac{p_1}{\eta}, p_2)|^2. \end{aligned} \quad (\text{C.155})$$

To repeat: This is the divergent part of the integrated dipoles in (C.141); thus to obtain the divergence of the integrated partonic cross section (ignoring the initial state for the moment), it has to be multiplied by the initial state averaging factor  $\mathcal{N}$  and the flux

factor  $1/(4F)$ , then multiplied by  $D_{\gamma/\gamma}(z) = \delta(1-z)$  and integrated over  $z$  and finally multiplied by the photon cuts  $F_J(p_1)$  and integrated over  $p^\gamma$ , where  $p^\gamma = zp_1$ :

$$\begin{aligned} d\hat{\sigma}_{ab \rightarrow \gamma x} &\sim - \sum_{i=2}^3 \int_0^1 \frac{d\eta}{\eta^2} d\Phi^{(2)}(p_1, p_2; p_a + p_b) \frac{1}{4F} |\overline{\mathcal{M}_{ab \rightarrow [\gamma i]c}(p_a, p_b, \frac{p_1}{\eta}, p_2)}|^2 \\ &\quad \cdot \frac{\alpha}{2\pi} \frac{1}{\Gamma(1-\varepsilon)} \left( \frac{4\pi\mu_R^2}{\mu_F^2} \right)^\varepsilon \frac{1}{\varepsilon} P_{\gamma i}(\eta) F_J(p_1) \\ &= - \sum_{i=2}^3 \int_0^1 d\eta d\hat{\sigma}_{ab \rightarrow [\gamma i]c}(p_a, p_b, \frac{p_1}{\eta}, p_2) \\ &\quad \cdot \frac{\alpha}{2\pi} \frac{1}{\Gamma(1-\varepsilon)} \left( \frac{4\pi\mu_R^2}{\mu_F^2} \right)^\varepsilon \frac{1}{\varepsilon} P_{\gamma i}(\eta) F_J(\eta p_1) \end{aligned}$$

which corresponds exactly to (3.12) (apart from  $F_J$  which was not introduced in that equation) and is thus identical to the  $\overline{\text{MS}}$ -subtraction term that is to be absorbed in the photon FF: The anomalous contribution to the FF. Hence, I can be sure that my choice of dipoles cancels only the final state collinear divergences, as it should.

As these divergences are absorbed, one can simply forget about them, but the collinear remnants of the integrated QED dipoles still have to be taken into account. Writing them in the form of an integrated cross section, by collecting the expressions for (C.147) in (C.145) and (C.153) in (C.151) and attaching the same quantities as done for the divergence above, I find

$$\begin{aligned} d\hat{\sigma}_{ab \rightarrow \gamma x} &\sim - \sum_{\substack{i,k=2 \\ i \neq k}}^3 \int_0^1 \frac{d\eta}{\eta^2} \frac{d^3 p_1}{(2\pi)^3 2p_1^0} d\Phi(\tilde{p}_k; Q - \frac{p_1}{\eta}) \frac{\mathcal{N}}{4F} F_J(p_1) \\ &\quad \cdot \langle \tilde{1}i, \tilde{k}, \dots; \dots | \frac{\mathbf{T}_k \cdot \mathbf{T}_{1i}}{\mathbf{T}_{1i}^2} | \tilde{1}i, \tilde{k}, \dots; \dots \rangle \frac{\alpha}{2\pi} R_i(\eta, \tilde{p}_k \cdot p_1, \mu_F) \\ &\quad - \sum_{i=2}^3 \sum_{k=a,b} \int_0^1 \frac{d\eta}{\eta^2} \frac{d^3 p_1}{(2\pi)^3 2p_1^0} d\Phi(\tilde{p}_j; Q - \frac{p_1}{\eta}) \frac{\mathcal{N}}{4F} F_J(p_1) \\ &\quad \cdot \langle \tilde{1}i, \tilde{j}, \dots; \dots | \frac{\mathbf{T}_k \cdot \mathbf{T}_{1i}}{\mathbf{T}_{1i}^2} | \tilde{1}i, \tilde{j}, \dots; \dots \rangle \frac{\alpha}{2\pi} R'_i(\eta, p_1, p_k, n, \mu_F). \end{aligned}$$

By simply renaming  $\tilde{p}_j$  and  $\tilde{p}_k$  to  $p_2$  and changing the integration over  $p_1$  to an integration over  $p_1/\eta$  and renaming  $p_1/\eta$  to  $p_1$  again, I find

$$\begin{aligned} d\hat{\sigma}_{ab \rightarrow \gamma x} &\sim - \sum_{\substack{i,k=2 \\ i \neq k}}^3 \int_0^1 d\eta d\Phi(p_1, p_2; p_a + p_b) \frac{\mathcal{N}}{4F} F_J(\eta p_1) \frac{\alpha}{2\pi} R_i(\eta, p_2 \cdot \eta p_1, \mu_F) \\ &\quad \cdot \langle \tilde{1}i(p_1), \tilde{k}(p_2), \dots; \dots | \frac{\mathbf{T}_k \cdot \mathbf{T}_{1i}}{\mathbf{T}_{1i}^2} | \tilde{1}i(p_1), \tilde{k}(p_2), \dots; \dots \rangle \\ &\quad - \sum_{i=2}^3 \sum_{k=a,b} \int_0^1 d\eta d\Phi(p_1, p_2; p_a + p_b) \frac{\mathcal{N}}{4F} F_J(\eta p_1) \frac{\alpha}{2\pi} R'_i(\eta, \eta p_1, p_2, n, \mu_F) \end{aligned}$$

$$\cdot \langle \tilde{1}i(p_1), \tilde{j}(p_2), \dots; \dots | \frac{\mathbf{T}_k \cdot \mathbf{T}_{1i}}{\mathbf{T}_{1i}^2} | \tilde{1}i(p_1), \tilde{j}(p_2), \dots; \dots \rangle,$$

now with  $n = p_a + p_b - \eta p_1$ .

As denoted in the phase space measure above, momentum conservation is given by  $p_a + p_b = p_1 + p_2$ . This can be used to simplify  $R'_i$ . By using (C.147), (C.153) and

$$n^2 = (p_a + p_b - \eta p_1)^2 = 2(1 - \eta)p_1 \cdot p_2,$$

I find

$$R'_i(\eta, \eta p_1, p_2, n, \mu_F) = R_i(\eta, p_2 \cdot \eta p_1, \mu_F). \quad (\text{C.156})$$

This leads to

$$\begin{aligned} d\hat{\sigma}_{ab \rightarrow \gamma x} \sim & - \sum_{i=2}^3 \sum_{\substack{k=a,b,2,3 \\ k \neq i}} \int_0^1 d\eta d\Phi(p_1, p_2; p_a + p_b) \frac{\mathcal{N}}{4F} F_J(\eta p_1) \frac{\alpha}{2\pi} R_i(\eta, p_2 \cdot \eta p_1, \mu_F) \\ & \cdot \langle \tilde{1}i(p_1), \dots; \dots | \frac{\mathbf{T}_k \cdot \mathbf{T}_{1i}}{\mathbf{T}_{1i}^2} | \tilde{1}i(p_1), \dots; \dots \rangle, \end{aligned}$$

which can be simplified further by again using charge-conservation (3.22)

$$\begin{aligned} d\hat{\sigma}_{ab \rightarrow \gamma x} \sim & \sum_i \int_0^1 d\eta d\Phi(p_1, p_2; p_a + p_b) \frac{1}{4F} F_J(\eta p_1) \frac{\alpha}{2\pi} R_i(\eta, p_2 \cdot \eta p_1, \mu_F) \\ & \cdot \overline{|\mathcal{M}_{ab \rightarrow [\gamma i]c}(p_a, p_b, p_1, p_2)|^2} \end{aligned} \quad (\text{C.157})$$

with

$$R_i(\eta, p_2 \cdot \eta p_1, \mu_F) = P_{\gamma i}(\eta) \left[ \ln(1 - \eta) - \ln\left(\frac{\mu_F^2}{2p_1 \cdot p_2}\right) \right] + Q_i^2 \eta, \quad (\text{C.158})$$

where, taking all the integrated dipoles into account, I extended the sum over  $i$  to a sum over all partons. Eq. (C.157) is the full collinear remnant. With other words: When subtracting from all the  $ab \rightarrow \gamma de$ -processes the final state collinear photon divergences by using the final state correlated QED dipoles  $\mathcal{D}_{ai,k}$  and the initial state correlated QED dipoles  $\mathcal{D}_{ai}^{(n)k}$ , one has to add (C.157) to the  $2 \rightarrow 2$  contribution. Furthermore, since (C.157) has the form of a fragmentation contribution with fragmentation function  $R_i$ , it is naturally treated along with the FF contribution to be discussed in the next section.

Up to this point, I did not specify what happens to the factorization and renormalization scales in these contributions if they depend on  $p_1$ . The integration of one of the partons  $i$  leading to the results (C.145) and (C.151) has the effect that, starting with a  $2 \rightarrow 3$  process as a function of momenta  $p_1, p_i, p_k$ , one ends up with a  $2 \rightarrow 2$  process as a function of momenta  $p_1/\eta, p_k$  times some function of  $\eta$ . Thus, if the process to begin with had  $\mu_F = \mu_R = h(p_1)$ , then after the integration it has to have  $\mu_F = \mu_R = h(p_1/\eta)$  to be consistent. Due to the substitutions of integration variables leading to (C.157),

there one has  $\mu_F = \mu_R = h(p_1)$  again, but  $p_1$  is no longer the photon momentum (as the photon-cuts  $F_J(\eta p_1)$  indicate)! It is the momentum of the parton fragmenting into the photon, thus, if one uses a version of (C.157) where the phase space integration is done over the photon momentum  $p^\gamma = \eta p_1$ , then  $\mu_F = \mu_R = h(p^\gamma/\eta)$ . If one were not to take care of this, then  $R_i$  would introduce a logarithm of  $\eta$  that becomes large for small values  $\eta \rightarrow 0$ .

### C.2.7 NLO cross section with CS dipoles

To summarize the calculation of the direct contribution to prompt photon production at NLO with CS dipole subtraction, I give the subtracted version of (C.86)

$$\begin{aligned}
 & \int d\sigma_{AB \rightarrow \gamma X}^{(\text{direct})}(p_A, p_B) \\
 &= \sum_{a,b} \int_0^1 dx_a \int_0^1 dx_b f_{a/A}(x_a) f_{b/B}(x_b) \\
 & \quad \cdot \left\{ \frac{1}{4F} \left[ \sum_c \int d\Phi^{(2)} \left( |\overline{\mathcal{M}_{ab \rightarrow \gamma c}}|^2 + \mathcal{N}\langle c; a, b | \mathbf{I}(\varepsilon) | c; a, b \rangle \right) \right. \right. \\
 & \quad \quad \quad + \sum_{c,d} \int d\Phi^{(3)} \left( \overline{|\mathcal{M}_{ab \rightarrow \gamma cd}|^2} F_J(p_1) - \sum_{i,k} \mathcal{D}_{\gamma i, k} \mathcal{N} F_J(p_1) \right. \\
 & \quad \quad \quad - \sum_{i,q} \mathcal{D}_{\gamma i}^{(n)q} \mathcal{N} F_J(p_1) - \sum_{i,j,q} \mathcal{D}_{ij}^q \mathcal{N} F_J(p_1) \\
 & \quad \quad \quad \left. \left. - \sum_{p,i,j} \mathcal{D}_k^{pi} \mathcal{N} F_J(p_1) - \sum_{p,i,q} \mathcal{D}^{pi,q} \mathcal{N} F_J(\tilde{p}_1) \right) \right] \\
 & \quad + \sum_{c,a'} \int_0^1 dz \int d\Phi^{(2)} \frac{\mathcal{N}}{4F} \langle c; a', b | \mathbf{K}^{a,a'} + \mathbf{P}^{a,a'} | c; a', b \rangle F_J(p_1) \\
 & \quad + \sum_{c,b'} \int_0^1 dz \int d\Phi^{(2)} \frac{\mathcal{N}}{4F} \langle c; a, b' | \mathbf{K}^{b,b'} + \mathbf{P}^{b,b'} | c; a, b' \rangle F_J(p_1) \\
 & \quad \left. + \sum_{c,d} \int_0^1 d\eta \int d\Phi^{(2)} \frac{1}{4F} \frac{\alpha}{2\pi} R_c |\overline{\mathcal{M}_{ab \rightarrow cd}}|^2 F_J(\eta p_1) \right\}, \tag{C.159}
 \end{aligned}$$

where  $a, b, c, d$  and  $a', b'$  run over all types of partons;  $i, j, k$  run over all final state partons and  $p, q$  run over the initial state partons of a specific partonic process. The specific dependencies of all the contributions on the momenta and momentum fractions can be extracted from the results (C.118), (C.121), (C.157).

### C.3 Leading Order Fragmentation

The amplitudes needed for the fragmentation contribution are simply the LO parton scattering amplitudes

$q\bar{q} \rightarrow gg$	$\bar{q}q \rightarrow gg$	$q\bar{q} \rightarrow q\bar{q}$	$\bar{q}q \rightarrow q\bar{q}$
$qq \rightarrow qq$	$\bar{q}\bar{q} \rightarrow \bar{q}\bar{q}$	$q\bar{q} \rightarrow q'\bar{q}'$	$\bar{q}q \rightarrow q'\bar{q}'$
$qq' \rightarrow qq'$	$\bar{q}\bar{q}' \rightarrow \bar{q}\bar{q}'$	$q\bar{q}' \rightarrow q\bar{q}'$	$\bar{q}q' \rightarrow q'\bar{q}$
$qg \rightarrow qg$	$gq \rightarrow qg$	$\bar{q}g \rightarrow \bar{q}g$	$g\bar{q} \rightarrow \bar{q}g$
$gg \rightarrow q\bar{q}$	$gg \rightarrow gg$		

These are of course well-known and well-documented and can be found for example in Ref. [6]. Using crossing the amplitudes for all these processes can be obtained from the following amplitudes (given in  $D$  dimensions) :

$$\begin{aligned} |\overline{\mathcal{M}}_{q\bar{q} \rightarrow gg}|^2 &= 8\pi^2 \alpha_s^2 (\varepsilon - 1) \frac{(N_c^2 - 1)}{N_c^3} \frac{((\varepsilon - 1)\hat{t}^2 + 2\varepsilon\hat{t}\hat{u} + (\varepsilon - 1)\hat{u}^2)}{\hat{t}\hat{u}} \\ &\quad \cdot \frac{((N_c^2 - 1)\hat{t}^2 + (N_c^2 - 1)\hat{u}^2 - 2\hat{t}\hat{u})}{\hat{s}^2}, \end{aligned} \quad (\text{C.160})$$

$$\begin{aligned} |\overline{\mathcal{M}}_{qq \rightarrow qq}|^2 &= 16\pi^2 \alpha_s^2 \frac{(N_c^2 - 1)}{N_c^3} \left( \hat{t}^3 \hat{u} (\varepsilon + N_c - 1) + (\varepsilon - 1) \hat{t}^2 \hat{u}^2 (\varepsilon - N_c + 2) \right. \\ &\quad \left. + \hat{t} \hat{u}^3 (\varepsilon + N_c - 1) + N_c \hat{t}^4 + N_c \hat{u}^4 \right) / (\hat{t}^2 \hat{u}^2), \end{aligned} \quad (\text{C.161})$$

$$|\overline{\mathcal{M}}_{qq' \rightarrow qq'}|^2 = 8\pi^2 \alpha_s^2 \frac{(N_c^2 - 1)}{N_c^2} \frac{((1 - \varepsilon)\hat{t}^2 + 2\hat{t}\hat{u} + 2\hat{u}^2)}{\hat{t}^2}, \quad (\text{C.162})$$

$$|\overline{\mathcal{M}}_{gg \rightarrow gg}|^2 = 64\pi^2 \alpha_s^2 \frac{N_c^2}{(N_c^2 - 1)} \frac{(\hat{t}^2 + \hat{t}\hat{u} + \hat{u}^2)^3}{\hat{t}^2 \hat{u}^2 (\hat{t} + \hat{u})^2}. \quad (\text{C.163})$$

The difference of the LO fragmentation contribution to the integration of the direct contribution at LO is of course the integration over the additional momentum fraction  $z$  which the photon inherits from its parent parton, so that the fragmentation contribution is given by

$$\begin{aligned} \int d\sigma_{AB \rightarrow \gamma X}^{(\text{frag})} &= \sum_{a,b,c,d} \int_0^1 dx_a \int_0^1 dx_b f_{a/A}(x_a, \mu_F) f_{b/B}(x_b, \mu_F) \frac{1}{4F} \int_0^1 dz \\ &\quad \cdot \int d\Phi^{(2)} |\overline{\mathcal{M}}_{ab \rightarrow cd}(x_a p_A, x_b p_B, p_1, p_2)|^2 D_{\gamma/c}(z, \mu_F) F_J(z p_1). \end{aligned} \quad (\text{C.164})$$

In principle one can for the practical implementation of this relation simply use the results of App. C.1, with the qualification that one has to take care of the fact that the quantity on which the cuts in  $F_J$  act is not the momentum  $p_1$  which is integrated over by  $d\Phi^{(2)}$ , but  $z p_1$ .

## D Splitting functions at LO

In this section, I include a derivation of the splitting functions, as it helped me a great deal to come to terms with the problems discussed in this thesis. An original derivation of the splitting functions can be found for example in [32], but formulated in terms of old-fashioned perturbation theory [82]. In the following, I use covariant perturbation theory instead for a demonstrative derivation of the unregularized splitting functions – unregularized, because the following expressions for the collinear limit of the  $n+1$ -particle cross section still include soft divergences and have to be added to the soft-collinear contributions of the virtual corrections to the  $n$ -particle cross section.

### D.1 Sudakov decomposition

To approach smoothly the limit of two particles collinearly branching from a parent particle, one has to choose a convenient parametrization of the momenta. If  $p_a$  is the initial particle's four-momentum and  $p'_a$ ,  $k$  are the momenta of the splitting particles then in the collinear limit

$$k = (1 - z)p_a \text{ and } p'_a = zp_a.$$

Taking  $p_a$  as a base vector of the 4-dimensional Minkowski space one needs three more linearly independent vectors to describe  $p'_a$ ,  $k$  in general. A spacelike four-vector  $k_T$  with  $p_a \cdot k_T = 0$  and a lightlike four-vector  $\eta$  with  $\eta \cdot k_T = 0$  and  $\eta \cdot p_a \neq 0$  will suffice.  $k_T$  describes the plane perpendicular to  $p_a$  while  $\eta$  and  $p_a$  are basis vectors of the plane spanned by the spacial direction of particle  $a$  and the time axis. Now, keeping in mind momentum conservation, one can write in full generality

$$k = (1 - z)p_a + k_T + \beta\eta, \tag{D.1}$$

$$p'_a = zp_a - k_T - \beta\eta, \tag{D.2}$$

with  $\beta$  determined by the square of one of the four-momenta. For definiteness let  $k^2 = 0$ , then

$$\beta = \frac{-k_T^2}{2(1 - z)p_a \cdot \eta}. \tag{D.3}$$

The relations (D.1) are known as the Sudakov decomposition. It follows that the off-shellness of  $p'_a$  is given by  $k_T^2$ , or more specific:

$$p_a'^2 = \frac{k_T^2}{1 - z}. \tag{D.4}$$



In the frame where particle  $a$  moves along the 3-axis, it is natural to chose the 4-vectors as

$$\begin{aligned} p_a &= (|\vec{p}_1|, 0, 0, |\vec{p}_1|), \\ k_T &= (0, \vec{k}_T) \text{ with } \vec{k}_T = (k_T^1, k_T^2, 0), \\ \eta &= (|\vec{p}_1|, 0, 0, -|\vec{p}_1|). \end{aligned} \quad (\text{D.5})$$

## D.2 Phase space factorization

The Lorentz-invariant phase space measure factorizes in the collinear limit. Take for example an initial state particle travelling along the 3-axis with momentum  $p_a$  and a final state momentum  $k$  related by (D.1), with the third particle with momentum  $p'_a$  entering the hard scattering. The phase space measure in  $D$  dimensions, denoting only the two relevant momenta, is

$$\begin{aligned} d\Phi^{(n+1)}(p_a, p_b) &= (2\pi)^D \delta^{(D)}(p_a + p_b - k - \dots) \frac{d^{D-1}k}{(2\pi)^{D-1} 2k^0} \dots \\ &= (2\pi)^D \delta^{(D)}(p'_a + p_b - \dots) \frac{d^D k}{(2\pi)^{D-1}} \delta(k^2) \theta(k^0) \dots \end{aligned} \quad (\text{D.6})$$

A change of variables  $d^D k \rightarrow dz d\beta d^{D-2} k_T$  is in order. The Jacobian, using (D.5), is  $-p_a^0 \eta^3 + p_a^3 \eta^0 = 2p_a^0 \eta^0$ , so

$$\begin{aligned} d^D k \delta(k^2) \theta(k^0) &= dz d\beta d^{D-2} k_T 2p_a^0 \eta^0 \delta(-|\vec{k}_T|^2 + 2(1-z)\beta p_a \cdot \eta) \theta((1-z)p_a^0 + \beta \eta^0) \\ &= dz d\beta d^{D-2} k_T 2p_a^0 \eta^0 \frac{\delta(\beta - \frac{|\vec{k}_T|^2}{2(1-z)p_a \cdot \eta})}{2|1-z|p_a \cdot \eta} \theta((1-z)p_a^0 + \beta \eta^0) \\ &= dz d^{D-2} k_T \frac{p_a^0 \eta^0}{(1-z)p_a \cdot \eta} \theta(1-z) \\ &= dz d^{D-2} k_T \frac{1}{2(1-z)} \theta(1-z). \end{aligned}$$

The collinear limit is determined only by diagrams in which the particle with momentum  $p'_a$  enters the interaction with the remaining particles, e.g. Fig. D.1. For this subprocess to produce on-shell particles, the invariant mass has to be positive, i.e.

$$(p'_a + p_b)^2 \geq 0.$$

Thus, the momentum conservation at the splitting vertex and the overall momentum conservation result in a lower limit on  $z$ ,

$$z \geq \frac{|\vec{k}_T|^2 + \frac{s}{2}}{s} - \sqrt{\frac{|\vec{k}_T|^4 + \frac{s^2}{4}}{s^2}} \geq 0. \quad (\text{D.7})$$

## D Splitting functions at LO

The  $\vec{k}_T$ -integration in (D.6) can be performed as long as the diagrams are independent of the direction of  $\vec{k}_T$ , giving

$$d^{D-2}k_T = \frac{2\pi^{(D-2)/2}}{\Gamma(\frac{D-2}{2})} d|\vec{k}_T| |\vec{k}_T|^{D-3}$$

Furthermore, as long as one is interested only in the leading divergence and the  $n$ -particle subprocess is not divergent for initial on-shell particles, one can safely set  $k_T = 0$  in the momentum conservation  $\delta$ -distribution in (D.6) and get in the collinear limit

$$d\Phi^{(n+1)}(p_a, p_b) \rightarrow d\Phi^{(n)}(p'_a, p_b) dz \frac{d^{D-2}k_T}{(2\pi)^{D-1}} \frac{1}{2(1-z)} \theta(1-z)\theta(z) \quad (D.8)$$

$$= d\Phi^{(n)}(p'_a, p_b) dz d|\vec{k}_T| \frac{2|\vec{k}_T|^{D-3}}{(4\pi)^{D/2}\Gamma(\frac{D-2}{2})} \frac{1}{(1-z)} \theta(1-z)\theta(z) \quad (D.9)$$

$$= d\Phi^{(n)}(p'_a, p_b) dz \frac{d|\vec{k}_T|^2}{|\vec{k}_T|^{2\varepsilon}} \frac{1}{16\pi^2} \frac{(4\pi)^\varepsilon}{\Gamma(1-\varepsilon)} \frac{1}{(1-z)} \theta(1-z)\theta(z). \quad (D.10)$$

### D.3 Quark to quark splitting

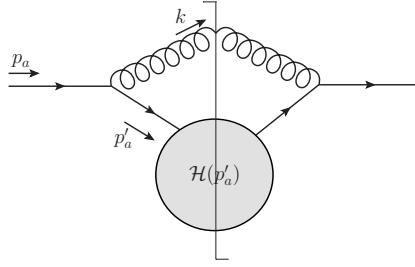


Figure D.1:  $qq$  initial state splitting with quark entering the hard scattering.

If a quark splits off a collinear gluon and the remnant quark participates in the hard scattering, the amplitude is dominated by diagrams of the form depicted in Fig. D.1. Writing the hard scattering as a matrix in spin,  $\mathcal{H}$ , and colour,  $\mathcal{H}_c$ , such that the  $n$ -particle subprocess would be given by

$$|\overline{\mathcal{M}}_n|^2 = \frac{1}{2N_c} \text{Tr} \left[ \not{p}'_a \mathcal{H} \right] \text{tr} [\mathcal{H}_c], \quad (D.11)$$

one can write those diagrams

$$|\overline{\mathcal{M}}_{n+1}|^2 = \frac{1}{2N_c} \frac{g_s^2 \mu^{2\varepsilon}}{(p'_a)^2} \text{Tr} \left[ \not{p}'_a \gamma^\mu \not{p}_a \gamma^\nu \not{p}'_a \mathcal{H} \right] \text{tr} [T^a T^a \mathcal{H}_c] \left( -g_{\mu\nu} + \frac{k_\mu \eta'_\nu + k_\nu \eta'_\mu}{k \cdot \eta'} \right). \quad (D.12)$$

Here,  $\eta'$  is some vector introduced for the physical polarization sum of the gluon polarizations. The colour-trace obviously factorizes. To see that the spin-trace factorizes, the

Sudakov decomposition (D.1) is used. Since one cares only for the leading divergence in  $p'_a \sim k_T$ , only the lowest order  $p'_a$ -terms in the trace have to be considered.

The contraction with the metric tensor gives

$$\begin{aligned}
 \text{Tr} \left[ \not{p}'_a \gamma^\mu \not{p}_a \gamma_\mu \not{p}'_a \mathcal{H} \right] &= (2-D) \text{Tr} \left[ \left( \not{p}_a - \not{k} \right) \not{p}_a \left( \not{p}_a - \not{k} \right) \mathcal{H} \right] \\
 &= (2-D) \text{Tr} \left[ \not{k} \not{p}_a \not{k} \mathcal{H} \right] \\
 &= (2-D) \sum_{s,s'} \text{Tr} \left[ u_{s'}(k) \overline{u_{s'}(k)} \not{p}_1 u_s(k) \overline{u_s(k)} \mathcal{H} \right] \\
 &= (2-D) \sum_{s,s'} \text{Tr} \left[ u_{s'}(k) (2p_a \cdot k) \overline{u_s(k)} \mathcal{H} \right] \\
 &= (D-2) p_a'^2 \text{Tr} [\not{k} \mathcal{H}] ,
 \end{aligned}$$

where the fact that  $k$  is on-shell has been used to decompose the slashed momentum into solutions of the Dirac equation. The contraction with the numerator of the  $k$ - and  $\eta'$ -dependent part of the polarization sum gives

$$\text{Tr} \left[ \not{p}'_a \not{k} \not{p}_a \not{\eta}' \not{p}'_a \mathcal{H} \right] + (\eta' \leftrightarrow k) = -p_a'^2 \text{Tr} \left[ \left( -2k \cdot \eta' \not{p}_a + 2p_a \cdot \eta' (\not{p}_a + \not{p}'_a) - p_a'^2 \not{\eta}' \right) \mathcal{H} \right] .$$

Thus, putting everything back together and using the Sudakov decomposition again, (D.12) becomes

$$\begin{aligned}
 \overline{|\mathcal{M}_{n+1}|^2} &= \frac{1}{2N_c} \frac{g_s^2 \mu^{2\varepsilon} C_F}{(p_a'^2)^2} \text{tr} [\mathcal{H}_c] \left\{ (2-D) p_a'^2 \text{Tr} [\not{k} \mathcal{H}] \right. \\
 &\quad \left. - p_a'^2 \text{Tr} \left[ \left( -2\not{p}_a + 2 \frac{p_a \cdot \eta'}{k \cdot \eta'} (\not{p}_a + \not{p}'_a) - \frac{p_a'^2}{k \cdot \eta'} \not{\eta}' \right) \mathcal{H} \right] \right\} \\
 &= \frac{1}{2N_c} \frac{g_s^2 \mu^{2\varepsilon} C_F}{(p_a'^2)^2} \text{tr} [\mathcal{H}_c] 2p_a'^2 \left\{ \frac{2-D}{2} \text{Tr} \left[ \left( \frac{1-z}{z} \not{p}'_a + \mathcal{O}(k_T) \right) \mathcal{H} \right] \right. \\
 &\quad \left. - \text{Tr} \left[ \left( -\frac{1}{z} (\not{p}'_a + \mathcal{O}(k_T)) \right. \right. \right. \\
 &\quad \left. \left. + \frac{1}{1-z} \frac{(k + \mathcal{O}(k_T)) \cdot \eta'}{k \cdot \eta'} \left( \frac{1}{z} \not{p}'_a + \mathcal{O}(k_T) + \not{p}'_a \right) + \mathcal{O}(k_T) \right) \mathcal{H} \right] \right\} \\
 &= \frac{4\pi \alpha_s \mu^{2\varepsilon} C_F}{(p_a'^2)^2} 2p_a'^2 \left\{ \frac{D(z-1)^2 - 2(z^2 - 4z + 1)}{2(z-1)z} \right\} \overline{|\mathcal{M}_n|^2} + \mathcal{O}\left(\frac{1}{k_T}\right) \quad (\text{D.13})
 \end{aligned}$$

In the cross section a flux factor (C.12) enters. For initial state splitting it has to be modified

$$F \rightarrow \frac{1}{z} F . \quad (\text{D.14})$$

## D Splitting functions at LO

Thus, using (D.13), (D.4) and (D.10), the cross section in the collinear limit for quark-quark-splitting in  $D = 4 - 2\varepsilon$  dimensions is

$$\begin{aligned} d\sigma^{(n+1)}(p_a) &\rightarrow d\sigma^{(n)}(zp_a) \frac{\alpha_s}{2\pi} C_F \frac{1+z^2-\varepsilon(1-z)^2}{1-z} dz \frac{d|\vec{k}_T|^2}{|\vec{k}_T|^{2+2\varepsilon}} \frac{(4\pi\mu^2)^\varepsilon}{\Gamma(1-\varepsilon)} \\ &\equiv d\sigma^{(n)}(zp_a) \frac{\alpha_s}{2\pi} \hat{P}_{qq}^{(\varepsilon)}(z) dz \frac{d|\vec{k}_T|^2}{|\vec{k}_T|^{2+2\varepsilon}} \frac{(4\pi\mu^2)^\varepsilon}{\Gamma(1-\varepsilon)} \end{aligned} \quad (\text{D.15})$$

or in 4 dimensions

$$\begin{aligned} d\sigma^{(n+1)}(p_a) &\rightarrow d\sigma^{(n)}(zp_a) \frac{\alpha_s}{2\pi} C_F \frac{1+z^2}{1-z} dz \frac{d|\vec{k}_T|^2}{|\vec{k}_T|^2} \\ &\equiv d\sigma^{(n)}(zp_a) \frac{\alpha_s}{2\pi} \hat{P}_{qq}(z) dz \frac{d|\vec{k}_T|^2}{|\vec{k}_T|^2} . \end{aligned} \quad (\text{D.16})$$

## D.4 Gluon to quark splitting

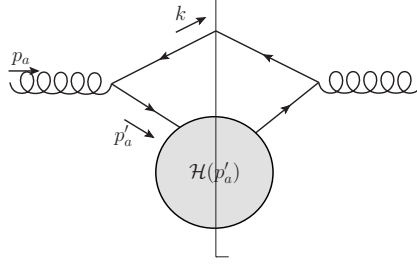


Figure D.2:  $gq$  initial state splitting with quark entering the hard scattering.

The splitting of a gluon into a quark-antiquark pair is completely analog to the quark-to-quark splitting with the squared diagram of the  $n+1$  process given by

$$\begin{aligned} |\overline{\mathcal{M}}_{n+1}|^2 &= \frac{1}{2(N_c^2 - 1)} \frac{g_s^2 \mu^{2\varepsilon}}{(p_a'^2)^2} \text{Tr} \left[ \not{p}'_a \gamma^\mu (-\not{k}) \gamma^\nu \not{p}'_a \mathcal{H} \right] \text{tr} [T^a T^a \mathcal{H}_c] \\ &\quad \cdot \left( -g_{\mu\nu} + \frac{p_{a\mu} \eta'_\nu + p_{a\nu} \eta'_\mu}{p_a \cdot \eta'} \right) , \end{aligned} \quad (\text{D.17})$$

and the underlying  $n$ -particle squared amplitude given by

$$|\overline{\mathcal{M}}_n|^2 = \frac{1}{2N_c} \text{Tr} \left[ \not{p}'_a \mathcal{H} \right] \text{tr} [\mathcal{H}_c] . \quad (\text{D.18})$$

The contraction of the metric tensor in the polarization sum and the spin-trace, calculated with the same trick as in the preceding section, gives

$$\text{Tr} \left[ \not{p}'_a \gamma^\mu \not{k} \gamma_\mu \not{p}'_a \mathcal{H} \right] = (D-2) p_a'^2 \text{Tr} \left[ \not{p}'_a \mathcal{H} \right] ,$$

and the contraction with the numerator of the other term gives

$$\text{Tr} \left[ \not{p}'_a \not{p}_a \not{k} \not{\eta}' \not{p}'_a \mathcal{H} \right] + (\eta' \leftrightarrow p_a) = 2p_a'^2 \text{Tr} \left[ \left( -2k \cdot \eta' \not{k} + k \cdot \eta' \not{p}_a + p_a \cdot \eta' \not{k} - k \cdot p_a \not{\eta}' \right) \mathcal{H} \right].$$

Assembling the result and making use of the Sudakov decomposition (D.1), one has

$$\begin{aligned} |\overline{\mathcal{M}}_{n+1}|^2 &= \frac{C_F}{2(N_c^2 - 1)} \frac{g_s^2 \mu^{2\varepsilon}}{(p_a'^2)^2} \text{tr} [\mathcal{H}_c] \left\{ (D - 2) p_a'^2 \text{Tr} [\not{p}_a \mathcal{H}] \right. \\ &\quad \left. - 2p_a'^2 \text{Tr} \left[ \left( -2 \frac{k \cdot \eta'}{p_a \cdot \eta'} \not{k} + \frac{k \cdot \eta'}{p_a \cdot \eta'} \not{p}_a + \not{k} - \frac{k \cdot p_a}{p_a \cdot \eta'} \not{\eta}' \right) \mathcal{H} \right] \right\} \\ &= \frac{1}{4N_c} \frac{g_s^2 \mu^{2\varepsilon}}{(p_a'^2)^2} \text{tr} [\mathcal{H}_c] 2p_a'^2 \left\{ \frac{D - 2}{2} \frac{1}{z} \text{Tr} [\not{p}'_a \mathcal{H}] + \mathcal{O}(k_T) \right. \\ &\quad \left. - \text{Tr} \left[ \left( -2((1 - z) + \mathcal{O}(k_T)) \frac{1 - z}{z} \not{p}'_a + ((1 - z) + \mathcal{O}(k_T)) \frac{1}{z} \not{p}'_a \right. \right. \right. \\ &\quad \left. \left. \left. + \frac{1 - z}{z} \not{p}'_a + \mathcal{O}(k_T) \right) \mathcal{H} \right] \right\} \\ &= \frac{4\pi \alpha_s^2 \mu^{2\varepsilon}}{p_a'^2} \frac{1}{z} \left\{ (1 - \varepsilon) + 2(1 - z)^2 - 2(1 - z) \right\} |\overline{\mathcal{M}}_n|^2 + \mathcal{O} \left( \frac{1}{k_T} \right), \quad (\text{D.19}) \end{aligned}$$

leading to

$$\begin{aligned} d\sigma^{(n+1)}(p_a) &\rightarrow d\sigma^{(n)}(zp_a) \frac{\alpha_s}{2\pi} \frac{1}{2} (z^2 + (1 - z)^2 - \varepsilon) dz \frac{d|\vec{k}_T|^2}{|\vec{k}_T|^{2+2\varepsilon}} \frac{(4\pi\mu^2)^\varepsilon}{\Gamma(1 - \varepsilon)} \\ &\equiv d\sigma^{(n)}(zp_a) \frac{\alpha_s}{2\pi} \hat{P}_{qg}^{(\varepsilon)}(z) dz \frac{d|\vec{k}_T|^2}{|\vec{k}_T|^{2+2\varepsilon}} \frac{(4\pi\mu^2)^\varepsilon}{\Gamma(1 - \varepsilon)} \end{aligned} \quad (\text{D.20})$$

or in 4 dimensions

$$\begin{aligned} d\sigma^{(n+1)}(p_a) &\rightarrow d\sigma^{(n)}(zp_a) \frac{\alpha_s}{2\pi} \frac{1}{2} (z^2 + (1 - z)^2) dz \frac{d|\vec{k}_T|^2}{|\vec{k}_T|^2} \\ &\equiv d\sigma^{(n)}(zp_a) \frac{\alpha_s}{2\pi} \hat{P}_{qg}(z) dz \frac{d|\vec{k}_T|^2}{|\vec{k}_T|^2}. \end{aligned} \quad (\text{D.21})$$

## D.5 Gluon to gluon splitting

For the splitting of a gluon off a gluon, as depicted in Fig. D.3, use of the Sudakov decomposition (D.1) is made again. The polarization sum for the incoming gluon with momentum  $p_a$  is then parametrized with the same vector  $\eta$  as in the Sudakov decomposition of the two other momenta, whereas the outgoing gluon is described by some vector  $\eta_k$  that approaches  $\eta$  in the collinear limit. For the internal gluon it is best to chose the axial gauge defined by  $\eta \cdot A = 0$ , such that the numerator has the same form

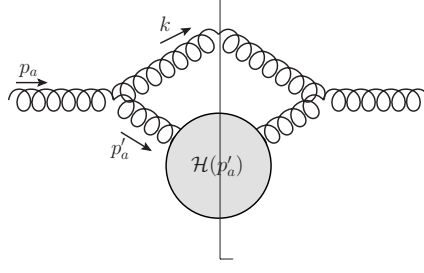


Figure D.3:  $gg$  initial state splitting with gluon entering the hard scattering.

as the polarization sum with auxiliary vector  $\eta$ . The hard scattering is a tensor with Minkowski and gluon indices, so that the  $n$ -particle amplitude can be written as

$$\overline{|\mathcal{M}_n|^2} = \frac{1}{N_C^2 - 1} \frac{1}{2(1 - \varepsilon)} \left( -g_{\mu\nu} + \frac{p'_{a\mu}\eta_\nu + p'_{a\nu}\eta_\mu}{p'_a \cdot \eta} \right) \mathcal{H}^{\mu\nu aa}(p'_a), \quad (\text{D.22})$$

and the  $n + 1$ -particle amplitude is

$$\begin{aligned} \overline{|\mathcal{M}_{n+1}|^2} = & \frac{1}{N_C^2 - 1} \frac{1}{2(1 - \varepsilon)} \left( -g_{\alpha\rho} + \frac{p_{a\alpha}\eta_\rho + p_{a\rho}\eta_\alpha}{p_a \cdot \eta} \right) \left( -g_{\beta\sigma} + \frac{k_\beta\eta_{k\sigma} + k_\sigma\eta_{k\beta}}{k \cdot \eta_k} \right) \\ & \cdot g_s \mu^\varepsilon f^{acb} \left[ g^{\alpha\mu}(p_a + p'_a)^\beta + g^{\mu\beta}(-p'_a + k)^\alpha + g^{\beta\alpha}(-k - p_a)^\mu \right] \\ & \cdot g_s \mu^\varepsilon f^{adb} \left[ g^{\rho\nu}(p_a + p'_a)^\sigma + g^{\nu\sigma}(-p'_a + k)^\rho + g^{\sigma\rho}(-k - p_a)^\nu \right] \\ & \cdot \frac{-g_{\mu\mu'} + \frac{p'_{a\mu}\eta_{\mu'} + p'_{a\mu'}\eta_\mu}{p'_a \cdot \eta}}{p'^2_a} \frac{-g_{\nu\nu'} + \frac{p'_{a\nu}\eta_{\nu'} + p'_{a\nu'}\eta_\nu}{p'_a \cdot \eta}}{p'^2_a} \mathcal{H}^{\mu'\nu'cd}(p'_a). \end{aligned} \quad (\text{D.23})$$

As long as one assumes all non-pictured, external particles subsumed in  $\mathcal{H}$  to be on-shell, one can use [184]

$$p'_{a\mu'} \mathcal{H}^{\mu'\nu'cd}(p'_a) = p'_{a\nu'} \mathcal{H}^{\mu'\nu'cd}(p'_a) = 0. \quad (\text{D.24})$$

Since the three-gluon interaction with two on-shell gluons is itself a matrix element, the result holds also for the contractions of  $p'_a$  and the vertex. Thus the non-metric terms in the numerator of the propagators vanish in (D.23):

$$\begin{aligned} \overline{|\mathcal{M}_{n+1}|^2} = & \frac{1}{N_C^2 - 1} \frac{1}{2(1 - \varepsilon)} g_s^2 \mu^{2\varepsilon} C_A \frac{1}{(p'^2_a)^2} \\ & \cdot \left( -g_{\alpha\rho} + \frac{p_{a\alpha}\eta_\rho + p_{a\rho}\eta_\alpha}{p_a \cdot \eta} \right) \left( -g_{\beta\sigma} + \frac{k_\beta\eta_{k\sigma} + k_\sigma\eta_{k\beta}}{k \cdot \eta_k} \right) \\ & \cdot \left[ g^{\alpha\mu}(p_a + p'_a)^\beta + g^{\mu\beta}(-p'_a + k)^\alpha + g^{\beta\alpha}(-k - p_a)^\mu \right] \\ & \cdot \left[ g^{\rho\nu}(p_a + p'_a)^\sigma + g^{\nu\sigma}(-p'_a + k)^\rho + g^{\sigma\rho}(-k - p_a)^\nu \right] \cdot \mathcal{H}^{cc}_{\mu\nu}(p'_a). \end{aligned} \quad (\text{D.25})$$

The auxiliary vector  $\eta_k$  is chosen to be  $(k^0, -\vec{k})$  in the frame described by (D.5) and can then be related to  $p_a$ ,  $k_T$  and  $\eta$  with the ansatz

$$\eta_k = ap_a + bk_T + c\eta$$

and the relations

$$\begin{aligned}\eta_k^2 &= 0, \\ \eta \cdot \eta_k &= -\beta p_a \cdot \eta, \\ k_T \cdot \eta_k &= -k_T^2.\end{aligned}$$

Solving the equations gives

$$\eta_k = -\beta p_a + k_T + (1 - z)\eta. \quad (\text{D.26})$$

It is then a matter of using some computer algebra to contract the Lorentz tensors in the square brackets and parentheses. I have used **FORM**. First to replace  $\eta_k$  and  $k$ . All terms in the result proportional to  $p_a'^\mu$  or  $p_a'^\nu$  give zero, when contracted with  $\mathcal{H}_{\mu\nu}^{cc}(p_a')$ . Disregarding those terms, one can replace  $p_a'$  with its Sudakov decomposition, and afterwards keep only terms of  $\mathcal{O}(k_T^2)$ . This gives then

$$\begin{aligned}|\overline{\mathcal{M}_{n+1}}|^2 &= \frac{1}{N_C^2 - 1} \frac{1}{2(1 - \varepsilon)} g_s^2 \mu^{2\varepsilon} C_A \left( \frac{1 - z}{k_T^2} \right)^2 \\ &\cdot \left( g^{\mu\nu} k_T^2 4 \frac{1 + (1 - z)^2}{(1 - z)^2} - k_T^\mu k_T^\nu 8 \frac{\varepsilon - 1}{z^2} \right) \mathcal{H}_{\mu\nu}^{cc}(p_a') + \mathcal{O}\left(\frac{1}{k_T}\right).\end{aligned} \quad (\text{D.27})$$

Since the matrix element still depends on the direction of  $k_T$  it has to be combined with (D.8) to integrate over the directions of  $k_T^\mu k_T^\nu / k_T^4$ . The integral can be decomposed in terms of the tensors available after integrating out  $k_T$ , i.e.

$$\int d^{D-2} k_T \frac{k_T^\mu k_T^\nu}{k_T^4} = c_1 g^{\mu\nu} + c_2 p_a^\mu p_a^\nu + c_3 \eta^\mu \eta^\nu + c_4 (p_a^\mu \eta^\nu + p_a^\nu \eta^\mu), \quad (\text{D.28})$$

which is solved by contraction with  $g_{\mu\nu}$ ,  $p_{a\mu}$ , etc. leading to

$$\int d^{D-2} k_T \frac{k_T^\mu k_T^\nu}{k_T^4} = \left( g^{\mu\nu} - \frac{p_a^\mu \eta^\nu + p_a^\nu \eta^\mu}{p_a \cdot \eta} \right) \frac{1}{D - 2} \int d^{D-2} k_T \frac{1}{k_T^2}. \quad (\text{D.29})$$

So, in the end,  $k_T^\mu k_T^\nu / k_T^2$  in (D.27) has just to be replaced by  $g^{\mu\nu} / (D - 2)$  and using (D.22) (keeping in mind that the contractions of  $p'_a \sim z p_a$  with  $\mathcal{H}$  vanish), one has in the collinear limit with (D.10)

$$\begin{aligned}
 d\sigma^{(n+1)}(p_a) &\rightarrow d\sigma^{(n)}(z p_a) \frac{\alpha_s}{4\pi} C_A \frac{z(1-z)^2}{k_T^2} \\
 &\cdot \left( -4 \frac{1 + (1-z)^2}{(1-z)^2} + \frac{8}{D-2} \frac{\varepsilon - 1}{z^2} \right) dz \frac{d|\vec{k}_T|^2}{|\vec{k}_T|^{2\varepsilon}} \frac{(4\pi\mu^2)^\varepsilon}{\Gamma(1-\varepsilon)} \frac{1}{(1-z)} \\
 &= d\sigma^{(n)}(z p_a) \frac{\alpha_s}{2\pi} 2C_A \left( \frac{z}{1-z} + z(1-z) + \frac{1-z}{z} \right) dz \frac{d|\vec{k}_T|^2}{|\vec{k}_T|^{2+2\varepsilon}} \frac{(4\pi\mu^2)^\varepsilon}{\Gamma(1-\varepsilon)} \\
 &= d\sigma^{(n)}(z p_a) \frac{\alpha_s}{2\pi} \hat{P}_{gg}^{(\varepsilon)}(z) dz \frac{d|\vec{k}_T|^2}{|\vec{k}_T|^{2+2\varepsilon}} \frac{(4\pi\mu^2)^\varepsilon}{\Gamma(1-\varepsilon)}, \tag{D.30}
 \end{aligned}$$

or in  $D = 4$  dimensions

$$d\sigma^{(n+1)}(p_a) \rightarrow d\sigma^{(n)}(z p_a) \frac{\alpha_s}{2\pi} 2C_A \left( \frac{z}{1-z} + z(1-z) + \frac{1-z}{z} \right) dz \frac{d|\vec{k}_T|^2}{|\vec{k}_T|^2} \tag{D.31}$$

$$\equiv d\sigma^{(n)}(z p_a) \frac{\alpha_s}{2\pi} \hat{P}_{gg}(z) dz \frac{d|\vec{k}_T|^2}{|\vec{k}_T|^2}. \tag{D.32}$$

## D.6 Quark to gluon splitting

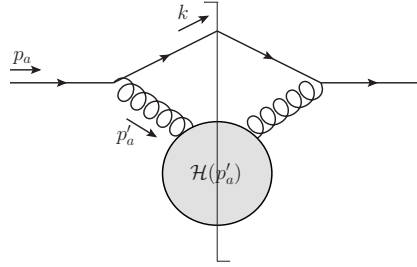


Figure D.4:  $qg$  initial state splitting with gluon entering the hard scattering.

The splitting depicted in Fig. D.4 could be computed similar to the gluon-gluon-splitting, in that the crucial point here is again the contraction of the splitting vertex and the hard scattering matrix through a gluon. Another way is just to take the result for the quark-quark-splitting, (D.15) or (D.16), and assert that the gluon in that splitting takes away a fraction  $1 - z$  of the momentum and one has

$$\hat{P}_{gq}^{(\varepsilon)}(z) = \hat{P}_{qq}^{(\varepsilon)}(1-z) = C_F \frac{1 + (1-z)^2 - \varepsilon z^2}{z}, \tag{D.33}$$

$$\hat{P}_{gq}(z) = C_F \frac{1 + (1-z)^2}{z}. \tag{D.34}$$



# Bibliography

- [1] G. Hanson *et al.*, “Evidence for Jet Structure in Hadron Production by  $e^+ e^-$  Annihilation,” *Phys. Rev. Lett.* **35** (1975) 1609–1612.
- [2] TASSO Collaboration, G. Wolf *et al.*, “TASSO results on  $e^+ e^-$  annihilation between 13-GeV and 31.6-GeV and evidence for three jet events,” *eConf C790823* (1979) 34.
- [3] M. Breidenbach, J. I. Friedman, H. W. Kendall, E. D. Bloom, D. H. Coward, H. C. DeStaebler, J. Drees, L. W. Mo, and R. E. Taylor, “Observed Behavior of Highly Inelastic electron-Proton Scattering,” *Phys. Rev. Lett.* **23** (1969) 935–939.
- [4] F. Halzen and A. D. Martin, *Quarks and Leptons: An Introductory Course in Modern Particle Physics*. 1984.
- [5] T. Muta, *Foundations of Quantum Chromodynamics: An Introduction to Perturbative Methods in Gauge Theories*, (3rd ed.), vol. 78 of *World scientific Lecture Notes in Physics*. World Scientific, Hackensack, N.J., 2010.
- [6] R. K. Ellis, W. J. Stirling, and B. R. Webber, *QCD and Collider Physics*, vol. 8 of *Camb. Monogr. Part. Phys. Nucl. Phys. Cosmol.* Cambridge University Press, 1996.
- [7] J. Collins, *Foundations of perturbative QCD*. Cambridge University Press, 2013.
- [8] M. Boehm, A. Denner, and H. Joos, *Gauge theories of the strong and electroweak interaction*. B.G. Teubner StuttgartLeipzigWiesbaden, Germany, 2001.
- [9] M. Gell-Mann, “A Schematic Model of Baryons and Mesons,” *Phys. Lett.* **8** (1964) 214–215.
- [10] G. Zweig, “An SU(3) model for strong interaction symmetry and its breaking. Version 1.” CERN-TH-401, Jan, 1964.
- [11] J. D. Bjorken, “Asymptotic Sum Rules at Infinite Momentum,” *Phys. Rev.* **179** (1969) 1547–1553.
- [12] R. P. Feynman, “Very high-energy collisions of hadrons,” *Phys. Rev. Lett.* **23** (1969) 1415–1417.
- [13] J. D. Bjorken and E. A. Paschos, “Inelastic Electron Proton and gamma Proton Scattering, and the Structure of the Nucleon,” *Phys. Rev.* **185** (1969) 1975–1982.

## Bibliography

- [14] M. Y. Han and Y. Nambu, “Three Triplet Model with Double SU(3) Symmetry,” *Phys. Rev.* **139** (1965) B1006–B1010.
- [15] H. Fritzsch and M. Gell-Mann, “Current algebra: Quarks and what else?,” *eConf* **C720906V2** (1972) 135–165, [arXiv:hep-ph/0208010](#) [hep-ph].
- [16] C.-N. Yang and R. L. Mills, “Conservation of Isotopic Spin and Isotopic Gauge Invariance,” *Phys. Rev.* **96** (1954) 191–195.
- [17] S. Weinberg, *The quantum theory of fields. Vol. 2: Modern applications*. Cambridge University Press, 2013.
- [18] D. J. Gross and F. Wilczek, “Ultraviolet Behavior of Nonabelian Gauge Theories,” *Phys. Rev. Lett.* **30** (1973) 1343–1346.
- [19] D. J. Gross and F. Wilczek, “Asymptotically Free Gauge Theories. 1,” *Phys. Rev.* **D8** (1973) 3633–3652.
- [20] D. J. Gross and F. Wilczek, “Asymptotically Free Gauge Theories. 2.,” *Phys. Rev.* **D9** (1974) 980–993.
- [21] H. D. Politzer, “Reliable Perturbative Results for Strong Interactions?,” *Phys. Rev. Lett.* **30** (1973) 1346–1349.
- [22] B. Delamotte, “A Hint of renormalization,” *Am. J. Phys.* **72** (2004) 170–184, [arXiv:hep-th/0212049](#) [hep-th].
- [23] H. Georgi and H. D. Politzer, “Electroproduction scaling in an asymptotically free theory of strong interactions,” *Phys. Rev.* **D9** (1974) 416–420.
- [24] R. J. Eden, P. V. Landshoff, D. I. Olive, and J. C. Polkinghorne, *The analytic S-matrix*. Cambridge Univ. Press, Cambridge, 1966.
- [25] G. F. Sterman, “QCD and jets,” in *Physics in  $D \geq 4$ . Proceedings, Theoretical Advanced Study Institute in elementary particle physics, TASI 2004, Boulder, USA, June 6-July 2, 2004*, pp. 67–145. 2004. [arXiv:hep-ph/0412013](#) [hep-ph].
- [26] F. Bloch and A. Nordsieck, “Note on the Radiation Field of the electron,” *Phys. Rev.* **52** (1937) 54–59.
- [27] T. Kinoshita, “Mass singularities of Feynman amplitudes,” *J. Math. Phys.* **3** (1962) 650–677.
- [28] T. D. Lee and M. Nauenberg, “Degenerate Systems and Mass Singularities,” *Phys. Rev.* **133** (1964) B1549–B1562. [,25(1964)].
- [29] S. Catani and M. H. Seymour, “A General algorithm for calculating jet cross-sections in NLO QCD,” *Nucl. Phys.* **B485** (1997) 291–419, [arXiv:hep-ph/9605323](#) [hep-ph]. [Erratum: Nucl. Phys.B510,503(1998)].

- [30] J. C. Collins, D. E. Soper, and G. F. Sterman, “Factorization of Hard Processes in QCD,” *Adv. Ser. Direct. High Energy Phys.* **5** (1989) 1–91, [arXiv:hep-ph/0409313](#) [hep-ph].
- [31] D. A. Kosower and P. Uwer, “Evolution kernels from splitting amplitudes,” *Nucl. Phys.* **B674** (2003) 365–400, [arXiv:hep-ph/0307031](#) [hep-ph].
- [32] G. Altarelli and G. Parisi, “Asymptotic Freedom in Parton Language,” *Nucl. Phys.* **B126** (1977) 298–318.
- [33] Y. L. Dokshitzer, “Calculation of the Structure Functions for Deep Inelastic Scattering and  $e^+e^-$  Annihilation by Perturbation Theory in Quantum Chromodynamics,” *Sov. Phys. JETP* **46** (1977) 641–653. [*Zh. Eksp. Teor. Fiz.* 73,1216(1977)].
- [34] V. N. Gribov and L. N. Lipatov, “Deep inelastic  $e p$  scattering in perturbation theory,” *Sov. J. Nucl. Phys.* **15** (1972) 438–450. [*Yad. Fiz.* 15,781(1972)].
- [35] B. Ioffe, V. Fadin, and L. Lipatov, *Quantum Chromodynamics: Perturbative and Nonperturbative Aspects*. Cambridge Monographs on Particle Physics, Nuclear Physics and Cosmology. Cambridge University Press, 2010.
- [36] G. Passarino and M. J. G. Veltman, “One Loop Corrections for  $e^+e^-$  Annihilation Into  $\mu^+\mu^-$  in the Weinberg Model,” *Nucl. Phys.* **B160** (1979) 151.
- [37] S. Catani and M. H. Seymour, “The Dipole formalism for the calculation of QCD jet cross-sections at next-to-leading order,” *Phys. Lett.* **B378** (1996) 287–301, [arXiv:hep-ph/9602277](#) [hep-ph].
- [38] S. Frixione, Z. Kunszt, and A. Signer, “Three jet cross-sections to next-to-leading order,” *Nucl. Phys.* **B467** (1996) 399–442, [arXiv:hep-ph/9512328](#) [hep-ph].
- [39] S. Frixione, “A General approach to jet cross-sections in QCD,” *Nucl. Phys.* **B507** (1997) 295–314, [arXiv:hep-ph/9706545](#) [hep-ph].
- [40] R. Frederix, S. Frixione, F. Maltoni, and T. Stelzer, “Automation of next-to-leading order computations in QCD: The FKS subtraction,” *JHEP* **10** (2009) 003, [arXiv:0908.4272](#) [hep-ph].
- [41] K. Hasegawa, S. Moch, and P. Uwer, “AutoDipole: Automated generation of dipole subtraction terms,” *Comput. Phys. Commun.* **181** (2010) 1802–1817, [arXiv:0911.4371](#) [hep-ph].
- [42] R. Frederix, T. Gehrmann, and N. Greiner, “Integrated dipoles with MadDipole in the MadGraph framework,” *JHEP* **06** (2010) 086, [arXiv:1004.2905](#) [hep-ph].

## Bibliography

- [43] S. Catani, S. Dittmaier, M. H. Seymour, and Z. Trocsanyi, “The Dipole formalism for next-to-leading order QCD calculations with massive partons,” *Nucl. Phys.* **B627** (2002) 189–265, [arXiv:hep-ph/0201036](#) [hep-ph].
- [44] S. Dittmaier, “A General approach to photon radiation off fermions,” *Nucl. Phys.* **B565** (2000) 69–122, [arXiv:hep-ph/9904440](#) [hep-ph].
- [45] S. Frixione, P. Nason, and C. Oleari, “Matching NLO QCD computations with Parton Shower simulations: the POWHEG method,” *JHEP* **11** (2007) 070, [arXiv:0709.2092](#) [hep-ph].
- [46] S. Alioli, P. Nason, C. Oleari, and E. Re, “A general framework for implementing NLO calculations in shower Monte Carlo programs: the POWHEG BOX,” *JHEP* **06** (2010) 043, [arXiv:1002.2581](#) [hep-ph].
- [47] K. G. Wilson, “Confinement of Quarks,” *Phys. Rev.* **D10** (1974) 2445–2459. [,45(1974)].
- [48] A. J. Niemi and G. W. Semenoff, “Finite Temperature Quantum Field Theory in Minkowski Space,” *Annals Phys.* **152** (1984) 105.
- [49] T. Altherr, “Introduction to thermal field theory,” *Int. J. Mod. Phys.* **A8** (1993) 5605–5628, [arXiv:hep-ph/9307277](#) [hep-ph].
- [50] E. Iancu, “QCD in heavy ion collisions,” in *Proceedings, 2011 European School of High-Energy Physics (ESHEP 2011)*, pp. 197–266. 2014. [arXiv:1205.0579](#) [hep-ph].
- [51] P. de Forcrand, O. Philipsen, and W. Unger, “QCD phase diagram from the lattice at strong coupling,” *PoS CPOD2014* (2015) 073, [arXiv:1503.08140](#) [hep-lat].
- [52] A. Bazavov *et al.*, “The chiral and deconfinement aspects of the QCD transition,” *Phys. Rev.* **D85** (2012) 054503, [arXiv:1111.1710](#) [hep-lat].
- [53] T. Schäfer, “Phases of QCD,” in *20th Annual Hampton University Graduate Studies Program (HUGS 2005) Newport News, Virginia, May 31-June 17, 2005*. 2005. [arXiv:hep-ph/0509068](#) [hep-ph].
- [54] H. Satz, “Quark Matter and Nuclear Collisions: A Brief History of Strong Interaction Thermodynamics,” *Int. J. Mod. Phys.* **E21** (2012) 1230006, [arXiv:1207.0341](#) [hep-ph].
- [55] A. Bazavov *et al.*, “Equation of state and QCD transition at finite temperature,” *Phys. Rev.* **D80** (2009) 014504, [arXiv:0903.4379](#) [hep-lat].
- [56] S. Weinberg, *Gravitation and Cosmology: Principles and Applications of the General Theory of Relativity*. Wiley, New York, NY, 1972.

- [57] T. P. Cheng, *Relativity, gravitation, and cosmology: A basic introduction*. Oxford Univ. Pr., Oxford, UK, 2010.
- [58] E. V. Shuryak, “Quantum Chromodynamics and the Theory of Superdense Matter,” *Phys. Rept.* **61** (1980) 71–158.
- [59] A. Unsöld and B. Baschek, *Der neue Kosmos: Einführung in die Astronomie und Astrophysik*. Springer Berlin Heidelberg, 2004.
- [60] F. V. Murphy and D. E. Yount, “Photons as hadrons,” *Sci. Am.* **225N1** no. 1, (1971) 94–104.
- [61] T. H. Bauer, R. D. Spital, D. R. Yennie, and F. M. Pipkin, “The Hadronic Properties of the Photon in High-Energy Interactions,” *Rev. Mod. Phys.* **50** (1978) 261. [Erratum: *Rev. Mod. Phys.* 51,407(1979)].
- [62] C. Berger and W. Wagner, “Photon-Photon Reactions,” *Phys. Rept.* **146** (1987) 1.
- [63] M. Erdmann, “The Partonic structure of the photon: Photoproduction at the lepton - proton collider HERA,” *Springer Tracts Mod. Phys.* **138** (1997) 1–114.
- [64] M. Klasen, “Theory of hard photoproduction,” *Rev. Mod. Phys.* **74** (2002) 1221–1282, [arXiv:hep-ph/0206169](#) [hep-ph].
- [65] C. Berger, “Photon structure function revisited,” *J. Mod. Phys.* **6** (2014) 1023–1043, [arXiv:1404.3551](#) [hep-ph].
- [66] **ATLAS** Collaboration, G. Aad *et al.*, “Observation of a new particle in the search for the Standard Model Higgs boson with the ATLAS detector at the LHC,” *Phys. Lett.* **B716** (2012) 1–29, [arXiv:1207.7214](#) [hep-ex].
- [67] **CMS** Collaboration, S. Chatrchyan *et al.*, “Observation of a new boson at a mass of 125 GeV with the CMS experiment at the LHC,” *Phys. Lett.* **B716** (2012) 30–61, [arXiv:1207.7235](#) [hep-ex].
- [68] **ATLAS** Collaboration, M. Aaboud *et al.*, “Search for resonances in diphoton events at  $\sqrt{s}=13$  TeV with the ATLAS detector,” [arXiv:1606.03833](#) [hep-ex].
- [69] **CMS** Collaboration, V. Khachatryan *et al.*, “Search for resonant production of high-mass photon pairs in proton-proton collisions at  $\sqrt{s} = 8$  and 13 TeV,” [arXiv:1606.04093](#) [hep-ex].
- [70] E. L. Berger, E. Braaten, and R. D. Field, “Large p(T) Production of Single and Double Photons in Proton Proton and Pion-Proton Collisions,” *Nucl. Phys.* **B239** (1984) 52–92.
- [71] P. Aurenche, A. Douiri, R. Baier, M. Fontannaz, and D. Schiff, “Prompt Photon Production at Large p(T) in QCD Beyond the Leading Order,” *Phys. Lett.* **B140** (1984) 87–92.

## Bibliography

- [72] J. F. Owens, “Large Momentum Transfer Production of Direct Photons, Jets, and Particles,” *Rev. Mod. Phys.* **59** (1987) 465.
- [73] P. Aurenche, P. Chiappetta, M. Fontannaz, J. P. Guillet, and E. Pilon, “Next-to-leading order bremsstrahlung contribution to prompt photon production,” *Nucl. Phys.* **B399** (1993) 34–62.
- [74] L. E. Gordon and W. Vogelsang, “Polarized and unpolarized isolated prompt photon production beyond the leading order,” *Phys. Rev.* **D50** (1994) 1901–1916.
- [75] S. Catani, M. L. Mangano, and P. Nason, “Sudakov resummation for prompt photon production in hadron collisions,” *JHEP* **07** (1998) 024, [arXiv:hep-ph/9806484](#) [hep-ph].
- [76] S. Catani, M. L. Mangano, P. Nason, C. Oleari, and W. Vogelsang, “Sudakov resummation effects in prompt photon hadroproduction,” *JHEP* **03** (1999) 025, [arXiv:hep-ph/9903436](#) [hep-ph].
- [77] N. Kidonakis and J. F. Owens, “Soft gluon resummation and NNLO corrections for direct photon production,” *Phys. Rev.* **D61** (2000) 094004, [arXiv:hep-ph/9912388](#) [hep-ph].
- [78] N. Kidonakis and J. F. Owens, “Next-to-next-to-leading order soft gluon corrections in direct photon production,” *Int. J. Mod. Phys.* **A19** (2004) 149–158, [arXiv:hep-ph/0307352](#) [hep-ph].
- [79] T. Becher and M. D. Schwartz, “Direct photon production with effective field theory,” *JHEP* **02** (2010) 040, [arXiv:0911.0681](#) [hep-ph].
- [80] M. D. Schwartz, “Precision direct photon spectra at high energy and comparison to the 8 TeV ATLAS data,” [arXiv:1606.02313](#) [hep-ph].
- [81] M. Maggiore, *A Modern Introduction to Quantum Field Theory*. Oxford Master Series in Statistical, Computational, and Theoretical Physics. Oxford Univ., Oxford, 2005.
- [82] S. Weinberg, *The Quantum theory of fields. Vol. 1: Foundations*. Cambridge University Press, 2005.
- [83] M. L. Bellac, *Quantum and Statistical Field Theory*. Oxford University Press, USA, 1992.
- [84] S. J. Brodsky, T. Kinoshita, and H. Terazawa, “Deep inelastic scattering of electrons on a photon target,” *Phys. Rev. Lett.* **27** (1971) 280–283.
- [85] T. F. Walsh and P. M. Zerwas, “Two photon processes in the parton model,” *Phys. Lett.* **B44** (1973) 195–198.

- [86] E. Witten, “Anomalous Cross-Section for Photon - Photon Scattering in Gauge Theories,” *Nucl. Phys.* **B120** (1977) 189–202.
- [87] C. von Weizsäcker, “Ausstrahlung bei Stößen sehr schneller Elektronen,” *Z.Phys.* **88** (1934) 612–625.
- [88] E. Williams, “Nature of the high-energy particles of penetrating radiation and status of ionization and radiation formulae,” *Phys.Rev.* **45** (1934) 729–730.
- [89] T. Hahn and M. Perez-Victoria, “Automatized one loop calculations in four-dimensions and D-dimensions,” *Comput.Phys.Commun.* **118** (1999) 153–165, [arXiv:hep-ph/9807565](#) [[hep-ph](#)].
- [90] Wolfram Research, Inc., *Mathematica*. Wolfram Research, Inc., Champaign, Illinois, version 10.1 ed., 2015.
- [91] T. Hahn, “CUBA: A Library for multidimensional numerical integration,” *Comput.Phys.Commun.* **168** (2005) 78–95, [arXiv:hep-ph/0404043](#) [[hep-ph](#)].
- [92] E. Byckling and K. Kajantie, *Particle Kinematics*. University of Jyväskylä, Jyväskylä, Finland, 1971.
- [93] A. Buckley, J. Ferrando, S. Lloyd, K. Nordström, B. Page, M. Rüfenacht, M. Schönherr, and G. Watt, “LHAPDF6: parton density access in the LHC precision era,” *Eur. Phys. J.* **C75** (2015) 132, [arXiv:1412.7420](#) [[hep-ph](#)].
- [94] M. Glück, E. Reya, and A. Vogt, “Parton fragmentation into photons beyond the leading order,” *Phys. Rev.* **D48** (1993) 116. [Erratum: *Phys. Rev.* **D51**, 1427(1995)].
- [95] J. Alwall, R. Frederix, S. Frixione, V. Hirschi, F. Maltoni, O. Mattelaer, H. S. Shao, T. Stelzer, P. Torrielli, and M. Zaro, “The automated computation of tree-level and next-to-leading order differential cross sections, and their matching to parton shower simulations,” *JHEP* **07** (2014) 079, [arXiv:1405.0301](#) [[hep-ph](#)].
- [96] S. Catani, M. Fontannaz, J. Guillet, and E. Pilon, “Cross-section of isolated prompt photons in hadron hadron collisions,” *JHEP* **0205** (2002) 028, [arXiv:hep-ph/0204023](#) [[hep-ph](#)].
- [97] H.-L. Lai, M. Guzzi, J. Huston, Z. Li, P. M. Nadolsky, J. Pumplin, and C. P. Yuan, “New parton distributions for collider physics,” *Phys. Rev.* **D82** (2010) 074024, [arXiv:1007.2241](#) [[hep-ph](#)].
- [98] S. Kawabata, “A New Monte Carlo Event Generator for High-Energy Physics,” *Comput. Phys. Commun.* **41** (1986) 127.

- [99] L. Bourhis, M. Fontannaz, and J. P. Guillet, “Quarks and gluon fragmentation functions into photons,” *Eur. Phys. J.* **C2** (1998) 529–537, [arXiv:hep-ph/9704447](#) [hep-ph].
- [100] D. de Florian, R. Sassot, P. Zurita, and M. Stratmann, “Global Analysis of Nuclear Parton Distributions,” *Phys. Rev.* **D85** (2012) 074028, [arXiv:1112.6324](#) [hep-ph].
- [101] I. Schienbein, J. Y. Yu, K. Kovarik, C. Keppel, J. G. Morfin, F. Olness, and J. F. Owens, “PDF Nuclear Corrections for Charged and Neutral Current Processes,” *Phys. Rev.* **D80** (2009) 094004, [arXiv:0907.2357](#) [hep-ph].
- [102] M. Klasen and F. König, “New information on photon fragmentation functions,” *Eur. Phys. J.* **C74** no. 8, (2014) 3009, [arXiv:1403.2290](#) [hep-ph].
- [103] T. Kaufmann, A. Mukherjee, and W. Vogelsang, “Access to Photon Fragmentation Functions in Hadronic Jet Production,” *Phys. Rev.* **D93** no. 11, (2016) 114021, [arXiv:1604.07175](#) [hep-ph].
- [104] **ATLAS** Collaboration, G. Aad *et al.*, “Measurement of the inclusive isolated prompt photon cross section in  $pp$  collisions at  $\sqrt{s} = 8$  TeV with the ATLAS detector,” [arXiv:1605.03495](#) [hep-ex].
- [105] **CMS** Collaboration, V. Khachatryan *et al.*, “Comparison of the  $Z/\gamma^* + \text{jets}$  to  $\gamma + \text{jets}$  cross sections in  $pp$  collisions at  $\sqrt{s} = 8$  TeV,” *JHEP* **10** (2015) 128, [arXiv:1505.06520](#) [hep-ex]. [Erratum: JHEP04,010(2016)].
- [106] **STAR** Collaboration, C. Yang, “Direct photon production in Au + Au collisions at  $\sqrt{s_{NN}} = 200$  GeV at STAR,” *Nucl. Phys.* **A931** (2014) 691–695, [arXiv:1408.2371](#) [hep-ex].
- [107] **PHENIX** Collaboration, A. Adare *et al.*, “Direct-Photon Production in  $p + p$  Collisions at  $\sqrt{s} = 200$  GeV at Midrapidity,” *Phys. Rev.* **D86** (2012) 072008, [arXiv:1205.5533](#) [hep-ex].
- [108] **ALICE** Collaboration, M. Wilde, “Measurement of Direct Photons in  $pp$  and Pb-Pb Collisions with ALICE,” *Nucl. Phys.* **A904-905** (2013) 573c–576c, [arXiv:1210.5958](#) [hep-ex].
- [109] **ALICE** Collaboration, J. Adam *et al.*, “Direct photon production in Pb-Pb collisions at  $\sqrt{s_{NN}} = 2.76$  TeV,” *Phys. Lett.* **B754** (2016) 235–248, [arXiv:1509.07324](#) [nucl-ex].
- [110] **PHENIX** Collaboration, A. Adare *et al.*, “Enhanced production of direct photons in Au+Au collisions at  $\sqrt{s_{NN}} = 200$  GeV and implications for the initial temperature,” *Phys. Rev. Lett.* **104** (2010) 132301, [arXiv:0804.4168](#) [nucl-ex].



- [111] **PHENIX** Collaboration, A. Adare *et al.*, “Direct photon production in  $d+Au$  collisions at  $\sqrt{s_{NN}} = 200$  GeV,” *Phys. Rev.* **C87** (2013) 054907, [arXiv:1208.1234](#) [[nucl-ex](#)].
- [112] S. Brandt, *Datenanalyse: Mit statistischen Methoden und Computerprogrammen*. Spektrum Akademischer Verlag, 1999.
- [113] F. Arleo *et al.*, “Hard probes in heavy-ion collisions at the LHC: Photon physics in heavy ion collisions at the LHC,” [arXiv:hep-ph/0311131](#) [[hep-ph](#)].
- [114] R. Snellings, “Elliptic Flow: A Brief Review,” *New J. Phys.* **13** (2011) 055008, [arXiv:1102.3010](#) [[nucl-ex](#)].
- [115] J. D. Bjorken, “Highly Relativistic Nucleus-Nucleus Collisions: The Central Rapidity Region,” *Phys. Rev.* **D27** (1983) 140–151.
- [116] M. L. Bellac, *Thermal Field Theory*. Cambridge University Press, 2011.
- [117] S. Jeon and U. Heinz, “Introduction to Hydrodynamics,” *Int. J. Mod. Phys.* **E24** no. 10, (2015) 1530010, [arXiv:1503.03931](#) [[hep-ph](#)].
- [118] B. Müller, “Investigation of Hot QCD Matter: Theoretical Aspects,” *Phys. Scripta* **T158** (2013) 014004, [arXiv:1309.7616](#) [[nucl-th](#)].
- [119] **ALICE** Collaboration, P. Kurashvili, “Photon and neutral pion production in pp and Pb-Pb collisions at LHC energies in the ALICE experiment,” in *LISHEP-International School on High Energy Physics- Session C MANAUS, Amazonas, Brazil, August 2-9, 2015*. 2015. [arXiv:1511.00306](#) [[hep-ex](#)].
- [120] **ALICE** Collaboration, S. Hayashi, “Dielectron measurements in pp, p-Pb, and Pb-Pb collisions with the ALICE detector,” *Nucl. Part. Phys. Proc.* **276-278** (2016) 245–248.
- [121] G. Diana, J. Rojo, and R. D. Ball, “High energy resummation of direct photon production at hadronic colliders,” *Phys. Lett.* **B693** (2010) 430–437, [arXiv:1006.4250](#) [[hep-ph](#)].
- [122] D. G. d’Enterria, “Hard scattering cross-sections at LHC in the Glauber approach: From pp to pA and AA collisions,” [arXiv:nucl-ex/0302016](#) [[nucl-ex](#)].
- [123] M. L. Miller, K. Reygers, S. J. Sanders, and P. Steinberg, “Glauber modeling in high energy nuclear collisions,” *Ann. Rev. Nucl. Part. Sci.* **57** (2007) 205–243, [arXiv:nucl-ex/0701025](#) [[nucl-ex](#)].
- [124] **ALICE** Collaboration, B. Abelev *et al.*, “Centrality determination of Pb-Pb collisions at  $\sqrt{s_{NN}} = 2.76$  TeV with ALICE,” *Phys. Rev.* **C88** no. 4, (2013) 044909, [arXiv:1301.4361](#) [[nucl-ex](#)].

- [125] M. Klasen, C. Klein-Bösing, F. König, and J. P. Wessels, “How robust is a thermal photon interpretation of the ALICE low- $p_T$  data?,” *JHEP* **10** (2013) 119, [arXiv:1307.7034 \[hep-ph\]](#).
- [126] **European Muon** Collaboration, J. Ashman *et al.*, “Measurement of the Ratios of Deep Inelastic Muon - Nucleus Cross-Sections on Various Nuclei Compared to Deuterium,” *Phys. Lett.* **B202** (1988) 603–610.
- [127] K. J. Eskola, H. Paukkunen, and C. A. Salgado, “EPS09: A New Generation of NLO and LO Nuclear Parton Distribution Functions,” *JHEP* **04** (2009) 065, [arXiv:0902.4154 \[hep-ph\]](#).
- [128] M. Hirai, S. Kumano, and T. H. Nagai, “Determination of nuclear parton distribution functions and their uncertainties in next-to-leading order,” *Phys. Rev.* **C76** (2007) 065207, [arXiv:0709.3038 \[hep-ph\]](#).
- [129] K. Kovarik *et al.*, “nCTEQ15 - Global analysis of nuclear parton distributions with uncertainties in the CTEQ framework,” *Phys. Rev.* **D93** no. 8, (2016) 085037, [arXiv:1509.00792 \[hep-ph\]](#).
- [130] D. Stump, J. Huston, J. Pumplin, W.-K. Tung, H. L. Lai, S. Kuhlmann, and J. F. Owens, “Inclusive jet production, parton distributions, and the search for new physics,” *JHEP* **10** (2003) 046, [arXiv:hep-ph/0303013 \[hep-ph\]](#).
- [131] A. D. Martin, R. G. Roberts, W. J. Stirling, and R. S. Thorne, “Parton distributions: A New global analysis,” *Eur. Phys. J.* **C4** (1998) 463–496, [arXiv:hep-ph/9803445 \[hep-ph\]](#).
- [132] A. D. Martin, W. J. Stirling, R. S. Thorne, and G. Watt, “Parton distributions for the LHC,” *Eur. Phys. J.* **C63** (2009) 189–285, [arXiv:0901.0002 \[hep-ph\]](#).
- [133] J. M. Campbell, J. W. Huston, and W. J. Stirling, “Hard Interactions of Quarks and Gluons: A Primer for LHC Physics,” *Rept. Prog. Phys.* **70** (2007) 89, [arXiv:hep-ph/0611148 \[hep-ph\]](#).
- [134] H. Paukkunen, “Nuclear PDFs in the beginning of the LHC era,” *Nucl. Phys.* **A926** (2014) 24–33, [arXiv:1401.2345 \[hep-ph\]](#).
- [135] I. Helenius, H. Paukkunen, and K. J. Eskola, “Nuclear PDF constraints from p+Pb collisions at the LHC,” *PoS DIS2015* (2015) 036, [arXiv:1509.02798 \[hep-ph\]](#).
- [136] M. Brandt, M. Klasen, and F. König, “Nuclear parton density modifications from low-mass lepton pair production at the LHC,” *Nucl. Phys.* **A927** (2014) 78–90, [arXiv:1401.6817 \[hep-ph\]](#).
- [137] **ATLAS** Collaboration, G. Aad *et al.*, “Centrality, rapidity and transverse momentum dependence of isolated prompt photon production in lead-lead

- collisions at  $\sqrt{s_{NN}} = 2.76$  TeV measured with the ATLAS detector,” *Phys. Rev. C* **93** no. 3, (2016) 034914, [arXiv:1506.08552 \[hep-ex\]](#).
- [138] I. Helenius, H. Paukkunen, and N. Armesto, “nPDF constraints from the Large Hadron Electron Collider,” in *Proceedings, 24th International Workshop on Deep-Inelastic Scattering and Related Subjects (DIS 2016): Hamburg, Germany, April 11-25, 2016*. 2016. [arXiv:1606.09003 \[hep-ph\]](#).
  - [139] X.-N. Wang, Z. Huang, and I. Sarcevic, “Jet quenching in the opposite direction of a tagged photon in high-energy heavy ion collisions,” *Phys. Rev. Lett.* **77** (1996) 231–234, [arXiv:hep-ph/9605213 \[hep-ph\]](#).
  - [140] F. Arleo, “Probing medium-modified fragmentation processes with prompt photons,” *Nucl. Phys. A* **782** (2007) 291–296.
  - [141] B. G. Zakharov, “Induced photon emission from quark jets in ultrarelativistic heavy-ion collisions,” *JETP Lett.* **80** (2004) 1–6, [arXiv:hep-ph/0405101 \[hep-ph\]](#). [*Pisma Zh. Eksp. Teor. Fiz.*80,3(2004)].
  - [142] **ALICE** Collaboration, B. B. Abelev *et al.*, “Neutral pion production at midrapidity in pp and Pb-Pb collisions at  $\sqrt{s_{NN}} = 2.76$  TeV,” *Eur. Phys. J. C* **74** no. 10, (2014) 3108, [arXiv:1405.3794 \[nucl-ex\]](#).
  - [143] **PHENIX** Collaboration, A. Adare *et al.*, “Photon-Hadron Jet Correlations in p+p and Au+Au Collisions at  $\sqrt{s} = 200$  GeV,” *Phys. Rev. C* **80** (2009) 024908, [arXiv:0903.3399 \[nucl-ex\]](#).
  - [144] R. Chatterjee, H. Holopainen, T. Renk, and K. J. Eskola, “Collision centrality and  $\tau_0$  dependence of the emission of thermal photons from fluctuating initial state in ideal hydrodynamic calculation,” *Phys. Rev. C* **85** (2012) 064910, [arXiv:1204.2249 \[nucl-th\]](#).
  - [145] D. G. d’Enterria and D. Peressounko, “Probing the QCD equation of state with thermal photons in nucleus-nucleus collisions at RHIC,” *Eur. Phys. J. C* **46** (2006) 451–464, [arXiv:nucl-th/0503054 \[nucl-th\]](#).
  - [146] **ALICE** Collaboration, M. Wilde, “Measurement of Direct Photons in pp and Pb-Pb Collisions with ALICE,” *Nucl. Phys. A* **904-905** (2013) 573c–576c, [arXiv:1210.5958 \[hep-ex\]](#).
  - [147] N. Armesto and E. Scomparin, “Heavy-ion collisions at the Large Hadron Collider: a review of the results from Run 1,” *Eur. Phys. J. Plus* **131** no. 3, (2016) 52, [arXiv:1511.02151 \[nucl-ex\]](#).
  - [148] **PHENIX** Collaboration, S. Mizuno, “Centrality dependence of soft photon production and its collective flow in Au+Au collisions at  $\sqrt{s_{NN}} = 200$  GeV,” *Nucl. Phys. A* **931** (2014) 686–690.

## Bibliography

- [149] **ALICE** Collaboration, D. Lohner, “Measurement of Direct-Photon Elliptic Flow in Pb-Pb Collisions at  $\sqrt{s_{NN}} = 2.76$  TeV,” *J. Phys. Conf. Ser.* **446** (2013) 012028, [arXiv:1212.3995 \[hep-ex\]](#).
- [150] O. Linnyk, V. Konchakovski, T. Steinert, W. Cassing, and E. L. Bratkovskaya, “Hadronic and partonic sources of direct photons in relativistic heavy-ion collisions,” *Phys. Rev.* **C92** no. 5, (2015) 054914, [arXiv:1504.05699 \[nucl-th\]](#).
- [151] **ATLAS** Collaboration, M. Saimpert, “Measurement of Photon Production Cross Sections with the ATLAS Detector,” *PoS DIS2015* (2015) 155.
- [152] T. Sjostrand, S. Mrenna, and P. Z. Skands, “PYTHIA 6.4 Physics and Manual,” *JHEP* **05** (2006) 026, [arXiv:hep-ph/0603175 \[hep-ph\]](#).
- [153] T. Sjöstrand, S. Ask, J. R. Christiansen, R. Corke, N. Desai, P. Ilten, S. Mrenna, S. Prestel, C. O. Rasmussen, and P. Z. Skands, “An Introduction to PYTHIA 8.2,” *Comput. Phys. Commun.* **191** (2015) 159–177, [arXiv:1410.3012 \[hep-ph\]](#).
- [154] J. Bellm *et al.*, “Herwig 7.0/Herwig++ 3.0 release note,” *Eur. Phys. J.* **C76** no. 4, (2016) 196, [arXiv:1512.01178 \[hep-ph\]](#).
- [155] S. Frixione and B. R. Webber, “Matching NLO QCD computations and parton shower simulations,” *JHEP* **06** (2002) 029, [arXiv:hep-ph/0204244 \[hep-ph\]](#).
- [156] S. Höche, S. Schumann, and F. Siegert, “Hard photon production and matrix-element parton-shower merging,” *Phys. Rev.* **D81** (2010) 034026, [arXiv:0912.3501 \[hep-ph\]](#).
- [157] L. D’Errico and P. Richardson, “Next-to-Leading-Order Monte Carlo Simulation of Diphoton Production in Hadronic Collisions,” *JHEP* **02** (2012) 130, [arXiv:1106.3939 \[hep-ph\]](#).
- [158] L. D’Errico, “Merging NLO QCD corrections with parton shower simulations,” PhD thesis, KIT, Karlsruhe, Dept. Phys., 2011.
- [159] A. Buckley *et al.*, “General-purpose event generators for LHC physics,” *Phys. Rept.* **504** (2011) 145–233, [arXiv:1101.2599 \[hep-ph\]](#).
- [160] S. Höche, “Introduction to parton-shower event generators,” in *Theoretical Advanced Study Institute in Elementary Particle Physics: Journeys Through the Precision Frontier: Amplitudes for Colliders (TASI 2014) Boulder, Colorado, June 2-27, 2014*. 2014. [arXiv:1411.4085 \[hep-ph\]](#).
- [161] T. Sjostrand and P. Z. Skands, “Transverse-momentum-ordered showers and interleaved multiple interactions,” *Eur. Phys. J.* **C39** (2005) 129–154, [arXiv:hep-ph/0408302 \[hep-ph\]](#).

- [162] **Particle Data Group** Collaboration, K. A. Olive *et al.*, “Review of Particle Physics,” *Chin. Phys.* **C38** (2014) 090001.
- [163] H. U. Bengtsson, “The Lund Monte Carlo for High  $p_T$  Physics,” *Comput. Phys. Commun.* **31** (1984) 323.
- [164] G. ’t Hooft, “A Planar Diagram Theory for Strong Interactions,” *Nucl. Phys.* **B72** (1974) 461.
- [165] G. Gustafson, “Topological Properties of the Color Field in Hard Processes,” *Z. Phys.* **C15** (1982) 155–160.
- [166] P. Nason and B. Webber, “Next-to-Leading-Order Event Generators,” *Ann. Rev. Nucl. Part. Sci.* **62** (2012) 187–213, [arXiv:1202.1251 \[hep-ph\]](#).
- [167] P. Nason, “A New method for combining NLO QCD with shower Monte Carlo algorithms,” *JHEP* **11** (2004) 040, [arXiv:hep-ph/0409146 \[hep-ph\]](#).
- [168] P. Nason, *The POWHEG BOX V2 framework*. distributed with the POWHEG BOX code rev. 3143.
- [169] E. Boos *et al.*, “Generic user process interface for event generators,” in *Physics at TeV colliders. Proceedings, Euro Summer School, Les Houches, France, May 21-June 1, 2001*. 2001. [arXiv:hep-ph/0109068 \[hep-ph\]](#).
- [170] J. M. Butterworth *et al.*, “THE TOOLS AND MONTE CARLO WORKING GROUP Summary Report from the Les Houches 2009 Workshop on TeV Colliders,” in *Physics at TeV colliders. Proceedings, 6th Workshop, dedicated to Thomas Binoth, Les Houches, France, June 8-26, 2009*. 2010. [arXiv:1003.1643 \[hep-ph\]](#).
- [171] L. Barze, G. Montagna, P. Nason, O. Nicrosini, and F. Piccinini, “Implementation of electroweak corrections in the POWHEG BOX: single W production,” *JHEP* **04** (2012) 037, [arXiv:1202.0465 \[hep-ph\]](#).
- [172] S. Alioli, K. Hamilton, P. Nason, C. Oleari, and E. Re, “Jet pair production in POWHEG,” *JHEP* **04** (2011) 081, [arXiv:1012.3380 \[hep-ph\]](#).
- [173] C. Schmidt, J. Pumplin, D. Stump, and C. P. Yuan, “CT14QED parton distribution functions from isolated photon production in deep inelastic scattering,” *Phys. Rev.* **D93** no. 11, (2016) 114015, [arXiv:1509.02905 \[hep-ph\]](#).
- [174] S. Alioli, P. Nason, C. Oleari, and E. Re, “Vector boson plus one jet production in POWHEG,” *JHEP* **01** (2011) 095, [arXiv:1009.5594 \[hep-ph\]](#).
- [175] P. Nason and C. Oleari, “Generation cuts and Born suppression in POWHEG,” [arXiv:1303.3922 \[hep-ph\]](#).

## Bibliography

- [176] L. Barze, M. Chiesa, G. Montagna, P. Nason, O. Nicrosini, F. Piccinini, and V. Prospero, “ $W\gamma$  production in hadronic collisions using the POWHEG+MiNLO method,” *JHEP* **12** (2014) 039, [arXiv:1408.5766 \[hep-ph\]](#).
- [177] L. Lönnblad, “Fooling Around with the Sudakov Veto Algorithm,” *Eur. Phys. J.* **C73** no. 3, (2013) 2350, [arXiv:1211.7204 \[hep-ph\]](#).
- [178] M. Cacciari, G. P. Salam, and G. Soyez, “FastJet User Manual,” *Eur. Phys. J.* **C72** (2012) 1896, [arXiv:1111.6097 \[hep-ph\]](#).
- [179] M. Cacciari, G. P. Salam, and G. Soyez, “The Anti- $k(t)$  jet clustering algorithm,” *JHEP* **04** (2008) 063, [arXiv:0802.1189 \[hep-ph\]](#).
- [180] **CMS** Collaboration, V. Khachatryan *et al.*, “Evidence for collectivity in pp collisions at the LHC,” *Submitted to: Physics Letters B* (2016) , [arXiv:1606.06198 \[nucl-ex\]](#).
- [181] **PHENIX** Collaboration, S. S. Adler *et al.*, “Dense-Medium Modifications to Jet-Induced Hadron Pair Distributions in Au+Au Collisions at  $s(NN)^{1/2} = 200$ -GeV,” *Phys. Rev. Lett.* **97** (2006) 052301, [arXiv:nucl-ex/0507004 \[nucl-ex\]](#).
- [182] R. K. Ellis and G. Zanderighi, “Scalar one-loop integrals for QCD,” *JHEP* **02** (2008) 002, [arXiv:0712.1851 \[hep-ph\]](#).
- [183] J. C. Collins, *Renormalization*, vol. 26 of *Cambridge Monographs on Mathematical Physics*. Cambridge University Press, Cambridge, 1986.
- [184] E. Leader and E. Predazzi, “A note on the implications of gauge invariance in QCD,” *J. Phys.* **G40** (2013) 075001, [arXiv:1101.3425 \[hep-ph\]](#).
- [185] A. Denner, “Techniques for calculation of electroweak radiative corrections at the one loop level and results for W physics at LEP-200,” *Fortsch. Phys.* **41** (1993) 307–420, [arXiv:0709.1075 \[hep-ph\]](#).
- [186] A. M. Gonzalez, “Spin and colour correlations for prompt photon production in heavy-ion collisions,” B.Sc. thesis, Westfälische Wilhelms-Universität Münster, 2013.

# Acknowledgements

- For giving me the opportunity and providing the resources to study and research the topic of this thesis, I thank Prof. Dr. Michael Klasen.
- In the years spent on this thesis, various people have been my office mates and served as much appreciated discussion partners, especially Michael Topp, Marcel Rothering and David Regalado Lamprea.
- Now and then, Dr. Karol Kovařík was willing to spend his time on listening to my thoughts on specific technical aspects of my calculations and discuss them.
- A big help have been the administrators I worked with, especially Dirk Sandbrink, Anton Daitche and Thomas Zub.
- Lots of lunches, dinners and BBQs provided much needed breaks, also thanks to the comedic talent of many people. I'm not listing all of them for fear of forgetting someone.
- Likewise, some days have been spend on hiking trips, often organized by Christoph Borschensky, which have been most welcome.
- Yet another thank you goes out to my family.





# Lebenslauf

Name	Florian König
Geburtsdatum	27 März 1986
Geburtsort	Coesfeld
Staatsangehörigkeit	deutsch
Eltern	Heinz-Peter und Annette König

## Schulausbildung

August 1992 - August 1993	Lambertischule, Coesfeld
August 1993 - August 1996	Jakobi-Schule, Coesfeld
August 1996 - Juni 2005	St.-Pius-Gymnasium, Coesfeld
25 Juni 2005	Abitur am St.-Pius-Gymnasium

## Studium

Oktober 2006 - Februar 2012	Studium der Physik an der Westfälischen Wilhelms-Universität Münster
29 September 2008	Diplom-Vorprüfung
April 2010 - Februar 2012	Diplomarbeit in Physik <i>Lösung der Feldgleichung einer durch Randbedingungen fixierten kritischen Grenzfläche</i>
24 Februar 2012	Diplomprüfung

## Promotionsstudium

März 2012	Beginn der Dissertation am Institut für Theoretische Physik Unter der Betreuung von Prof. Dr. Michael Klasen
-----------	---

## Berufstätigkeit

Dezember 2005 - März 2006	Produktionshilfe bei PVE DT, Coesfeld
April 2010 - Februar 2012	Studentische Hilfskraft am ITP, WWU Münster
März 2012 - Februar 2016	Wissenschaftlicher Mitarbeiter am ITP, WWU Münster